University of Southampton

FACULTY OF PHYSICAL SCIENCES AND ENGINEERING

DEPARTMENT OF ELECTRONICS AND COMPUTER SCIENCE

Digital Optical Fibre Aided Virtual MIMO Systems in Multicell Multiuser Networks

by

Xinyi Xu

A thesis submitted in partial fulfillment of the
requirements for the award of Doctor of Philosophy
at the University of Southampton

April 2013

SUPERVISOR: *Professor Lajos Hanzo*
FREng, FIEEE, FIEE, DSc, EIC IEEE Press
Chair of Communications, Signal Processing and Control Group
Department of Electronics and Computer Science
University of Southampton
Southampton SO17 1BJ
United Kingdom

Dedicated to my family and our would be baby.

UNIVERSITY OF SOUTHAMPTON

ABSTRACT

FACULTY OF PHYSICAL SCIENCES AND ENGINEERING
DEPARTMENT OF ELECTRONICS AND COMPUTER SCIENCE

Doctor of Philosophy

Digital Optical Fibre aided Virtual Multiple-input and Multi-output in Multicell Multiuser Networks

by Xinyi Xu

Advanced communication networks are conceived by amalgamating the techniques of distributed antennas (DAS) and fractional frequency reuse (FFR), where the cell-edge area additionally relies on FFR for the sake of reducing the co-channel interference (CCI). Since DASs rely on the availability of a backhaul, we consider a realistic - rather than perfect - optical fibre backhaul and develop a model for a composite optical fibre and wireless channel, which is capable of representing the effects of the fibre-induced imperfections imposed on the attainable throughput and the BER performance of the entire system. More explicitly, we demonstrate the effects of the fibre's linear dispersion and nonlinearity on both noncooperative and cooperative DAS aided FFR schemes.

The proposed pervasive DAS/FFR scheme has a low complexity, since it employs a single omni-directional transmit element at each remote antenna (RA) and a single receive element at each mobile station (MS). The resultant system is jointly modelled as a virtual multiple-input and multi-output (MIMO). Hence, jointly designing the transmit pre-processing (TPP) matrix of all the cooperative RAs in the case of the downlink (DL) is shown to be beneficial. Similarly, the joint design of the multiuser detector (MUD) coefficients for all the active MSs transmitting in the uplink (UL) is carried out by the central processor of the base station (BS).

The dominant interference of our DAS/FFR scheme is caused by the intra-cell interference (ICI) for both cases of DL and UL, especially in the 'worst-case direction' when the MS is roaming near the angle halfway between two adjacent RAs. In order to mitigate the ICI, the TPP matrix is designed for all the cooperative RAs is capable of achieving an increased throughput for the entire cell-edge area in DL, regardless of the specific geographic distribution of the users. Our novel combined probabilistic data association (PDA)

multiuser detector is invoked by the mobile relays (MR) aided pervasive DAS/FFR architecture, which is capable of substantially reducing the bit-error ratio (BER) for the MS roaming at arbitrary positions, especially in the 'worst-case direction'.

Practically, the generation of perfect Channel State Information (CSI) remains an open challenge, whilst having an imperfect CSI leads to a reduced performance. Hence, we also investigate the impact of practical impairments including the effects of CSI estimation errors, CSI quantisation errors as well as Orthogonal Frequency Division Multiplexing (OFDM) signal timing and frequency synchronisation errors in DL scenario. We further extended the Single-Input Single-Output (SISO) based non-coherent 16StQAM scheme to a Single-Input Multiple-Output (SIMO) system in UL scenario, when both the Turbo-Coded 16StQAM and 16QAM schemes in the multicell, multiuser uplink system considered without the perfect CSI.

Finally, we consider a practical multiuser, multicell scenario, where a particular user's position is mapped to a specific Signal-to-Interference-plus-Noise-Ratio (SINR). This method allows us to portray the geographic of the SINR across the entire cellular area. In the DL of the cooperative DAS aided FFR scheme, a throughput of $\eta = 5bits/s/Hz$ may be maintained for an imperfect optical fibre backhaul, regardless of the specific geographic distribution of the users roaming in the cell edge area. Provided that an idle MR may be activated in the vicinity of the optimum relay position, in the UL of the cooperative DAS aided FFR scheme, 80% of the cell-edge area exhibits a BER, which is better than 10^{-4}, while the remaining 20% has a BER value of $[10^{-4} \cdots 10^{-2}]$. Naturally, this BER performance improvement is achieved at the cost of potentially halving the throughput, because the MR has to receive and retransmit its information in different time-slots. When applying power control (PC), the BER recorded across the entire cellular area may be reduced, below 10^{-3} even without the assistance of MRs.

Declaration of Authorship

I, **Xinyi Xu**, declare that the thesis entitled **Digital Optical Fibre Aided Virtual MIMO Systems in Multicell Multiuser Networks** and the work presented in it are my own and has been generated by me as the result of my own original research. I confirm that:

- This work was done wholly or mainly while in candidature for a research degree at this University;
- Where any part of this thesis has previously been submitted for a degree or any other qualification at this University or any other institution, this has been clearly stated;
- Where I have consulted the published work of others, this is always clearly attributed;
- Where I have quoted from the work of others, the source is always given. With the exception of such quotations, this thesis is entirely my own work;
- I have acknowledged all main sources of help;
- Where the thesis is based on work done by myself jointly with others, I have made clear exactly what was done by others and what I have contributed myself;
- Parts of this work have been published.

Signed: ..... Date: .....

Acknowledgements

I would like to express my heartfelt gratitude to Professor Lajos Hanzo for his outstanding supervision and support throughout my research. His guidance, inspiration and encouragement have greatly benefited me not only in work but also in life. He has also managed to cultivate in me the desire to be a good researcher through his enthusiasm and perseverance in research. Most importantly, I would like to thank him for his invaluable friendship.

Many thanks also to my colleagues and the staff of the Communications Group, both past and present, for their support, help and discussions throughout my research. I would like to thank Dr. Rong Zhang for his suggestions and help to solve the problem when we cooperated. I also want to thanks Dr. Soon Xin Ng for his effort and help to point the incorrections in my work. I also want to thank Dandan Liang, Shaoshi Yang and Salman Ghafoor for their help when I once work with them. Thanks to Professor Sheng Chen, Professor Lie-Liang Yang, Dr. Rob Maunder and Dr. Mohammed El-Hajjar for the knowledge I learn from them. Thanks to my friends I have during my PhD years, Jing Zuo, Wei Liu, Ke Yuan, Wei Liang, Jia Shi, Shida Zhong, Jiao Feng, and all other colleagues and staff in our group, too numerous to mention here explicitly. Special thanks are also due to Denise Harvey and Lauren J Dampier for her help in the administrative matters.

The financial support of the UK-China Scholarship for Excellent projects is also gratefully acknowledged.

I would also like to express my appreciation to my parents for their love and support. Especially, to my beloved husband Dr. Ke Li, for his love, support, encourage and care for me. Finally, to our would be baby, for her/his birth giving me courage, motivation and harmony.

List of Publications

1. **X. Xu, R. Zhang, S. Ghafoor, L. Hanzo**, “Imperfect Digital Fibre Optic Link Based Cooperative Distributed Antennas with Fractional Frequency Reuse in Multi-cell Multiuser Networks”, IEEE Transactions on Vehicular Technology, vol. 60, pp. 4439-4449, Nov. 2011.

2. **X. Xu, S. Yang, R. Zhang, Q. Zhu, L. Hanzo**, “Pervasive distributed antennas and mobile relays for fractional frequency reuse based multicell multiuser networks”, IEEE Transactions on Vehicular Technology (Submitted)

3. **D. Liang, V. A. Thomas, X. Xu, S. X. Ng, L. Hanzo**, “Adaptive Soft-Decision Aided Differential Modulation for Cooperative Wireless and Optical-Fiber Communications”, IEEE Transactions on Vehicular Technology (Submitted)

4. **X. Xu, R. Zhang, L. Hanzo**, “Imperfect Radio Over Fibre Aided Distributed Antennas with Fractional Frequency Reuse”, Proceedings of IEEE Vehicular Technology Conference (VTC) Fall, Ottawa, Canada, September 2010, pp. 1-5.

5. **X. Xu, R. Zhang, L. Hanzo**, “Digital RoF Aided Cooperative Distributed Antennas with FFR in Multicell Multiuser Networks”, Proceedings of IEEE Vehicular Technology Conference (VTC) Fall, San Francisco, United States, May 2011, pp. 1-5.

6. **R. Zhang, X. Xu, L. Hanzo**, “Co-channel Interference Mitigation Capability of Fixed Relays Connected by Optical Fibre”, Proceedings of IEEE Vehicular Technology Conference (VTC) Fall, Ottawa, Canada, September 2010, pp. 1-5.

7. **D. Liang, X. Xu, S. X. Ng, L. Hanzo**, “Turbo-coded star-QAM for cooperative wireless and optical-fiber communications“. 3rd International Conference on Photonics, Penang, Malaysia, 01 - 03 Oct 2012. 5pp, 267-271.

8. **J. Zhang, R. Zhang, X. Xu, G. Li, L. Hanzo**, ”Effects of practical impairments on cooperative distributed antennas combined with fractional frequency reuse”. In, IEEE WCNC2012: 2012 IEEE Wireless Communications and Networking Conference, Paris, FR, 01 - 04 Apr 2012. 5pp.

Contents

Abstract **ii**

Declaration **iv**

Acknowledgements **v**

List of Publications **vi**

1 Introduction **1**

1.1 Motivation 1

1.1.1 Fractional Frequency Reuse 2

1.1.2 Distributed Antenna Systems 3

1.1.3 Coordinated Multipoint Transmission 7

1.1.4 Optical Fibre Backhaul 8

1.2 Organization of the Thesis and Novel Contributions 10

2 Optical Fibre Backhaul **15**

2.1 Introduction and Outline 15

2.2 Optical Fibre Backhaul 17

2.2.1 Digital Over Fibre and Radio Over Fibre Techniques 17

2.2.2 Characteristics of the Optical Fibre Channel 19

2.2.2.1 Linear Effects 19

2.2.2.2 Nonlinear Effects 22
2.3 The Composite Channel of a DOF-Aided Wireless Relaying System . . . 23
2.3.1 Optical Fibre Based Fixed Relay Aided System 24
2.3.1.1 Shamai-Wyner Interference Model 24
2.3.2 Analysis of The Interference Mitigation Techniques 25
2.3.2.1 Received Signal Strength 25
2.3.2.2 Interference Mitigation Techniques 27
2.3.2.3 System Throughput 30
2.3.3 Performance Evaluation 32
2.3.3.1 Throughput of the Classic Direct-Relaying Scheme . . 32
2.3.3.2 Throughput of the Eigen-Beamforming Technique . . . 34
2.3.3.3 Throughput of the Reduced-Power Technique 34
2.3.3.4 Throughput of the Hybrid Technique 34
2.3.3.5 Effects of IPI 35
2.4 Chapter Conclusions 37

3 Distributed Antennas for the Fractional Frequency Reuse Aided Multicell, Multiuser Downlink 40

3.1 Introduction 40
3.2 System Description and Optical Fibre Modelling 43
3.2.1 Multicell, Multiuser System Topology 43
3.2.2 Imperfect Optical Fibre Model 44
3.3 Received Signal of DOF Aided DAS Assisted FFR Systems 48
3.3.1 DOF aided Non-Cooperative DAS Assisted FFR system 48
3.3.1.1 Received Signal in the Cell-Centre Area 48
3.3.1.2 Received Signal in the Cell-Edge Area 49
3.3.1.3 Idealistic Received Signal in the Cell-Edge Area 49
3.3.1.4 Benchmarker Systems 50
3.3.2 DOF Aided Cooperative DAS Assisted FFR 50

3.3.2.1 Received Signal-to-Interference-plus-Noise-Ratio . . . 50
3.3.2.2 Linear Transmit PreProcessing . . . 52
3.4 Performance Evaluation . . . 54
3.4.1 Simulation Assumptions . . . 54
3.4.2 Propagation regimes in the DOF Link . . . 54
3.4.3 Throughput Performance . . . 56
3.4.3.1 IRI Inflicted by the Tier-two Cells . . . 56
3.4.3.2 Throughput of the Cell-center Area . . . 58
3.4.3.3 Cell-edge Area of Non-cooperative DAS Relying on FFR 58
3.4.3.4 Cell-edge Area of Cooperative DAS Relying on FFR . 63
3.4.3.5 Throughput Enhancement Across the Entire Cell . . . 65
3.4.4 Power Control for a Multiuser DL Scenario . . . 66
3.4.5 Chapter Summary . . . 70
3.5 Chapter Conclusions . . . 71

4 Distributed Antennas for the Fractional Frequency Reuse Aided Multicell, Multiuser Uplink 73

4.1 Introduction . . . 73
4.2 System Description . . . 76
4.2.1 Multicell, Multiuser System Topology . . . 76
4.2.1.1 Pervasive DAS/FFR Combined with Mobile Relays . . 76
4.2.1.2 Conventional BS Cooperation Aided Networks . . . 78
4.2.1.3 Digital Fibre Soliton Aided Backhaul . . . 80
4.3 Received Signal of the Pervasive DAS/FFR System . . . 82
4.3.1 Received Signal of a Single Link . . . 83
4.3.2 Received Signal of a Virtual MIMO . . . 84
4.3.3 Correlation Between the Channel Coefficients of MS_i and MR_i . 85
4.3.4 Central Signal Processing . . . 86
4.3.4.1 Joint ML Multiuser Detector . . . 86

4.3.4.2 PDA Aided Multiuser Detector 87
4.3.5 Combining the Soft-information of the MRs Using PDA 89
4.3.6 MMSE-OSIC Detector 90
4.4 Performance Evaluation 90
4.4.1 Simulation Assumptions 90
4.4.2 Conventional BS Cooperation 92
4.4.3 Pervasive DAS/FFR 93
4.4.3.1 Cell-Edge Area 94
4.4.3.2 Cell-Center Area 97
4.4.3.3 MR Selection 97
4.4.4 Conventional BS Cooperation versus Pervasive DAS/FFR 98
4.4.5 Power Control for Multiuser in the UL Scenario 100
4.4.6 Chapter Summary 102
4.5 Chapter Conclusions 103

5 Effects of Imperfect Channel Knowledge on the DL and Non-coherent Systems for the UL 106

5.1 Introduction and Outline 106
5.2 Effects of Practical Impairments on the DAS/FFR Scheme in DL 108
5.2.1 System Description 108
5.2.1.1 Configurations and Assumptions 108
5.2.1.2 DAS Aided FFR Scenario 109
5.2.2 Practical Impairments in COMP-Aided DAS 111
5.2.2.1 COMP-Aided DAS with FFR 111
5.2.2.2 Practical Impairments 112
5.2.2.3 Synchronisation Errors 113
5.2.3 Performance Evaluation 116
5.2.3.1 Achievable SINR of Users in the Worst-case Direction . 117
5.2.3.2 Effects of Time-Offset and Frequency-Offset 117

5.2.4 Summary of Section 5.2 119
5.3 Turbo-Coded Star-QAM for Distributed Antennas Relying on FFR in the UL 119
5.3.1 System Model and Analysis 119
5.3.2 Imperfect Optical Fibre Model 120
5.3.3 Detection Model 122
5.3.4 Simulation Results 124
5.3.5 Summary of Section 5.3 127
5.4 Chapter Conclusions 128

6 Conclusions of the Thesis **130**
6.1 Summary and Conclusions 130
6.2 Suggestions for Future Work 135

Appendix A **i**

Appendix B **i**

Bibliography **iii**

Subject Index **xxi**

Author Index **xxiv**

List of Symbols

General notation

- The superscript * is used to indicate complex conjugation. Therefore, a^* represents the complex conjugate of the variable a.
- The superscript ^{T} is used to indicate matrix transpose operation. Therefore, $\mathbf{a}^T$ represents the transpose of the matrix $\mathbf{a}$.
- The superscript ^{H} is used to indicate complex conjugate transpose operation. Therefore, $\mathbf{a}^H$ represents the complex conjugate transpose of the matrix $\mathbf{a}$.
- The notation $*$ denotes the convolutional process. Therefore, $a * b$ represents the convolution between variables a and b.

Special symbols

α: The kilometric attenuation coefficien of optical fibre.

α_{dB}: The units of kilometric attenuation in dB of optical fibre.

P: The transmit power.

ΔT: The kilometic pulse broadening.

c: The speed of light.

β_2: TheGroup-Velocity Dispersion parameter.

D: The wavelength-dependent dispersion parameter.

L: The optical fibre's length.

L_D: The dispersion length.

L_N: The nonlinear length.

R: The radius.

n: The complex-valued Additive White Gaussian Noise.

η: The attainable throughput.

γ: The nonlinearity parameter.

χ: The normalised power-scaling factor.

ψ_{ga}: the large-scale slow fading.

ρ: The distance ratio.

θ: The angular rotation.

R_M: The rate of the modulation scheme.

R_C: The rate of channel code.

I: The mutual information per bit.

y_i: The ith signal received.

$\mathbf{y}$: The the received signal vector.

$\mathbf{h}_i$: The ith channel vector.

$\mathbf{n}$: The circularly symmetric complex Gaussian noise vector.

$\mathbf{x}$: The transmitted signal vector.

$\mathbf{H}$: The estimate of the channel matrix.

$\mathbf{T}$: The transmit matrix.

$\mathbf{G}$: The linear transmit matrix.

$\tilde{\mathbf{n}}$: The colored Gaussian noise.

$\tilde{\mathbf{y}}$: The decorrelated signal.

$E(\cdot)$: The mean function.

$V(\cdot)$: The covariance function.

$U(\cdot)$: The pseudocovariance function.

$\mathbf{P}$: The probability vector.

F: : The bandwidth.

$\sum$: The sum operation.

$exp(\cdot)$: The exponential operation.

$||\cdot||$: The Frobenius norm.

$|\cdot|$: The absolute value.

$sgn(\cdot)$: The sign function.

$\mathbf{E}(\cdot)$: The expectation.

$log(\cdot)$: The logarithm operation.

$\mathit{trace}(\cdot)$: The trace operator.

$\mathbf{I}_n$: The $n \times n$ identity matrix.

Glossary

4G: The fourth-generation

3GPP-LTE: The Third Generation Partnership Program Long Term Evolution

CCI: Co-channel interference

FFR: Fractional frequency reuse

ASE: Area-spectral-efficiency

UFR: Unity Frequency Reuse

IMT: International Mobile Telecommunications

DL: Downlink

UL: Uplink

COMP: Coordinated Multicell Processing

CAS: Centralized Antennas

RAs: Remote Antennas

DAS: Distributed antennas

APP: A Posteriori Probability

MS: Mobile Station

TPP: Transmit Pre-Processing

MIMO: Multiple-Input and Multi-Output

MISO: Multiple-Input and Single-Output

MUD: Multiuser Detection

MR: Mobile Relay

PDA: Probabilistic Data Association

CPDA: Combined PDA

PC: Power Control

CSI: Channel State Information

CQI: Channel Quality Information

ICI: Intra-Cell Interference

OFDM: Orthogonal Frequency Division Multiplexing

SISO: Single-Input Single-Output

SIMO: Single-Input Multiple-Output

CDMA: Code Division Multiple Access

FDMA: Frequency Division Multiple Access

WDM: Wavelength-Division Multiplexing

TDM: Time-Division Multiplexing

SDM: Space-Division Multiplexing

OOK: On-Off Keying

DPSK: Differential Phase-Shift Keying

PSK: Phase-Shift Keying

ASK: Amplitude-Shift Keying

ROF: Radio Over Fiber

DOF: Digital Optical Fibre

MSC: Mobile Switching Centre

MC-CDMA: Multi-Carrier Code Division Multiple Access

3GPP: Third Generation Partnership Project's

DAC: Digital to Analog

ADC: Analog to Digital converter

EDFA: Erbium Doped Fibre Amplifier

SMF: Single Mode Fibre

OFC: Optical Fibre Communication

ASEN: Amplified Spontaneous Emission Noise

SPM: Self-Phase Modulation

XPM: Cross-phase Modulation

FWM: Four-wave Mixing

NLS: Nonlinear Schrödinger

DDFs: Dispersion Decreasing Fibres

RF: Radio Frequency

SSF: Split-Step Fourier

MMSE: Minimum Mean Square Error

TC: Turbo Coded

StQAM: Star-Quadrature Amplitude Modulation

PB: Pulse Broadening

IPI: Inter Pulse Interference

GVD: Group Velocity Dispersion

IRI: Inter RA Interference

egBF: EigenBeamformer

ED: Euclidean Distances

BLER: BLock Error Rate

BICM: Bit Interleaved Coded Modulation

RCPTC: Rate Compatible Punctured Turbo Codes

MCS: Modulation and Coding Scheme

JSLNR: Linear Joint Signal to Leakage Noise Ratio

FFT: Fast Fourier Transform

CIR: Channel Impulse Response

CP: Cyclic Prefix

BER: Bit error ratio, the number of the bits received incorrectly

SNR: Signal to Noise Ratio, noise energy compared to the signal energy

QAM: Quadrature Amplitude Modulation

PDF: Probability Density Function

SINR: Signal to Interference plus Noise ratio

SIR: Signal to Interference ratio

GSM: A Pan-European digital mobile radio standard, operating at 900MHz.

AWGN: Additive White Gaussian Noise

FEC: Forward Error Correction

CDMA: Code Division Multiple Access

BS: A common abbreviation for Base Station

MS: A common abbreviation for Mobile Station

WLAN: Wireless Local Area Network

QoS: Quality of Service

QAM: Quadrature Amplitude Modulation

OFDM: Orthogonal Frequency Division Multiplexing

BPSK: Binary Phase Shift Keying

QPSK: Quadrature Phase Shift Keying

MAP: Maximum A Posteriori

LLR: Log Likelihood Ratio

ML: Maximum Likelihood

Chapter 1

Introduction

1.1 Motivation

The fourth-generation (4G) wireless communication systems are expected to support a high performance for anyone, anywhere and anytime, predominantly relying on the Third Generation Partnership Program Long Term Evolution (3GPP-LTE) [1]. The target of 3GPP- LTE is that of increasing the system's throughput and transmission integrity across the entire cell area [1] [2] [3] [4]. Hence, improving the performance of the users roaming in the cell-edge area becomes the main challenge [5], because the users' Quality-of-Service (QoS) perception is typically predetermined by the worst-case QoS. To elaborate a little further, the perceived QoS is generally predetermined by diverse metrics, such as the delay, the signal-to-noise ratio (SNR), the throughput, the Signal-to-Interference-plus-Noise-Ratio (SINR), bit error ratio (BER), etc. One of the promising solutions conceived for mitigating the CCI is to invoke the FFR concept [3], albeit this results in a reduced ASE [6] in comparison to the radical unity frequency reuse (UFR) [5]. In this thesis, we focus our attention on the interference management of multiuser, multicell scenarios. Fig. 1.1a portrays two tiers of 19 cells invoking the above-mentioned UFR pattern, where the users suffer from strong CCI imposed by all the active BS. By contrast, Fig. 1.1b shows two tiers of 19 cells relying on the FFR pattern, where the CCI is reduced since the users only suffer from the CCI inflicted by the active BSs in the second tier, which are allocated the same frequency as the reference cell [7] [8].

The LTE standard (Release 8) [1] [2] has been further developed by the LTE-Advanced (Release 10) [9] initiative, which is capable of meeting the International Mobile Telecommunications (IMT) specification [10]. The LTE-Advanced [9] systems is expected to rely on a bandwidth of $100MHz$ and potentially may support a rate of $1Gb/s$ for the down-

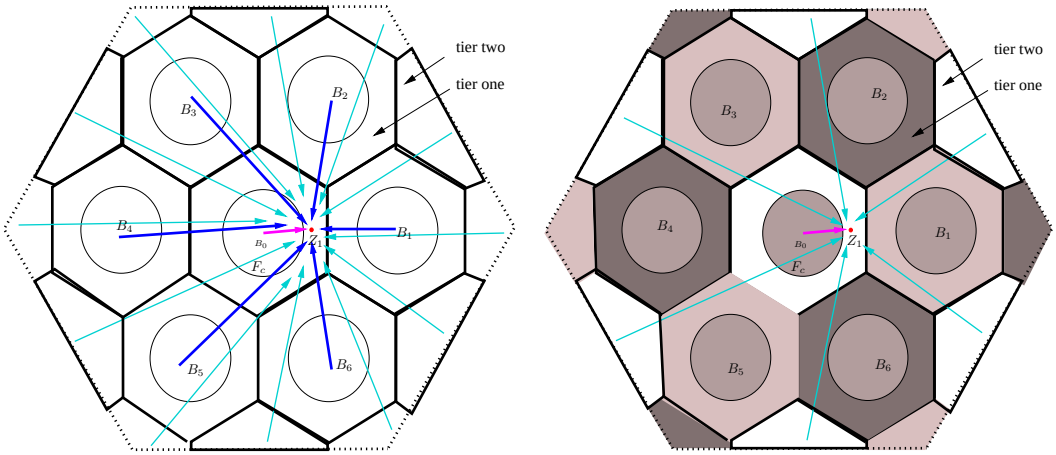

(a) Unity Frequency Reuse (b) Fractional Frequency Reuse

Figure 1.1: The topology of two tiers of nineteen cells relying on a UFR and FFR scheme

link (DL), whilst $500MBit/s$ for the UL. DAS [11], Coordinated Multicell Processing (COMP) [12] regime and relaying techniques [13] are attractive in terms of further improving the attainable system performance [14]. Hence, the conventional cellular network relying on Centralized Antennas (CAS) at the BS may evolve to a DAS architecture combined with the FFR scheme, as seen in Fig. 1.2. In comparison to the conventional CAS used at the BS, the DAS may improve the coverage of the entire cell by positioning the Remote Antennas (RAs) of the DAS in both the cell-center area and the cell-edge area. We refer to this regime as a pervasive DAS/FFR scheme, while the BS simply plays the role of the central signal processing (CSP) unit in our pervasive DAS architecture, which will be studied in Chapter 4. More explicitly, our goal is to design an architecture, which would offer a high SINR across the entire cellular area [15]. The resultant system is capable of increasing the throughput for the entire coverage area without requiring extra transmit power. We will investigate a range of sophisticated techniques, such as TPP for the DL and COMP for the UL in the context of a practical system model, where any particular user's position is characterised by a specific SINR.

1.1.1 Fractional Frequency Reuse

The concept of FFR was proposed first for the second-generation (2G) wireless communication systems also known as the Global System of Mobile Communications (GSM) [16]. This concept was then also invoked for 3GPP-LTE [1]- [2], which is an attractive strategy due to its low complexity and as a benefit of its significant gains. As demonstrated in the Table. 1.1, the FFR concept has been proposed for diverse communication systems. There

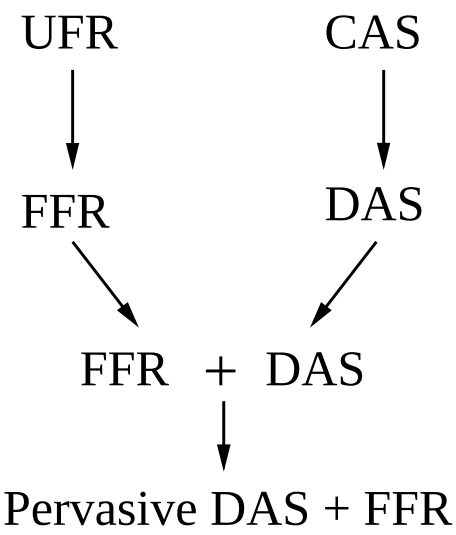

Figure 1.2: Evolution of communication network architecture.

are two basic types of FFR, namely *strict FFR* and *soft FFR* [17]. In case of strict FFR, the total frequency band is partitioned between the cell-center area f_c and cell-edge area f_e. The users roaming in the cell-center area of all cells are allocated the same frequency band f_c, while the users roaming in the cell-edge area are allocated separate subbands in the adjacent cells with a reuse factor 3, hence we have $f_1 + f_2 + f_3 = f_e$. The primary advantage of strict FFR is the significant reduction in interference for users in the cell-edge area as portrayed in Fig. 1.1b. By contrast, in soft FFR users in the cell-center area are allowed to share their frequency band with users in the cell-edge area of other cells. In comparsion to soft FFR, strict FFR reduced the interference imposed on the users in the cell-edge area at the cost of reducing the bandwidth available to both the cell-center and cell-edge users. Hence, we opted for using strict FFR for the DAS aided FFR systems in both Chapter 3 and Chapter 4.

1.1.2 Distributed Antenna Systems

The FFR regime is capable of reducing the CCI, as shown in Fig. 1.1b. However, the pathloss of the distant users roaming in the cell-edge area still improves a low SINR. Hence, we configured our DAS to install RAs closer to the cell-edge area. The early studies of the DASs [27] [28] and [29] exploited that the RA are capable of reducing the pathloss and increasing the diversity gain. In [30] a cooperative technique was invoked for mitigating the interference imposed by the DAS system. In this thesis, we first combined the DAS concept with the FFR technique for mitigating the CCI, as shown in Fig. 1.3.

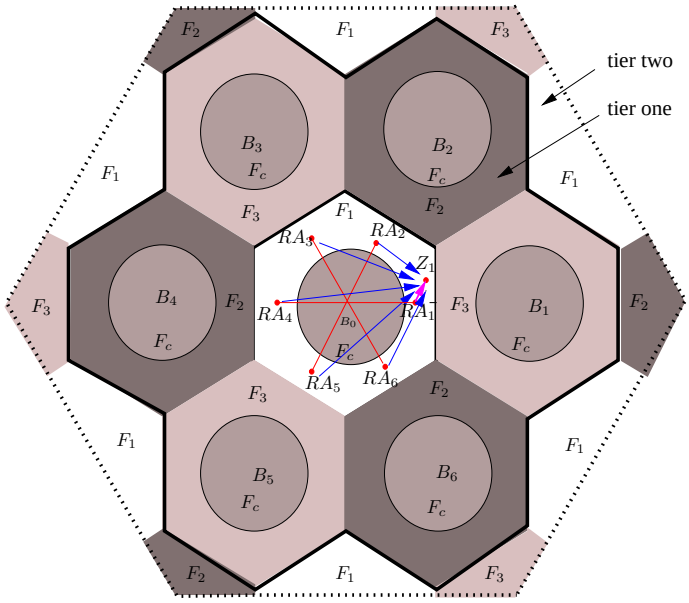

Figure 1.3: The topology of two tiers of nineteen cells relying on a FFR and DAS aided arrangement, where a single omni-directional transmit element is invoked in each RA. Hence the coverage area of each RA is in reality a circle, not a hexagonal area.

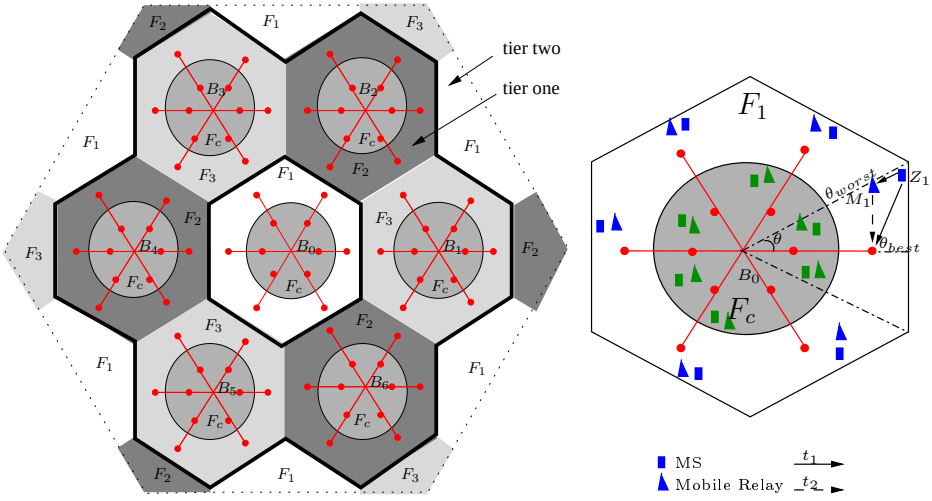

(a) (b)

Figure 1.4: The topology of a pervasive DAS/FFR scheme assisted by a MR in a two-tier, nineteen-cell scenario.

Table 1.1: Contributions to FFR in cellular networks

Year	Authors	Contribution
1996	Riva *et al.* [18]	Provided frequency planning techniques such as the concept of fractional reuse.
2001	Cardieri and Rappaport [19]	Proposed the FFR concept relying on smart antennas for mitigating the CCI.
2002	Begain *et al.* [20]	Investigated the FFR concept in the context of GSM systems.
2003	Sternad *et al.* [21]	Advocated coordinated scheduling of the cell-sector using FFR for OFDM systems.
2008	Chang *et al.* [22]	Combined cooperative interference mitigation with FFR.
2009	Chandrasekhar and Andrews [23]	Proposed the FFR strategy for femtocells in two-tier networks.
2010	Novlan *et al.* [17]	Investigated the concept of strict FFR and soft FFR in OFDMA systems.
2011	Xu *et al.* [24]	Proposed a DAS-aided FFR scheme for multiuser multicell scenarios.
2012	Xu *et al.* [25]	Proposed the optimal threshold for FFR schemes for OFDMA Cellular Networks
2013	Novlan and Andrews [26]	Analyzed the evaluation of FFR in UL.

More explicitly, Fig. 1.3 shows that in comparison to the conventional FFR scheme of Fig. 1.1b, the DAS-aided FFR scheme is capable of substantially reducing the CCI. The CCI imposed by the first-tier cells is mitigated by invoking the FFR, whilst the CCI arising from the second-tier may be ignored, because the DAS scheme operates at a low transmit power. Hence, it is possible for us to focus our attention purely on the ICI, as seen in Figure 1.3. Secondly, we also cooperative techniques for our DAS aided system, which may further reduce the ICI. On the other hand, although the DAS is capable of reducing the CCI, when combined with FFR, but the cooperative diversity gain gleaned from the adjacent cells may be eroded. Hence, as a further enhancement we introduce MR into the proposed pervasive DAS/FFR arrangement, as seen in Fig. 1.4a for the UL, in order to improve the achievable cooperative diversity gain at the cost of reserving an additional time-slot for the MRs, as seen in Fig 1.4b.

Table 1.2: Contributions to DAS in cellular networks

Year	Authors	Contribution
1987	Saleh *et al.* [31]	Proposed the DAS concept for indoor scenarios.
1996	Kerpez [27]	Conceived a radio access system relying on multiple antennas spatially distributed throughout each cell, instead of using a single antenna for each cell.
2003	Hairuo *et al.* [32]	Proposed a sub-optimal power allocation strategy for a DAS relying on random RAs.
2005	Dai *et al.* [33]	Investigated a DAS aided CDMA system.
2006	Han *et al.* [34]	Designed a transmit antenna selection scheme relying on a power- and rate- allocation scheme for DAS systems.
2007	Wan and Andrews [35]	Studied a DAS-aided DL multicell scenario.
2008	Zhang and Andrews [28]	Considered a DAS systems operating in the scenario of random channel effects and randomly positioned mobile users as well as the RAs.
2009	Park *et al.* [30]	Proposed different cooperation strategies for DASs.
2010	Castanheira and Gameiro [29]	Demonstrated that the most important DAS system property in multiuser scenarios is the symmetric allocation of the RAs for attaining the highest capacity gains.
2010	Wake *et al.* [36]	Proposed Radio over Fibre aided DASs.
2011	Xu *et al.* [24]	Proposed a DAS-aided FFR scheme and studied imperfections of the digital optical backhaul in a multiuser, multicell scenario.
2012	Park *et al.* [37]	Proposed algorithms for determining the antenna location of downlink DASs in both single-cell and two-cell environments.
2013	Ozgur*et al.* [38]	Characterize how the capacity of the distributed MIMO transmission scales with the number of cooperating users the area of the clusters and the separation between them.

1.1.3 Coordinated Multipoint Transmission

As highlighted above, the DAS aided FFR scheme significantly mitigated both the CCI among the adjacent cells, as well as the ICI imposed by the RAs in the reference cell, especially near the angle halfway between two adjacent RAs [39]. Despite these benefits, the achievable performance still remains limited in specific regions of the cellular area. For the sake of mitigating these limitations, the COMP technique is invoked as an effective way of managing the intercell interference. The evolution of the COMP technique is summarized in Table 1.3. The COMP philosophy was first considered in 3GPP LTE-Advanced in September 2011 as one of the core features of Release 11 [40] [12], where the two basic COMP schemes aimed for interference avoidance, while is relying on perfect CSI [41]. In the case of the DL, there are three classic COMP categories: coordinated scheduling/beamforming, dynamic point selection and joint transmission [40]. More explicitly, in coordinated DL scheduling/beamforming schemes [42] [43], either the BS or the RA is selected to transmit its data to users. Dynamic point selection [44] constitutes a low complexity COMP scheme where the actived BS or RA transmitter may be switched according to both the availability of wireless resources and the channel quality [45]. In the more complex joint transmission scheme of [46] [47], multiple transmitters are actived to transmit to a single user either coherently or noncoherently. In coherent joint transmission, the signal transmitted from multiple transmitters is jointly preprocessed for supporting coherent combining at the receiver [48]. This TPP technique [49] is invoked for our DAS-aided FFR scheme in Chapter 3, which belongs to the coherent joint transmission class. By contrast, in the noncoherent joint transmission class, the user would receive multiple transmissions individually precoded by each transmitters without aiming for coherent combining [50]. There are two typical coordinated techniques for the UL, namely those that create orthogonal channels for the individual users and those that create receiver algorithms [40], such as MUD [51]. The optimum maximum-likelihood detector is based on the concept of “full search“, where the computational complexity increases exponentially with the number of users. Hence, near-optimal multiuser detection has been widely investigated [52], including the probabilistic data association (PDA) based MUD [53], where the multiuser interference will be assumed to be Gaussian noise [54]. More explicitly, the received coordinated signals were treated as the interference to be mitigated in [55] [56]. By contrast, we will treat the interference as desired signals, which will be decoded at the BS [57] [12] with the aid of our PDA detector designed for the coordinated cells [58]. This PDA-aided detector is base on the philosophy of ”knowledge sharing and data fusion”, which will be invoked in the DAS aided FFR scheme of Chapter 4

Table 1.3: Contributions to COMP in cellular networks

Year	Authors	Contribution
1996	Moshavi [51]	Proposed the MUD concept for DS-CDMA systems.
1997	Poor and Verdu [55]	Designed the MMSE multiuser detector.
2000	Wei and Qi [52]	Conceived a near-optimal limited-search based detector for CDMA systems.
2001	Meurer *et al.* [59]	Proposed joint detection and joint transmission in the CDMA downlink.
2007	Koutsopoulos and Tassiulas [44]	Advocated joint optimal access point selection.
2008	Chae *et al.* [42]	Proposed coordinated beamforming for the multiuser MIMO broadcast channel.
2010	Sawahashi *et al.* [60]	Presented the CoMP among multiple cell sites.
2011	Papadogiannis *et al.* [61]	Investigated the selective feedback concept in the context of COMP systems.
2012	Annapureddy *et al.* [62]	Studied the degrees of freedom in the multiuser interference channel relying on COMP.
2013	Yang*et al.* [41]	Gave an overview of state-of-the-art approaches for solve the potential limitations of CoMP.

1.1.4 Optical Fibre Backhaul

The conventional backhaul is defined as the connection between the BS and the BS controllers in cellular systems, which typically relies on copper, optical fiber or microwave radio links. In the USA for example, copper represents approximately 90% of the backhaul implementations, microwave links about 6% and optical fibers about 4% [63]. However, recently the backhaul capacity required has significantly increased due to the increasing number of mobile subscribers using high-speed data services [64]. Hence, with the ever-increasing penetration of the optical fibre transmission technique, optical fibre may be used on a larger scale to meet the growing requirements for high-capacity backhaul. The concepts developed for wireless communication systems are increasingly invoked in optical fibre communication systems, such as Code Division Multiple Access

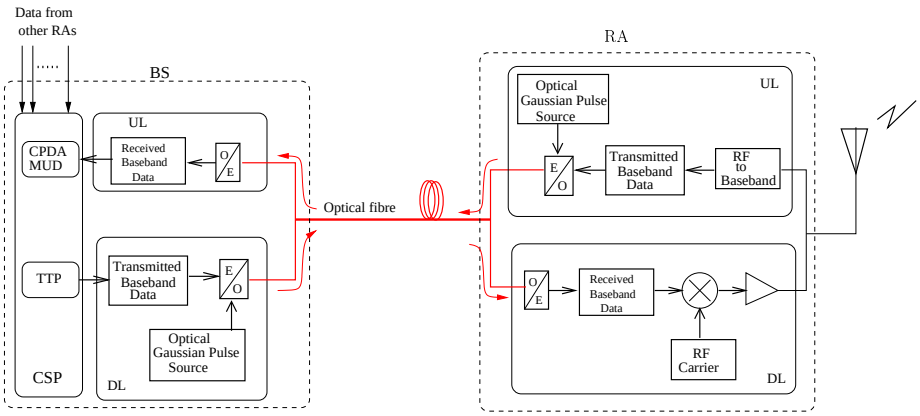

Figure 1.5: The system structure of DAS aided FFR scheme introduced in the thesis.

(CDMA) [65] [66], Frequency Division Multiple Access (FDMA) or Wavelength-Division Multiplexing (WDM) [67],Time-Division Multiplexing (TDM) [68], OFDM [69] and Space-Division Multiplexing (SDM) [70]. Originally the most dominate optical modulation scheme was On-Off Keying (OOK) [71]. However, in recent years, the modulation schemes developed for wireless communication have increasingly found their way into optical fibre communication, including differential phase-shift keying (DPSK) [72], as well as multi-level modulation schemes constituted by a combination of phase-shift keying (PSK) and amplitude-shift keying (ASK), leading to M-ary Quadrature Amplitude Modulation (QAM) $(M = 2^b, b = 2, 4, 6, \cdots)$ [73]. In order to transmit the multi-level modulated optical signal, two typical methods has been proposed, which are Digital Optical Fibre (DOF) based technique [74] and the Radio Over Fiber (ROF) technique [75]. More explicitly, in the case of DOF, the wireless baseband signal is transmitted through the optical fibre, while in the case of a ROF system, the modulated wireless radio frequency (RF) signal is conveyed directly through the optical fibre. A rudimentary comparsion of DOF and ROF will be provided in Chapter 2. The system architecture of the DAS aided FFR scheme used in the thesis is shown in Fig. 1.5, where the DOF link is invoked for connecting the BS and RAs.

Table 1.4: Contributions to optical fibre communications.

Year	Authors	Contribution
1989	Saleh [65] [66]	Proposed CDMA for optical fibre networks.
1990	Brackett [67]	Conceived WDMA for optical fibre networks.
1996	Barry *et al.* [68]	Introduced the TDM into optical fibre networks.
2003	Sinkin*et al.* [76]	Proposed the split-step Fourier method for modeling both the linear and non-linear distortions of optical-fiber communications systems.
2005	Gnauck and Winzer [72]	Invoked DPSK for optical fibre networks.
2007	Sauer *et al.* [75]	Suggested the employment of ROF aided cellular networks.
2009	Nirmalathas *et al.* [77]	Proposed the DOF-aided optical fibre networks.
2010	Essiambre *et al.* [78]	Estimated the capacity limit of optical fibre communication systems.
2011	Liu *et al.* [69]	Proposed coherent OFDM for high speed long-haul optical transmission.
2012	Winzer [70]	Proposed the SDM principle for optical communication.
2013	Dar. *et al.* [79]	Presented a new fading MIMO mode, the Jacobi fading model, for optical fiber communication.

1.2 Organization of the Thesis and Novel Contributions

The outline of the thesis as shown in Fig. 1.6 is presented below:

- **Chapter 2:** The DAS concept effectively moves the antennas from the BS to positions distributed across the cell. Two typical optical fibre backhaul techniques will be considered for connecting the antennas to the BS, namely the DOF link and the ROF techniques. The DOF link relies on the classic optical pulse propagation theory. In our preliminary study of Section 2.3, a DOF link is used for connecting the BS to a fixed relay. The so-called Wyner interference model [80] is combined with a FFR arrangement as well as with three different interference mitigation techniques, namely the eigen-beamforming technique [81], the Reduced-power based technique of [82] and a hybrid technique of combining eigen-beamforming with the reduced-power technique.

- **Chapter 3:** Based on the preliminary study of a DOF link in Chapter 2, which is invoked for the Shamai-Wyner interference modelling of two adjacent cells, we

focus our attention on a more practical scenario in Chapter 3, where a DAS-aided combined FFR scheme is investigated in the context of a multiuser multicell network designed for the DL. TPP techniques are invoked for improving the attainable throughput across the entire cellular coverage area. The DOF link is modelled by the classic Split-Step Fourier (SSF) method [83] which is capable of analysing the effects of both the linear dispersion and of the nonlinearity imposed by the optical fibre link on the throughput of the wireless channel. We will also demonstrate that increasing the number of DAS elements may not always lead to an improved coverage in the entire cellular area and characterize the power-control effects on the achievable system performance.

- **Chapter 4:** In contrast to Chapter 3, which dealt with the DL, Chapter 4 considers the UL. More explicitly, the pervasive DAS/FFR scheme of Fig. 1.4, which was designed for a multiuser, multicell network is investigated in an UL scenario. In order to increase the attainable cooperative diversity gain, cooperative relaying is invoked in our pervasive DAS/FFR. Different COMP techniques, such as the Minimum Mean Square Error (MMSE) [84] based successive interference cancellation combined with optimal user ordering (MMSE-OSIC), maximum-likelihood MUD [84], probabilistic data association (PDA) aided MUD [85] and our new PDA technique specifically designed for our mobile-relay aided scenario are invoked for improving the achievable BER for the users roaming across the entire cell area. Again, we will also demonstrate the beneficial effects of power-control on the attainable system performance.

- **Chapter 5:** Relying on the previous chapters, in this chapter we investigated the DL of our DAS/FFR scheme by taking into account the effects of practical imperfections. More explicitly, the impact of CSI estimation errors, CSI quantisation errors as well as OFDM signal timing and frequency synchronisation errors are considered. Naturally, the attainable performance of the COMP technique will be degraded in conjunction with imperfect channel knowledge for both the DL and UL. As an attractive design alternative, we conceive a Turbo Coded (TC) 16-level Star-Quadrature Amplitude Modulation (StQAM) scheme for supporting optical-fiber-aided cooperative wireless transmissions, where the receiver does not have to estimate the channel state information.

- **Chapter 6:** The main findings of the thesis are summarized and suggestion for future research are presented.

The fundamental motivation and the rationale of the thesis is that we design a superior communication network by intrinsically amalgamating the FFR, DAS and relaying techniques for the sake of mitigating the CCI, for reducing the pathloss and for increasing the cooperative diversity gain. The system's architecture relies on the components seen in Fig. 1.4b. Instead of simply varying the SINR of a single user, we consider a more practical multiuser, multicell scenario relying on practical cellular parameters, where any particular user's position is mapped to a specific SINR. This method allow us to observe, whether a particular communication architecture is capable of efficiently improving the SINR across the entire cellular area. Then sophisticated TPP techniques are conceived for the DL and COMP techniques are invoked for the UL in order to improve both the attainable throughput and the BER.

The novel contributions of the thesis are as follows:

1. We design a pervasive DAS/FFR-aided architecture for the sake of reducing the CCI in the the cell-edge area. Our pervasive DAS/FFR scheme has a low complexity, since it invokes a single omni-directional transmit antenna at each remote antenna (RA) and a single receive antenna at each mobile station (MS). We jointly model the resultant virtual multiple-input and multi-output (MIMO) system. Hence, we jointly design the TPP matrix of all the cooperating RAs in case of the DL in our paper [24]. By contrast, Multi User Detection (MUD) techniques are invoked for all the active MSs in the UL by centrally processing all the received UL signals, as detailed.

2. Rather than simply characterizing the achievable performance of a single user as a function of the SINR, we consider a more practical multiuser, multicell scenario relying on practical cellular parameters, where any particular user's position is mapped to a specific SINR. This method is capable of demonstrating the geographic distribution of the SINR across the entire cellular area. We demonstrate that although the pervasive DAS/FFR scheme is capable of outperforming the conventional networks, the so-called 'worst-case direction' problem persists as characterized in our paper [86].

3. We aim for improving the entire system's performance across the cellular area, and for mitigating the above-mentioned worst-case direction problem. In the case of the DL, the TPP matrix of all the cooperative RAs combined with FFR assists in achieving an increased throughput for the entire cell-edge area, regardless of the specific geographic distribution of the users, as demonstrated in our paper [24]. By contrast, in the case of the UL, the above-mentioned MMSE-OSIC and the PDA MUD

techniques are unable to solve the 'worst-case direction' problem. As a remedy, the CPDA MUD invoked by our MR aided pervasive DAS/FFR architecture is capable of substantially reducing the BER for the MS roaming at arbitrary positions, especially in the 'worst-case direction' as demonstrated in Chapter 4.

4. More explicitly, in the case of the UL, the intra-cell interference (ICI) is the dominant problem of the pervasive DAS/FFR scheme, which may in fact be stronger in the cell-center area than in the cell-edge area, since the interfering MSs tend to be in a dense cluster in the central area, they are scattered less densely in the outer ring. Hence, the MSs roaming in the cell-center area may in fact have a lower SINR. Hence, an efficient Mobile Relay (MR) selection strategy is required by the Pervasive DAS/FFR scheme, which is capable of significantly reducing the BER right across the entire cell area, as quantified in Chapter 4.

5. The baseband DOF model relying classic optical pulse propagation theory is appropriate for analysing the wireless system model considered. Hence, we treat the BS-RA-MS link as a composite channel, where the effects of the fibre-induced imperfections both on the attainable throughput and on the BER performance of the wireless channel can be calculated, when applying different wireless transmission strategies, relying on diverse modulation scheme and cooperative processing techniques, as detailed in our paper [24].

6. We investigate the impact of practical impairments on our CoMP aided DAS in the context of a FFR arrangement in the case of the DL, including the effects of CSI estimation errors, CSI quantisation errors as well as OFDM signal timing and frequency synchronisation errors [87]. Furthermore, we extended the Single-Input Single-Output (SISO) based non-coherent 16StQAM scheme of [88] to a Single-Input Multi-Output (SIMO) system, which is capable of operating without any channel knowledge

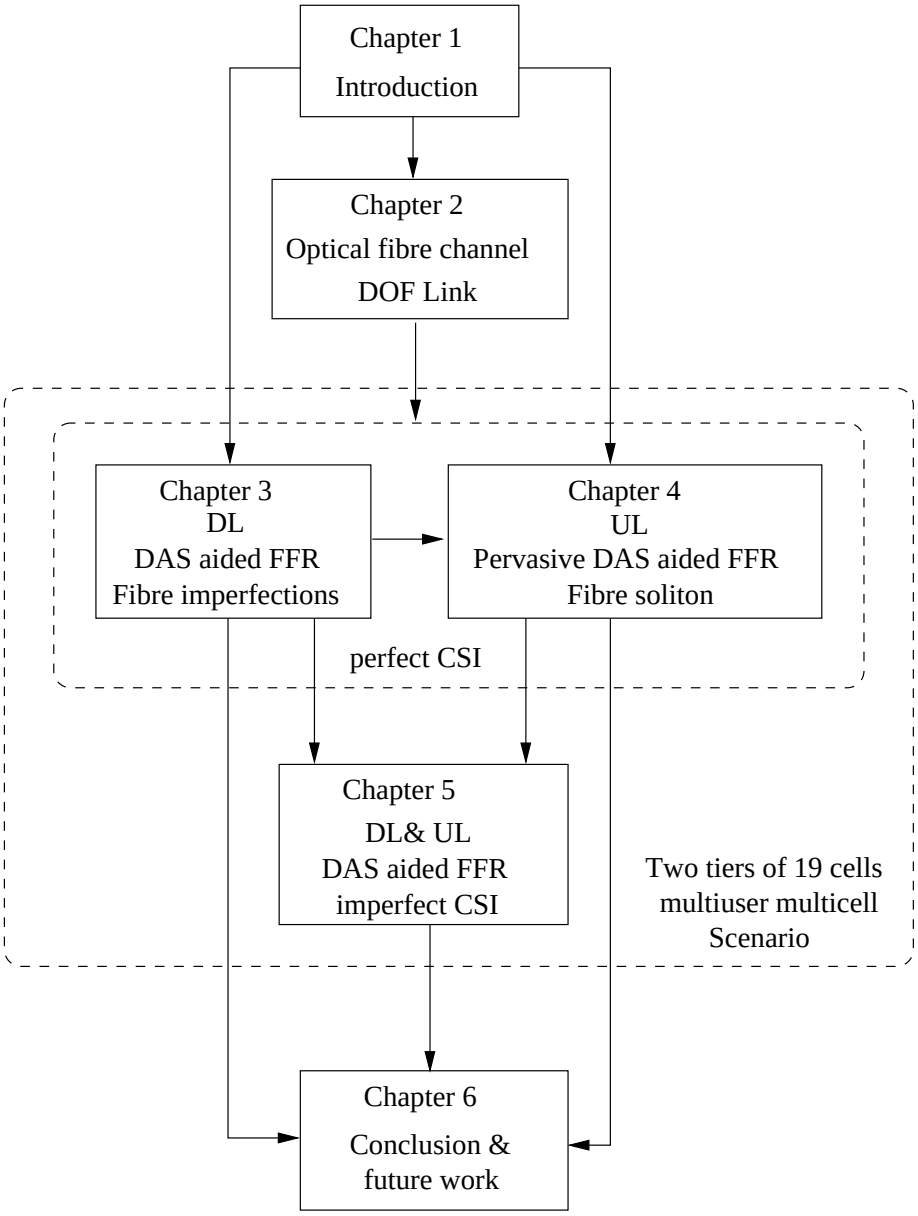

Figure 1.6: Organization of the thesis.

Chapter 2

Optical Fibre Backhaul

2.1 Introduction and Outline

The backhaul of a conventional cellular network is defined as the communication link between the Base Station (BS) and the associated Mobile Switching Centre (MSC). Usually, the physical medium of the backhaul is based on copper, microwave radio links and optical fibre [89], [90]. Having a high capacity backhaul for the LTE-Advanced (LTE Release 10) system is highly desirable [91] and in this context using optical fibre is more reliable than copper and microwave radios. On the other hand, when considering a Distributed Antenna (DAS) assisted communication network, which aims for improving the coverage of the entire cell area, optical fibre may be adopted for the communication link between the BS and the Remote Antennas (RA). Hence, the backhaul of a DAS aided communication network is extended to the RAs, as demonstrated in Fig. 2.1, where the entire communication network may be treated as an optical fibre network having wireless access points. More explicitly, in a DAS aided communication network, the BS plays the role of a central processing unit, where the extra complexity of multiple user transmission [92] and multiple user detection techniques [93] [94] is affordable.

For the sake of maximising the attainable area spectral efficiency, Multi-Carrier Code Division Multiple Access (MC-CDMA) and Orthogonal Frequency Division Multiple Access (OFDMA) [93] have been proposed, which may be capable of operating without partitioning the total bandwidth into cell-specific frequency sets, although this so-called 'unity frequency-reuse pattern' is typically achieved at the cost of an increased co-channel interference level. This severely interference-limited wireless access system often becomes incapable of supporting a sufficiently high throughput, especially at the cell-edge. Hence, a different form of frequency reuse has been adopted in the Third Generation Partner-

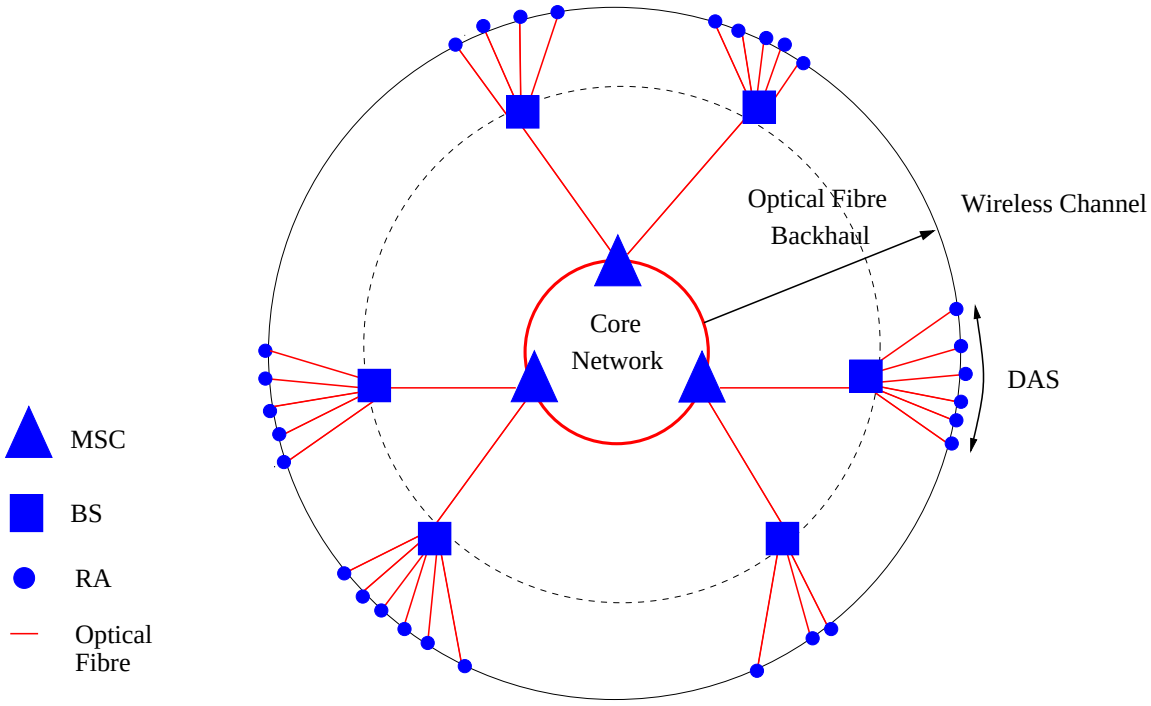

Figure 2.1: An architecture of cellular network aided by the DAS.The exact size of the architecture is dependent on the realistic requirement.

ship Project's (3GPP) Long Term Evolution (LTE) initiative [95] and in the Worldwide interoperability for Microwave Access (WiMAX) [96] system, both of which rely on the so-called Fractional Frequency Reuse (FFR). According to the FFR philosophy, the users roaming near the cell-center occupy the total bandwidth, while the cell-edge users are allowed access only a third of the total bandwidth, in order to allow the creation of three non-interfering frequency sets. More explicitly, the frequency sets of the cell-edge users in the adjacent cells are arranged to be orthogonal in order to improve their Signal to Interference plus Noise Ratio (SINR).

Moreover, wireless relays may be employed in the cell in order to improve the achievable cell-edge SINR and throughput [97], which would otherwise remain low, as a result of the pathloss between the Base Station (BS) and the cell-edge Mobile Station (MS). As a beneficial effect of the relay, the reception quality is improved and an enhanced cell-edge SINR is achieved. Despite the numerous benefits of wireless relays, the capacity of a wireless relay aided system is limited by that of the 'weakest' link in the entire communication chain [98], regardless whether *amplify-forward* or *decode-forward* relaying is used. On the other hand, it is widely recognized that the capacity of optical fibre links is higher than that of the wireless medium. Therefore, the optical fibre backhaul [99] is eminently applicable to the construction of the BS to relay link and the capacity of the resultant RoF based relay system is essentially only limited by the 'last-mile' wireless link.

The outline and contributions of this chapter may be summarised as follows. In Section 2.2, we introduce the optical fibre backhaul. More explicitly, we briefly compare the digital over fibre (DOF) [100] and radio over fibre (ROF) [101] techniques in Section 2.2.1 and introduce a range of fibre-induced imperfections invoking optical pulse propagation theory in Section 2.2.2. In Section 2.3, a DOF link is combined with the Wyner interference model [102] of two cells, each having a radius of R and relying on a fractional frequency reuse arrangement. We consider the benefits of different wireless interference mitigation strategies and the effects of the fibre-induced imperfections.

2.2 Optical Fibre Backhaul

A substantial benefit of the LTE-Advanced system [91] is that the signals transmitted and received by the distributed antennas may be jointly processed with the aid of the so-called coordinated multipoint (COMP) [103] techniques relying on a high capacity backhaul. Hence, we focus our attention on the optical fibre link between the BS and RAs [104] [105] [99] in our DAS assisted scheme, which is more reliable than a wireless backhaul, albeit it is also more costly.

2.2.1 Digital Over Fibre and Radio Over Fibre Techniques

The optical fibre based backhaul techniques may be classified into the broad categories of DOF and ROF [27] [106]. In the case of DOF backhaul aided systems it is the wireless baseband signal that is transmitted through the optical fibre, while in the case of a ROF system , the modulated wireless radio frequency (RF) signal is conveyed directly through the optical fibre. In the recent literature, the concept of the so-called digitized-RoF system [107] was proposed, where the modulated wireless RF signal is digitized by a high sampling-rate analog-to-digital converter (ADC) before being transmitted through the optical fibre. Naturally a high-rate digital-to-analog (DAC) converter is required [108].

In contrast to the analogue-ROF family, the DOF subclass is immune to the sideband cancellation phenomenon[1], which occurs in the ROF system [109] [110] and additionally, it is capable of avoiding both the inter-modulation distortions of the optical fibre as well as the nonlinearity imposed by the optical components [111]. Naturally, these benefits are typically achieved at an increased complexity and cost [106]. Additionally, multilevel optical signaling transmission[2] techniques [112] [113] may be applied, which are capable

[1] a fluctuation amplitude caused by the phase shift due to fibre dispersion.

[2] noncoherent multi-level amplitude and phase-shift keying.

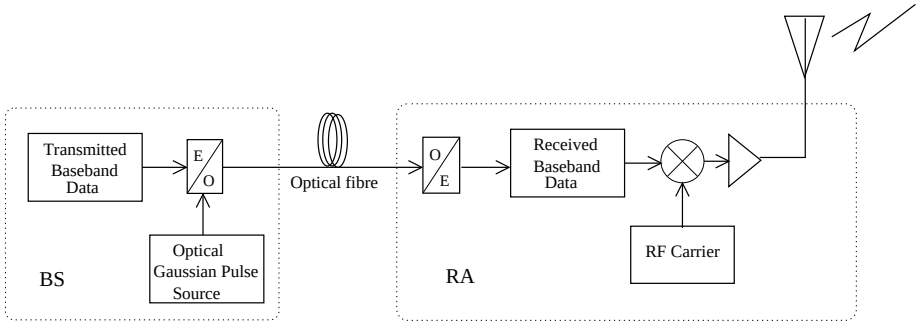

(a) DOF link

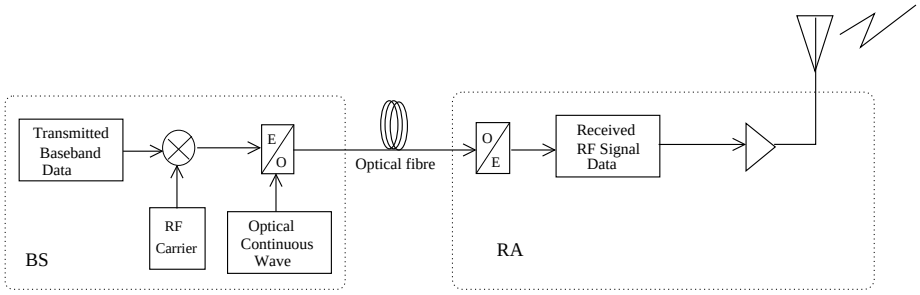

Radio−over−Fibre

(b) ROF link

Figure 2.2: The structure of DOF link and ROF link.

of reducing the complexity of the optical receiver at the RA. Hence in this study we rely on a DOF link. As a further benefit, RoF techniques also allow us to preprocess the DownLink (DL) transmit signal for all the users in the central BS, before it is transmitted to the mobile station (MS). Hence the RoF backhaul may also support the extension of BS cooperation techniques to DASs.

The DOF and ROF system structures are shown in Fig. 2.2. In the case of the DOF link shown in Fig. 2.2a, the transmitted baseband data modulates a stream of Gaussian-shaped time-domain (TD) optical pulses, where an ideal optical modulator is assumed, which does not impose any chirp[3] on the optical pulse. Then the Gaussian-shaped TD optical signalling pulses are transmitted through the optical fibre, which imposes both linear and nonlinear distortions. At the RA, the optical signalling pulses output by a photo-detector are converted back to the corresponding baseband electronic signals. By contrast, in the case of the ROF technique shown in Fig. 2.2b, the transmitted baseband signal is first upconverted to the analogue RF carrier and the resultant signal is then used for modulating a continuous-wave optical carrier. Hence, a simple RA maybe used, which converts the signal from the optical carrier to the RF carrier for transmission over the wireless channel.

[3]a signal in which the frequency increases ('up-chirp') or decreases ('down-chirp') due to the dispersion as the signal propagates.

However, the ROF scheme may suffer both from the sideband cancellation phenomenon detailed in [109] [114] and from the inter-modulation distortion imposed by the nonlinearity of the optical components, as we mentioned above. Furthermore, the baseband DOF model is appropriate for analysing the wireless system considered. Hence, we treat the BS-RA-MS link as a composite channel, where the effects of the fibre-induced imperfections on the attainable throughput and the BER performance of the wireless channel can be calculated, when applying both non-cooperative and cooperative processing techniques.

2.2.2 Characteristics of the Optical Fibre Channel

Based on our brief portrayal of the DOF and ROF techniques provided in Section 2.2.1, we opt for invoking the DOF aided backhaul for the following reasons:

1. The up- and down-conversion of RF may be carried out with the aid of well- developed techniques at both the RA and the BS.

2. In the DOF link, the baseband signal is used for modulating the Gaussian-shaped TD optical pulses. This technique may be able to avoid the above-mentioned sideband cancellation phenomenon and inter-modulation distortion of the optical fibre as well as the nonlinearity imposed by the optical components in the case of the ROF technique;

3. The baseband DOF model is appropriate for analysing the wireless system considered.

Despite the above-mentioned advantages, the system's performance is affected by the fibre-induced imperfections. Hence, in this section, we briefly characterise the optical fibre channel [83] [115]. Its linear effects are summarized in Fig. 2.3, while its nonlinear effects are highlighted in Fig. 2.4, when optical pulses propagate along it.

2.2.2.1 Linear Effects

1. **Fibre Loss**. Usually, we take into account the fibre loss, which is due to the attenuation, absorption, reflections, refractions, Rayleigh scattering and optical component insertion losses.[4] When the Gaussian-shaped TD optical pulses propagate along the optical fibre, the average optical power P of a bit stream is governed by Beer's law

[4]The insertion losses is usually independent of wavelength which are imposed by the insertion of optical components, such as couplers, filters, multiplexers/demultiplexers, and switches [115].

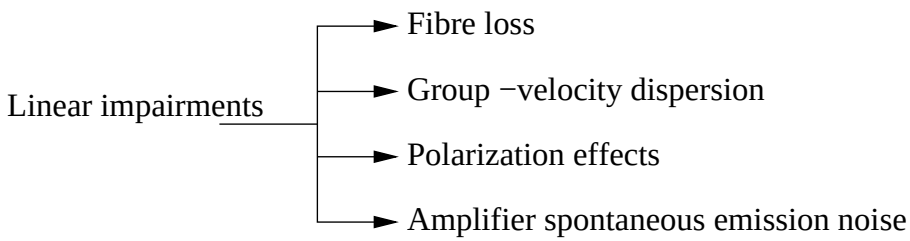

Figure 2.3: Classification of linear effects in the optical fibre channel.

formulated as [83] $dP/dz = -\alpha P$, where α is the kilometric attenuation coefficient given by the ratio between the input power P_{in} and the output power P_{out} after propagating over a length of L.

Hence we have:

$$P_{out} = P_{in} exp(-\alpha L), \tag{2.1}$$

$$\alpha_{dB} = -\frac{10}{L} log_{10}(\frac{P_{out}}{P_{in}}) \approx 4.343\alpha, \tag{2.2}$$

where α_{dB} is expressed in units of dB/km. More explicitly, we have $\frac{P_{out}}{P_{in}} = exp(-\alpha L)$ from Eq. (2.1) which is substituted into Eq. (2.2), where we have $\alpha_{dB} = (10log_{10}e)\alpha \approx 4.343\alpha$. The lowest practical value of the fibre loss is $\alpha_{dB} \sim 0.2dB/km$ in the wavelength region of $1.55\mu m$[5], which was first achieved in 1979. The effects of fibre loss may become serious for long-haul transmissions, but they may be substantially reduced with the aid of erbium-doped fibre amplifier (EDFA) based repeaters [116].

2. *Group-Velocity Dispersion*. When Gaussian-shaped TD optical pulse propagates along the optical fibre, the different spectral components of the pulse typically travel at slightly different group velocities, which leads the pulses broadening. This phenomenon is referred to as group-velocity dispersion (GVD), which is characterized as [83]:

$$\Delta T = \frac{d}{d\lambda}(\frac{L}{v_g})\Delta\lambda = DL\Delta\lambda,$$
$$D = \frac{d}{d\lambda}(\frac{1}{v_g}) = -\frac{2\pi c}{\lambda^2}\beta_2, \tag{2.3}$$

where ΔT is the kilometic pulse broadening for a fiber of length L, λ is the wavelength, v_g is the group velocity, $\Delta\lambda$ is the wavelength interval of the transmitted signal, c is the speed of light and β_2 is the GVD parameter. The dispersion parameter D of Eq. (2.2) is wavelength-dependent and it is expressed in units of $ps/(km \cdot nm)$. The effect of dispersion on the bit rate B may obey the criterion $B\Delta T < 1$, which

[5]The third-generation fiber-optic systems operated at $1.55m$

may be substituted into Eq. (2.3), yielding:

$$BL|D|\Delta\lambda < 1. \tag{2.4}$$

As an example, the wavelength-dependent dispersion parameter D becomes $1ps/(k \cdot nm)$, when a wavelength of $1.3\mu m$[6] is applied. Hence, if the bitrate times fibre-length product of BL of a single-mode fibre (SMF) exceeds $(1Tb/s) \cdot km$, the range of wavelength $\Delta\lambda$ may be reduced below 1. Hence, in high-rate future communication networks, the GVD may become considerable in the network of Fig. 2.1. Usually the dispersion compensation technique [117] which satisfies $DL + D_cLc = 0$ is applied for mitigating the dispersion effects. More explicitly, D_c and L_c are the dispersion parameter and fibre length of the dispersion compensation fibre. However, it is difficult to find a dispersion compensation fibre, which is capable of compensating the dispersion exactly. Hence, in this thesis we take into account the effects of the dispersion and model a composite channel of the optical fibre and of the wireless communication medium.

3. *Polarization Effects* Polarization is the term used for describing the orientation of the electromagnetic field, when the waves propagate in free space or through the optical fiber [83]. We may use orthogonal vertical and horizontal polarization. Ideally, the core of the optical fibre has a perfectly circular symmetry, where the two orthogonal polarizations travel at the same speed. However, the irregularities and imperfections of the fiber, such as its non-circular, shape and its impurities, result in the two polarizations propagating at different speeds [118], which is termed as Polarization Mode Dispersion (PMD). There are three polarization modes: linear polarization, circular polarization and elliptical polarization. A SMF may be fed in a single polarization mode and in an ideal scenario its output is also in the same polarization mode. However, again, realistic fibers are imperfect. When transmitting light with linear polarization over the fibre, it can be randomly changed to the above-mentioned other two states, since different polarization modes travel at different group velocity, which results in the input pulse broadening phenomenon. Typically, the PMD may be ignored for pulse widths of $>$ 10ps and only becomes a limiting factor, when transmitting at a high bit rate over a long distance [83].

4. *Amplifier Spontaneous Emission Noise*. Optical amplifiers are widely used in state-of-the-art optical fibre communication (OFC) systems, especially for long-haul systems, which can amplify the optical signal directly in the optical domain by stimulated emission, rather than converting it back to electronic signals for amplification.

[6]The second generation of fiber-optic communication operated at $1.3m$

However, the stimulated emissions typically also generate random noise by the phenomenon of amplified spontaneous emission Noise (ASEN). The ASEN is usually modeled as an independent complex-valued additive white Gaussion noise (AWGN). More details about the physical mechanism of the optical amplifier and ASEN noise can be found in [83].

2.2.2.2 Nonlinear Effects

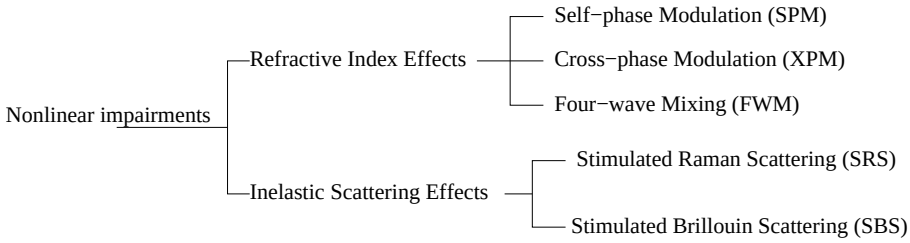

Figure 2.4: Classification of non-linear effects in the optical fibre channel.

The fibre nonlinearity plays an important role, when designing high capacity optical fibre communication. Hence, an understanding of the various nonlinear effects imposed by the optical fibre is necessary. The nonlinearity effects may be classified in two categories, as shown in Fig. 2.4. Specifically, the inelastic-scattering phenomenon of Fig. 2.4 is due to the optical signals being transmitted at high power levels which then interact with the phonons of the fiber medium. This phenomenon induces two important stimulated effects, i.e. stimulated Brillouin scattering (SBS) [119] and stimulated Raman scattering (SRS) [120]. The SBS effect generates coherent phonons and gives rise to a macroscopic wave in the fiber, while the SRS effect generates non-coherent phonons, but no macroscopic wave [115]. The main difference between the SBS and SRS is that acoustic phonons participate in SBS, while optical phonos participate in SRS [111]. Usually the SBS and SRS effects are considerd in high-rate transmission system, which use an external modulator [121] and continuous wave (CW) laser source [122].

By contrast, the refractive index effects of Fig. 2.4 (also termed as Kerr effect) produces three different kinds of effects, namely self-phase modulation (SPM), cross-phase modulation (XPM), and four-wave mixing (FWM) defined as follows [83]:.

1. **Self-phase Modulation**. On SPM is encountered, when an ultra-short optical pulse traveling through the fibre will result in a time varying refractive index for the medium [111] [123]. This temporally varying refractive index fluctuation results in a temporally varying phase change, leading to frequency chirping. The effects

produced by nonlinear SPM and the linear dispersion phenomenon introduced in Section 2.2.2.1 are complementary in nature and may mutually compensate each other by the appropriate choice of the pulse shape and input power. The resultant technique is known as the optical soliton [111], which is capable of facilitating for the optical pulse propagate through the optical fibre without distortions. We will invoke the optical soliton technique for creating a perfect fibre-based backhaul in Chapter 4.

2. **Cross-phase Modulation**. XPM occurs, when two or more optical channels are transmitted simultaneously in the same optical fibre, where the intensity of the co-propagating optical pulses result in a varying the refractive index [111]. The total phaseshift caused by XPM depends on the total transmit power of all channels, which ultimately impose interference on the optical signal of the neighboring channels, hence leading to pulse broadening [83]. The effects of XPM can be reduced by increasing the frequency-domain guard band, i.e. the wave-length difference between the individual channels [124] and by selecting different bit-rates for the adjacent channels [115].

3. **Four-wave Mixing**. FWM occurs, when three optical signals having different carrier frequencies propagate through the fibre simultaneously[7], which results in a fourth signal having a fourth carrier frequency of $\omega_{ijk} = \omega_i + \omega_j + \omega_k$ [111]. In WDM systems, the FWM may be avoided with the aid of sophisticated dispersion management techniques [83] or by employing unequal channel spacing for the sake of ensuring that the undesired non-linear distortion products do not interfere with the original signals [115].

2.3 The Composite Channel of a DOF-Aided Wireless Relaying System

By using the optical fibre for the BS to relay link, the relay is typically closer to the cell-edge MS, hence providing an improved signal quality. Naturally, relaying is capable of reducing the pathloss owing to the reduced distance from the relay to the MS, but it will consequently increase the interference imposed on the adjacent cell's MSs roaming near

[7] $\mathbf{P} = \varepsilon_0(\chi^1 \cdot \mathbf{E} + \chi^2 : \mathbf{EE} + \chi^3 \vdots \mathbf{EEE} + \cdots)$, where $\mathbf{P}$ is the total polarization induced by electric dipoles, $\mathbf{E}$ is the electric field, χ^j is the jth order susceptibility which is a tensor of rank$(j+1)$ and ε_0 is the vacuum permitivity [111].

the cell-center, which may use the same frequency as the current cell's cell-edge MS in a typical FFR arrangement. Against this background, in this chapter, *we investigate three different interference mitigation techniques designed for a realistically modeled optical fibre based relay aided system in the context of the Shamai-Wyner interference model [125], where we aim for improving the attainable throughput of the MS roaming at the cell-edge, while minimising the interference imposed on the adjacent cell's MS roaming near the cell-center and using the same frequency-band. Recall that the cell-edge MS will not impose interference on the adjacent cell's cell-edge users, which is an explicit benefit of the FFR philosophy employed.*

2.3.1 Optical Fibre Based Fixed Relay Aided System

2.3.1.1 Shamai-Wyner Interference Model

Let us focus our attention on investigating an optical fibre based fixed relay aided system using the Shamai-Wyner interference model of [125] seen in Fig. 2.5, which illustrates two partially overlapping circular cells having a radius of R, each of which consists of three 120° sectors, where the distance between the BS O_1 and BS O_2 is $\overline{O_1O_2} = \sqrt{3}R$. We assume that the serving cell is O_1 and a cell-edge MS is placed at position 'a' of Fig. 2.5 with the polar coordinates denoted by $(\theta_a, L_a) = [0, \sqrt{3}R/2]$, while the adjacent cell's near cell-center MS is placed at position 'c' of Fig. 2.5 having the polar coordinates of $(\theta_c, L_c) = (-\pi, R/2)$. For the sake of improving the throughput of the cell-edge MS 'a', the relay is placed at position 'g' described by the polar coordinates (θ, L). Hence, the distances from the relay 'g' to both MSs may be expressed as $D_a = (L^2 + L_a^2 - 2LL_a\cos\theta)^{1/2}$ and $D_c = (L^2 + L_c^2 - 2LL_c\cos\theta)^{1/2}$, respectively.

Having described the associated geometric properties, let us now characterize the interference generated in the context of this system model. Again, let us assume that the above-mentioned FFR regime is employed in the system, where the cell-center users of both cells have access to the entire spectral resources F, while the cell-edge users have access to only a third of the total bandwidth and are mutually orthogonal, hence we have $F_a \cap F_c = \varnothing$. For the cell-edge MS 'a', relay aided transmission is required, where the link from BS O_1 to the relay is constituted by an imperfect optical fibre, while the last-mile connection relies on wireless access. On the other hand, for the cell-center MS 'c', a direct wireless link dispensing with relaying is established by the BS O_2. Hence, the transmissions from the relay to the cell-edge MS 'a' impose interference upon the cell-center MS 'c', and similarly, the transmissions from the BS O_2 to its cell-center MS 'c' also inflict

interference upon the cell-edge MS 'a'.

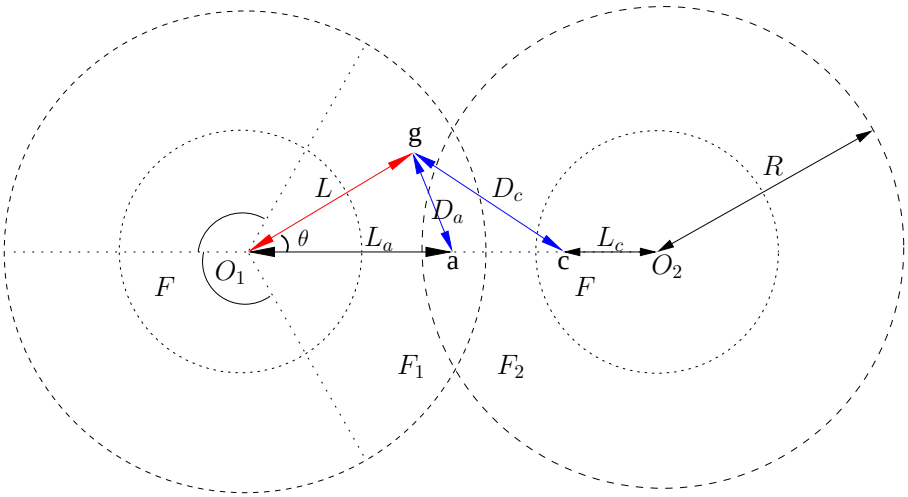

Figure 2.5: Wyner interference model of two cells with radius R and FFR arrangement.

2.3.2 Analysis of The Interference Mitigation Techniques

2.3.2.1 Received Signal Strength

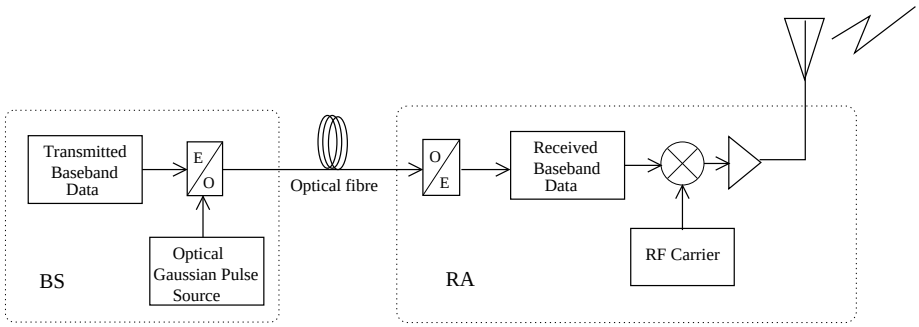

Figure 2.6: System structure of DOF aided fixed relay.

Optical fibre channel: Before discussing the different interference mitigation techniques considered, let us first describe the received SINR model of the link, where the BS O_1 transmits signal x via the realistic optical fibre aided relay 'g' to the cell edge MS 'a'. The system structure of DOF link aided fixed relay is shown in Fig. 2.6. The signal received at the relay after passing through the 'lossy' optical fibre may be written as:

$$y_g = A_p x + I_p + n_f. \tag{2.5}$$

More explicitly, we have $n_f \sim \mathcal{CN}(0, \sigma_f)$ the complex-valued Additive White Gaussian Noise (AWGN) is n_f. Furthermore, the so-called *pulse-broadening* effect of the optical

fibre is also taken into account, where the pulse propagated over the fibre is subject to both the peak power reduction and the Inter-Pulse-Interference (IPI) as illustrated in Fig. 2.7. The peak power reduction is given by a factor of $A_p = T_0/(T_0^2 - i\kappa^2 L^2)^{1/2}$ [126], where $T_0 = 10ps$ represents the Half-Width-Half-Maximum (HWHM) of the initial Gaussian-shaped TD signalling pulse, when the wavelength of light is $\lambda = 1.55\mu m$, $\kappa = 20$ ps^2/km is a constant. The IPI is accumulated as a result of the pulse broadening and it is a function of the optical fibre's length L, which may be modeled as a linear function of the distance yielding $I_p = \gamma L$, with the kilometric IPI taken into account having dimension of $W^{1/2}/km$.

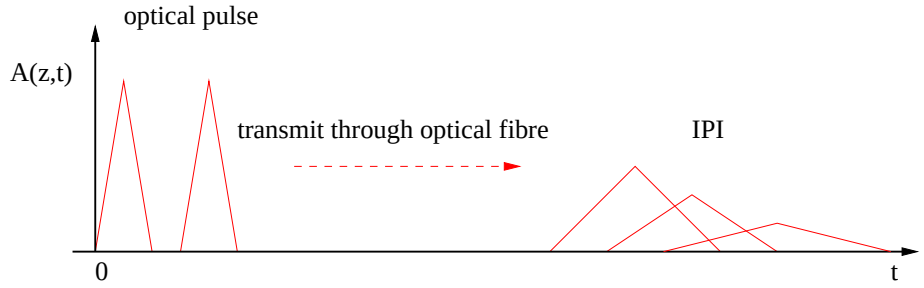

Figure 2.7: Schematic of the optical pulse propagation through the optical fibre, where IPI may be imposed by the optical pulse-broadening.

Wireless channel This noise-contaminated signal y_g in Eq(2.5) is normalised by a power-scaling factor χ which compensates fir the fibre's attenuation and then forwarded to the destination, namely to the cell-edge MS through the wireless channel, where again the power-scaling factor χ is employed in order to maintain a constant transmit power at the relay. The signal received over the wireless channel at the destination MS may be written as

$$y_a = \psi_{ga} h_{ga} \chi y_g + I_a + n, \tag{2.6}$$

where ψ_{ga}, h_{ga}, I_a and $n \sim \mathcal{CN}(0, \sigma_0)$ represent the large-scale slow fading, small-scale fast Rayleigh fading, the co-channel interference generated by cell O_2 of Fig. 2.5 and the complex-valued AWGN, respectively. Furthermore, the subscript $(\cdot)_{ij}$ denotes the channel spanning from point 'i' to point 'j'. More explicitly, we consider both the pathloss and the shadowing component, which are given by $\psi_{ga} = (D_1^{-\mu} 10^{\sigma_s/10})^{1/2}$, where μ and σ_s denote the negative-exponential power-decay factor and the standard deviation of the lognormal shadowing.

By defining $A = A_p$ and $N_f = I_p^2 + 2\sigma_f^2$ as the equivalent optical fibre attenuation factor and equivalent optical fibre noise power, the SINR of MS 'a' in cell O_1 in Fig. 2.5

is given by:

$$\gamma_a = \frac{(\psi_{ga}|h_{ga}|\chi A)^2}{2\sigma_0^2 + (\psi_{ga}|h_{ga}|\chi)^2 N_f + (\psi_{O_2a}|h_{O_2a}|)^2}, \tag{2.7}$$

where the second term and the third term in the denominator represent the noise generated by the components in the lossy optical fibre and the co-channel interference generated by the adjacent cell's transmission. On the other hand, MS 'c' near the cell-center of O_2 receives both the signal transmitted from O_2 via the wireless channel and the interference imposed by the relay in cell O_1. Hence the SINR at the input of the receiver of MS 'c' in cell O_2 is given by:

$$\gamma_c = \frac{(\psi_{O_2c}|h_{O_2c}|)^2}{2\sigma_0^2 + (\psi_{ga}|h_{ga}|\chi)^2 N_f + (\psi_{gc}|h_{gc}|\chi A)^2}, \tag{2.8}$$

where the second term and the third term in the denominator represent the noise generated by the components in the lossy optical fibre and the co-channel interference generated by the transmissions of the relay.

Fig. 2.8a shows the average SINR of both MS 'a' and of MS 'c' as a function of the position of relay 'g' described by the distance ratio of $\rho = L/R$ and the angular rotation of $\theta = 0$ and IPI of the optical fibre is ranging from $\gamma = 0.2, 0.5, 0.7$, where the average was calculated for 1000 simulation runs using the parameters listed in Table 2.1. It can be seen in Fig 2.8a that all SINR curves recorded for the cell-edge MS 'a' are monotonically increasing and saturate at high values of the distance ratio ρ. On the other hand, all SINR curves plotted for MS 'c' are monotonically decreasing with the distance ratio ρ. These two distinct trends indicate the complementary characteristics experienced by the two MSs, namely that increasing the SINR for one of the MSs will inevitably impose an SINR degradation on the other MS. When the accumulated IPI is increased, the SINR of the cell-edge MS 'a' of Fig. 2.8a decreases dramatically, while that of the cell-center MS 'c' of Fig. 2.8a is slightly reduced. Since pulse-broadening is on the order of pico-seconds, which is substantially lower than the signalling interval typically being on the order of nano-seconds, hence in this chapter we simply assume that no IPI is observed, namely that we have a kilometeric pulse-broadening of $\gamma = 0$.

2.3.2.2 Interference Mitigation Techniques

Intuitively, as detailed in the context of Fig. 2.8a, placing a relay close to the cell-edge MS will improve its reception quality, while imposing increased interference upon the neighbouring cell. Hence the natural design methodology of a relay aided system is to improve the throughput of the cell-edge MSs, while minimising the throughput reduction

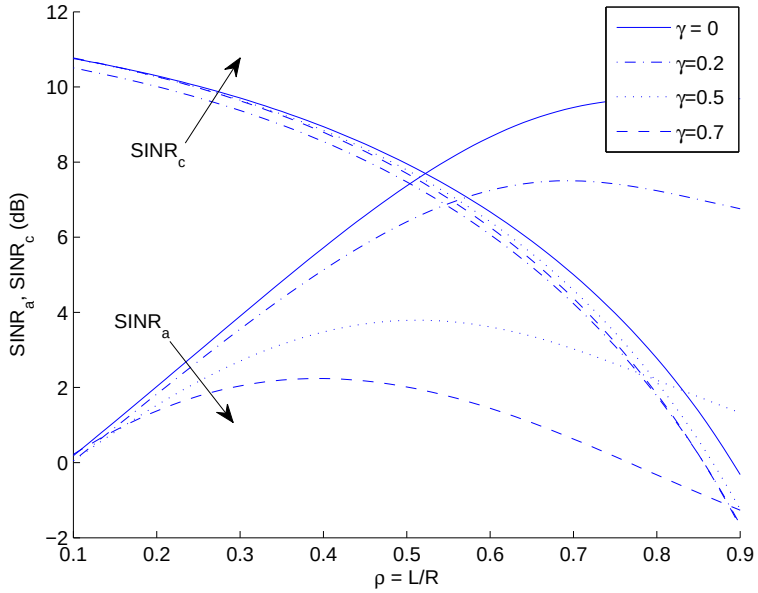

(a)

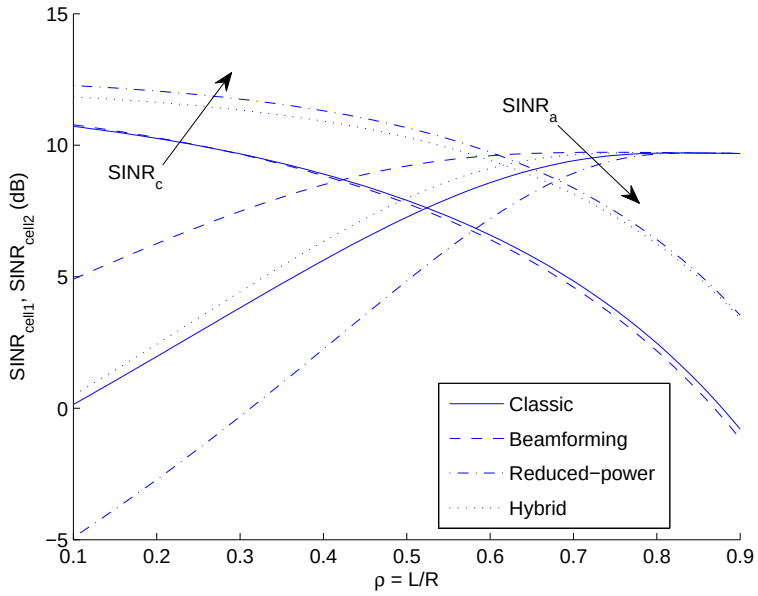

(b)

Figure 2.8: SINR of both the cell-edge MS 'a' and the cell-center MS 'c' of Fig 2.5. having different amount of IPI as a function of the distance ratio ρ in Fig. 2.8a and employing different interference mitigation techniques and assuming no IPI that imposed by the optical fibre, i.e. we have $\gamma = 0$ in Fig. 2.8b.

inflicted upon the neighbouring cell owing to the increased interference. Let us now discuss three different interference mitigation techniques, namely a beneficial reduced-power transmission technique, the classic eigen-beamforming technique and a hybrid combination of them.

1. **Reduced-power technique** The signal received at the relay after passing through the 'lossy' optical fibre of Eq. (2.5) is also written as $y_g = Ax + N_f^{(\frac{1}{2})}$, where A and N_f are the equivalent optical fibre attenuation factor and the equivalent optical fibre noise power as defined in Eq. (2.5). This 'green', reduced-power technique refers to the arrangement, where the transmit power of the relay is scaled down by the normalisation factor of

$$\chi = \beta/(A^2 + N_f)^{1/2} \tag{2.9}$$

with $\beta \in (0,1]$. The underlying principle of this technique is that the interference imposed on MS 'c' of Fig. 2.5 may be substantially reduced by the reduction of the relay's transmission power. This technique becomes identical to the classic direct-relaying, when we have $\beta = 1$ in eq(2.9).

2. **Eigen-beamforming technique** It belongs to the family of smart antenna aided interference mitigation techniques, transmitting a narrow beam towards the desired user instead of the conventional omni-directional or sectorized transmission. It requires short-term or long-term Channel State Information (CSI) provided by the MS via a feedback channel, where the achievable performance is heavily dependent on the accuracy of the CSI estimated at the MS, which is then predicted into the future at the relay. In this chapter, we stipulate the simplifying assumption that the instantaneous CSI is perfectly known at the relay's transmitter antenna, which is a uniformly spaced linear array of four antenna elements, while the two MSs are equipped with a single receive antenna. Again, the eigen-beamforming technique [81] is considered, where the transmit antenna array weights are given by the eigenvector $\mathbf{v} \in \mathcal{C}^{4\times 1}$ corresponding to the largest eigenvalue of the spatial channel's covariance matrix in the Multiple Input Single Output (MISO) system, considered. Explicitly, this corresponds to $\mathbf{H_{ga}} \in \mathcal{C}^{1\times 4}$, where $\mathbf{H_{ga}}$ represents the channel matrix. As a result, the equivalent fast-fading channels become $h_{ga} = \mathbf{H_{ga}}\mathbf{v}$ and $h_{gc} = \mathbf{H_{gc}}\mathbf{v}$, respectively. Hence the channel's magnitude $|h_{ga}|$ is maximised, while $|h_{gc}|$ remains the same. The underlying principle of this technique is that by transmitting in the direction associated with the maximum equivalent channel gain of $|h_{ga}|$, the received SINR of the cell-edge MS 'a' is improved at a given transmit power, while the co-channel interference imposed on MS 'c' remains unchanged.

3. **Hybrid technique** We may combine the benefits of the above two techniques, leading to a hybrid technique. Specifically, the co-channel interference imposed on MS 'c' of Fig. 2.5 may be mitigated by the above-mentioned reduced-power solution, while the resultant degraded SINR at the cell-edge MS 'a' of Fig. 2.5 imposed by the reduced-power transmission may be compensated by the eigen-beamforming gain of our directional technique, because it enhances the SINR of the cell-edge MS 'a', while at the same time maintaining a reduced co-channel interference.

   Fig. 2.8b shows the average SINR of both MS 'a' and of MS 'c' as a function of the position of relay 'g' described by the distance ratio of $\rho = L/R$ and angular rotation of $\theta = 0$, while assuming that no IPI is imposed by the optical fibre, i.e. we have a kilometeric pulse broadening of $\gamma = 0$. The SINR average was calculated for 1000 simulation runs using the parameters listed in Table 2.1. When comparing the above-mentioned three interference mitigation techniques with respect to the classic benchmarker curves represented by the solid lines of Fig 2.8b, it is clearly seen that employing the eigen-beamforming technique represented by the dashed lines of Fig 2.8b improves the SINR of the cell-edge MS 'a', while maintaining the SINR of the cell-center MS 'c'. By contrast, employing the reduced-power technique represented by the dash-dot lines of Fig 2.8b, when transmitting at a quarter of the full power, namely using $\beta = 1/2$, substantially improves the SINR of the cell-center MS 'c' by sacrificing the SINR of the cell-edge MS 'a'. By amalgamating the benefits of both techniques, the hybrid solution represented by the dotted lines of Fig 2.8b leads to both a beneficial SINR improvement for MS 'c' and to a noticeable SINR improvement for the cell-edge MS 'a'. This figure has to be contrasted to Fig. 2.8a, where no interference mitigation was used.

2.3.2.3 System Throughput

Although different interference mitigation techniques result in different SINR characteristics with respect to the relay's position, the ultimate system performance metric is the achievable throughput. This is because an increased SINR does not necessarily lead to an increased throughput in the absence of adaptive transceivers, hence transmitting at a power higher than absolutely necessary for achieving the required throughput is irrational. The throughput of the system may be defined as the maximum successfully transmitted information rate, which is referred to as the system's *goodput* given by:

$$\eta(\gamma) = R_M R_C [1 - P_{bl}^b(\gamma)], \tag{2.10}$$

where R_M and R_C denote the rate of the modulation scheme and channel code, respectively, while P_{bl}^b represents the BLock Error Rate (BLER) corresponding to the particular Modulation and Coding Scheme (MCS) employed. More explicitly, the goodput represents the fraction of error-free by received transmission blocks. In this chapter, we assume that Bit Interleaved Coded Modulation (BICM) [127] is employed, which relies on high-throughput M-ary Quadrature Amplitude Modulation (QAM) [128], where we have $M = 2^b$ and $b = 2, 4, 6$ represents the number of bits per QAM symbol, namely the rate $R_M = b$.

Again, we employ M-ary QAM combined with Rate Compatible Punctured Turbo Codes (RCPTC) [129] having six selected MCSs, namely Mode $1, \ldots, 6$ of

$$[R_M, R_C] = [(2, 1/2), (2, 3/4), (4, 1/2), (4, 3/4), (6, 2/3), (6, 6/7)], \tag{2.11}$$

where the first number in the round bracket specifies the modulation scheme, while the second the overall coderate.

In practice, obtaining the BLER curves for all the MCSs by simulation is time-consuming, especially in our multicell multiuser system-level evaluations. Let us hence circumvent this time-consuming process with the aid of a more efficient semi-analytical process. We commence by briefly highlighting the derivation of the BLER $P_{bl}(b, \gamma)$ of a 2^b-ary QAM aided BICM scheme based on the BLER $P_{bl}(b = 1, \gamma_0)$ of a BPSK modulated BICM scheme transmitting over an AWGN channel, where only $P_{bl}(b = 1, \gamma_0)$ is evaluated by simulation. To this effect, we first define the appropriate *base-line* SINR γ_0 as that of a binary BPSK scheme, at which we have the same BLER as an arbitrary b-bit/symbol modem, which would typically require an SINR of $\gamma > \gamma_0$, i.e. where we have $P_{bl}(b, \gamma) = P_{bl}(b = 1, \gamma_0)$. We note that the above-mentioned BLER equality holds only, when the mutual information per bit output by the demodulator obeys the relation of $I(b, \gamma) = I(b = 1, \gamma_0)$. This is because I serves as the input of the channel decoder, and as long as I remains the same, the ultimate BLER also remains the same. Hence, the mutual information I per bit may be expressed as [127]:

$$I(b, \gamma) = 1 - \frac{2^{-b}}{b} \sum_{i=1}^{b} \mathbb{E}_w \times \left\{ \ln \left[1 + \sum_{j=1, j \neq i}^{b} \exp \left(- \frac{|u_j - u_i + w|^2 - |w|^2}{1/\gamma} \right) \right] \right\}, \tag{2.12}$$

where $w \sim \mathcal{CN}(0, 1/2\gamma)$ is the complex-valued zero-mean Gaussian noise process and $u \in \mathcal{A}$ represents the constellation points in the QAM alphabet, with the ith bit $\mathcal{A}$ being represented by $u_i, i \in [1, b]$. When fixing the mutual information per bit as $I(b, \gamma) =$

$I(b=1,\gamma_0)$, we may find the *base-line* SINR γ_0 for $b=1$, where this BPSK modulated scheme achieves the same per-bit mutual information (MI) I as a higher-throughput 2^b-ary QAM-aided BICM scheme. More explicitly, since the MI per pit $I(b=1,\gamma_0)$ is a monotonically increasing function of γ_0, its unique inverse exists. Hence this *base-line* SINR γ_0 may be expressed as the inverse-function $\gamma_0 = I^{-1}[b=1, I(b,\gamma)]$. This reveals the relation between γ and γ_0, hence allowing us to find the BLER $P_{bl}(b,\gamma)$ of a 2^b-ary QAM-aided BICM scheme from that of the simulated BLER of a BPSK modulated BICM scheme, i.e. from $P_{bl}(b=1,\gamma_0)$, which may be formulated as:

$$P_{bl}(b,\gamma) \quad = \quad P_{bl}\left\{b=1, I^{-1}[b=1, I(b,\gamma)]\right\}. \tag{2.13}$$

As a result, the BLER $P_{bl}(b,\gamma)$ of the above MCSs may be obtained with the aid of Eq (2.13), where $P_{bl}(b=1,\gamma_0)$ is obtained from the Monte-Carlo simulation of a BPSK modulated BICM scheme employing the above-mentioned RCPC having constituent code-rates of $R_C = [1/2, 3/4, 2/3, 6/7]$ in an AWGN channel. Finally, the associated effective throughput $\eta(\gamma)$ of Eq (2.10) expressed in terms of 'bits/s/Hz' may be obtained by assuming a Nyquist roll-off factor of zero.

The associated throughput is illustrated in Fig 2.9 in terms of 'bits/s/Hz', assuming a Nyquist roll-off factor of zero and $P_{bl}^{b}, b=1$ is obtained by Monte-Carlo simulation of the RCPTC of rate $R_C = [1/2, 3/4, 2/3, 6/7]$ employing BPSK modulation in an AWGN channel.

2.3.3 Performance Evaluation

The throughput calculation introduced in Section 2.3.2.3 facilitates the throughput analysis of different interference mitigation schemes as a function of the relay's position ratio ρ and $\theta = 0$, when assuming that no IPI is imposed by the optical fibre, i.e. we have $\gamma = 0$, as seen in Fig 2.10. The SINR γ was averaged over 1000 simulation runs and then it was substituted into Eq (2.10) and Eq (2.13), while the simulation parameters are listed in Table 2.1.

2.3.3.1 Throughput of the Classic Direct-Relaying Scheme

The well-recognized SINR tradeoff between the cell-edge MS 'a' and cell-center MS 'c' was demonstrated in Fig 2.8b for all three schemes of Section 2.3.2.2 employed for relay aided transmission. This translates into the usual throughput tradeoff, where increasing the throughput of one of the MSs results in the throughput reduction of the other. For

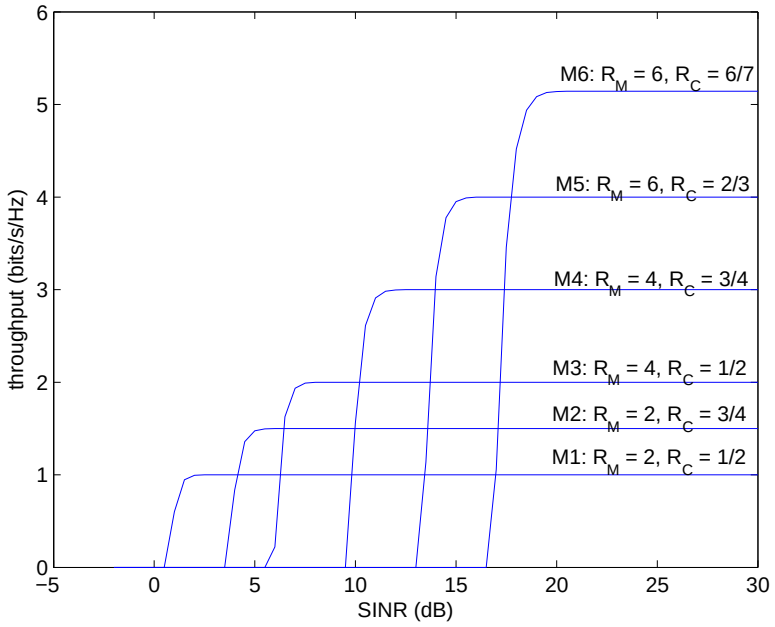

Figure 2.9: The throughput of the BICM schemes employing M-ary QAM combined with RCPC having the MCSs $[R_M, R_C]$. These curves were extracted from [127].

Table 2.1: Simulation parameters, which are based on the 3GPP-LTE standard [1].

Optical fibre channel	assuming IPI γ
Urban Macro BS to BS distance	$\overline{O_1O_2} = 3$ km
Inverse-power decaying pathloss factor	$\mu = 4$
Shadowing standard derivation	$\sigma_s = 8$ dB
Normalised optical fibre link SNR	10 dB
Normalised wireless link SNR	2 dB
QAM	$M = 2^b, b = 2, 4, 6$
RCPC code	$[R_M, R_C] = [(2,1/2), (2,3/4),$ $(4,1/2), (4,3/4), (6,2/3), (6,6/7)]$
	$R_m = b$, R_c is code rate

the classic scheme using no interference mitigation the throughput of MS 'c' drops from $\eta = 2.7$ bits/s/Hz to $\eta = 0$ bits/s/Hz, as the ratio ρ increases along the x-axis. By contrast, the throughput of MS 'a' increases from $\eta = 0$ bits/s/Hz to $\eta = 2$ bits/s/Hz, attaining the maximum throughput at the position ratio of $\rho = 0.5$.

2.3.3.2 Throughput of the Eigen-Beamforming Technique

As seen in Fig. 2.8b, the eigen-beamforming technique is capable of increasing the SINR at MS 'a', when compared to the classic direct-relaying technique. Hence we may observe a throughput improvement, when the position ratio ρ is low and hence the maximum throughput of $\eta = 2$ bits/s/Hz is achieved, provided that the relay is positioned farther away from the cell-edge MS, namely at the position ratio of $\rho = 0.27$. However, since the total transmission power remains unchanged for this technique, the co-channel interference remains the same as for the classic direct-relaying technique and the throughput of MS 'c' also remains the same.

2.3.3.3 Throughput of the Reduced-Power Technique

When considering the reduced-power 'green' technique and comparing it to the classic direct-relaying technique, we may expect a right shift of the throughput curves of both MS 'a' and of MS 'c', simply because the transmission power is reduced to one fourth of the full power, namely we have $\beta = 1/2$. It can be seen in the third plot of Fig 2.10 that the maximum achievable throughput of the cell-center MS 'c' becomes $\eta = 3$ bits/s/Hz and is kept constant, when the position ratio is in the range of $\rho \leq 0.4$. The throughput is then gradually reduced to $\eta = 1$ bits/s/Hz, when ρ is increased. This substantial improvement of the cell-center throughput compared to the classic technique is achieved at the cost of a reduced cell-edge throughput for MS 'a', which attains a maximum of $\eta = 2$ bits/s/Hz at $\rho = 0.6$.

2.3.3.4 Throughput of the Hybrid Technique

All the above techniques are capable of attaining the same maximum throughput of $\eta = 2$ bits/s/Hz for the cell-edge MS 'a', while maintaining the same throughput of $\eta = 2$ bits/s/Hz for the cell-center MS 'c'. The only difference occurs at the position of the relay. In this respect, we must not conclude that the eigen-beamforming technique or the reduced-power technique is superior to the classic direct-relaying scheme. In fact, the employment of both techniques may be viewed as redundant. This is why the SINR characterized in

Fig 2.8b is not the ultimate performance metric.

When combining the benefits of both the eigen-beamforming technique and of the reduced-power technique, the throughput of the cell-center MS 'c' is substantially increased, similarly to the reduced-power technique, while the throughput of the cell-edge MS 'a' is maintained, as in the case of the classic technique. This is because the throughput reduction of the cell-edge MS 'a' imposed by the reduced-power technique is compensated by the eigen-beamforming gain, which does not impose additional co-channel interference. Hence the hybrid technique is capable of improving the throughput of the cell-edge MS upto its maximum of $\eta = 2$ bits/s/Hz, while at the same time maintaining the maximum attainable throughput of the cell-center MS, which is seen to be $\eta \approx 3$ bits/s/Hz in the fourth plot of Fig 2.10 at the position ratio of $\rho = 0.45$. This justifies the superiority of the hybrid technique compared to the other techniques.

2.3.3.5 Effects of IPI

When the IPI is taken into account and we have $\gamma = 0.2$, the throughput of the cell-edge MS 'a' is shown in the first plot of Fig 2.11, which obeys similar trends to the no IPI scenario shown in the fourth plot of Fig 2.10. More particularly, at the relay position ratio of $\rho = 0.45$, the throughput of cell-edge MS 'a' associated with $\gamma = 0.2$ is slightly lower than that of the no IPI scenario, i.e. we have $\eta < 2$ bits/s/Hz. However, when $\gamma = 0.5$ is considered, as shown in the second plot of Fig 2.11, the cell-edge MS 'a' employing the hybrid technique suffers from a dramatic throughput reduction compared to the fourth plot of Fig 2.10. The reduction of the cell-edge throughput is imposed by the SINR reduction, when IPI is encountered, evidenced by as shown in Fig 2.8a. Hence, we may conclude that as long as the IPI is not severe, e.g. we have $\gamma < 0.2$, the hybrid technique remains effective.

In conclusion, we considered both the SINR as well as throughput tradeoffs between supporting a cell-center MS and a cell-edge MS using a lossy optical fibre based fixed-relay aided and FFR assisted interference limited wireless system, where the Shamai-Wyner cellular model of [130] was employed and three interference mitigation techniques were investigated. Our simulation results demonstrated that the reduced-power technique and the eigen-beamforming arrangement are only capable of improving either the throughput of the cell-center MS or of the cell-edge MS, while the hybrid technique is capable of maximising the throughout of the cell-edge MS without imposing any throughput reduction on the cell-center MS.

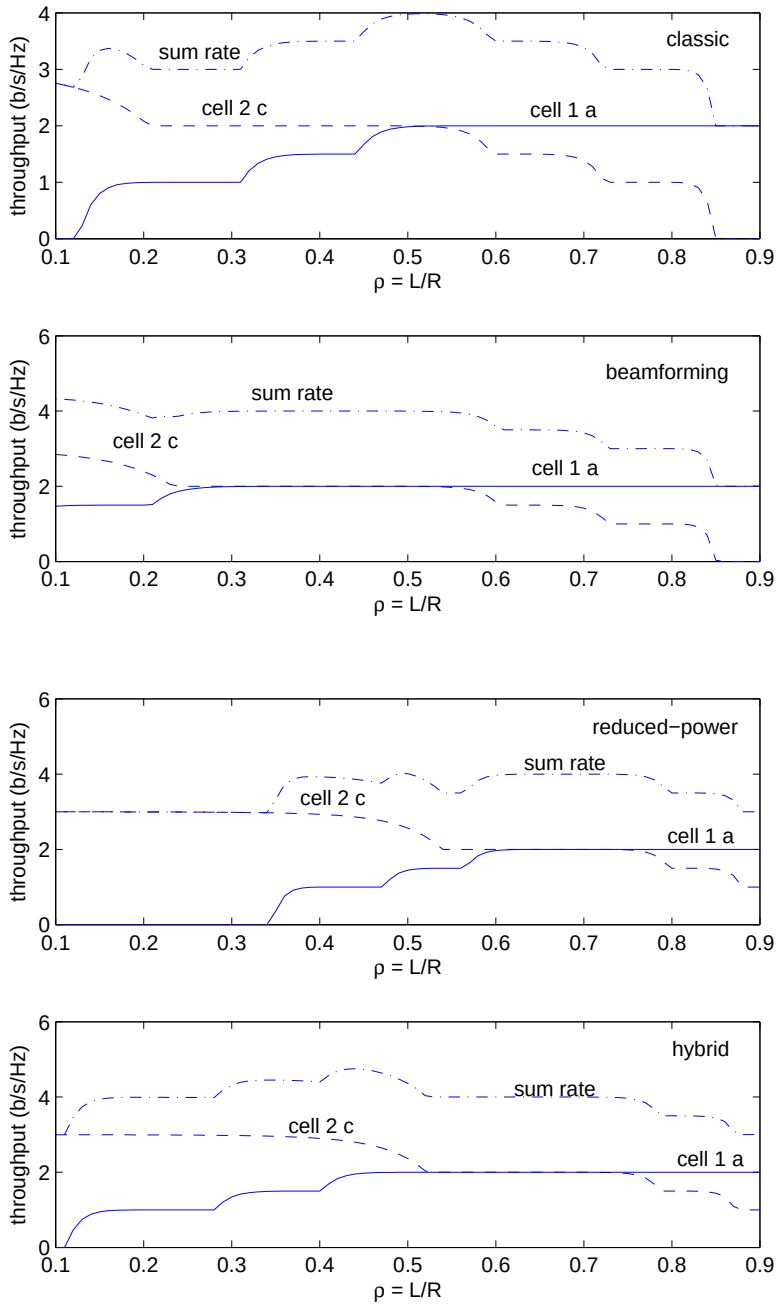

Figure 2.10: Throughput of different interference mitigation techniques compared to the classic technique relying on no interference cancellation as a function of the position ratio ρ and assuming that no IPI is inflicted by the optical fibre, i.e. we have $\gamma = 0$. The system parameters were listed in Table 2.1, while the MS positions were shown in Fig. 2.5. Subfigures from the top to the bottom represent the classic no-cancellation based scheme, the eigen-beamforming, the reduced-power and the hybrid schemes of Section 2.3.2.2, respectively.

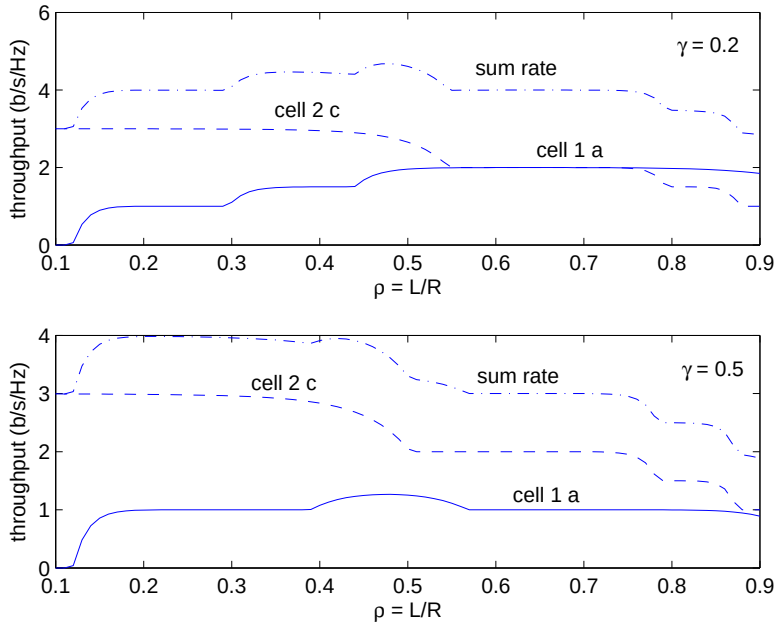

Figure 2.11: Throughput of the hybrid technique of Section 2.3.2.2 as a function of the position ratio ρ and assuming the presence of IPI imposed by the optical fibre, associated with $\gamma = 0.2, 0.5$. The system parameters were listed in Table 2.1, while the MS position were shown in Fig. 2.5. The subfigures represent the hybrid schemes of Section 2.3.2.2.

2.4 Chapter Conclusions

In this chapter, we proposed and characterized a network-architecture relying on an optical fibre backhaul supported by the DAS of Fig. 2.1. In Section 2.2.1, we briefly highlighted two typical optical backhaul techniques, namely the DOF of Fig. 2.2a and the ROF of Fig. 2.2b. We then dedicated our attention to the DOF link for the reasons detailed in Section 2.2.1.

1. The Up-and down-conversion of RF signals relies on well-developed techniques, which may be applied both at the RA and at the BS;

2. In the DOF link, the baseband signal is mapped to TD Gaussian-shaped optical pulses, which may avoid the sideband cancellation phenomenon and inter-modulation distortion of the optical fibre, as well as the nonlinearity imposed by the optical components in the case of the ROF technique;

3. The baseband DOF model is appropriate for analysing the wireless system model considered.

More explicitly, we modelled the DOF link based on the optical pulse propagation theory of [83], which suffers from a range of fibre-induced imperfections, as summarized the linear effects in Fig. 2.3 and nonlinear effects in Fig. 2.4 in Section 2.2.2 as following:

1. Fibre loss;
2. Group-velocity dispersion;
3. Polarization Effects;
4. Amplified spontaneous Emission Noise;
5. Nonlinear effects: SPM, XPM and FWM;

Since a realistic fibre suffers from the above-mentioned linear and nonlinear imperfections, we will use the Nonlinear Schrödinger (NLS) equation [111], which takes into account both the linear and nonlinear effects imposed when the optical pulse is propagating through the optical fibre as discussed in Chapter 3 and Chapter 4.

In Section 2.3, a DOF link was used for connecting the BS to a fixed relay and the case of Shamai-Wyner interference model of two cells was combined with the FFR arrangement of Fig. 2.5. A fixed relay may be allocated close to the cell-edge, in order to reduce the pathloss and to improve the signal quality, but it will consequently increase the interference imposed on the adjacent cell's MSs roaming near the cell-center, which may use the same frequency as the current cell's cell-edge MS in the FFR arrangement of Fig. 2.5. Hence, we jointly considered the DOF link aided fixed relay and the wireless channel between the relay and the MS, where the IPI characterized in Eq (2.5) and induced by optical pulse broadening was also taken into account, as shown in Fig. 2.11. The three different interference mitigation techniques considered in Section 2.3.2.2 were characterized in Fig. 2.10. The results are corresponding summarized in Table 2.2:

1. Eigen-beamforming may only improve the throughput of the cell-edge MS;
2. The reduced-power technique may improve the throughput of the cell-center MS, but reduces that of the cell-edge MS;
3. The hybrid arrangement of combing both eigen-beamforming and the reduced-power technique may improve the throughput of the cell-edge MS without reducing that of the cell-center MS;

Table 2.2: Throughput of the MS in the cell-edge area and cell-center area, when relying on the interference mitigation techniques of Section 2.3.2.2. The the position of the RA is arranged be close to the cell-edge area, namely at $L = 0.7$. The topology is shown in Fig. 2.5 and the parameters are summarized in Table. 2.1

	"a" in cell-edge area	"c" in cell-edge area
	$\gamma = 0$	
Classic	$2bits/s/Hz$	$1 \sim 2bits/s/Hz$
Beamforming	$2bits/s/Hz$	$1 \sim 2bits/s/Hz$
Reduced-power	$2bits/s/Hz$	$2bits/s/Hz$
Hybrid	$2bits/s/Hz$	$2bits/s/Hz$
	$\gamma = 0.2$	
Hybrid	$2bits/s/Hz$	$2bits/s/Hz$
	$\gamma = 0.5$	
Hybrid	$1bits/s/Hz$	$2bits/s/Hz$

4. In the urban macro-cellular scenario, where the parameters are shown in Table 2.1 and the Relay is located close to the cell-edge area at $L = 0.7R$, the effect of IPI is not severe, when we have $\gamma < 0.2$.

Chapter 3

Distributed Antennas for the Fractional Frequency Reuse Aided Multicell, Multiuser Downlink

3.1 Introduction

Based on the composite channel model of the DOF aided wireless relay system of Section 2.3.1, which considered the linear distortion imposed by the optical fibre channel and the CCI of the two adjacent cells, in this chapter we use a more comprehensive optical fibre channel model, which calculates both the linear and nonlinear distortion imposed by the fibre. Furthermore, we consider a more practical cellular topology of two tiers of nineteen cells relying on the FFR and DAS arrangement of Fig. 3.1. We will quantity the throughput of the entire cellular area. The classic UFR pattern of Fig. 1.1a may be applied by wireless systems in order to maximize the attainable area spectral efficiency (ASE), albeit its employment is only feasible at the cost of increasing the CCI level, hence the UFR typically exhibits a low throughput at the cell-edge. As a remedy, the FFR [131] philosophy of Fig. 1.1b may be invoked, which reduced the CCI at the cell-edge at the cost of a reduced ASE. Hence the FFR scheme is capable of improving the cell-edge SINR [132]. As a result, FFR has also been adopted in the Third Generation Partnership Project's (3GPP) Long Term Evolution (LTE) initiative [95] and in the Worldwide interoperability for Microwave Access (WiMAX) [96] system.

By contrast, a DAS improves the cell-edge throughput by placing the remote antennas (RA) [133] more close to the cell-edge terminals, hence naturally reducing the pathloss [134]. However, the reduced pathloss will increase the interference imposed on

the cell-edge terminals served by the neighbouring RAs. In practice only those MSs can be granted a high throughput, which roam in the vicinity of the RA. When the MS is roaming near the angle halfway between two adjacent RAs [39], its throughput is reduced, hence we will refer to this as the 'worst-case direction' problem. As a potential remedy, cooperative processing techniques which have been considered for Base Stations (BS) [132] [135] may be adopted for the DAS scenario considered in order to mitigate the Inter-RA-Interference (IRI), especially in the worst-case direction. The family of BS cooperation techniques is capable of efficiently mitigating the CCI, hence it was also considered as a candidate for next generation wireless networks by the 3GPP organization [1]. However, the family of BS cooperation techniques still relies on the classic architecture of a single centralized BS covering the entire cell, where the pathloss-and shadow-fading induced problem of the cell-edge users may not be readily solved. Hence, in order to achieve a high throughput for the entire cellular area, especially for the cell-edge terminals, we propose to combine DASs with cooperative BS processing techniques.

For the practical application of DASs, the connection between the BS and RAs may be coaxial cable, optical fibre or a radio frequency link [104] [105]. The Radio over Fibre (ROF) [99] transmission technique may also be used for the central BS to RA links, which is more reliable than a wireless backhaul, albeit it is also more costly. The ROF techniques may be classified into the broad categories of digital over fibre (DOF) [136] and analogue-ROF [108] [106]. In the case of DOF systems it is the wireless baseband signal that is transmitted through the optical fibre, while in the case of an analogue-RoF system, the modulated wireless radio frequency (RF) signal is conveyed through the optical fibre. In the recent literature, another type of so-called digitized RF-over Fibre (DROF) system [107] was also proposed, where the modulated wireless RF signal is digitized by a high sampling-rate ADC before being transmitted through the optical fibre. More explicitly, the optical modulation depth of the digitized-RFoF approach is 100% [107], while that of the analog-RoF is lower [108]. In contrast to the analog-ROF family, the DOF subclass is immune to the sideband cancellation phenomenon, which occurs in the analog-ROF system [109] [110] and capable of avoiding both the inter-modulation distortions of the optical fibre as well as the nonlinearity imposed by the optical components, but this is typically achieved at an increased complexity and cost [106]. Additionally, optical multilevel DOF signalling transmission techniques [112] [113] may be applied, which are capable of reducing the complexity of the optical receiver at the RA. Hence in this study we invoke DOF techniques. As a further benefit, DOF techniques also allow us to preprocess the DownLink (DL) transmit signal for all the users in the central BS, before it is transmitted to the mobile station (MS). Hence the DOF backhaul may also support the extension of

BS cooperation techniques to DASs. Furthermore, when aiming for supporting Gigabit-transmissions, which is the goal of LTE-Advanced (LTE Release 10) [91], these high-rate systems may suffer from the effects of dispersion and nonlinearity imposed by the optical fibre links of the DASs [36]. Hence jointly considering the effects of DOF and wireless links becomes important, when analyzing the performance of DAS systems designed for LTE-Advanced applications.

Our outline and novel contributions in this chapter may be summarised as follows:

Against this background, in this chapter *we quantify the attainable throughput across the entire cellular coverage area in a multicell, multiuser scenario, when employing cooperative techniques beneficially combined both with realistically modelled imperfect optical fibre aided DASs as well as with FFR. More explicitly, we introduced the Split-Step Fourier (SSF) method [111] to analyse how the dispersion and nonlinearity of the optical fibre link affect the throughput of the cell-edge area*.

1. Although the dispersion of the optical signalling pulse may be viewed as an undesirable imperfection of a pure optical fibre system, ironically, it might result in beneficial throughput enhancements in the cell-edge area of the non-cooperative RA aided FFR system. This is because the dispersion-induced attenuation of the optical signalling pulses may be capable of mitigating the IRI in the multicell, multiuser scenario. However, we will demonstrate that due to the worst-case direction problem caused by the IRI, the non-cooperative RA aided FFR system may not always lead to an improved attainable throughput in the entire cell-edge area.

2. We will also demonstrate that employing a single omni-directional transmit antenna at each RA and a single receive antenna at each MS, but jointly designing the Transmit PreProcessing (TPP) matrix of all the cooperative RAs combined with FFR is capable of achieving an increased throughput for the entire cell-edge area, regardless of the specific geographic distribution of the users. Furthermore, even though conventional cooperative signal processing techniques are unable to directly mitigate the optical fibre receiver's self-inflicted noise, the proposed cooperative RA-aided FFR system exhibits a higher attainable throughput than conventional non-cooperative FFR aided systems, especially in the worst-case direction.

This chapter is organised as follows. In Section 3.2 we introduce the multicell multiuser topology considered, describe the imperfect optical fibre model. In Section 3.3.1, we outline the received signal model of the non-cooperative DAS combined with our FFR aided system. In Section 3.3.2 we introduce several cooperative linear processing tech-

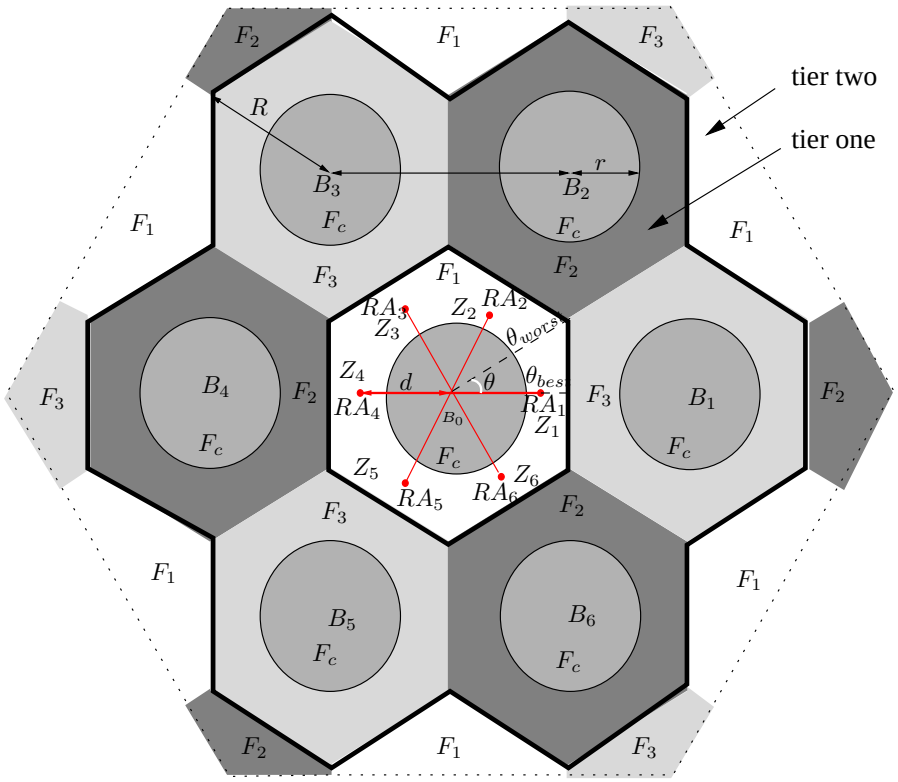

Figure 3.1: The topology of two tiers of nineteen cells relying on a FFR and DAS arrangement, where $N_r = 6$ RAs are employed. The structure of the cells in tier two is the same as the ones in tier one. This system is significantly more realistic than the two-cell system of Chapter 2 seen in Fig. 2.5.

niques, while we present our link level results recorded for a range of practical modulation and coding schemes followed by our performance evaluations in Section 3.4. Finally, we conclude our discourse in Section 3.5.

3.2 System Description and Optical Fibre Modelling

3.2.1 Multicell, Multiuser System Topology

The multicell multiuser scenario based on the FFR scheme is illustrated in Fig. 3.1, which consists of two tiers of nineteen hexagonal cells [137] surrounding the central BS B_0, where B_0 is assumed to be located at the origin. We assume *symmetry*, where every cell has the same system configuration and focus our attention on cell B_0 of Fig. 3.1 without any loss of generality. The frequency partitioning strategy of the total available bandwidth F is characterzed by $F_c \cap F_e = \oslash$, where F_c and F_e represent the cell-centre's frequency band and the cell-edge's frequency band, respectively. F_e is divided into three orthogonal frequency bands $F_i, i \in [1,3]$, exclusively used at the cell-edge of one of the three adjacent

cells.

To simplify the structure, we assume that the number of active MSs N_m and RAs N_r is the same ($N_m = N_r$), which implies that each RA may support a single MS. The users are assumed to be randomly distributed in the cell-edge area, and a total of N_m MSs are roaming at any point Z_i, as described by the polar coordinates of $[\theta_{Zi}, L_{Zi}], i \in [1, N_m]$. A total of N_r RAs are employed in each cell described by its polar coordinates denoted by $[\theta_{Ri}, L_{Ri}] = [2\pi(i-1)/N_r, d], i \in [1, N_r]$. Likewise, the BSs in tier-one are described by their polar coordinates of $[\theta_{Bj}, L_{Bj}] = [2\pi(j-1)/6, \sqrt{3}R], j \in [1, 6]$ and the polar coordinates of the BSs in tier-two may also be readily obtained from the underlying simple geometry.

Table 3.1: Topology parameters.

DAS aided FFR	Location	Polar coordinates
RA	cell-edge R_i	$[\theta_{R_i}, L_{R_i}] = [2\pi(i-1)/N_r, d]$ $i \in [1, N_r]$
BS	B_0	origin
	tier-one	$[\theta_{Bj}, L_{Bj}] = [2\pi(j-1)/6, \sqrt{3}R]$ $j \in [1, 6]$
MS	Z_i	$[\theta_{Z_i}, L_{Z_i}]$ $i \in [1, N_m]$, roaming randomly

3.2.2 Imperfect Optical Fibre Model

Fig. 3.2 shows a single optical fibre link spanning from the BS to the RA. The transmitted baseband data is used to modulate a stream of optical Gaussian pulses, where an ideal optical modulator is assumed, therefore it does not impose any chirp on the optical pulse. Then the optical signalling Gaussian pulses are transmitted through the optical fibre, which imposes both linear dispersion and nonlinear distortions. However, when transmitting optical Gaussian signalling pulses through the fibre, the DOF system remains immune to the sideband cancellation phenomenon, which persists in the ROF system [109]. Nonetheless, some fibre-induced imperfections still persist in the DOF system, as is discussed late in this chapter.

In order to investigate the system topology of Fig. 3.1 introduced above, we assume that the links from BS B_0 of Fig. 3.1 to the RAs are constituted by a realistic imperfect optical fibre, rather than simply assuming a perfect optical fibre. The phase rotation imposed by the optical fibre link on the modulated signal constellation diagram is supposed to be

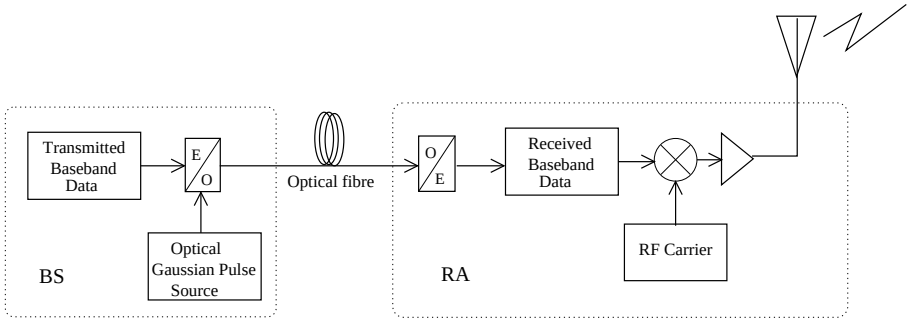

Figure 3.2: System architecture of the DOF link, showing a single optical fibre link spanning from the BS to the RA. The transmitted baseband data is used to modulate a stream of optical Gaussian pulses, where an ideal optical modulator is assumed, therefore it does not impose any chirp on the optical pulse. Then the Gaussian-shaped TD optical signalling pulses are transmitted through the optical fibre, which imposes both linear and nonlinear distortions. At the RA, after an ideal photo-detector, the optical signalling pulses are converted back to the corresponding baseband electronic signals, which was repeated from Fig. 2.2a for convenience.

compensated, hence in this chapter we only considered the fibre-induced imperfections imposed on the modulated signal's amplitude. Hence, the signal received at the RA i after passing through the realistically modelled optical fibre may be written as:

$$s_i = A_L x_i + n_f, \tag{3.1}$$

where A_L, x_i and $n_f \sim \mathcal{CN}(0, \sigma_f^2)$ represent the received amplitude of the optical pulse after passing through the optical fibre having a total length of L, the transmitted signal and the complex-valued Additive White Gaussian Noise (AWGN), respectively. Furthermore, the so-called *pulse-broadening* (PB) effect caused by the fibre-induced dispersion [83] may not impose a significant performance limitation in pure optical fibre links, since the Inter-Pulse-Interference (IPI) of Eq. (2.5) may be negligible for the transmission of the relatively low-rate baseband signal through the DOF link. However, the PB additionally imposes an attenuation of the optical signalling pulse, which may affect the attainable throughput of the cell-edge area, when considering our DOF aided DAS combined with FFR in a multicell, multiuser scenario.

In contrast to the IPI of Eq.(2.5), in this chapter we will elaborate on our optical fibre model a little further. Explicitly, we introduce the parameter A_L, which takes into account the fibre's kilometric attenuation, its dispersion and the fibre's nonlinearity characterized

by the generalized Nonlinear Schrödinger (NLS) equation [111] expressed in the form of:

$$\frac{\partial A}{\partial z} = \underbrace{\left(\frac{\beta_3}{6}\frac{\partial^3}{\partial t^3} - \frac{i\beta_2}{2}\frac{\partial^2}{\partial t^2} - \frac{\alpha}{2}\right)}_{\widehat{D}} A + \underbrace{i\xi\left(|A|^2 + \frac{i}{\omega_0}\frac{1}{A}\frac{\partial}{\partial t}\left(|A|^2 A\right) - T_R\frac{\partial |A|^2}{\partial t}\right)}_{\widehat{N}} A, \tag{3.2}$$

where $A(z,t)$ is the Gaussian-shaped TD signalling pulse envelope, which is a function of both the time t and of the propagation distance z. The term $\widehat{D}$ characterizes the dispersion and fibre loss effects, while $\widehat{N}$ characterizes the nonlinearity effects, as the pulse propagates along the optical fibre. Still considering Eq (3.2), in the term $\widehat{D}$, α represents the fibre attenuation, β_2 is the group-velocity dispersion (GVD) parameter, and β_3 is the third-order dispersion coefficient, which becomes significant for ultra-narrow signalling pulses, as detailed in [83]. Considering the term $\widehat{N}$ in Eq (3.2), ξ describes the fibre's nonlinearity, ω_0 is the angular frequency of the carrier wave and T_R is related to the slope of the Raman gain spectrum, as detailed in [111]. In the case of having a pulse width of $T_0 > 5$ps which is typical for telecommunication fibres [111], the first term of $\widehat{D}$ and the last two terms of $\widehat{N}$ may be neglected [111]. These simplifications allow us to focus our attention on the nonlinearity and dispersion effects in this chapter, hence the fibre loss parameter is assumed to be $\alpha = 0$. Then Eq (3.2) may be further simplified to:

$$\frac{\partial A}{\partial z} = \left(-i\frac{\beta_2}{2}\frac{\partial^2}{\partial t^2} + i\xi|A|^2\right) A = \left(\widehat{D'} + \widehat{N'}\right) A, \tag{3.3}$$

where the terms $\widehat{D'}$ and $\widehat{N'}$ are the simplified forms of the dispersion character $\widehat{D}$ and of the nonlinear character $\widehat{N}$ in Eq (3.2).

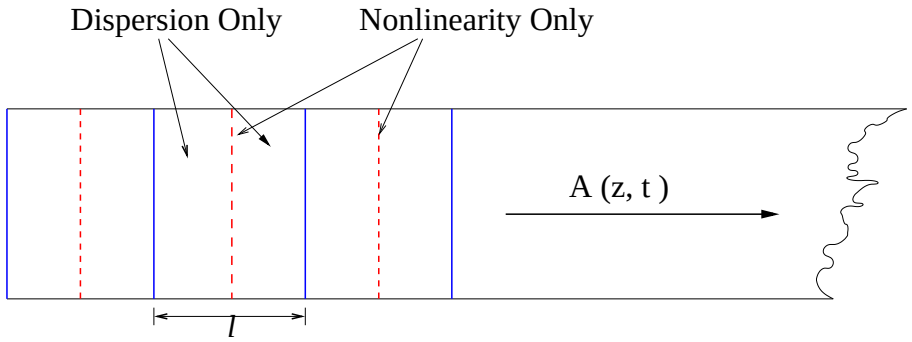

Figure 3.3: Split-Step Fourier Method

More explicitly, the general formula of Eq (3.2) or its simplified form in Eq (3.3) describes the pulse propagation problem [111], but in this form it is not directly suitable for analyzing how the throughput of the wireless link is affected by the parameters of the

Table 3.2: Characteristics of the optical fibre channel

$\widehat{D}$ dispersion characters and fibre loss	
$\frac{\alpha}{2}$	fibre attenuation
β_2	GVD
β_3	third-order dispersion coefficient
$\widehat{N}$ nonlinearity characters	
ξ	fibre's nonlinearity
ω_0	the angular frequency of the carrier wave
T_R	the slope of the Raman gain spectrum

imperfect optical fibre backhaul. The more practical SSF may be applied for analyzing the solutions of the NLS equation [111], which has been considered for modelling the family of optical-fibre communication systems [138]. Hence we employ the SSF method for jointly analyzing the attainable throughput of the RoF link. The SSF method delivers an approximate numerical solution, where the dispersive and nonlinear effects observed in Eq (3.3) may be separated into independent phenomena over a small segment-length l stretching from z to $(z+l)$ in Eq (3.2), yielding:

$$A(z+l,t) \approx F_T^{-1}\left\{exp\left[l\widehat{D'}(-i\omega)\right] F_T\left[exp(l\widehat{N'})A(z,t)\right]\right\}, \tag{3.4}$$

where F_T and F_T^{-1} denotes the Fourier-transform and inverse Fourier-transform operation, respectively. Firstly, the exponential nonlinearity-related term $exp(l\widehat{N'})$ of Eq (3.4) may be taken into account directly in the time domain. Secondly, before characterizing the dispersive effects, we take the Fourier-transform of the term $exp(l\widehat{N'})A(z,t)$, since the exponential dispersion-related term $exp(l\widehat{D'})$ may be evaluated in the frequency domain. The Fourier-transform of the dispersion character $\widehat{D'}$ is obtained by replacing the operator $\partial/\partial T$ by $-i\omega$ in Eq (3.2). Then, following the inverse Fourier-transform of Eq (3.4), we obtain the time domain representation of the received signal after propagating through the l-length fibre. The total optical fibre length satisfies $L = ml$, which suggests that the whole fibre length is decomposed into m consecutive l-length segments. Hence the optical pulse propagating through an L-length fibre may be obtained by evaluating Eq (3.4) in m consecutive steps, yielding a solution denoted as A_L. The characters of optical fibre channel considered in this section are summarized in Table 3.2

3.3 Received Signal of DOF Aided DAS Assisted FFR Systems

3.3.1 DOF aided Non-Cooperative DAS Assisted FFR system

Compared to the topology of Fig. 2.5 in Chapter 2 where a single interferer was considered, in this chapter we use the more practical topology of two tiers of nineteen cells relying on the DAS aided FFR system of Fig. 3.1, where multiple interferes are considered. Focus our attention on the cell B_0 of Fig. 3.1, when non-cooperative DASs are employed, the transmit power P_B of the BS and the transmit power P_R of each RA should obey the total transmit power constraint of $P_B + N_r P_R = P$, where P is the full power of the conventional UFR and FFR scheme at the BS .

3.3.1.1 Received Signal in the Cell-Centre Area

The interference at any MS located at point Z_i in the cell-center area is imposed by the direct wireless links of BSs $\{1, \ldots, N_b\}$, with N_b being the number of BSs, which we refer to as the Inter-BS-Interference (IBI). In contrast to the received signal of Eq (2.6) of Section 2.3.2 which only takes in to account a single interfer, while in this chapter multiple interferes are taken into account. Hence, the received signal may be written as:

$$y_c = \sqrt{P_B}\psi_{B0}h_{B0}x_0 + \sum_{j=1}^{N_b}\sqrt{P_B}\psi_{Bj}h_{Bj}x_j + n, \tag{3.5}$$

where ψ_{Bj}, h_{Bj}, $j \in [0, N_b]$ and $n \sim \mathcal{CN}(0, \sigma_0^2)$ represent the combined pathloss plus shadowing based large-scale signal attenuation, small-scale fast Rayleigh fading and the complex-valued AWGN, respectively. More explicitly, we jointly consider both the pathloss and the lognormal shadowing component, which is formulated as:

$$\psi_{Bj} = [\rho 10^{\varsigma(\sigma_s)/10}]^{1/2}, j \in [0, N_b],$$

where ρ denotes the pathloss that obeys a predefined pathloss model [139], while ς denotes a real valued Gaussian random variable having a standard deviation of $\sigma_s = 8$ dB [139]. Hence, $G_{Bj} = \psi_{Bj}|h_{Bj}|$ denotes the equivalent channel gain, while the SINR of any of the MSs near the cell-center is given by:

$$\gamma_c = \frac{G_{B0}^2 P_B}{2\sigma_0^2 + \sum_{j=1}^{N_b} G_{Bj}^2 P_B}. \tag{3.6}$$

In contrast to the Eq (2.7) and Eq (2.8) of Section 2.3.2 which only takes in to account a single interfer, here in Eq. (3.6) multiple interferes are taken into account.

3.3.1.2 Received Signal in the Cell-Edge Area

When considering the cell-edge area, we assume that the links spanning from the BS B_0 of Fig. 3.1 to the RAs are constituted by a realistic imperfect optical fibre, while the last-mile connection from the RAs to the MS relies on the wireless link. The signal received at the RA i after passing through the realistically modelled optical fibre is introduced in Section 3.2.2.

The noise-contaminated, faded signal $s_i, i \in [1, N_r]$ denoted in Eq (3.1) at the wireless channel's input is normalised by a power-scaling factor and then forwarded through the wireless channel to the destination, namely to the MS roaming in the cell-edge area, where the power-scaling factor χ is employed in order to maintain a constant transmit power at the RAs. In contrast to the received signal of Eq (2.6) of Section 2.3.2 which only takes in to account a single interfer, while in this chapter multiple interferes are taken into account. As a result, the signal received by MS i at any point Z_i in the cell-edge area in the absence of any cooperative techniques, may be written as

$$y_{ei} = \sqrt{P_R}\psi_{Ri}h_{Ri}\chi s_i + \sum_{k=1,k\neq i}^{N_r} \sqrt{P_R}\psi_{Rk}h_{Rk}\chi s_k + n. \tag{3.7}$$

Let $A = \chi A_L$ and $N_f = 2\sigma_f^2\chi^2$ denote the equivalent optical fibre-induced amplitude attenuation and the equivalent power spectral density of the optical fibre noise, respectively. The details of the parameters s_i and A_L are introduced above in Section 3.2.2. Then, the SINR at any MS roaming in the cell-edge area is given by:

$$\gamma_{ei} = \frac{G_{Ri}^2 A^2 P_R}{2\sigma_0^2 + \sum_{i=1}^{N_r} G_{Ri}^2 N_f P_R + \sum_{k=1,k\neq i}^{N_r} G_{Rk}^2 A^2 P_R}, \tag{3.8}$$

where $G_{Ri} = \psi_{Ri}|h_{Ri}|$ denotes the equivalent channel gain. In contrast to the Eq (2.7) and Eq (2.8) of Section 2.3.2 which only takes in to account a single interfer, here in Eq. (3.6) multiple interferes are taken into account.

3.3.1.3 Idealistic Received Signal in the Cell-Edge Area

We assume the employment of perfect adaptive beamforming [93], where each MS is served with the aid of a narrow beam. We also assume that the MSs would be served only by the nearest RAs and that their reception is not contaminated by the other RAs, hence no IRI is received by the MSs roaming in the cell-edge area. Hence their reception is only contaminated by the noise N_f imposed at the optical fibre receiver. Then the interference-

free upper bound of the SINR can be rewritten from Eq (3.8) as:

$$\gamma_u = \frac{G_{Ri}^2 A^2 P_R}{2\sigma_0^2 + G_{Ri}^2 N_f P_R}. \tag{3.9}$$

In contrast to Eq (2.7) and Eq (2.8), which consider a single dominant interferer, in the idealistic interference-free scenario of Eq. (3.9) no interference is taken into account.

3.3.1.4 Benchmarker Systems

Finally, when the classic UFR technique is employed, the received signal model is described by Eq (3.5), but bearing in mind that the full power P is transmitted by each BS instead of P_B. When the FFR technique is employed, similarly to the classic UFR, the signal received in the cell-center area is also described by Eq (3.5). On the other hand, the signal received in the cell-edge area both from the serving BS and from the cells using the same frequency band in tier-two obeys Eq (3.5).

3.3.2 DOF Aided Cooperative DAS Assisted FFR

In a multicell, multiuser scenario cooperative DAS techniques may be used, in order to provide a high throughput for the MSs roaming near the cell-edge area, especially for mitigating the worst-case direction problem caused by IRI. To simplify the entire system, only a single omni-directional antenna is applied for each RA. Nonetheless, when jointly designing the TPP matrix $\mathbf{T}$, the N_R cooperative RAs operate in a concerted action as a virtual multiple-input and single-output (MISO) or virtual multiple-input and multi-output (MIMO) system. On the other hand, only a single receiver antenna is applied at the MS. We will show that the proposed system architecture is capable of substantially enhancing the throughput achievable in the cell-edge area with the advent of our cooperative TPP aided FFR scheme.

3.3.2.1 Received Signal-to-Interference-plus-Noise-Ratio

The principle of cooperative DAS schemes is essentially the same as that of cooperative BSs [135], where the transmit signal destined for the MSs is spread over all the N_r cooperative RAs. In the multicell multiuser scenario there are N_m MSs roaming in the cell-edge area of Fig 3.1, which are simultaneously supported by the N_r RAs ($N_r = N_m$). Provided that the different propagation delays of all the N_r RA links measured with respect to all the served N_m MSs can be pre-compensated, the vector of received signal can be written

as:

$$\mathbf{y} = \mathbf{HTx} + \mathbf{n}, \tag{3.10}$$

where $\mathbf{y}_{N_m \times 1}$ and $\mathbf{n}_{N_m \times 1}$ denote the received signal vector and the circularly symmetric complex Gaussian noise vector. Furthermore, $\mathbf{x} = [x_1, x_2, \cdots, x_{N_m}]^T_{1 \times N_m}$, x_i is defined as the signal transmitted from RA i to MS i. More explicitly, $x_i = \chi_i s_i, i \in [1, N_r]$ represents the signal passing through the realistic 'lossy' optical fibre, where χ_i and s_i is the same as that defined in Section 3.3.1.2. If the central BS has an estimate of the channel matrix $\mathbf{H} = [\mathbf{h}_1^T, \mathbf{h}_2^T, \cdots, \mathbf{h}_{N_m}^T]^T_{N_m \times N_r}$, we can design a transmit matrix $\mathbf{T}$ for mitigating the IRI, where $\mathbf{T} = [\mathbf{t}_1, \mathbf{t}_2, \cdots, \mathbf{t}_{N_m}]_{N_r \times N_m}$ is uniquely and unambiguously determined by $\mathbf{H}$. We also have a dedicated TPP matrix $\mathbf{T}$, which obeys the per RA power constraint of:

$$\mathbf{T}_{i,\forall} \mathbf{T}^H_{i,\forall} \leq \frac{P - P_B}{N_r}, \tag{3.11}$$

where $\mathbf{T}_{i,\forall}$ is the row vector of the matrix $\mathbf{T}$.

Furthermore, $\mathbf{h}_i = [\psi_1 h_1, \psi_2 h_2, \cdots, \psi_{N_r} h_{N_r}]_{1 \times N_r}, i \in [1, N_m]$, represents the channel of all the N_m RA to MS i links, which takes into account both the large-scale signal attenuation and the small-scale fast Rayleigh fading channel, where ψ_i and h_i is the same as that defined in Section 3.3.1.2. Hence, a unified discrete-time model for the signal received by MS i may be formulated based on Eq (3.10) as:

$$y_i = \|\mathbf{h}_i \mathbf{t}_i\| x_i + \sum_{k \neq i} \|\mathbf{h}_i \mathbf{t}_k\| x_k + n_i. \tag{3.12}$$

When we have $k \neq i$, x_k is the IRI imposed by the transmit signal intended for MS k, but received at MS i. Hence, the RoF links' SINR encountered at MS i in the cell-edge area may be written as:

$$\begin{aligned} \gamma_i = {} & A^2 \mathbf{h}_i \mathbf{t}_i \mathbf{t}_i^H \mathbf{h}_i^H \ \times \\ & [2\sigma_0^2 + \underbrace{N_f \mathbf{h}_i \mathbf{t}_i \mathbf{t}_i^H \mathbf{h}_i^H}_{IRI_2} + \underbrace{(A^2 + N_f) \mathbf{h}_i (\sum_{k \neq i} \mathbf{t}_k \mathbf{t}_k^H) \mathbf{h}_i^H}_{IRI_1}]^{-1}, \end{aligned} \tag{3.13}$$

where A and N_f represent the equivalent optical fibre attenuation factor and the equivalent power spectral density of the optical fibre' noise, respectively, as defined in Section 3.3.1.2. It can be seen from Eq (3.13), that for MS i, the IRI is composed of two terms. Specifically, the term IRI_1 of Eq (3.13) is the desired signal of MS $k \neq i$ that is also contaminated by the optical fibre link's noise N_f, which can be mitigated by appropriately designing the corresponding TPP matrix. The other term, namely IRI_2 of Eq (3.13), is the optical fibre link's noise contaminating the desired signal of MS i, which is the self-inflicted noise, hence the TPP matrix is unable to mitigate it.

3.3.2.2 Linear Transmit PreProcessing

Again, we assume that there is only a single transmit antenna at each RA and a single receive antenna at each MS, hence our system is fully described by the number of RAs N_r and by the number of MSs N_m served. Hence our design is based on the $(N_m \times N_r)$-element channel matrix $\mathbf{H}$ associated with the central BS and the TPP facilitates a low-complexity matched-filter-based receiver design at each MS. Our linear TPP matrix $\mathbf{T}$ may be written as:

$$\mathbf{T} = \mathbf{G} \cdot \mathbf{W}, \tag{3.14}$$

where $\mathbf{W}_{N_m \times N_m}$ is a diagonal matrix representing the power [135] allocated to each RA and $\mathbf{G}_{N_r \times N_m}$ is the linear TPP matrix jointly designed on the basis of $\mathbf{H}$, which is assumed to be perfectly estimated and perfectly fed back by the feedback channel [49]. The TPP matrix $\mathbf{G}$ can be calculated with the aid of different linear preprocessing algorithms. In this chapter we consider the minimum mean square error (MMSE) beamformer [140] and the eigenbeamformer (egBF) [81] as our design example.

The classic MMSE beamforming technique strikes an attractive tradeoff between the achievable interference cancellation and noise enhancement, hence it is attractive for practical applications. The TPP weight matrix $\mathbf{G}_{MMSE} = \mathbf{H}^H(\mathbf{H}\mathbf{H}^H + \frac{2\sigma_0^2}{P_R}\mathbf{I})^{-1}$, which is entirely based on the channel matrix $\mathbf{H}$, remains unaffected by the transmit signal. The employment of the TPP matrix $\mathbf{G}_{MMSE}$ mitigates the IRI_1 component in Eq (3.13), eliminating the interference inflicted on the desired signal.

In cooperative egBF, the TPP matrix $\mathbf{G}_{BF} = [\mathbf{g}_1, \mathbf{g}_2, \cdots, \mathbf{g}_{N_m}]$ is used, where $\mathbf{g}_i, i \in [1, N_m]$ is the right-hand-side singular vector of $\mathbf{H}$, which only achieves a power gain, while the mitigation of the term IRI_1 in Eq (3.13) is dependent on the instantaneous geographic distribution of the users. Hence the mitigation of the IRI_1 cannot always be achieved by appropriately selecting the direction of the transmitted beam, unless we employ an idealistic infinitesimally narrow beam for each MS. The associated performance will be characterized in Section 3.4.3.4.

However, in contrast to the IRI_1, the link's self-noise imposed by the optical fibre receiver's noise contribution, namely the IRI_2 terms of Eq (3.13) cannot be mitigated by the TPP matrix employed, regardless, whether the cooperative MMSE or the cooperative egBF is used. In fact, the self-interference may even be boosted, when the desired signal of MS i is amplified. Summarized as Table 3.3

As shown in Fig. 1.6 portraying the organization of the thesis, we focus our attention on the design of the TPP matrix for the DL in this chapter. By contrast the MUD of the

UL is designed in Chapter 4. Both in this chapter and in Chapter 4 we will stipulate the idealized simplifying assumption of having perfect CSI knowledge. However, in practice the CSI has to be estimated at the receiver and then quantized at the receiver for feeding it back to the transmitter. Hence, in Chapter 5 we will study the effects of imperfect CSI knowledge on the DL. Specifically, we will investigate the effects of the CSI estimation error, of the CSI quantisation errors and of synchronisation errors in Chapter 5. As a further design alternative, we will conceive a non-coherent detection aided system for the UL, which dispenses with CSI.

Table 3.3: Linear transmit processing configurations

Cooperative	Weight matrix **G**	Terms of interference
MMSE	$\mathbf{H}_T^H(\mathbf{H}_T\mathbf{H}_T^H + \frac{N_0}{P_R}\mathbf{I})^{-1}$	$IRI_2 \neq 0$
egBF	$\mathbf{G}_{BF}$ is the right-hand-side singular vector of **H**	IRI_1 is up to Z_i $IRI_2 \uparrow$

System Throughput may be characterised by the maximum *successfully transmitted* information rate, which is referred to as the system's *goodput* which is detailed in Section 2.3.2.3. These SINR expressions may be mapped to the ultimate system performance metric formulated in terms of the achievable throughput η as following which is repeated of Eq (2.10) for convenience.

$$\eta(\gamma) = R_M R_C[1 - P_{bl}(b,\gamma)], \tag{3.15}$$

The SINR γ may represent either γ_c of Eq (3.6) or γ_{ei} of Eq (3.8) or γ_u of Eq (3.9) or γ_i of Eq (3.13), R_M denotes the 'rate' i.e. the throughput of the modulation scheme, while R_C is that of the channel code. $P_{bl}(b,\gamma)$ represents the BLER corresponding to the particular Modulation and Coding Scheme employed which is the same as defined in Eq (2.10). We have $M = 2^b$ and $b = 2,4,6$ represents the number of bits per QAM symbol. Hence the modem's throughput is $R_M = b$. In this chapter, we employ 2^b-ary QAM combined with Rate Compatible Punctured Codes (RCPC) [129] having six selected MCSs, namely Mode $[1,\ldots,6]$ of $[R_M, R_C] = [(2,1/2),(2,3/4),(4,1/2),(4,3/4),(6,2/3),(6,6/7)]$. More details would be found in Section 2.3.2.3.

3.4 Performance Evaluation

3.4.1 Simulation Assumptions

The system topology considered is illustrated in Fig. 3.1, where each hexagonal cell has a radius of R, and the distance between the two adjacent BSs is $D = \sqrt{3}R$, e.g. $\overline{B_2B_3} = \sqrt{3}R$. We considered the Urban-Macro propagation scenario of [139], where we have $D = 3km$ and the pathloss expressed in dB is $34.5 + 35\log_{10}(d_0)$, with d_0 being the distance between any transmitter and receiver in km. We assume furthermore that the total transmitter power is $P = 46$dBm and the noise power at the MS is -174dBm/Hz, when an operating in bandwidth of 10 MHz is considered [139]. Moreover, the optical fibre link's normalised Signal-to-Noise-Ratio (SNR) is assumed to be 50dB and the length of the optical fibre is assumed to be five times the distance between the BS and RA [141], where we have $L = 5d$, and d is the line-of-sight distance. We opted for $d = 0.7R, \forall i$.

The cell-center area's radius r may be defined as the maximum radius, where a throughput of at least $\eta = 2bits/s/Hz$ may be maintained in a conventional cellular system employing the classic UFR technique, but beyond this coverage-radius it drops below $\eta = 2bits/s/Hz$. When employing DASs in a FFR-based cellular system, the transmit power of the BS should be sufficiently high to ensure that the average throughput maintained at a distance of r remains exactly as high as that of the classic UFR technique, while the rest of the power is evenly allocated to the RAs. Hence, when considering the $N_r = 6$ RAs operating in a non-cooperative DAS aided FFR scenario, the resultant power sharing regime of all the transmitters obeys $P_B = 2P/5$, while for the relay we have $P_R = P/10$. By contrast, when considering the $N_r = 6$ RAs operating in a cooperative DAS assisted FFR scenario, the power constraint of Eq (3.11) is applied. Finally, the ultimate throughput is obtained by averaging the SINR over 4000 simulation runs, and then substituting it into Eq (2.10) and Eq (2.13). The simulation parameters are summarized in Table 3.4.

3.4.2 Propagation regimes in the DOF Link

Before detailing our performance results, the propagation scenario encountered has to be introduced. When the pulses propagate along the optical fibre, both the nonlinearity and the dispersion depend on the peak power P_0 and on the initial width T_0 of the incident pulse. The critical fibre-lengths L_N and L_D quantify the length of fibre over which either the nonlinear, or the dispersive effects become dominant during the signalling pulse's

Table 3.4: Simulation parameters of the DL, which are based on the 3GPP-LTE standard [1].

Urban macro BS to BS distance	$\overline{B_2B_3} = 3$ km
The pathloss expressed in dB	$34.5 + 35\log_{10}(d_0)$
Total transmitter power	$P = 46$dBm
Noise power at the MS	-174dBm/Hz
Shadowing standard derivation	$\sigma_s = 8$ dB
Normalised optical fibre link SNR	50 dB
Line-of-sight distance of BS-RA	$d = 0.7R$
Length of the optical fibre	$L = 5d$
Number of RAs	$N_r = 6$
Number of MSs	$N_m = 6$
QAM	$M = 2^b, b = 2, 4, 6$
RCPC code	$[R_M, R_C] = [(2, 1/2), (2, 3/4),$ $(4, 1/2), (4, 3/4), (6, 2/3), (6, 6/7)]$ $R_m = b$, R_c is code rate

Table 3.5: Propagation regimes

Curve	P_0	T_0	l	L_D	L_N
1	10mW	10ps	5m	5km	50km
2	160mW	10ps	5m	5km	3km
3	10mW	10ps	10m	5km	50km
4	10mW	20ps	5m	20km	50km
5	10mW	50ps	5m	125km	50km

propagation. The relations between L_N and P_0, L_D and T_0 are calculated as follows [111]:

$$L_N = \frac{1}{\xi P_0}, L_D = \frac{T_0^2}{|\beta_2|}. \tag{3.16}$$

The typical values of the GVD parameter β_2 and the nonlinearity parameter ξ at a wavelength of $1.55\mu m$ are [111] $|\beta_2| \approx 20ps^2/km$ and $\xi \approx 2W^{-1}km^{-1}$ for standard telecommunication fibres. For a given optical fibre length of L, we have:

- if $L \ll L_N$ and $L \ll L_D$, neither the nonlinear nor the dispersive effects impose a significant performance degradation during the pulse's propagation.
- if $L \ll L_N$ and $L \sim L_D$, the nonlinear effects may be ignored and the the dispersion will play the dominant role.

- for $L \sim L_N$ and $L \ll L_D$, the dispersion is negligible compared to the nonlinear distortion.
- for $L \sim L_N$ and $L \sim L_D$, both of the nonlinear and dispersion effects are non-negligible.

In this chapter, according to the Urban-Macro cell scenario introduced in Section 3.4.1, we assume the set of P_0 and T_0 values shown in Table 3.5 in order to investigate how the nonlinear and dispersion effects of the optical fibre influence the attainable throughput of the wireless channel in the cell-edge area.

3.4.3 Throughput Performance

We only simulated one typical location in the Wyner interference model of two cells, as shown in Fig. 2.5 of Section 2.3. In this chapter, we will characterized the throughput across the entire cellular area in the multiuser, multicell scenario of Fig. 3.1. First of all, we demonstrate that the IRI inflicted by the tier-two cells will be neglected in order to simplify our analysis in the DAS aided FFR assisted multicell, multiuser scenario of Fig. 3.4. Hence we only have to calculate the IRI emanating from the local cell of the DAS aided FFR assisted multicell, multiuser scenario. The throughput of the non-cooperative DAS system combined with FFR will be demonstrated in typical directions of θ_{best}, θ_{worst} and θ_{mid} which are portrayed in Fig. 3.5 Fig. 3.6 and Fig. 3.7. The throughput across the entire cellular area recorded for $N_r = 6 and 12$ is shown in Fig. 3.8 and Fig. 3.9. The throughput of the cooperative DAS combined with FFR will be characterized for the typical directions of θ_{best}, θ_{worst} in Fig. 3.10 and the throughput improvement compared to the non-cooperative DAS aided FFR will be quantified in Fig. 3.11.

3.4.3.1 IRI Inflicted by the Tier-two Cells

The IRI experienced in the local cell dominates the interference experienced in the DOF aided DAS combined with FFR. We also found that the DAS combined with FFR requires a reduced transmit power at each RA, which naturally limits the IRI imposed by the cells using the same frequency band in a tier-two cell. Hence, the IRI inflicted by the tier-two cells will be neglected to simplify our analysis in the multicell, multiuser scenario considered. [1]

[1] In DAS-aided FFR-assisted cellular system effectively a handover procedure has to be initiated, when the MS moves from the cell-center area covered by the BS antenna to the cell-edge area covered by the DAS in order to avoid a catastrophic performance degradation.

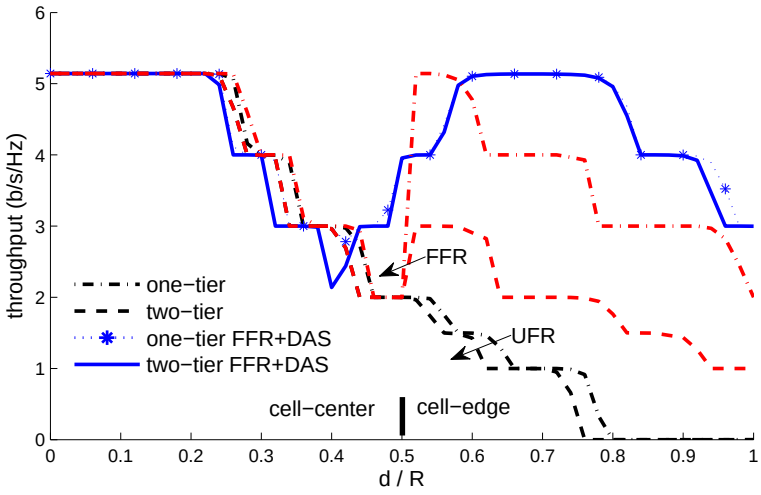

Figure 3.4: Throughput comparison of the traditional UFR system, FFR system and the $N_r = 6$ DAS aided FFR both in single-tier and two-tier scenarios along the θ_{best} direction . All system parameters were summarized in the context of curve 1 of Table 3.5.

Fig. 3.4 compares the throughput of the classic UFR system, of the conventional FFR system and of the DAS aided FFR assisted systems using $N_r = 6$ in both single-tier and two-tier scenarios. It can be seen in Fig. 3.4 that upon assigning a transmit power of $P_B = 2P/5$ in the cell-center area, the throughput of the DAS aided FFR assisted system is almost the same as that of the conventional UFR and FFR systems, when these two systems assign the full transmit power to the BS. By contrast, when the cell-edge area is considered, the throughput of the conventional UFR scheme becomes lower than $\eta = 2$ bits/s/Hz and when taking into account the IBI inflicted by the tier-two cells, the throughput is only moderately reduced. However, for the conventional FFR scheme, the throughput is reduced below $2 bits/s/Hz$, since there is no IBI from tier-one, when taking into account the IBI imposed by tier-two. When a DAS aided FFR assisted system is employed in conjunction with $N_r = 6$ RAs, an increased throughput of $\eta > 3$ bits/s/Hz is achieved, despite the presence of IRI from tier-two, as illustrated by the solid line of Fig. 3.4. This is an explicit benefit of the DAS aided FFR scheme, where the reduced power of $P_R = P/10$ was allocated to each RA instead of the full-power-based UFR transmit strategy and the IRI arising from tier-two was naturally reduced owing to the increased co-channel distance. Nonetheless, the increased amount of IRI only slightly reduced the throughput in Fig. 3.4. Therefore, when considering the DAS aided FFR assisted system, the IRI arising from tier-two may be ignored, provided that the IRI of the local cell can be efficiently mitigated.

3.4.3.2 Throughput of the Cell-center Area

The attainable throughput of the non-cooperative DAS combined with FFR system and of the cooperative DAS combined with FFR is characterized in Fig. 3.5, Fig. 3.6 and Fig. 3.10 in the cell-center area relies on the SINR of Eq (3.6), as introduced in Section 3.3.1. Hence, both of systems have the same throughput. Explicitly, upon assigning a transmit power of $P_B = 2P/5$ in the cell-center area, the throughput of the non-cooperative DAS combined with FFR and that of cooperative DAS combined with FFR become similar to that of the traditional UFR and FFR systems, provided that the latter two systems assign the full transmit power to the BS.

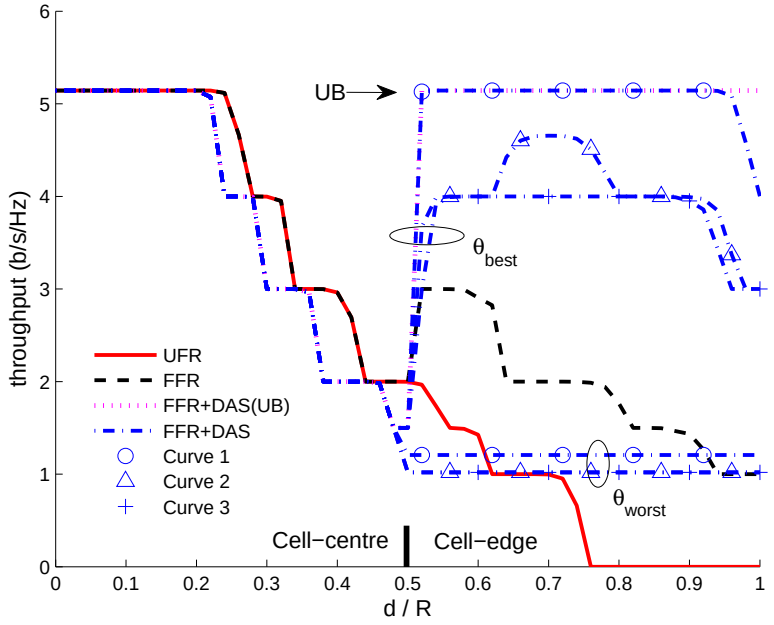

Figure 3.5: Throughput comparison of the traditional UFR system, FFR system and of the $N_r = 6$ non-cooperative DAS aided FFR system in two-tier scenarios along the θ_{best} and θ_{worst} directions recorded for characterizing the nonlinear effects of the optical fibre and the accuracy of the SSF Method. All system parameters were summarized in Table 3.5.

3.4.3.3 Cell-edge Area of Non-cooperative DAS Relying on FFR

Fig. 3.5, Fig. 3.6 and Fig. 3.7 compare the throughput of the classic UFR system, of the traditional FFR system and of the non-cooperative RA-aided FFR assisted systems using $N_r = 6$, $N_m = 6$ in the best, the worst and intermediate direction in a two-tier scenario. The four sets of optical fibre parameters shown in Table 3.5 were used.

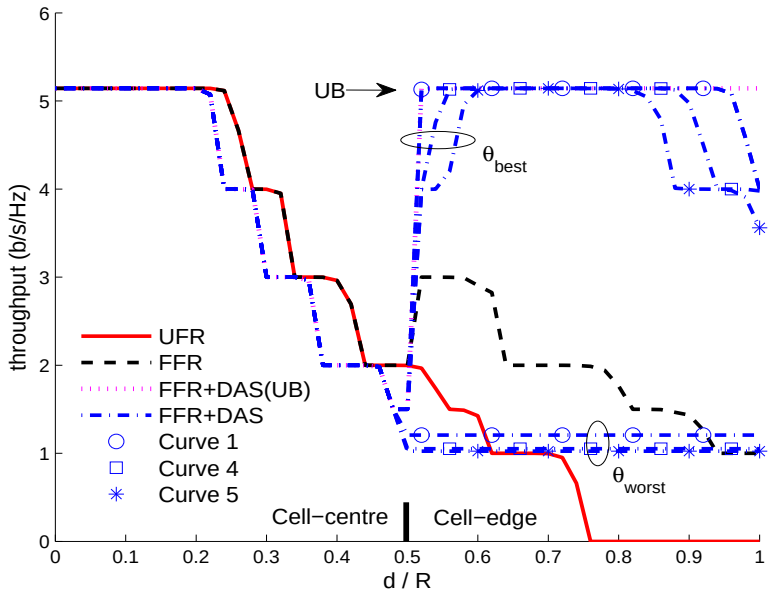

Figure 3.6: Throughput comparison of the traditional UFR system, FFR system and of the $N_r = 6$ non-cooperative DAS aided FFR system along the θ_{best} and θ_{worst} directions for characterizing the dispersion effects of the optical fibre. All system parameters were summarized in Table 3.5.

Throughput in the Best Direction By contrast, when the cell-edge area is considered, observe in Fig. 3.5 and Fig. 3.6 that the throughput of the conventional UFR scheme becomes lower than $\eta = 2$ bits/s/Hz, while that of the conventional FFR scheme is in the range of $\eta \in [1, 3]$ bits/s/Hz. When the non-cooperative RA-aided FFR-assisted system is employed in conjunction with $N_r = 6$ RAs, a throughput in the range of $\eta \in [3, 5]$ bits/s/Hz is achieved along the best direction.

More explicitly, when using the parameters of Table 3.5, Curves 1 - 5 in Fig. 3.5 and Fig. 3.6, suggest that:

- *Nonlinear Effect of the DOF Link*: The comparison of Curve 1 ($P_0 = 10$mW) and Curve 2 ($P_0 = 160$mW) in Fig. 3.5 shows how the power assigned to the optical pulses affects the throughput of the wireless link, which was demonstrated by setting $P_0 = 10$mW and 160mW of peak power for the optical signalling pulse. Again, the corresponding optical parameters are shown in Table 3.5. Observe by comparing Curves 1 and 2 of Fig. 3.5 that assigning a $P_0 = 160$mW power to the optical pulse makes the nonlinearity-induced impairments dominant, which will broaden the spectrum of the optical pulse in the frequency domain. The nonlinearity indirectly results in an increased attenuation for the optical pulses, but this cannot be compensated by an increased transmit power, hence this leads to a boost of the IRI. As a

net-result, the system suffers from an approximate throughput loss of 1 bits/s/Hz in the cell-edge area along the best direction.

- *Accuracy of SSF Method*: Comparing Curve 3 to Curve 1 of Fig. 3.5, the former is associated with a longer segment l used by the SSF method, which reduces the analysis complexity. However, as a result, the predicted throughput is reduced by about 1 bits/s/Hz. By contrast, a shorter segment l results in a more accurate of the SSF model at the cost of a higher offline analysis complexity. But selecting the probable segment length will strongly affect the results of simulation, which is important for whom doing the relative research. For a typical urban cell size our Monte-Carlo simulation results suggest that $l = 5$m is an appropriate compromise, which may be trusted as the real attainable throughput of our RoF aided DAS combined with FFR system.

- *Dispersion Effect of the DOF Link*: Fig. 3.6 demonstrates by increasing the width of the optical signalling pulse from $T_0 = 10$ps to 20ps and 50ps for Curves 4 and 5, how this affects the throughput of the wireless link, when the non-cooperative RA-aided FFR-assisted system is employed in conjunction with $N_r = 6$ RAs. Again, when using the optical parameters shown in Table 3.5 and setting a peak power of $P_0 = 10$mW, the nonlinear effects of the optical fibre become negligible. Comparing Curve 4 ($T_0 = 20$ps) and Curve 5 ($T_0 = 50$ps) to Curve 1 ($T_0 = 10$ps) of Fig. 3.6, the throughput at the cell-edge remains in the range of $\eta \in [4, 5]$ bits/s/Hz, but when the optical pulse width is increased, according to Table 3.5 from $T_0 = 10$ps to 20ps and 50ps, the attainable throughput of the cell-edge area is reduced. The reason for this observation is that wide pulses are typically broadened to a lesser relative degree along the optical fibre, which also leads to a reduced attenuation both at the optical receiver of the serving RA as well as at the interfering RAs.

Throughput in the Worst Direction: When considering the worst direction in both Fig. 3.5 and Fig. 3.6, regardless of the specific choice of the five parameter sets of Table 3.5, we only achieve a throughput of about $\eta = 1$ bits/s/Hz. This is due to the above-mentioned worst-case direction problem [39], which becomes the limiting factor in the case of the conventional non-cooperative RA-aided FFR assisted system.

Throughput in the Intermediate Direction:

The attainable throughput of the non-cooperative RA-aided FFR systems along arbitrary directions is between that of the θ_{best} and θ_{worst} directions, as seen from the throughput contours of Fig. 3.9. Consider the intermediate direction for example, which is defined

as the direction half-way between θ_{best} and θ_{worst} in Fig. 3.1. Comparing Curve 1, Curve 2, Curve 4 and Curve 5 of Fig. 3.7 to those along the best direction in Fig. 3.5 and Fig. 3.6, we observe a reduction of the attainable throughput along the intermediate direction, which remains in the range of $\eta \in [3,5] bits/s/Hz$ at the cell-edge. However, this is still better than that of the conventional FFR scheme residing in the range of $\eta \in [1,3] bits/s/Hz$. Nonetheless, when the MS is roaming near the θ_{worst} direction, the attainable throughput is substantially reduced, since the IRI becomes strong. Hence, the non-cooperative RA-aided FFR is unable to achieve a throughput improvement across the entire cell-edge area. Practically, when considering the cost and complexity of installing RAs in the cell-edge area, we may not be able to conclude that the non-cooperative RA-aided FFR systems is always superior in comparison to the conventional FFR scheme. Indeed, the conventional FFR scheme may be deemed to be a low-complexity solution capable of achieving an improvement of the throughput in the entire cell-edge area, especially in the θ_{worst} direction, as you astutely noted. Hence we also stated in the chapter that the worst-case direction problem constitutes a limiting factor in the case of conventional non-cooperative RA-aided FFR systems. However, the study of non-cooperative RA-aided FFR systems provided in this chapter shows a potential in terms of improving the attainable throughput in the cell-edge area by combining DASs with the FFR scheme. Hence, we propose to invoke cooperative processing techniques for solving the worst-case direction problem of non-cooperative RA-aided FFR systems, which may be a better solution than that constituted by the conventional FFR scheme. The nonlinear effects and the dispersion effects of the RoF link were analysed in Section IV-D. Apart from its detrimental effects, the dispersion of the optical fibre also has some benefits, as seen by observing Curve 1 ($T_0 = 10ps$), Curve 4 ($T_0 = 20ps$) and Curve 5 ($T_0 = 50ps$) in Fig. 3.7 of this response (Fig. 5 in the manuscript). When a narrow pulse (Curve 1) is applied, there is a $1 bits/s/Hz$ throughput improvement in comparison to applying wide pulses (Curve 4 and 5) along the intermediate direction of the cell-edge area.

Comparison of the Entire Cell's Throughput:

In order to compare the attainable throughput across the entire cell, we calculated the corresponding percentage of the entire cell over which a certain throughput η was maintained, as illustrated in Fig. 3.8. It can be seen that employing $K = 6$ RAs achieves a higher throughput than $K = 12$ RAs for both the ideal and realistic imperfect optical fibre scenarios. However, we emphasis that this does not necessarily lead to the conclusion that the $K = 6$ RA-aided configuration is better than the $K = 12$ RA configuration. Fig. 3.9 demonstrates the attainable throughput across the entire cell for the different configurations of our non-cooperative RA-aided FFR assisted system associated with Curve 1 of

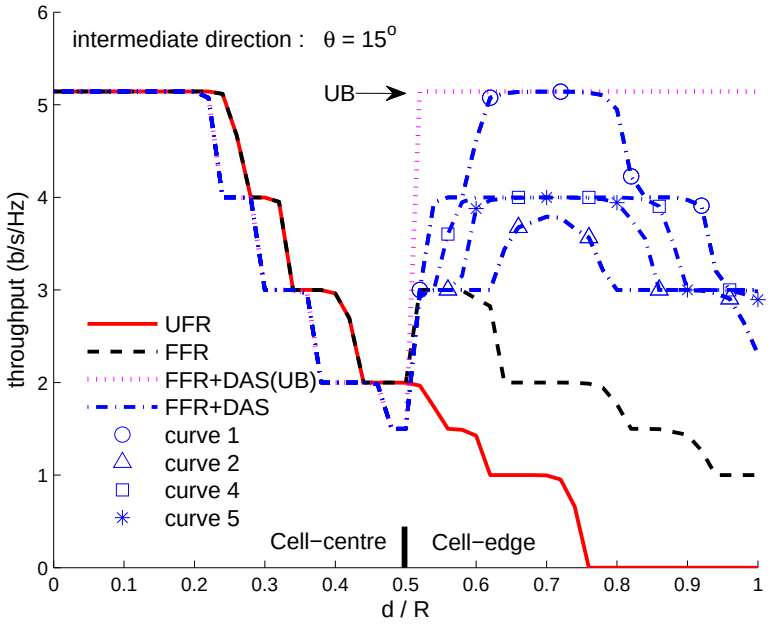

Figure 3.7: Throughput comparison of the traditional UFR system, FFR system and of the $N_r = 6$ non-cooperative DAS aided FFR system along the intermediate direction for characterizing the nonlinear and dispersion effects of the optical fibre. All system parameters were summarized in Table 3.5

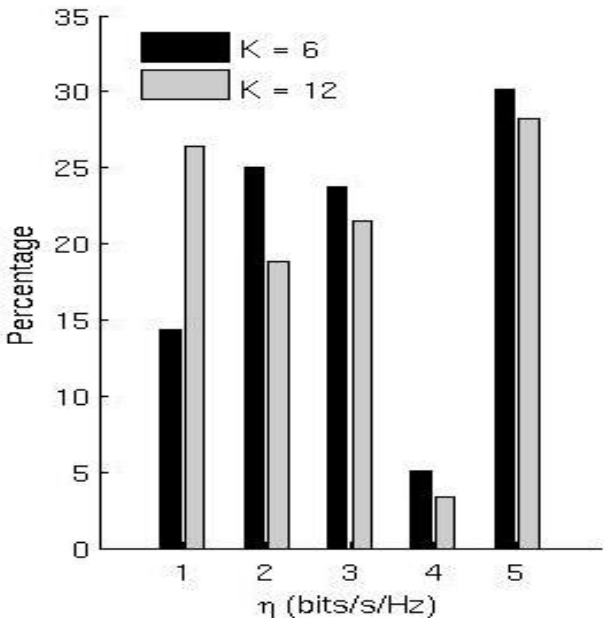

Figure 3.8: The percentage of the cell throughput for both $K = 6$ and $K = 12$ RAs aided FFR enabled system with and without IPI.

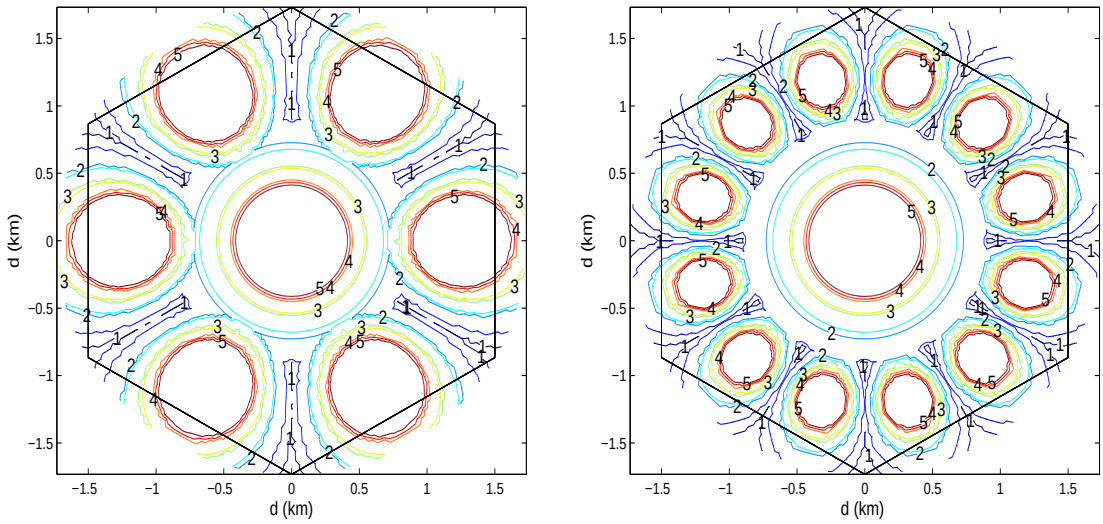

Figure 3.9: Throughput contours in Bit/second/Hz for the $N_r = 6$ and $N_r = 12$ non-cooperative DAS aided FFR system. All system parameters were summarized in the context of Curve 1 of Table 3.5.

Table 3.5. More explicitly, the cell-center area's throughput contours recorded in Fig. 3.9 for both configurations are similar. However, the throughput distribution of the $N_r = 6$ RA-aided configuration recorded for the cell-edge area tends to be more 'patchy', while that of the $N_r = 12$ RA-assisted configuration tends to cover the entire outer ring more evenly. As a result, the general conclusion emerging for the comparison of these two configurations is that the optimum positioning of DASs should take into account the expected user-distribution and user-load. However, the "worst-case direction" problem persists in both of these two configurations.

3.4.3.4 Cell-edge Area of Cooperative DAS Relying on FFR

Fig. 3.10 compares the throughput of the classic UFR based arrangement and of the traditional FFR aided system, as well as of the cooperative RA-aided FFR assisted system using $N_r = 6$, which was evaluated along both the best and worst angular directions respectively and employing the five sets of parameters seen in Table 3.5 for the optical fibre link. We consider supporting $N_m = 6$ MSs roaming in the cell-edge area, where MS i is close to the RA i, as illustrated in Fig. 3.1. The N_m MSs are served simultaneously by the N_r cooperative RAs and they are randomly distributed around the point $Z_i, i = 1, \ldots, N_m$ of Fig. 3.1, where Z_i belongs to the corresponding 60°-sector surrounding RA i. The MSs are allowed to randomly cross the cell-edge area, but only once, in order to investigate the histogram of the attainable throughput for the N_m MSs.

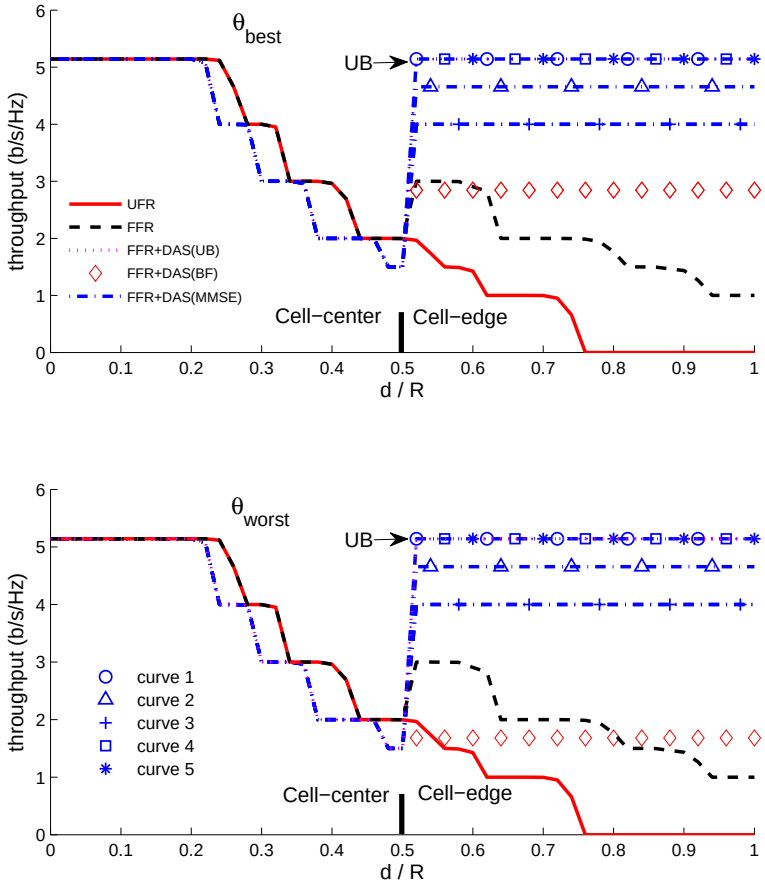

Figure 3.10: Throughput comparison of the traditional UFR system, FFR system and the $N_r = 6$ cooperative DAS aided FFR system along the best direction with 5 sets of optical parameters in Table 3.5 multicell multiuser scenario. The legends are shared between the top and bottom graphs. All system parameters were summarized in Table 3.5

Throughput in the Best Direction: When the cell-edge area is considered, observe the upper figure in Fig. 3.10 that the throughput of the conventional UFR scheme becomes lower than $\eta = 2$ bits/s/Hz, while that of the conventional FFR scheme is in the range of $\eta \in [1,3]$ bits/s/Hz, as illustrated in Fig. 3.10. When the cooperative RA-aided FFR-assisted system using the parameters associated with Curves 1, 4 and 5 of Table 3.5 is considered, observe in Fig. 3.10 that linear TPP achieves a throughput of $\eta = 5$ bits/s/Hz, which is similar to the throughput upper bound of the RA-aided FFR-assisted system. Hence, when the nonlinearity effects can be ignored, the dispersion does not overly affect the throughput of the wireless channel.

Comparing Curve 2 and Curve 1 in Fig. 3.10, when using a peak power of $P_0 =$

160mW for the signalling pulses, the MMSE TPP techniques achieve a slightly higher throughput than 4 bits/s/Hz. Since the term IRI_1 in Eq (3.13) is mitigated by the MMSE TPP, the throughput reduction is imposed by the further attenuation of the received optical signalling pulses inflicted by the fibre's nonlinearity. When employing the parameters associated with Curve 3 with a segment length of $l = 10$m for the SSF method, a throughput reduction of $\Delta\eta = 1$ bits/s/Hz is encountered.

Observe in Fig. 3.10 that the throughput of cooperative egBF is between that of the linear TPP techniques and of the traditional UFR system, and it is not always higher than that of the conventional FFR scheme. The reason for this phenomenon is that the performance of the cooperative egBF is also dependent on the geographic distribution of the N_m users. Hence the served MS may suffer from an increased interference, which imposes an increased throughput erosion in comparison to the conventional FFR scheme.

Throughput in the Worst direction: It is demonstrated in the lower figure of Fig. 3.10 that the cooperative RA-aided FFR assisted system does not suffer from the worst-case angular direction problem and hence the linear TPP techniques achieve a throughput of $\eta = 5$ bits/s/Hz, which is the upper bound of the RA-aided FFR-assisted system. The other curves exhibit the same throughput performance as that shown in the upper figure of Fig. 3.10. The cooperative egBF does not solve the worst-case angular direction problem, hence its throughput is lower than that of the traditional FFR.

Remarks: overall, we conclude from Figure 3.10 that when the nonlinearity effects can be ignored, the dispersion does not overly affect the throughput of the wireless channel. The cooperative MMSE scheme is capable of significantly improving the throughput in the cell-edge area, hence all MSs benefit from a consistently high throughput, which is close to the attainable upper bound. By contrast, a strong nonlinearity imposes an approximate throughput reduction of 1 bits/s/Hz. However, as evidenced by Fig. 3.10 the performance of the egBF arrangement is significantly dependent on the instantaneous geographic distribution of the N_m users, hence it does not always achieve a higher throughput than the traditional FFR scheme, which make the cooperative egBF less attractive than the other linear transmit preprocessing techniques.

3.4.3.5 Throughput Enhancement Across the Entire Cell

In order to observe the attainable throughput improvement $\Delta\eta$ achieved by the cooperative RA aided FFR assisted systems over their non-cooperative counterparts across the entire cell, the resultant throughput contour profile associated with Curve 1 of Table 3.5 is portrayed in Fig. 3.11. We configured the cooperative techniques for enhancing the attainable

throughput in the cell-edge area, hence in the cell-center area we have $\Delta\eta = 0$. In the cell-edge area, when considering the cooperative MMSE arrangement for example, there is a significant throughput improvement in the worst-case angular direction, since we have $\Delta\eta = 4$bits/s/Hz in the direction θ_{worst}. By contrast, when the MS is roaming close to the RA, the throughput improvement achieved by the cooperative MMSE technique remains limited. When however the MS is roaming far from the RA, the benefits of the cooperative techniques become more pronounced.

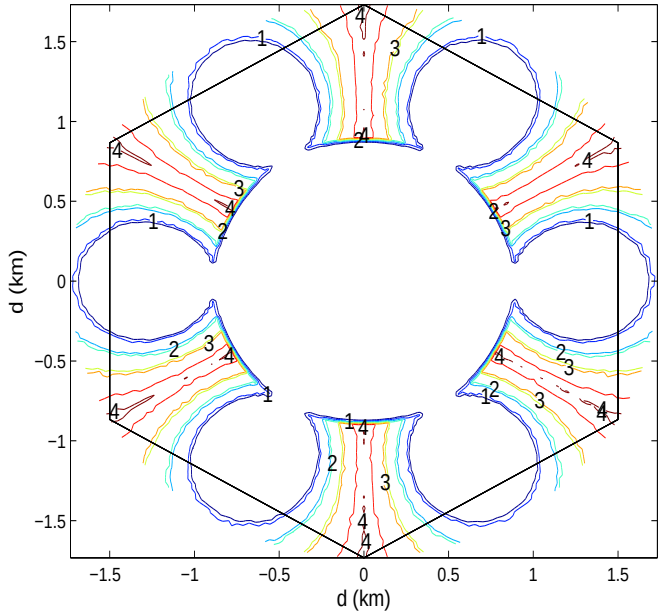

Figure 3.11: Contours $\Delta\eta$ of throughput in Bit/s/Hz enhancement for the $N_r = 6$ cooperative DAS aided FFR systems, over the non-cooperative DAS aided FFR. All system parameters were summarized in the context of Curve 1 in Table 3.5.

3.4.4 Power Control for a Multiuser DL Scenario

The DAS aided FFR architecture proposed in this chapter aims for reducing the CCI in a DL scenario, i.e. for enhancing the SINR of the MSs roaming in the cell-edge area. However, the ”worst-case direction” problem exemplified in Fig. 3.9 degrades the average throughput of the cellular area. Hence, TTP is invoked for mitigating the CCI, which relies on the idealized simplifying assumption of having perfect CSI as discussed in Section 3.3.2.2. Practically, the generation of perfect CSI is difficult to achieve, whilst having an imperfect CSI obviously leads to a reduced performance. Hence, we introduce power control (PC) for improving the SINR of the MSs roaming in the cell-edge area.

In this section, the task of the PC designed for the DAS aided FFR systems is to im-

prove the SINR of the active users roaming in the cell-edge area. As an example, when the MS "a" of Fig. 3.1 roams in the cell-edge area hence suffers from a low SINR, the transmit power will be increased in order to improve the SINR of MS "a". However, this increased power will increase the interference imposed on the other MSs, hence the SINR of the other MSs will be decreased. More explicitly, among the other MSs, MS "b" may also be suffering from a reduced SINR and hence may request an increased transmit power. As a result, the increased power for MS "b" will more substantially interfer with the other MSs, including MS "a". Hence, although the transmit power reduction of MS "a" is compensated, it is hard to achieve the desired SINR. Nonetheless, we attempt to demonstrate the effects of the PC in our multiuser scenario, where there may be multiple MSs in the cell-edge area, requesting an increased transmit power.

First of all, we use the normalized Signal-to-Interference Ratio (SIR) model to analyze the CCI in the multiuser scenario, since the AWGN of both the wireless and receiver of the optical fibre channel is moderate, hence in the multiuser, multicell scenario considered the effects of the interference dominate the attainable performance. We refer to this situation as an interference-limited scenario [142]. More explicitly, in interference-limited situations we have $SINR \simeq SIR$, and we record the SIR for all users randomly roaming across the entire cell area. For the DOF aided DAS using the FFR architecture we assume to have the same distance between each BS-RA pair and also the same length of fibre between each BS-RA pair. Hence the attenuation of all the optical fibre channels is the same. As a result, the SIR model using no PC is solely based on the path-lass and it takes no account of fading of any kind. Finally, we assumes an equal DL transmit power for each RA which is expressed as [142]:

$$SIR_i(dB) = Pahtloss_{dB}(d_s) - Pathloss_{dB}(d_i), \tag{3.17}$$

where in our DL scenario, the SIR_i is defined as the SIR experienced by the observed user, as determined by the ith interfering RA, d_s is the distance between the RA and the observed user, while d_i is the distance between the ith interfering RA and the observed user. Assuming a $40dB/decade$ inverse power path-loss law, the SIR_i associated with the i interferer can be simplified to:

$$SIR_i(dB) = 40log_{10}(\frac{d_i}{d_s}). \tag{3.18}$$

For our multiuser scenario of Fig. 3.1, the SIR_{user} is defined as the SIR at any user roaming across the cell-edge area, who suffers from the contaminating effects of n interferers, where S and $I_i, i = 1 \cdots n$ represent the transmitted signal power and the power of

the ith interfer, respectively. Then, SIR_{user} is formulated as:

$$\begin{aligned} SIR_{user} &= \frac{S}{I} = \frac{S}{\sum_{i=1\cdots n} I_i} \\ &= \frac{S}{I_1 + I_2 + \cdots I_n} \\ &= \frac{1}{\frac{I_1}{S} + \frac{I_2}{S} + \cdots \frac{I_n}{S}} \\ &= \frac{1}{SIR_1^{-1} + SIR_2^{-1} + \cdots SIR_n^{-1}}, \end{aligned} \tag{3.19}$$

which can be written in dBs as:

$$\begin{aligned} SIR_{user}(dB) &= -10\log_{10}[10^{-(\frac{SIR_1(dB)}{10})} + 10^{-(\frac{SIR_2(dB)}{10})} + \cdots 10^{-(\frac{SIR_n(dB)}{10})}], \\ &= -10\log_{10}[\sum_i 10^{-(\frac{SIR_i(dB)}{10})}]. \end{aligned} \tag{3.20}$$

In Section 3.3.1.2, we use the SINR model of Eq. (3.8). In order to simplify the multiuser scenario considered, the $SIR(dB)$ model of Eq.(3.20) is useful for comparing different network architectures. Our multiuser, multicell scenario is an interference-limited scenario, where we have $SINR \simeq SIR$ and the SIR is only related to the distances d_s and d_i, as discussed above.

The geographic SIR distribution of the cell-edge area is based on Eq. (3.20), where the specific MSs suffering from a lower SIR will be assisted by increasing the transmit power. When applying the above PC technique, the SIR associated with the ith interfer may be written as:

$$SIR_i^{'}(dB) = 40log_{10}(\frac{d_i}{d_s}) + P_{dB}^s - P_{dB}^i, \tag{3.21}$$

where d_i and d_s are defined in the same was as in Eq. (3.18). Furthermore, P_{dB}^s and P_{dB}^i represent the transmit power of the destined user and that of the interfering user, respectively. More explicitly, when the MS roaming in the cell-edge area suffers from a lower SIR_{user}^s, the transmit power will be increased in the interest of maintaining the target SIR. Correspondingly, the interfering MS may also suffer from a lower SIR_{user}^i and hence its transmit power will be increased, which will increase the interference imposed on the other MSs.

The SIR recorded in the presence of PC for our multiuser scenario remains similar to that without PC, which may by written based on Eq. 3.20 as followings:

$$SIR_{user}^{'}(dB) = -10\log_{10}[\sum_i 10^{-(\frac{SIR_i^{'}(dB)}{10})}]. \tag{3.22}$$

The SIR record both with and without PC for our DAS aided FFR architecture in the cell-edge area is characterized in Fig. 3.12. Observing the cell-edge area of Fig. 3.12 while operating without the PC technique, the SIR is calculated using Eq. (3.20). When the MS roams close to the RA, a high SIR $(SIR_{user}(dB) \geq 20dB)$ may be guaranteed, hence there is no need to increase the transmit power. By contrast, when the MS roams far away from the RA, the SIR is reduced $(SIR_{user}(dB) < 20dB)$, especially in the "worst-case directions" $(SIR_{user}(dB) \sim -20dB)$, where the transmit power will have to be increased in order to aim for an adequate SIR. Observing the cell-edge area of Fig. 3.12 in conjunction with the PC technique, the SIR is calculated from Eq. (3.22). The SIR of the MSs roaming close to the RAs is slightly reduced in comparison to that in the absence of PC, but still remains a high value $(SIR'_{user}(dB) \geq 20dB)$. On the other hand, when the MS in roaming far away from the RA, especially in the "worst-case directions", the SIR is significantly increased $(SIR'_{user}(dB) \in [0 \sim 20dB)$ in comparison to the no-PC scenario.

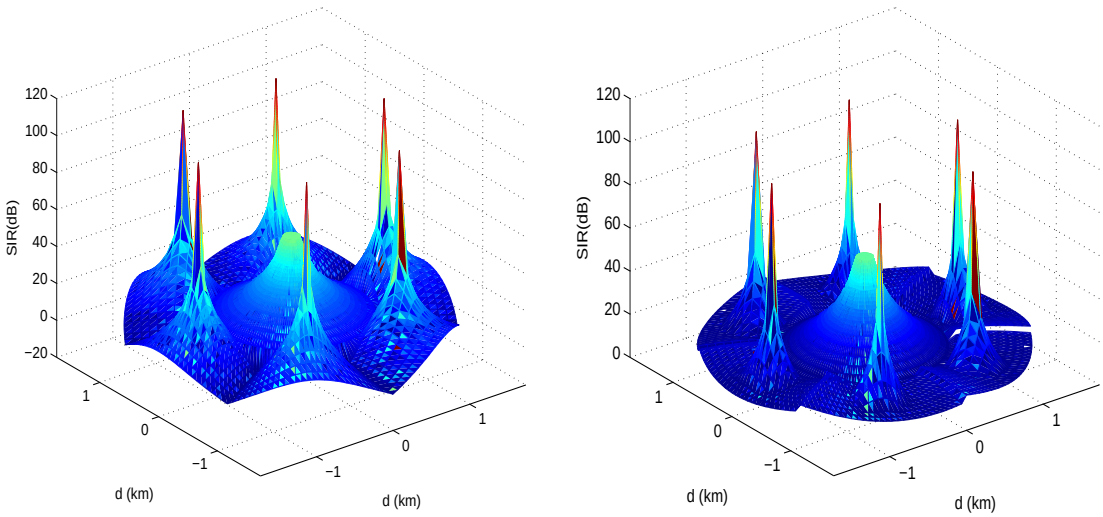

(a) no power control (b) power control

Figure 3.12: The SIR of noncooperative DAS aided FFR systems, both without and with the assistance of power control. All system parameters were summarized in Table 3.5.

The achievable throughput of the DAS aided FFR system is characterized in Fig. 3.13, where the throughput of the entire cell-edge area is enhanced to $\eta \geq 3bits/s/Hz$, provided that PC is used. To a degree the throughput is expected to obey the SIR-trends. More explicitly, when the MSs roam close to the RAs, the throughput remains similar to that achieved without applying the PC technique, which was shown in Fig. 3.11. Again, in line with the SIR improvements, when the MSs are roaming far away from the RAs, the throughput is increased to $\eta \geq [3 \sim 3.5]bits/s/Hz$ with the assistance of

the PC technique, as shown in Fig. 3.13. By contrast, the throughput remains as low as $\eta \geq [1 \sim 2] bits/s/Hz$ without any PC and without TPP, as shown in Fig. 3.9. When applying TPP, we can observe in Fig. 3.11 that the throughput of the entire cell-edge area may be as high as $\eta = 5 bits/s/Hz$, provided that perfect CSI is available.

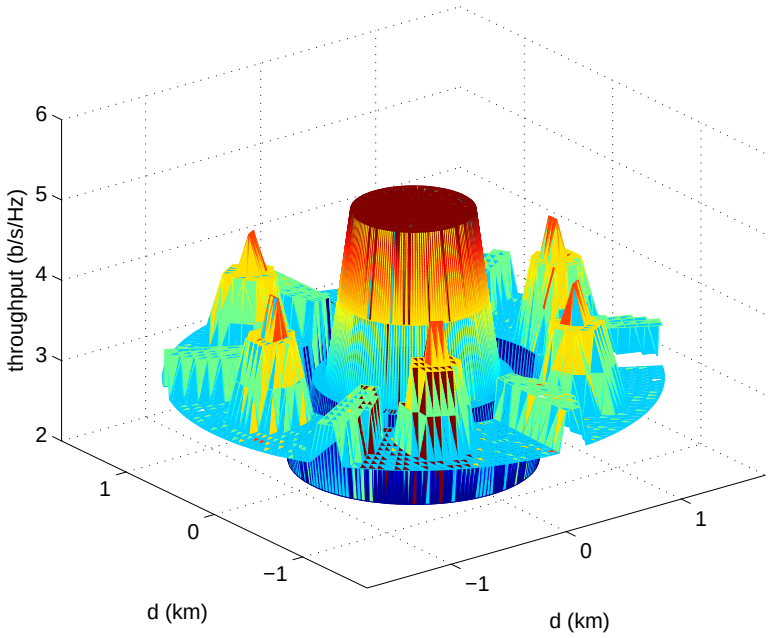

Figure 3.13: The 3D throughput profile recorded for the $N_r = 6$ noncooperative DAS aided FFR scenario assisted by power control across the entire cellular area. All system parameters were summarized in Table 3.5.

3.4.5 Chapter Summary

The achievable throughput of a DOF aided DAS relying on FFR and a realistic optical fibre backhaul was investigated in practical multicell, multiuser scenarios. Our work demonstrated that the non-cooperative DAS aided FFR system is capable of gleaning some benefits from the imperfections of the optical fibre, because the dispersion of the optical signalling pulse might indirectly increase the attainable throughput of the cell-edge area, as argued in Section 3.2.2. More explicitly, when applying the configurations of $N_r = 6$ and $N_r = 12$, the geographic throughput distribution becomes different, which may be beneficially exploited for supporting different geographic users-distributions. Correspondingly, the cooperative RA-aided FFR relying on the linear TPP techniques advocated in Section 3.3.2.2 is capable of efficiently mitigating the IRI in the worst-case direction. As a result, the system may be capable of supporting a throughput of $\eta = 5$ bits/s/Hz, regard-

less of the specific geographic user-distribution encountered. Furthermore, the cooperative RA-aided FFR system may become tolerant to the dispersion of the optical pulse, but sensitive to the fibre-induced nonlinearity, if the optical pulse has a high power.

Indeed, efficient TPP requires efficient feedback control, which involves an accurate and frequent channel estimation, quantisation and feedback process, where sophisticated signal processing improvements may result in an increased throughput. The overhead associated with this cooperative transmission, or closed-loop design in general, is constituted by the Doppler-dependent channel-sounding pilot overhead and the feedback quantisation overhead, where the latter potentially depends not only on the quantisation method performed, but also on the specific cooperative structure employed, i.e. on whether centralised or distributed cooperation is used. Regarding the effect of the numbers of RAs, an intuitive observation is that the more cooperative RAs, the more overhead will be incurred. However, no simple quantitative relationship may be established. Furthermore, since the amount of overhead imposed may offset the potential gain achieved, we have to strike an attractive tradeoff, as discussed in [143]. The rate of change of the channel will indeed significantly decrease the resultant performance gains, since the feedback may become more outdated and the TPP matrix will be subject to strong mismatch. Hence, closed-loop designs in general may not be suitable for high-velocity applications, where in addition to an increased normalized feedback delay, the channel estimation becomes more challenging in the downlink.

3.5 Chapter Conclusions

In this chapter, the DAS aided FFR architecture was investigated in a more practical multiuser, multicell scenario characterized by a topology of two-tiers of nineteen cells, as shown in Fig. 3.1. The BS-RA backhaul was the DOF link of Fig. 3.2 which was modeled by the SSF method of Eq. (3.4) in Section 3.2.2, which is capable of taking into account both the fibre's linear dispersion and non-linear dispersion. The received signal model and the SINR definitions of the noncooperative DAS aided FFR scheme were introduced in Section 3.3.1 while those of the cooperative DAS aided FFR scheme in Section 3.3.2. The throughput of the noncooperative DAS aided FFR scheme was portrayed in Fig. 3.5, Fig. 3.6, Fig. 3.9 and Fig. 3.8 and that of the cooperative DAS aided FFR scheme in Fig. 3.10 and Fig. 3.11. Observe in Fig. 3.10 that the TPP technique of Section 3.3.2.2 is capable of mitigating the "worst-case direction" problem. The achievable throughput of the entire cellular area was investigated in Fig. 3.9 and Fig. 3.11, when employing

Table 3.6: Performance of DAS aided FFR architecture in cell-edge area

	Noncooperative scheme	Cooperative scheme
CSI	not necessary	perfect
θ_{best} Direction	$4 \sim 5 bits/s/Hz$	$5 bits/s/Hz$
θ_{worst} Direction	$1 \sim 2 bits/s/Hz$	$5 bits/s/Hz$
Upper bound	$5 bits/s/Hz$	$5 bits/s/Hz$
Entire cell	"worst-case" directions	no "worst-case" directions
Fibre model	SSF	SSF
Fibre nonlinearity	$P_0 \uparrow \rightarrow$ throughput$\downarrow$	ignored
Fibre dispersion	$T_0 \uparrow \rightarrow$ throughput$\downarrow$	not overly affected

FFR techniques in conjunction with a realistically modelled imperfect optical fibre aided DAS operating in a multiuser scenario. Given a fixed total transmit power, a substantial improvement of the cell-edge area's throughput can be achieved without reducing the cell-centre's throughput. The cell-edge's throughput supported in the worst-case direction is significantly enhanced by the cooperative linear transmit processing technique advocated. Explicitly, a cell-edge throughput of $\eta = 5 bits/s/Hz$ may be maintained for an imperfect optical fibre model, regardless of the specific geographic distribution of the users. We also demonstrated the effects of PC technique in multiuser scenario which is based on the SIR model in Section 3.4.4, when the MSs roaming in the cell-edge area suffering a low SIR as shown in Fig. 3.12, the transmitting power will be compensated. Although the compensated transmitting power of other MSs will increase the interference as shown in Eq. (3.21), a final enhancement of SIR is capable of being achieved as shown in Fig. 3.12. As a result, the throughput of MSs in the cell-edge area is capable of achieving $\eta \geq 3 bits/s/Hz$ as shown in Fig. 3.13. The simulation results of the noncooperative and cooperative DAS aided FFR scheme are compared in Table 3.6.

Chapter 4

Distributed Antennas for the Fractional Frequency Reuse Aided Multicell, Multiuser Uplink

4.1 Introduction

In Chapter 3, the DAS aided FFR architecture was studied in a DL multiuser, multicell scenario which was based on the extension of the DOF aided fixed RA associated with a single interfer, as detailed in Chapter 2. In both Chapter 2 and Chapter 3, the DAS was invoked for improving the DL performance in the cell-edge area. By contrast in this chapter we will employ the DAS in the UL of both the cell-center and cell-edge areas of a multiuser multicell scenario. The DOF link between the BS and RA was assumed to be rendered the optical distortion-free by soltion technique of [111].

Wireless communication systems are expected to support a high performance for anyone, anywhere and anytime. Hence, one of the main challenges to be tackled by the Long Term Evolution (LTE)/Advanced (LTE Release 10) [91] standard is to improve the attainable performance of the mobile stations (MS) roaming in the cell-edge area. The typical low Signal-to-Interference-plus-Noise-Ratio (SINR) experienced at the cell-edge is caused by the combined effects of co-channel interference (CCI), pathloss, shadow-fading and fast-fading. In order to reduce the CCI, the Fractional Frequency Reuse (FFR) [131] philosophy has been adopted in the Third Generation Partnership Project's (3GPP) LTE initiative [95], which improves the geographic distribution of the CCI at the cost of a reduced Area-Spectral Efficiency (ASE). In order to reduce the pathloss, Distributed Antennas (DAS) may be employed [134], where the remote antennas (RA) are positioned

more close to the cell-edge terminals. Hence, the received SINR at the RA is increased by combining the benefits of FFR and DAS. The authors of [24] studied the downlink (DL) performance of such a system architecture in a multicell, multiuser scenario, which significantly improved the throughput in the cell-edge area. In comparison to the conventional Centralized Antennas (CAS) used at the BS [144], the DAS may improve the coverage of the entire cell by positioning the RAs of the DAS in both the cell-center area and cell-edge area, which we refer to as a pervasive DAS/FFR scheme, while the BS simply plays the role of the central signal processing (CSP) unit in our pervasive DAS architecture studied in this chapter.

However, although the MSs roaming close to the RAs do indeed benefit from a high SINR, the DAS combined with FFR suffers from increased intra-cell interference (ICI). When the MSs roaming near the angular direction halfway between two adjacent RAs, the received SINR is substantially degraded, which we refer to here as the 'worst-case direction' problem [24]. In the DL of the DAS combined with FFR, the ICI imposed by the RAs may be mitigated by Transmit PreProcessing (TPP). By contrast, in the UL scenario, the ICI constituted by the multiuser interference (MI), may be mitigated by multiuser detection (MUD) based on the philosophy of "interference cancellation". Alternatively, BS cooperation techniques based on the philosophy of "knowledge sharing and data fusion" may be invoked [58]. These BS cooperation techniques [13] [58] may also be adopted for the DAS architecture [145] in the UL scenario. The results of [58] [145] illustrate that BS cooperation is indeed capable of enhancing the performance of the MSs roaming in the cell-edge area, but only, when the MSs are capable of transmitting at a rather high power. Hence, it may be necessary to further improve the family of cooperation techniques in a more practical MS distribution scenario, where any particular MS position is mapped to a specific SINR.

Essentially, BS cooperation achieves a cooperative diversity gain with the aid of the adjacent BSs. In contrast to the traditional BS cooperation philosophy [13] [58] , which relies on BSs having centralized antennas, the pervasive DAS/FFR architecture proposed in this chapter relies purely on distributed antennas positioned in both the cell-center and cell-edge area, where there is an optical fibre link between the BS and the RA [24] [99]. More explicitly, both architectures facilitate CSP. Explicitly, the BS cooperation technique invokes an independent MUD at each BS and then exchanges the resultant soft decision information among the BSs, while the pervasive DAS/FFR requires a single MUD at the BS. The latter scheme is capable of increasing the attainable spatial diversity gain as well as additionally reducing the pathloss, albeit it may be deemed to be more costly. On the other hand, although the DAS might reduce the CCI when combined with FFR, the

cooperative diversity gain gleaned from the adjacent cells may be eroded. Hence, as a further enhancement we introduce Mobile Relays (MR) [146] into the proposed pervasive DAS/FFR for the UL, in order to improve the achievable cooperative diversity gain at the cost of allocating an additional time-slot for the MRs [147]. Base on the cooperative relaying philosophy [148], a single antenna is allocated to the MS, MR and RA for each MS-MR-RA link, which avoids the cost and complexity of employing multiple antennas at both the transmitter and receiver. However, both the MS-RA and the MR-RA links have to be modelled as a virtual MIMO scheme. Hence, we can exploit the soft information gleaned from the MSs and MRs at the central BS.

Our outline and novel contributions in this chapter may be summarised as follows:

Against this background, in this chapter *we propose a pervasive DAS infrastructure for improving the coverage of both the cell-center and cell-edge area, where the latter additionally relies on FFR. We compare the conventional BS cooperation aided scheme and the proposed pervasive DAS/FFR infrastructure operating both with and without MRs in a multicell, multiuser scenario, when employing four different cooperation techniques. More explicitly, we invoke "interference cancellation" Minimum Mean Square Error (MMSE) based successive interference cancellation combined with optimal user ordering (MMSE-OSIC) [149], "full search" based maximum-likelihood detection (ML) [150], probabilistic data association (PDA) [151] and finally, "knowledge sharing" based combined PDA (CPDA) [58]. Our new CPDA MUD was specifically designed for the MR aided scenario.* We will demonstrate that

1. In the case of conventional BS cooperation a high BER is experienced, when the MSs are roaming in the cell-edge area, unless the transmit power P_t is appropriately increased. On the other hand, the conventional BS cooperation architecture is capable of improving the cell-edge coverage at the cost of a high power P_t and at the expense of increasing the complexity by invoking pervasive "knowledge sharing" amongst the BSs.

2. In the case of the proposed Pervasive DAS/FFR system, the MSs roaming across the entire cell area are capable of achieving a reduced BER at a low transmit power P_t. However, the MMSE-OSIC and the PDA MUD techniques are unable to solve the above-mentioned 'worst-case direction' problem detailed in [24], even when P_t is increased. As a remedy, the CPDA MUD invoked by the MR aided pervasive DAS/FFR architecture is capable of substantially reducing the BER for the MS roaming at arbitrary positions, especially in the 'worst-case direction'.

3. The ICI is a dominant problem of the pervasive DAS/FFR scheme, which may in fact be stronger in the cell-center area than in the cell-edge area, since the interfering MSs tend to be in a dense cluster in the central area, while the interfering MSs are scattered less densely in the outer ring. Hence, the MSs roaming in the cell-center area may in fact have a lower SINR. Hence, an efficient MR selection strategy is required by the Pervasive DAS/FFR scheme, which is capable of significantly reducing the BER right across the entire cell area.

This chapter is organized as follows. In Section 4.2, we introduce the system topology. In Section 4.3, we detail the received signal model of the DAS combined with FFR, of the conventional BS cooperation as well as of our MUD techniques. We present our performance results in Section 4.4 and conclude our discourse in Section 4.4.6.

4.2 System Description

4.2.1 Multicell, Multiuser System Topology

4.2.1.1 Pervasive DAS/FFR Combined with Mobile Relays

The proposed Pervasive DAS/FFR system supporting a multicell, multiuser operating scenario [24] consists of two tiers of 19 hexagonal cells, as seen Fig 4.1a. The frequency partitioning strategy of the total available bandwidth F is characterzed by $F_c \cap F_e = \oslash$, where F_c and F_e represent the cell-centre's frequency band and the cell-edge's frequency band, respectively. Furthermore, F_e is divided into three orthogonal frequency bands $F_i, i \in [1,3]$, which are exclusively used at the cell-edge of one of the three adjacent cells. We will demonstrate that this regime is capable of sufficiently reducing the CCI in our DAS/FFR system [24], hence we can focus our attention on mitigating the ICI in a single cell, as seen in Fig. 4.1b. We assume *symmetry*, where every cell has the same system configuration and without any loss of generality focus our attention on cell B_0, which is assumed to be at the origin of Fig. 4.1b .

In the case of our pervasive DAS/FFR arrangement of Fig. 4.1b, we assume that N_r RAs and N_m MSs are roaming in the cell-center and cell-edge area, respectively. Furthermore, each RA supports a single MS, where a single antenna is employed both by the RA and by the MS. Hence, our DAS/FFR scheme may be modeled as a pair of independent $(N_r \times N_t)$-element virtual MIMOs, where N_t is the number of transmit antennas $(N_t = N_m)$. Although the virtual MIMO matrix of the cell-center and cell-edge has the

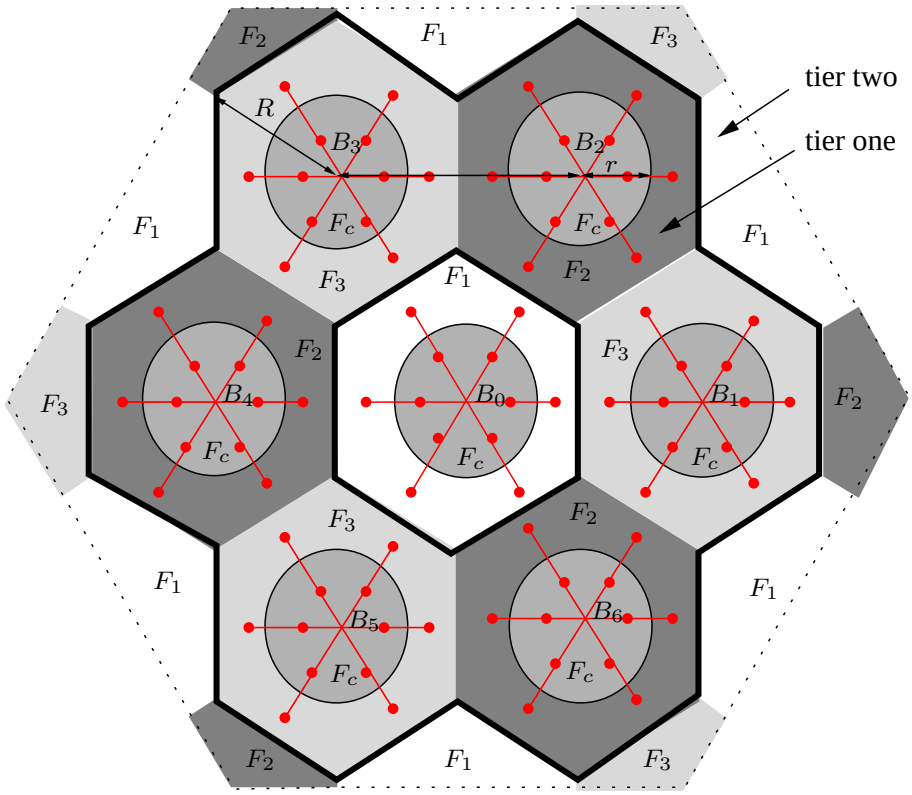

(a) Pervasive DAS/FFR Nteworks

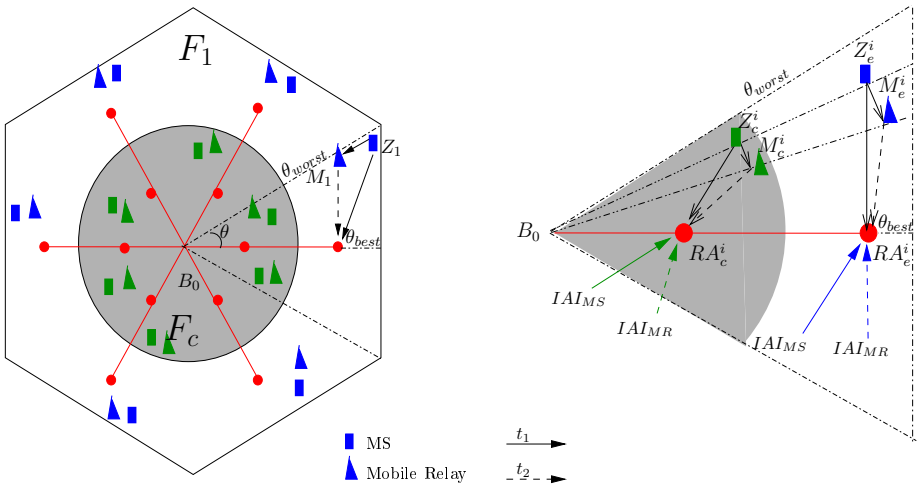

(b) MR aided DAS/FFR Cell

Figure 4.1: The cellular topology of the MR aided pervasive DAS/FFR network, where $N_r = 6$ distributed antennas are employed and $N_m = 6$ MSs randomly roam in the entire cell area. In contrast to the DAS aided FFR DL topology of Fig. 3.1, the cell-center of the pervasive DAS aided FFR architecture was illuminated by our pervasive DAS, while the cell-center of DAS aided FFR architecture of Chapter 3 relied on the CAS. No MR was considered in the DL of the DAS aided FFR architecture of Chapter 3.

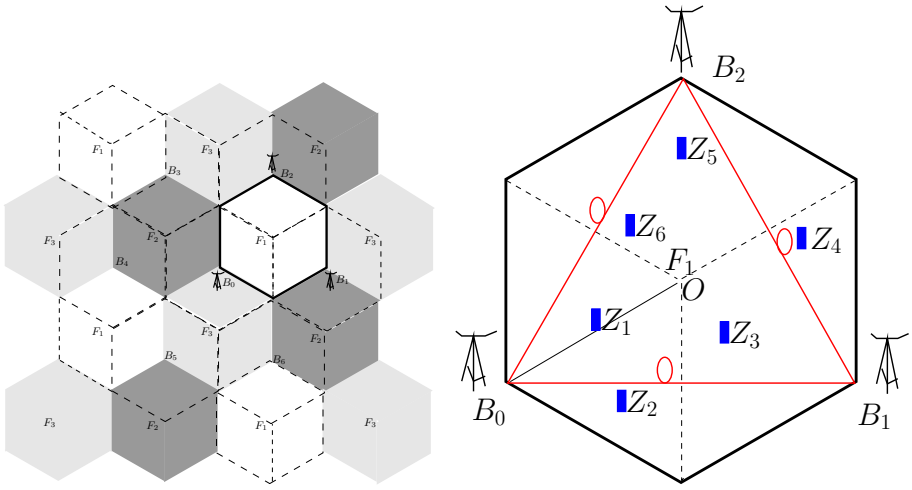

(a) BS Cooperation aided network

(b) BS Cooperation aided cell

Figure 4.2: The cellular toplogy of the conventional BS cooperation network and the details of a BS cooperation aided cell supported by three adjacent BSs, each of which emploied $N_r = 6$ centralized antennas at the BS and $N_m = 6$ MSs were randomly roaming across the entire cell area .

same size, the N_m MSs roaming in the cell-center and the cell-edge area have different pathloss values. More explicitly, the N_m MSs that are roaming at an arbitrary point in the cell-center Z_i^c and cell-edge Z_i^e of Fig 4.1b are identified by their polar coordinates of $[\theta_{Z_i^c}, L_{Z_i^c}]$ and $[\theta_{Z_i^e}, L_{Z_i^e}]$, $i \in [1, N_m]$, respectively. Likewise, the N_r RAs are uniformly located in the cell-center R_i^c and cell-edge R_i^e of Fig 4.1b, which are described by their polar coordinates of $[\theta_{R_i^c}, L_{R_i^c}] = [2\pi(i-1)/N_R, d]$ and $[\theta_{R_i^e}, L_{R_i^e}] = [2\pi(i-1)/N_R, d]$, $i \in [1, N_R]$, respectively.

In order to increase both the attainable diversity and cooperative gain, MRs are invoked for supporting our pervasive DAS/FFR system at the cost of allocating an additional time slot for relaying at the MRs. The N_m MRs roaming in the cell-center and cell-edge area are denoted by M_i^c and M_i^e, $i \in [1, N_m]$, respectively, which are identified by their polar coordinates, similarly to the actively communicating MSs, as seen in Fig. 4.1b.

4.2.1.2 Conventional BS Cooperation Aided Networks

The conventional BS cooperation aided system is shown in Fig. 4.2, where the entire cell area is divided into three 120° sectors $S_i, i \in [1,3]$ [152] and for every sector $N_r = 6$ sectorized antennas are employed at the central BS [153]. Classic Frequency Division Multiplexing (FDM), associated with $F_i, i \in [1,3]$ is used for the corresponding sectors

S_i. Hence the three adjacent BSs compose a Coordinated Multicell Processing (COMP) regime, as shown in Fig. 4.2b, where B_0 is assumed to be at the origin. Likewise, the other two BSs in the COMP regime are described by their polar coordinates of $[\theta_{Bj}, L_{Bj}] = [2\pi(j-1)/6, \sqrt{3}R], j \in [1,2]$. In the COMP area of Fig. 4.2b all the MSs are assumed to transmit at the same frequency in the UL. More explicitly, we assume the same number of $N_m = N_r$ MS transmitters, which employ a single antenna, while roaming in the COMP area.

The BS coordination aided cellular area of Fig. 4.2b is also *symmetric*, hence without any loss of generality we may consider the direction between B_0 and the coordination-aided cellular center O. More explicitly, we assume that the MS roams along the line $\overline{OB_0}$, while the remaining MSs $Z_i^b, i \in [2, N_m]$ randomly roam across the entire cell area. Their polar coordinates are $[\theta_{Z_i^b}, L_{Z_i^b}], i \in [1, N_m]$.

Hence, when observing the N_m active MSs, the virtual MIMO matrix of the cell-center and cell-edge area of our pervasive DAS/FFR scheme of Fig. 4.1b as well as that of the conventional BS cooperation scheme of Fig. 4.2b has the same size of ($N_r \times N_t$)-elements. Our DAS/FFR gleans a further cooperative diversity gain from the MRs, albeit this is achieved at the cost of introducing the classic two-slot cooperative protocol. Explicitly, the N_m active MSs transmit during the first time slot and the corresponding N_m MRs retransmit their received signal in the second time slot, again, with the aid of a ($N_r \times N_t$)-element virtual MIMO. By contrast, the conventional COMP scheme achieves its cooperative gain without any need for introducing a second time slot, where the gain is gleaned from the adjacent two BSs.

Table 4.1: Topology parameters.

Pervasive DAS/FFR	Location	Polar coordinates
RA	cell-center R_i^c	$[\theta_{R_i^c}, L_{R_i^c}] = [2\pi(i-1)/N_R, d]$
	cell-edge R_i^e	$[\theta_{R_i^e}, L_{R_i^e}] = [2\pi(i-1)/N_R, d]$
		$i \in [1, N_R]$
MS	cell-center Z_i^c	$[\theta_{Z_i^c}, L_{Z_i^c}]$
	cell-edge Z_i^e	$[\theta_{Z_i^e}, L_{Z_i^e}]$
		$i \in [1, N_m]$, roaming randomly
MR	cell-center M_i^c	$[\theta_{M_i^c}, L_{M_i^c}]$
	cell-edge M_i^e	$[\theta_{M_i^e}, L_{M_i^e}]$
		$i \in [1, N_m]$, close to MS or RA
BS Cooperation	Location	Polar coordinates
BS	B_0	origin
	Tier-one	$[\theta_{Bj}, L_{Bj}] = [2\pi(j-1)/6, \sqrt{3}R]$
		$j \in [1, 6]$
MS	Z_i	$[\theta_{Z_i}, L_{Z_i}]$
		$i \in [1, N_m]$, roaming randomly

4.2.1.3 Digital Fibre Soliton Aided Backhaul

Until recently the optical fibre backhaul has been assumed to be a perfect channel, when transmitting low-rate data using On and Off Keying (OOK). However, when aiming for supporting Gigabit-transmissions, which is the ambitions goal of LTE-Advanced (LTE Release 10) [91], the high-rate fibre-based backhaul may suffer from the detrimental effects of both linear dispersion and nonlinear distortions [36]. Furthermore, our Pervasive DAS/FFR system relies on central signal processing at the BS, where again, the signal received from the wireless channel via the RA may be contaminated both by dispersion and nonlinearity [154]. Hence, the fibre soliton technique of [111] may be invoked for a reliable optical fibre backhaul, where the optical pulse can propagate undistorted over the optical fibre as a result of the interplay between the dispersive and nonlinear effects [111].

Fig. 4.3 shows a single optical fibre link spanning from the BS to the RAs, where the RA^c of the cell-center area and RA^e of the cell-edge area to make use of the same optical fibre link. In this chapter, QPSK modulation is applied in the UL of the pervasive DAS/FFR system for the UL. The signals received by the RAs from the wireless channel are down-converted to the baseband. Then the I and Q streams are modulated by optical

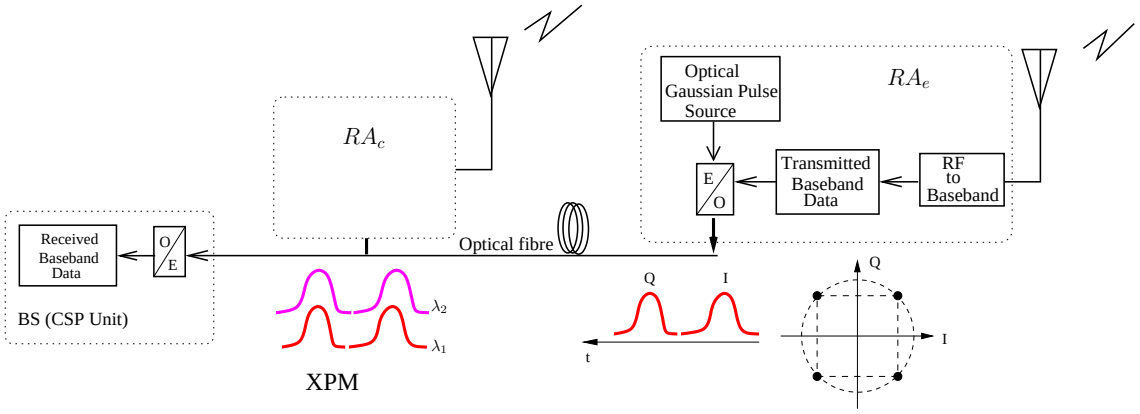

Figure 4.3: System architecture of the digital fibre optical link of the pervasive DAS aided FFR scheme, where the RA in the cell-center area and the RA in the cell-edge area are connected to the BS by the same optical fibre link. In contrast to the system architecture of Fig. 3.2, where only the RAs illuminating in the cell-edge area are connected to the BS, here the signals of both the cell-center and cell-edge area are transmitted through the same fibre. This may lead to nonlinear XPM effects, which were introduced in Section 2.2.2.2.

pulses. Then the optical signaling pulses are transmitted through the optical fibre. The Wavelength Division Multiple Access (WDMA) technique may be applied for the optical fibre backhaul, where the optical signaling pulses transmitted from RA^c and RA^e are separated by using different wavelength.

In contrast to the generalized Nonlinear Schrödinger (NLS) equation of Eq. (3.2), here we use the normalized form of NLS [111] may be written as

$$i\frac{\partial u}{\partial \xi} - sgn(\beta_2)\frac{1}{2}\frac{\partial^2 U}{\partial \tau^2} + |u|^2 u = -\frac{i\alpha L_D}{2}u, \tag{4.1}$$

where $u = N\frac{A}{\sqrt{P_0}}$, $\xi = \frac{z}{L_D}$, $\tau = \frac{T}{T_0}$, and P_0 is the peak power, T_0 is the width of the incident pulse, while $A(z,T)$. α is the fiber loss parameter. Furthermore, the parameter N is defined as:

$$N^2 = \frac{L_D}{L_N} = \frac{\gamma P_0 T_0^2}{|\beta_2|}. \tag{4.2}$$

where we have $L_D = \frac{T_0^2}{|\beta_2|}$ and $L_N = \frac{1}{\gamma P_0}$ is the dispersion length and the nonlinear length, respectively. γ is the nonlinearity parameter. β_2 is GVD parameter, when the choice $sgn(\beta_2) = -1$ has been made to focus on the case of anomalous GVD, which is also called bright soliton.

More explicitly, N is the soliton order parameter, the first order soliton ($N = 1$) is referred to as the fundamental soliton because its shape does not change on propagation. Hence, the fundamental soliton in the case of bright soliton maybe applied for the optical

backhaul in our pervasive DAS/FFR scheme, which the Eq (4.1) maybe rewritten as below:

$$i\frac{\partial u}{\partial \xi} + \frac{1}{2}\frac{\partial^2 U}{\partial \tau^2} + |u|^2 u = -\frac{i\alpha L_D}{2}u,, \tag{4.3}$$

In contrast to the generalized Nonlinear Schrödinger (NLS) equation of Eq. (3.2), here the NLS equation is written in the form of fundamental soliton Eq (4.3). The solution of the equation Eq (4.1) maybe written as

$$u(\xi,\tau) = \eta(\xi)sech[\eta(\xi)\tau]exp[i\phi(\xi)] \tag{4.4}$$

The ξ dependence parameters of η and ϕ represent amplitude and phase of soliton, respectively. In the condition of ideal lossless fibre $N = 1$, the peak power $P_0 = \frac{|\beta_2|}{\gamma T_0^2}$ is required from the Eq (4.2) to support the fundamental soliton, where the pulse will propagate undistorted without change in shape for arbitrarily long distances. However, the soliton amplitude η and phase ϕ are affected by fibre losses. Fibre losses reduce the peak power of solitons along the fiber length which lead to increase the width of a fundamental soliton. As a result, the balance Eq (4.2) between the nonlinear and dispersive effects is broken, if the pulse is unable to maintain its peak power.

In order to keep the pulses' soliton character in a lossy optical fibre, the dispersion-decreasing fibres (DDFs) and soliton amplification maybe applied. Inside a DDF, the GVD decreases exponentially as $|\beta_2(z)| = |\beta_2(0)|exp(-\alpha z)$. Seen from Eq (4.2), both the soliton peak power P_0 and GVD β_2 reduce exponentially with z, hence the fiber losses have no effect on soliton propagation. Hence, the requirement $N = 1$ can still be maintained.

On the other hand, lumped and distributed amplification can be used to periodically compensate the broadening of pulses introduced by the fibre. In a nutshell, the soliton based technique of [111] maybe applied for approaching the condition of perfect distortion less optical backhaul in the future communication networks, where the optical signaling pulses are able to propagate along the optical fibres without distortion. More explicitly, in contrast to the optical fibre model of Eq (3.4) which calculates the effects of the dispersion and nonlinearity, in this chapter the soliton technique of [111] was employed for striking a balance between the linear dispersion and nonlinear distortion.

4.3 Received Signal of the Pervasive DAS/FFR System

As mentioned in Section 4.2, both the pervasive DAS/FFR system of Fig. 4.1 operating either with or without the assistance of MRs, as well as the conventional COMP system of Fig. 4.2 may be modeled as a virtual MIMO having ($N_r \times N_m$) elements. We commence by considering the pervasive DAS/FFR system.

Table 4.2: Characteristics of the optical fibre channel relying on the soliton technique [111].

L_D	dispersion length
L_N	nonlinear length
N	soliton order
β_2	GVD
$sgn(\beta_2) = -1$	bright soliton
$sgn(\beta_2) = +1$	dark soliton
P_0	peak power
T_0	width of the incident pulse
γ	nonlinearity parameter
η	soliton amplitude
ϕ	soliton amplitude

4.3.1 Received Signal of a Single Link

For the ith MS-RA-BS single link, the fundamental soliton technique may be applied for virtually a perfect optical fibre backhaul, as mentioned in Section 4.2.1.3, where the optical signaling pulses are capable of propagating undistorted. Hence the phase rotation imposed by the optical fibre link on the modulated signal constellation diagram is negligible and the modulated signal's amplitude is also maintained, albeit naturally, it is contaminated by the complex-valued Additive White Gaussian Noise (AWGN) of the receiver $n_f \sim \mathcal{CN}(0, \sigma_f^2)$. In contrast to the signal received of Eq. (2.5) in Section 2.3.1 where IPI was taken into account, in this chapter the IPI is ignored. In contrast to the signal received at the RA is that after passing through the optical fibre channel in Eq. (3.1) of Section 3.2.2, while in this chapter the signal received at RA_i after passing through a wireless channel may be written as:

$$s_i = \zeta_i h_i x_i + n_w, \tag{4.5}$$

where x_i, ζ_i, h_i and $n_w \sim \mathcal{CN}(0, \sigma_w^2)$ represent the transmitted signal, the pathloss, the fast Rayleigh fading and the AWGN at the RA, respectively. Then the received signal of the ith link at the BS may be written as $y_i = \chi s_i + n_f$, which is expressed more explicitly as:

$$y_i = \underbrace{\chi\zeta_i}_{g_i} h_i x_i + \underbrace{\chi n_w + n_f}_{n_i}, \tag{4.6}$$

where $g_i = \chi\zeta_i$ and n_i denote the equivalent MS-RA-BS link's distortion and the equivalent receiver noise jointly induced by the optical fibre and the wireless components. Fi-

nally, χ is the power-scaling factor invoked for ensuring that the peak power of the optical signaling pulse obeys the fundamental soliton requirement of [111]. In contrast to the signal received of Eq. (2.5) in Section 2.3.1 where IPI was taken into account.

4.3.2 Received Signal of a Virtual MIMO

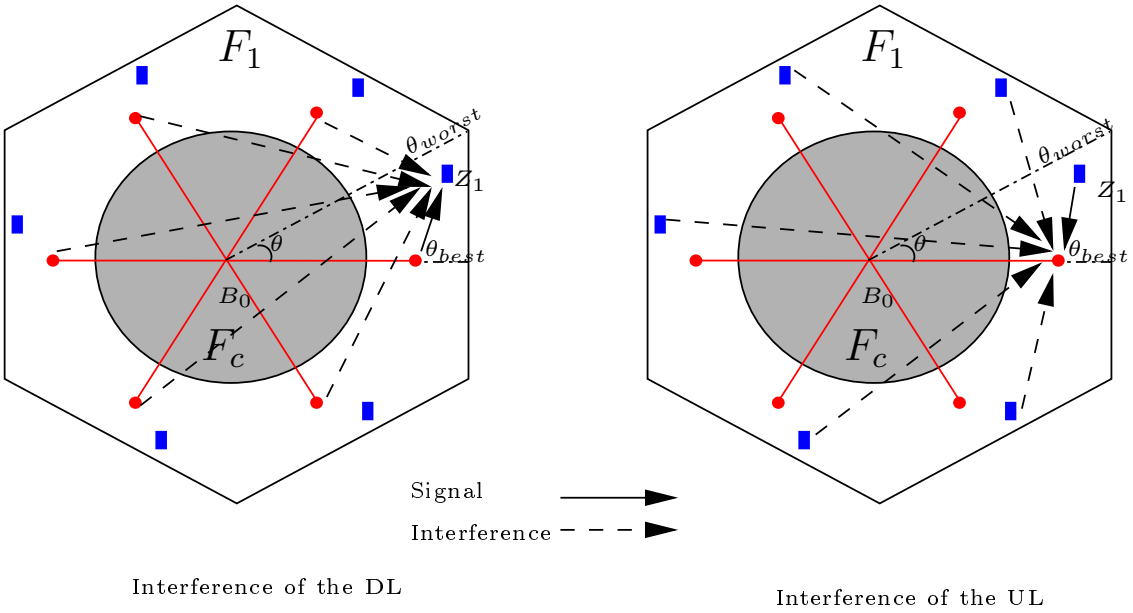

Figure 4.4: In contrast to the DL interference model of the DAS aided FFR architecture of Chapter 3, here we considered an UL scenario.

The received signal of the DAS aided FFR architecture may be modelled as a virtual MIMO, where the interference of the DL is generated by the RAs and that of the UL are generated by the MSs, as shown in Fig. 4.4. Hence, the received signal model of the UL is similar to that of the DL introduced in Eq. (3.10) of Section 3.3, where the only difference is associated with calculating the interference without being considered the linear TPP matrix. The entire MS-RA-BS link is assumed to be perfectly estimated at the central BS. Based on Eq (4.6), the vector of received signals of the idealized synchronous UL may be written as:

$$\mathbf{y} = \mathbf{H}\mathbf{x} + \mathbf{n}, \tag{4.7}$$

where $\mathbf{y}_{N_r \times 1}$, $\mathbf{H}_{N_r \times N_m}$ and $\mathbf{n}_{N_r \times 1}$ denote the transmit symbol vector, the estimated channel matrix associated with perfect channel state information (CSI) and the circularly symmetric complex Gaussian noise vector. Furthermore, $\mathbf{x} = [x_1, x_2, \cdots, x_{N_m}]^T_{1 \times N_m}$, x_i represents the symbols transmitted from MS i to RA i, while $\mathbf{n} = [n_1, n_2, \cdots, n_{N_r}]^T$, n_i is the equivalent noise at the BS, which was defined in Section 4.3.1. Still referring to Eq (4.7),

we have $\mathbf{H} = [\mathbf{h}_1^T, \mathbf{h}_2^T, \cdots, \mathbf{h}_{N_r}^T]_{N_r \times N_m}^T$, where $\mathbf{h}_i = [g_1 h_1, g_2 h_2, \cdots, g_{N_r} h_{N_r}]_{1 \times N_m}, i \in [1, N_r]$, represents the channel of all the N_m MS-RA_i links, which takes into account both the pathloss of the wireless channel and the fast Rayleigh fading channel, where g_i and h_i were also defined in Section 4.3.1. The fibre-induced attenuation may be negligible, since the soliton technique of [111] is applied, which allows the optical signaling pulses to propagate through the optical fibre undistorted. Hence, a unified discrete-time model may be formulated for the signal received by RA_i based on Eq (4.7) as:

$$y_i = \|\mathbf{h}_i\| x_i + \sum_{k \neq i} \|\mathbf{h}_i\| x_k + n_i. \tag{4.8}$$

When we have $k \neq i$, as indicated in the second term of Eq (4.8), this sum of terms represents the ICI imposed by the transmit signal intended for RA_k, but received at RA_i. Without being considered the linear TPP matrix for DL in Eq. (3.12) of Section 3.3, Eq. (4.8) and Eq. (3.12) will be the same.

The received signal model introduced above in Eq (4.6)-(4.8) can be applied for both the cell-center and cell-edge area of the pervasive DAS/FFR scheme of Fig. 4.1, we only have to update the pathloss parameter ζ [155]. Similarly, we also have $g_i = \zeta_i$ and $n_i = n_w$ for the conventional COMP system of Fig. 4.2.

4.3.3 Correlation Between the Channel Coefficients of MS_i and MR_i

When considering the MR aided pervasive DAS/FFR scheme during the cooperative time slot, the channel model is the $(N_r \times N_m)$-element virtual MIMO model of Eq(4.6)-(4.8). The channel matrix $\mathbf{H}$ of Eq (4.7) is denoted by $\mathbf{H}_M$ and $\mathbf{H}_R$ for the MSs and MRs, respectively, where $\mathbf{H}_M = [\bar{\mathbf{h}}_1, \bar{\mathbf{h}}_2, \cdots, \bar{\mathbf{h}}_{N_m}]_{N_r \times N_m}$ and $\mathbf{H}_R = [\hat{\mathbf{h}}_1, \hat{\mathbf{h}}_2, \cdots, \hat{\mathbf{h}}_{N_m}]_{N_r \times N_m}$. More explicitly, for the MSs transmitting their source signal during the first time slot, $\bar{\mathbf{h}}_i, i \in [1, N_m]$ is a $(N_r \times 1)$-element column vector of the channel matrix $\mathbf{H}_M$, which represents the channel between the ith MS and all the N_r RAs links, taking into account both the pathloss of the wireless channel and the fast Rayleigh fading. Similarly, for the MRs retransmitting their received signal during the second time slot, $\hat{\mathbf{h}}_i, i \in [1, N_m]$ is the $(N_r \times 1)$-element column vector of the channel matrix $\mathbf{H}_R$, representing the channel between the ith MR and all the N_r RAs links. The correlation of the mobile relays' channel coefficients during the broadcast and cooperation phase is given by

$$\rho_{ij} = \langle |\bar{\mathbf{h}}_{i(j)}|^2, |\hat{\mathbf{h}}_{i(j)}|^2 \rangle \tag{4.9}$$

for the ith MS-MR pair transmitting to the jth RA, where we have $i \in [1, N_m], j \in [1, N_r]$. For $\rho_{ij} = 0$ the channels of MS_i during the first time slot and its corresponding MR_i in the second time slot are uncorrelated.

4.3.4 Central Signal Processing

The philosophy of the DAS architecture relies on invoking the RA for receiving and forwarding the signals, which allows the central signal processor to appropriately process the virtual MIMO signals at the BS, since at the BS it may be affordable to apply more complex MUD techniques. For a channel coded system, the soft MUD calculates the log-likelihood ratio (LLR) of each coded bit from the received symbol vectors. Then the LLR of each bit is subjected to soft decoding, since soft decoding is capable of achieving a better performance than hard decoding. In this section, we design a powerful soft MUD imposing a moderate complexity.

4.3.4.1 Joint ML Multiuser Detector

For a Forward Error Correction (FEC) coded system, the soft ML-MUD is the optimum detector for the virtual MIMO signal, albeit it imposes a potentially excessive complexity. When all the received signals are equi-probable, the soft ML-MUD calculates the LLR for the nth bit $b_{s,n}$ of the sth RA as:

$$L(b_{s,n}) = \log(P\{\mathbf{y}|b_{s,n}=1\}/P\{\mathbf{y}|b_{s,n}=0\}). \tag{4.10}$$

The max-log approximation may be applied for reducing the complexity at a negligible performance degradation. Hence, the LLR in Eq (4.10) may be represented as:

$$\begin{aligned} L(b_{s,n}) = & \\ & \log\left(\sum_{x_1\in\mathbf{X},\cdots,x_s\in\mathbf{X}_n^{(1)},\cdots,x_{N_t}\in\mathbf{X}} exp(-\|\mathbf{y}-\mathbf{hx}\|^2/\sigma^2)\right) \\ & -\log\left(\sum_{x_1\in\mathbf{X},\cdots,x_s\in\mathbf{X}_n^{(0)},\cdots,x_{N_t}\in\mathbf{X}} exp(-\|\mathbf{y}-\mathbf{hx}\|^2/\sigma^2)\right) \\ & \approx\frac{1}{\sigma^2}\left(\min_{x_1\in\mathbf{X},\cdots,x_s\in\mathbf{X}_n^{(0)},\cdots,x_{N_t}\in\mathbf{X}}\|\mathbf{y}-\mathbf{hx}\|^2-\min_{x_1\in\mathbf{X},\cdots,x_s\in\mathbf{X}_n^{(1)},\cdots,x_{N_t}\in\mathbf{X}}\|\mathbf{y}-\mathbf{hx}\|^2\right), \end{aligned} \tag{4.11}$$

where $\mathbf{X}_n^{(b)}$ is the set of transmit symbols that has a bit value of $b, b = 0$ or 1 for the nth bit and sth RA. More explicitly, Eq (4.11) calculates all the Euclidean Distances (ED) for all possible $\mathbf{x}$ values and finds the minimum ED in every bit group. In our pervasive DAS/FFR, we have $N_m = N_r$, hence naturally, the size of the solution-space increases exponentially with the number N_r of RAs.

The BER performance of the joint ML Multiuser Detector using a convolutional channel code is demonstrated in Fig. 4.5, where (2×2) ,(4×4) and (6×6)-element virtual MIMOs are considered.

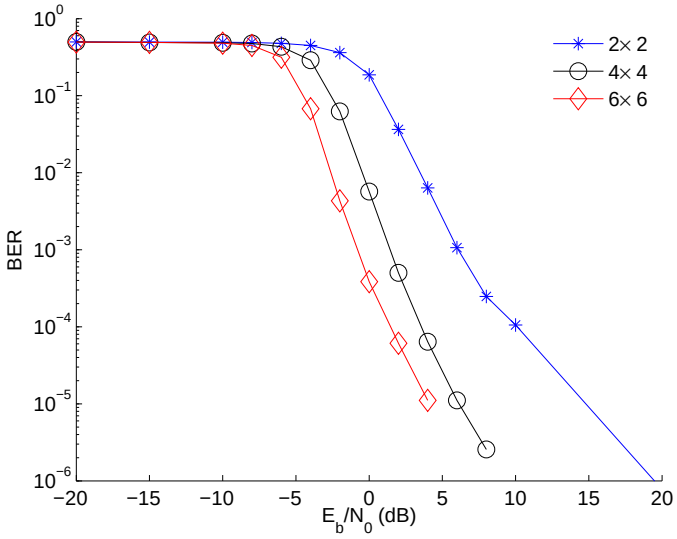

Figure 4.5: BER performance of the Joint ML MUD for $(N \times N), N = 2, 4, 6$ MIMOs, where N is the number of transmit and receive antennas.

4.3.4.2 PDA Aided Multiuser Detector

As noted in Section 4.3.4.1, the joint ML MUD has a complexity, which increases exponentially with the number of RAs and hence may not be invoked in practical applications. As an attractive design alternative, the reduced-complexity PDA algorithm may be applied for our pervasive DAS/FFR scheme, which generates the LLRs for the concatenated channel decoder. In the UL scenario, the UL channel information $\mathbf{H}$ is assumed to be unknown at the MS transmitters, but it is assumed to be estimated accurately at the BS's UL receiver. In our pervasive DAS/FFR scheme, we assumed $N_t = N_r$ for the sake of computational efficiency and the decorrelated signal model of Section 4.3.2 was adopted. Hence Eq (4.8) may be rearranged as

$$\tilde{\mathbf{y}} = \mathbf{x} + \tilde{\mathbf{n}} = x_i \mathbf{e}_i + \underbrace{\sum_{k \neq i} x_k \mathbf{e}_k + \tilde{\mathbf{n}}}_{\mathbf{V}_k}, \tag{4.12}$$

in contrast to the Eq. (4.8, here $\tilde{\mathbf{y}} = (\mathbf{H}^H \mathbf{H})^{-1} \mathbf{H}^H \mathbf{y}$, $\tilde{\mathbf{n}}$ is a colored Gaussian noise with zero mean and covariance of $N_0 (\mathbf{H}^H \mathbf{H})^{-1}$, $\mathbf{e}_i$ is a column vector with 1 in the ith position and 0 elsewhere, while $\mathbf{V}_k$ denotes the interference plus noise term for symbol $x_i, i \in [1, N_r]$. For each symbol x_i, we have a probability vector $\mathbf{P}_i$, whose mth element

$P_m(x_k|\mathbf{y})$ quantifies the current estimate of the a *posteriori probability* (APP) of having $x_i = a_m, m \in [1, M]$, with a_m being the mth element of the modulation constellation.

The key philosophy of the PDA algorithm is to approximate $\mathbf{V}_k$ with the aid of the multimodal Gaussian mixture distribution as a single multivariate colored Gaussian distributed random vector having an updated mean of $E(\mathbf{V}_k)$, covariance of $V(\mathbf{V}_k)$ and pseudocovariance of $U(\mathbf{V}_k)$, which are given by:

$$\begin{aligned} E(\mathbf{V}_k) &= \sum_{k\neq i} \bar{x}_k \mathbf{e}_k, \\ V(\mathbf{V}_k) &= \sum_{k\neq i} V\{x_k\}\mathbf{e}_k\mathbf{e}_k^T + N_0(\mathbf{H}^H\mathbf{H})^{-1}, \\ U(\mathbf{V}_k) &= \sum_{k\neq i} U\{x_k\}\mathbf{e}_k\mathbf{e}_k^T, \end{aligned} \tag{4.13}$$

where we have

$$\begin{aligned} \bar{x}_k &= \sum_{m=1}^{M} a_m P_m(x_k|\mathbf{y}), \\ V(x_k) &= \sum_{m=1}^{M} (a_m - \bar{x}_k)(a_m - \bar{x}_k)^* P_m(x_k|\mathbf{y}), \\ U(x_k) &= \sum_{m=1}^{M} (a_m - \bar{x}_k)(a_m - \bar{x}_k)^T P_m(x_k|\mathbf{y}). \end{aligned} \tag{4.14}$$

The current estimate of the APP $P_m(x_k|\mathbf{y})$ is initialized based on the uniform distribution $1/M$, which will then be updated at each iteration of the PDA algorithm. Let

$$\mathbf{w}_m^{(i)} = \tilde{\mathbf{y}} - a_m^{(i}\mathbf{e}_i - \sum_{k\neq i} \bar{x}_k \mathbf{e}_k, \tag{4.15}$$

and

$$\varphi(x_i) \triangleq exp\left(- \begin{pmatrix} \Re(\mathbf{w}_m^{(i)}) \\ \Im(\mathbf{w}_m^{(i)}) \end{pmatrix}^T \Lambda_i^{-1} \begin{pmatrix} \Re(\mathbf{w}_m^{(i)}) \\ \Im(\mathbf{w}_m^{(i)}) \end{pmatrix} \right), \tag{4.16}$$

where we have

$$\Lambda_i^{-1} \triangleq \begin{pmatrix} \Re[V(\mathbf{V}_i) + U(\mathbf{V}_i)] & -\Im[V(\mathbf{V}_i) - U(\mathbf{V}_i)] \\ \Im[V(\mathbf{V}_i) + U(\mathbf{V}_i)] & \Re[V(\mathbf{V}_i) - U(\mathbf{V}_i)] \end{pmatrix} \tag{4.17}$$

and a_m^i indicates that a_m is assigned to x_i, while $\Re(\cdot)$ and $\Im(\cdot)$ represent the real and imaginary parts of a complex variable, respectively.

Since it is assumed that the transmitted symbols have equal a *priori* probabilities, the APP of x_i is given as $p_m(\mathbf{y}|x_i) \cdot P(x_i = a_m)$, where we have

$$P_m(x_i|\mathbf{y}) = \frac{p_m(\mathbf{y}|x_i)P(x_i = a_m)}{\sum_{m=1}^{M} p_m(\mathbf{y}|x_i)P(x_i = a_m)} \approx \frac{\varphi_m(x_i)}{\sum_{m=1}^{M} \varphi_m(x_i)}. \tag{4.18}$$

For further details on the PDA-aided MUD please see [58] [156] [157]. The BER performance of the PDA aided multiuser detector using a convolutional channel code is demonstrated in Fig. 4.6, where the (2×2) ,(4×4) and (6×6)-element virtual MIMOs are considered.

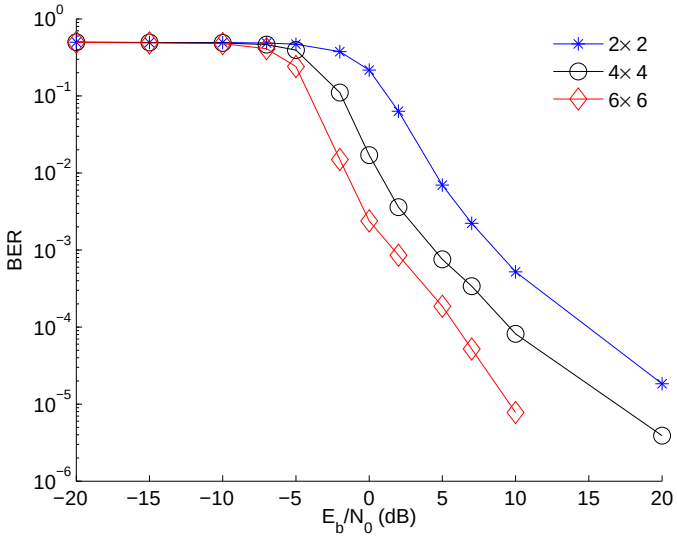

Figure 4.6: BER performance of the PDA aided MUD for $(N \times N), N = 2, 4, 6$ MIMOs, where N is the number of transmit and receive antennas.

4.3.5 Combining the Soft-information of the MRs Using PDA

Let us now invoke the PDA for our MR-aided pervasive DAS/FFR scheme for the sake of combining the soft decision information gleaned from the MRs in a manner similar to that proposed for the BS cooperation aided system of [58]. In order to achieve a diversity gain, each MS may be aided by an appropriately selected MR, albeit this is only possible at the cost of creating an additional cooperative time slot in the pervasive DAS/FFR scheme. More explicitly, each MS $M_i, i \in [1, N_m]$ broadcasts its signal to a MR R_i, during the 1st time slot, which are received by the N_r RAs. The MRs then retransmit the received copies to the RAs using low-complexity amplify-forward relaying.

Based on the aggregated decision information gleaned from $R_i, i \in [1, N_m]$, when the PDA algorithm is adopted for the BS's MUD, the soft information $P_m(x_i|\mathbf{y}_{MS})$ of the MSs and that of the MRs $P_m(x_i|\mathbf{y}_{MR})$ are combined as follows [58]

$$P_m(x_i|\mathbf{y}_C) = \frac{P_m(x_i|\mathbf{y}_{MS})P_m(x_i|\mathbf{y}_{MR})}{\sum_m P_m(x_i|\mathbf{y}_{MS})P_m(x_i|\mathbf{y}_{MR})}. \tag{4.19}$$

Finally, the BS's MUD makes a decision for each transmitted symbol x_i, yielding $\hat{x}_i = a_{m'}$, where we have:

$$m' = \arg \max_{m=1,2,\cdots M} \{P_m(x_i|\mathbf{y}_C)\}. \tag{4.20}$$

4.3.6 MMSE-OSIC Detector

A practical reduced-complexity suboptimum MUD solution is constituted by the MMSE-OSIC detector, which is capable of maximizing the signal strength received from the MS of interest, while suppressing the ICI imposed by the other MSs [81]. Once the highest-power signal was decoded and remodulated, the corresponding regenerated transmit signal is subtracted from the composite multi-antenna signal, before the next interference cancellation stage is activated. Naturally, the MMSE-OSIC detector is prone to inter-layer error propagation in the presence of decision errors [81].

4.4 Performance Evaluation

4.4.1 Simulation Assumptions

We considered the Urban-Macro propagation scenario of [139], where we have a distance of $D = 3km$, e.g. $\overline{B_0B_2} = \sqrt{3}R$ between the two adjacent BSs, and each hexagonal cell has a radius of R. The pathloss is expressed in dB as $128.1 + 37.6\log_{10}(d_0)$ for the UL, while d_0 is the distance between any transmitter and receiver pair in kilometers. We assume furthermore that the transmit power P_t is in the range of $P_t = 0 \sim 33dBm$ and the noise power at the RA is -174dBm/Hz, when an operational bandwidth of 10 MHz [1]. Moreover, the optical fibre link's normalised Signal-to-Noise-Ratio (SNR) is assumed to be 50dB and the length of the optical fibre is assumed to be five times the distance between the BS and RA, i.e. we have $L = 5d$. We defined the cell-edge region as the area outside the radius of $r = 0.5R$, hence the cell-center area is within the radius of $r = 0.5R$, as seen in the system topology illustrated in Fig. 4.1. The RAs in the cell-center $R_i^c, i \in [1, N_r]$ area and cell-edge area $R_i^e, i \in [1, N_r]$ are assumed to be located at $d_c = 0.2R$ and $d_e = 0.7R$, respectively. The parameters considered for pervasive DAS aided FFR scheme are summarized in Table 4.3.

Table 4.3: Simulation parameters of the pervasive DAS/FFR scheme in the UL which is based on the 3GPP-LTE standard [1].

Urban macro BS to BS distance	$\overline{B_2B_3} = 3$ km
Pathloss expressed in dB	$128.1 + 37.6 \log_{10}(d_0)$
Transmit power	$0, 10, 20, 30dBm$
Noise power at the RA	-174dBm/Hz
Shadowing standard derivation	$\sigma_s = 8$ dB
Normalised optical fibre link SNR	50 dB
Line-of-sight distance of BS-RA in cell-center area	$d_c = 0.2R$
Line-of-sight distance of BS-RA in cell-edge area	$d_e = 0.7R$
Length of the optical fibre	$L = 5d$
Number of RAs in cell-center area	6
Number of MSs in cell-center area	6
Number of MRs in cell-center area	6
Number of RAs in cell-edge area	6
Number of MSs in cell-edge area	6
Number of MRs in cell-center area	6
Virtual MIMO	2 independent (6×6)-element matrices
	2 correlated (6×6)-element matrices
Modulation	QPSK
Bit-to-Symbol mapping	Gray
Coding	punctured convolutional code, $R = \frac{2}{3}$
Trellis	constraint lengt, 7
	CodeGenerator 171, 133
Decoder	Viterbi algorithm
MUD	Joint ML, PDA, CPDA and MMSE-OSIC
Channel	Fast Rayleigh fading channel

Table 4.4: Simulation parameters of the BS-cooperation aided UL scenario, which is based on the 3GPP-LTE standard [1].

Topology	BS cooperation aided cell Fig. 4.2
Number of BSs	1 BS in every $\frac{2\pi}{3}$ sector area
Number of antennas	6 CAS in every $\frac{2\pi}{3}$ sector area
Number of MSs	2 MSs in every $\frac{2\pi}{3}$ sector area
Virtual MIMO	3 independent 6×6-element matrix
Transmit power	$0, 10, 20, 30dBm$
Modulation	QPSK
Bit-to-Symbol mapping	Gray
Coding	punctured convolutional code, $R = \frac{2}{3}$
Trellis	constraint lengt, 7
	CodeGenerator 171, 133
Decoder	Viterbi algorithm
MUD	Joint ML, PDA, CPDA, MMSE-OSIC
Urban macro BS to BS distance	$\overline{B_2B_0} = 3$ km
The pathloss expressed in dB	$128.1 + 37.6 \log_{10}(d_0)$
Total transmitter power	$P = 0 \sim 33$dBm
Noise power at the RA	-174dBm/Hz
Shadowing standard deviation	$\sigma_s = 8$ dB

We applied the classic QPSK modulation scheme, combined with a code rate $2/3$, constraint length-7 punctured convolutional code for both of the wireless and optical fibre channel. Finally, the BER curves were obtained by averaging the SINR over 10^3 simulation runs. Again, we compare four types of MUDs, i.e. the Joint ML, PDA, CPDA and MMSE-OSIC, where the MMSE-OSIC MUD is unable to generate soft information for the concatenated soft channel decoder. Hence the BER performance of the MMSE-OSIC remains poor, as shown in Fig. 4.7 -4.10, because as expected, the hard-decision MUD fails to outperform the soft-decision MUD. Naturally, the superiority of the soft-decision MUD (Joint ML, PDA, CPDA) is achieved at the cost of an increased complexity.

4.4.2 Conventional BS Cooperation

When observing the conventional BS cooperation characterized in Fig. 4.7, we considered $N_m = 6$ MSs roaming randomly across the entire area composed of the 3 adjacent BSs seen in Fig. 4.2b. Again, $N_r = 6$ centralized antennas were applied to the three sectors of the BS, hence our COMP scheme relies on using an $(N_r \times N_m)$-element virtual MIMO.

When P_t is increased according to $0, 10, 20, 30dBm$, the BER only becomes adequate, when the MSs are close to the BS. By contrast, when the MSs are roaming in the cell-edge area, even an increased transmit power P_t fails to lead to an improved SINR and BER for the MS of interest, since the pathloss is rather high.

More explicitly, the CPDA MUD is adopted for the COMP scheme, which requires the cooperation of three adjacent BSs. Observe from Fig. 4.7 that the CPDA MUD only achieves a useful cooperation diversity, when the transmit power is as high as $P_t = 30dBm$. By contrast, when the MSs transmit at a low power of $P_t = [0dBm \sim 20dBm]$, the CPDA MUD has a similarly poor BER performance to that of the PDA MUD, which operates without exchanging soft information among the adjacent BSs. As a result, when the MSs roam close to their own anchor-BS but quite far from the adjacent BSs, the cooperative gain remains rather limited, since the pathloss of the MS with regard to the adjacent BS is high, which leads to inefficient cooperative BS processing. On the other hand, when the MSs roam close to the cell-edge, a sufficiently high SINR may only be guaranteed for a high transmit power, since the pathloss of the MSs with regard to any of the BSs remains high. The parameters considerd for BS cooperation in UL are summarized in Table 4.4

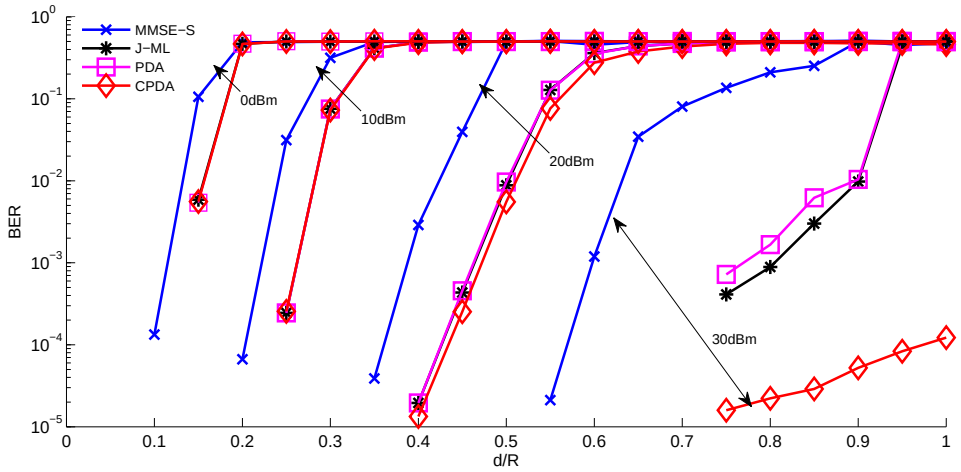

Figure 4.7: BER performance of the BS cooperation scheme of Fig. 4.2 employing the MMSE-OSIC, Joint-ML, PDA and CPDA MUD techniques. All system parameters were summarized in Table 4.4

4.4.3 Pervasive DAS/FFR

Again, we consider $N_m = 6$ MSs and $N_r = N_m$ RAs both in the cell-center and in the cell-edge area, where each RA may support a single MS, where the received UL signal is contaminated by the other MSs transmitting within the same time slot of our pervasive

DAS/FFR system of Fig. 4.1. In contrast to the conventional BS COMP scheme, the DAS/FFR scheme attains a diversity gain with aid of the RAs, which is attained at the cost of creating an additional cooperative time slot. Our simulation results will characterized the typical directions of θ_{best}, θ_{worst},and θ_{mid} using the system parameters in Table 4.3.

4.4.3.1 Cell-Edge Area

In Fig. 4.8 we focus our attention on the BER performance of the θ_{best} direction as shown in Fig. 4.1b. When the MSs roam close to the RAs, a high SINR is guaranteed, even when the transmit power is as low as $0dBm$, as seen in Fig. 4.8c. When the MSs roam far away from the RAs, even using an increased transmit power of $P_t = [0dBm, 30dBm]$ may not significantly improve the SINR, since the ICI caused by the other MSs is also increased, as shown in Fig. 4.8.

More explicitly, let us consider Fig. 4.8b as our example. A MR is appointed close to the MS for the sake of attaining a diversity gain, where the CPDA MUD is capable of efficiently combining the soft information gleaned from the MSs and MRs. Hence, the CPDA is capable of attaining a low BER of 10^{-5} in most locations of the cell-edge defined as $d/R \in [0.5, 0.9]$. Observe by comparing the θ_{worst} direction characterized in Fig. 4.9a to θ_{mid} in Fig. 4.9b that the BER performance of the CPDA MUD is degraded, since MS i may be roaming in the areas, where the received signal provided by RA i may in fact be weaker than the interference imposed by MSs $k \neq i$. The BER performance across the entire cell is between the best-case angle θ_{best} characterized in Fig. 4.8b and the worst-case scenario of θ_{worst} documented in Fig. 4.9a. Finally, the θ_{mid} direction is characterized in Fig. 4.9b, which exhibits a performance between those of the directions θ_{best} and θ_{worst}.

The dotted curves seen in Fig. 4.8 and Fig. 4.9 quantify the effects of the correlation of the relaying channels, defined in Eq (4.9), when the correlation coefficient ρ increases from 0 to 1. More explicitly, when the MS-MR channel and the corresponding MR-RA channel are uncorrelated, i.e. we have $\rho = 0$, the CPDA MUD benefits from having two independent channel matrices, namely H_M and H_R. By contrast, when the correlation of the MS-MR channel and the corresponding MR-RA channel is approaching $\rho = 1$, the diversity is completely eroded, hence the CPDA MUD has a similar BER performance to that of the PDA.

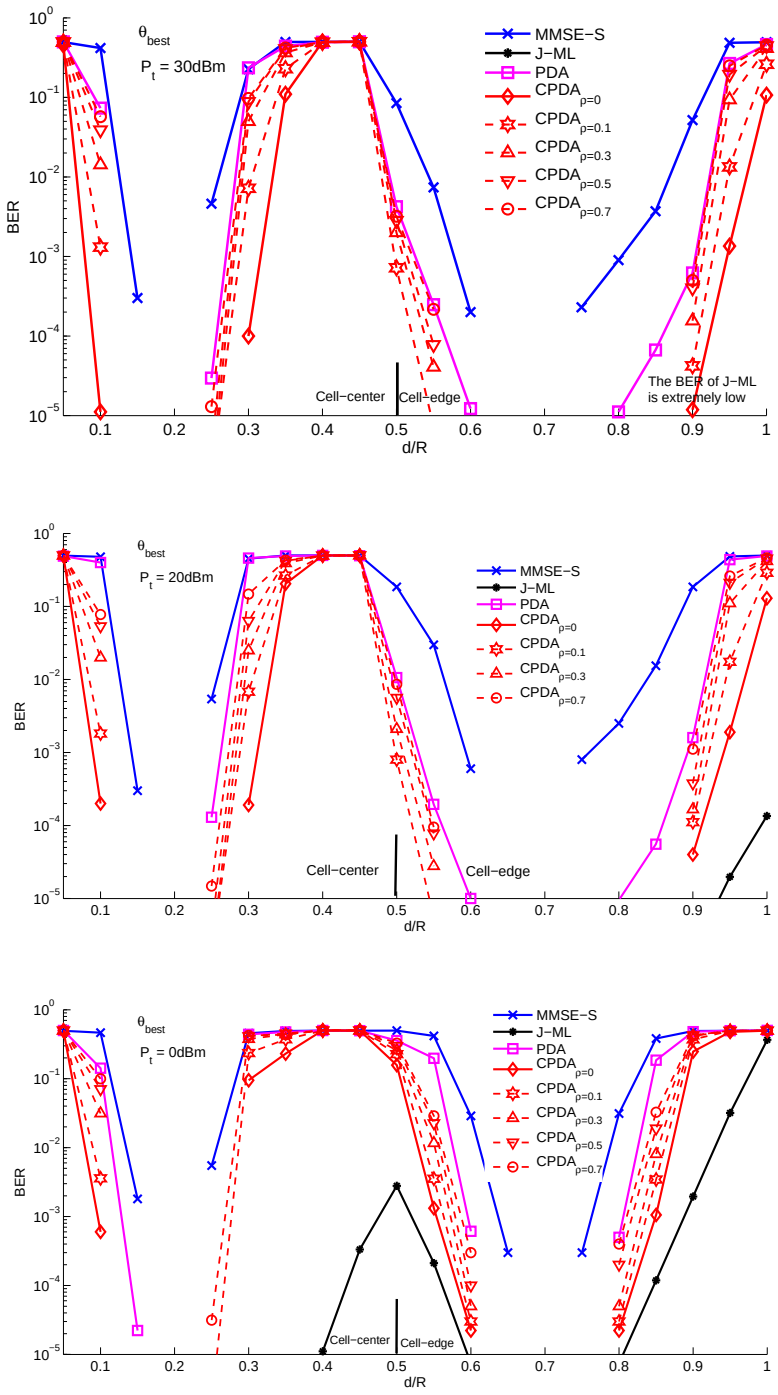

Figure 4.8: BER performance of pervasive DAS/FFR scheme of Fig. 4.1b when appling the MMSE-OSIC, Joint-ML, PDA, CPDA MUD techniques in the θ_{best} direction. The MSs are aided by the MRs, which are close to the MSs, when the CPDA MUD is applied. All system parameters were summarized in Table 4.3.

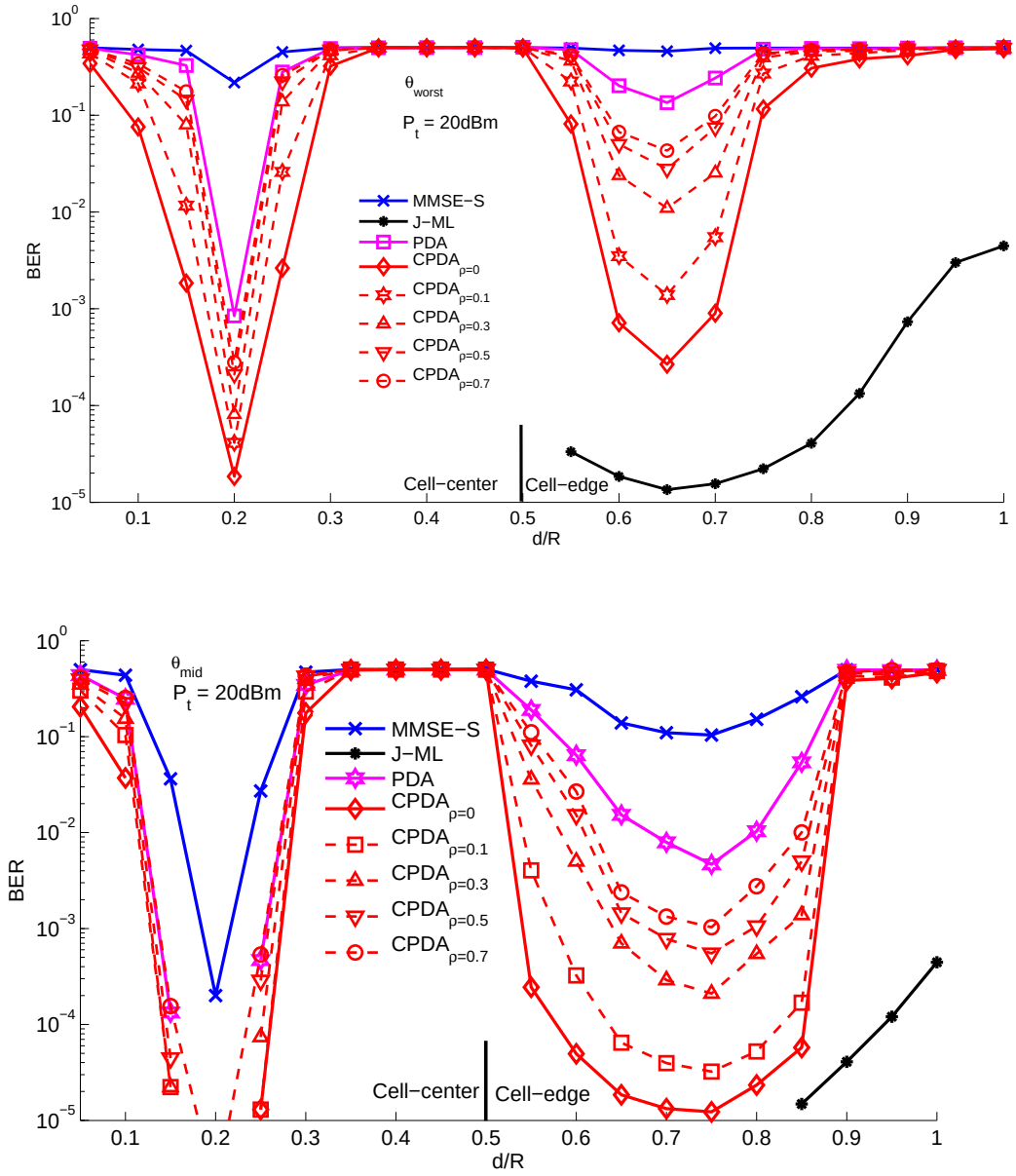

Figure 4.9: BER performance of pervasive DAS/FFR scheme of Fig. 4.1b, when appling the MMSE-OSIC, Joint-ML, PDA, CPDA MUD techniques in the θ_{mid} and θ_{worst} directions. The MSs are aided by the MRs, which are close to the MSs, when the CPDA MUD is applied. All system parameters were summarized in Table 4.3.

4.4.3.2 Cell-Center Area

Let us now observe the BER performance of the cell-center area along the above-mentioned typical directions, as shown in Fig. 4.8 and Fig. 4.9. Similarly to the cell-edge area, a high SINR and low BER may only be guaranteed when the MSs are roaming close to the RAs, When the MSs roam along the θ_{worst} direction, the BER performance is seen to be reduced in Fig. 4.9a, for the same reason as argued in Section 4.4.3.1.

Let us now compare the BER performance of the cell-center and the cell-edge area for $P_t = 20dBm$ in Fig. 4.8b, as an example. When the MS roams far away from the RAs, the BER is seriously degraded, even when the more complex CPDA MUD is applied. Quantitatively, the BER exceeds 10^{-1} in the area of $d/R \in [0.3, 0.45]$, because the entire area may be viewed as being divided into the inner circle and outer ring area of Fig. 4.11. Hence, the MSs are more densely clustered in the cell-center area, while they are more scattered in the cell-edge area. Therefore the ICI is significantly stronger in the cell-center than in the cell-edge area, which led to a reduced SINR.

4.4.3.3 MR Selection

In Fig. 4.8 and Fig. 4.9, we consider MRs roaming relatively close to the MSs, but sufficiently far for having $\rho = 0$ and hence to increase the diversity. The CPDA MUD combines the soft information gleaned from the transmit signal of both the MSs and that of the MRs. Although the BER of the CPDA MUD is lower than of that the PDA and of the MMSE-OSIC MUD, there is still a "problem area", as demonstrated in Fig. 4.10, where the BER cannot be significantly reduced, even when applying the CPDA MUD. By contrast, when the MSs are roaming within the "reliable area" in the vicinity of θ_{best}, the BER is substantially reduced by the CPDA MUD. More explicitly, the "reliable area" is close to the RAs and the "problem area" is far away from the RAs. Observe in Fig. 4.8 and Fig. 4.9 that the MRs are appointed close to MSs, when the MSs are within the "problem area" where the pathloss is high , hence the corresponding MRs also suffer from a high level of interference. Hence, the CPDA MUD is unable to reduce the BER.

One of the potential solutions to this predicament is to appoint a MR close to the RA in the "reliable area". Assuming that the received signal of the MR is error-free, the high BER experienced in the "problem area" may be reduced by applying the CPDA MUD, as evidenced by the curve marked by the hollow stars in Fig. 4.10.

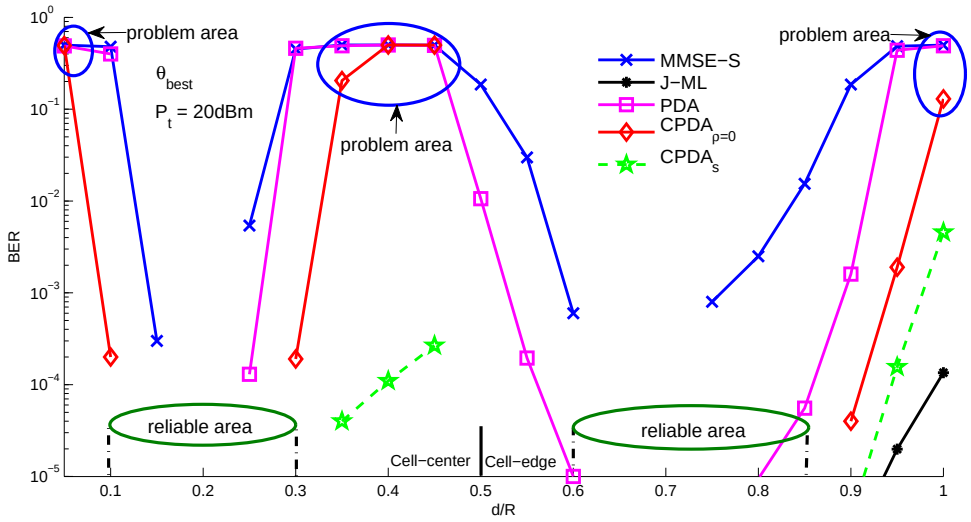

Figure 4.10: BER performance of the pervasive DAS/FFR scheme of Fig. 4.1b, when applying the MMSE-OSIC, Joint-ML, PDA, CPDA MUD techniques in θ_{best} direction. The MSs are aided by the MRs, which are close to the RAs when the CPDA MUD is applied. All system parameters were summarized in Table 4.3.

4.4.4 Conventional BS Cooperation versus Pervasive DAS/FFR

1. **BER performance of the entire cell**: when comparing the two system structures, an impartial method may use the observation of the BER performance across the entire cell area of Fig. 4.13. First of all, observe the BER performance of the Joint-ML detector of both the BS COMP and of our pervasive DAS/FFR in Fig. 4.13 when applying $P_t = 20dBm$. We extracted from Fig. 4.13 that for the conventional BS COMP scheme, in 40% of the locations the BER is lower than 10^{-4}, but in almost 50% locations that the BER is higher than 10^{-2}. By contrast, our pervasive DAS/FFR exhibits a BER lower than 10^{-4} across 80% $\sim$ 95% of the area, and the BER is always lower than 10^{-2}. For our novel low-complexity CPDA MUD invoked in our pervasive DAS/FFR scheme, 70% $\sim$ 85% of the area exhibits a BER lower than 10^{-4}. However, if a MR is appointed close to the MS, the coverage is degraded, as shown by the dotted lines marked by the bars in Fig. 4.13, albeit only in the θ_{worst} directions, where the BER of our pervasive DAS/FFR is worse than that of the conventional COMP. Hence, in conjunction with an efficient MR appointment strategy, our pervasive DAS/FFR is capable of improving the BER performance across the entire cell.

2. **The Transmit power required**: upon observing the CPDA curves of Fig. 4.7, 4.8 and 4.9 in the cell-edge area, we infer that the COMP scheme only achieves a coop-

eration gain for a high transmit power of $P_t = 30dBm$. By contrast, our DAS/FFR scheme in capable of gleaning a diversity gain from the MRs operating at a lower transmit power, even at $P_t = 0dBm$. When considering $P_t = 20dBm$ for both the COMP and DAS/FFR schemes, the conventional COMP scheme has the worse BER performance over half the cell-edge area, when the DAS/FFR operates in conjunction with the perfect MR selection strategy introduced in Section 4.4.3.3. The CPDA MUD designed for the pervasive DAS/FFR has the potential of significantly reducing the BER right across the entire cell, as shown in Fig. 4.10.

3. **Complexity imposed by attaining a diversity-gain**: the conventional COMP attains a cooperation gain by exchanging the soft information gleaned from the three adjacent BSs, which implies that the CPDA algorithm has to combine the soft information calculated from the received signal through three independent channels. Hence, the CPDA is capable of attaining a significantly reduced BER in comparison to the joint ML MUD for a transmit power of $P_t = 30dBm$, as shown in Fig. 4.7. However, the DAS/FFR scheme achieves a diversity gain with the aid of the MRs by invoking an additional cooperative time slot. Hence, the CPDA MUD combined the soft information gleaned from the signal received through two independent channel. However, the diversity gain may be eroded, if the correlation coefficient ρ is increased.

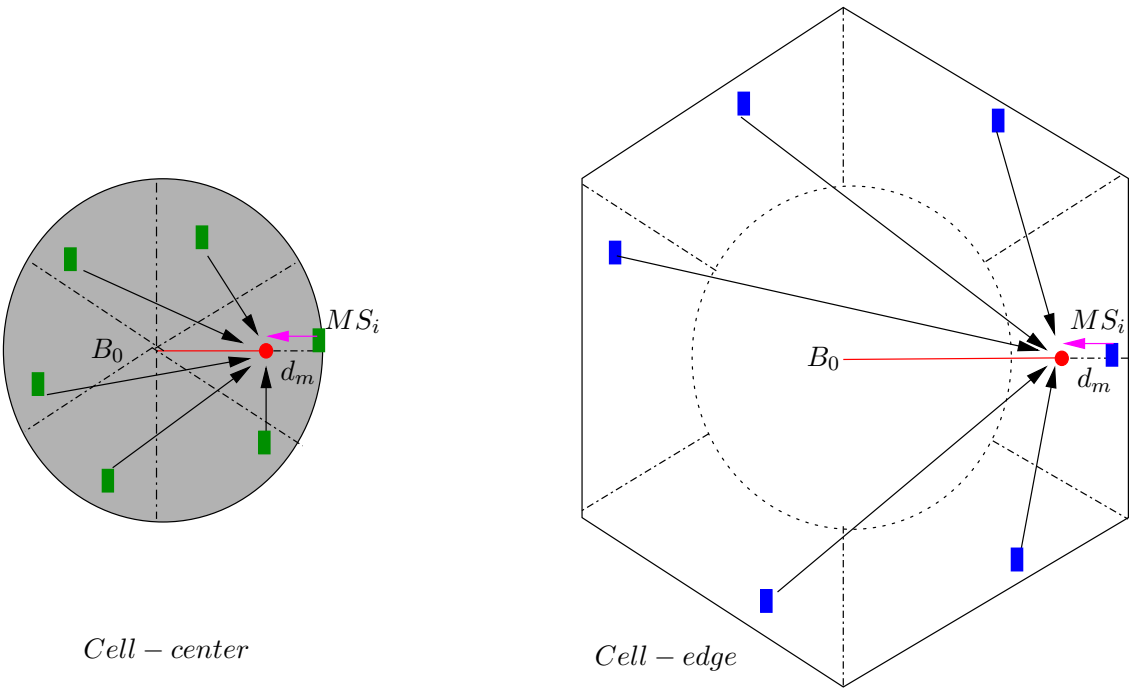

Figure 4.11: The ICI in the cell-center area and cell-edge area.

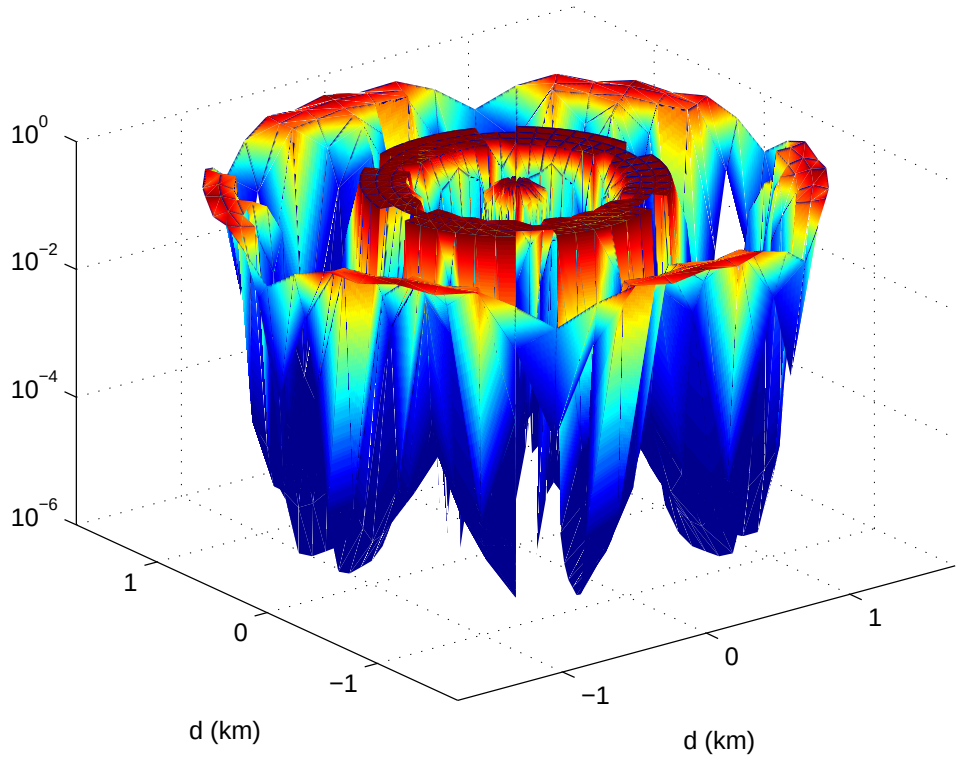

Figure 4.12: The BER performance of the pervasive DAS/FFR scheme of Fig. 4.1b in the entire cellular area, where the CPAD MUD aided by MR close to MS strategy.All system parameters were summarized in Table 4.3.

4.4.5 Power Control for Multiuser in the UL Scenario

Throughout this chapter no power control (PC) has been used, although PC is capable of substantially improving the SINR [1]. The PC technique invoked for our multiuser UL scenario is also based on the normalized SIR model of Section 3.4.4, except that the interferers are the fix RAs in the DL scenario, while here, the interferers are the roaming MSs, as shown in Fig. 4.4. Hence, when calculating the SIR without PC, we may still use Eq. (3.18) repeated here for convenience as following:

$$SIR_i(dB) = 40log_{10}(\frac{d_i}{d_s}), \tag{4.21}$$

$$SIR_{user}(dB) = -10\log_{10}[\sum_i 10^{-(\frac{SIR_i(dB)}{10})}]. \tag{4.22}$$

Similarly to the DL, d_i and d_s are defined as the distance of the interfering MS-RA pair and that of the desired MS-RA pair. When the MSs roaming in the area suffer from low SIR, their transmit power may be increased. The SIR recorded in the presence of the PC

[1] In interference-limited situations we have $SINR \simeq SIR$, as mentioned in Section 3.4.4.

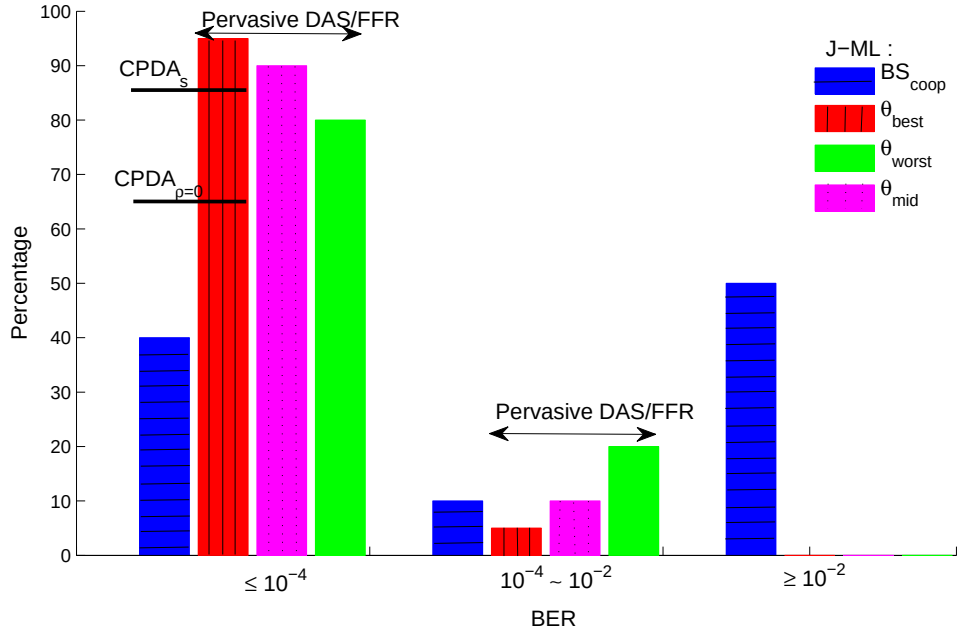

Figure 4.13: The pervasive DAS/FFR scheme in the entire Cell relying on the system parameters of Table 4.3, in contrast to the BER performance of the BS COMP scheme of Fig. 4.7 using the system parameters Table 4.4, where having the transmit power $P_t = 20dBm$.

technique is the same as that of DL introduced in the Section 3.4.4, which is repeated here for convenience:

$$SIR_i'(dB) = 40log_{10}(\frac{d_i}{d_s}) + P_{dB}^s - P_{dB}^i, \tag{4.23}$$

$$SIR_{user}'(dB) = -10\log_{10}[\sum_i 10^{-(\frac{SIR_i'(dB)}{10})}]. \tag{4.24}$$

The SIR's geographic distribution recorded in the absence of the PC technique and in the presence of the PC technique invoked for our pervasive DAS aided FFR systems in an UL scenario are shown in Fig. 4.14. When the MSs are roaming close to the RAs in both the cell-center area and the cell-edge area, a high SIR $(SIR_{user}(dB) \geq 20dB)$ is guaranteed without increasing the transmit power. More explicitly, when PC is used, a high SIR $(SIR_{user}'(dB) \geq 20dB)$ is experienced by the MSs roaming close to the RAs which is similarly as high as that recorded in the absence of PC, although the interference improved by the other MSs may be increased due to increasing their transmit power in the interest of maintaining their link-quality. In the absence of PC, the SIR of MSs roaming far away from the RAs is seriously reduced in both the cell-center and in the cell-edge area, especially in the "worst-case directions" $(SIR_{user}(dB) \sim -20dB)$. On the other hand, when applying PC technique, the transmit power of the MSs, which suffer from a low SIR

$(SIR_{user}(dB) < 20dB)$ will be increased.

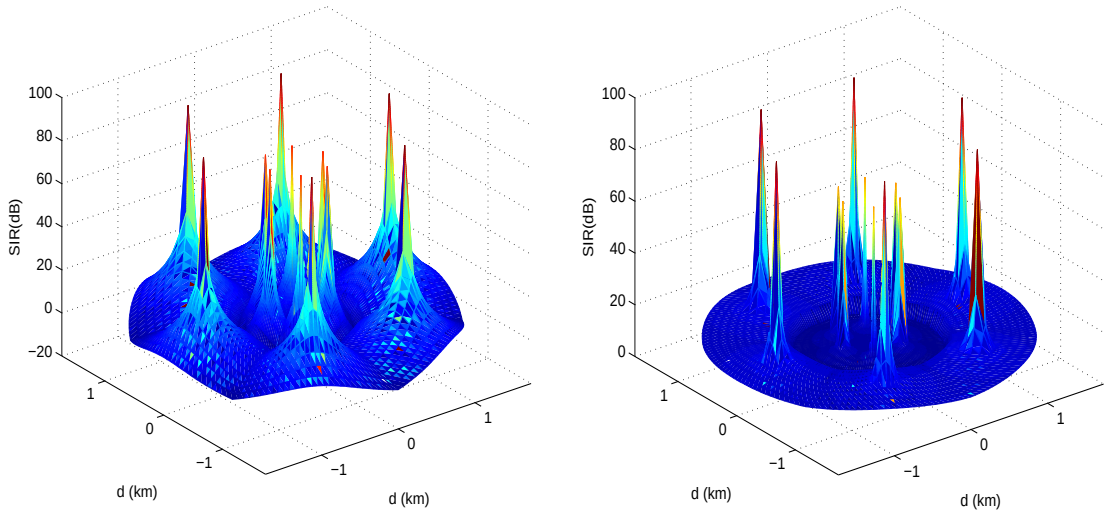

(a) no power control (b) power control

Figure 4.14: The SIR of the pervasive DAS aided FFR systems of Fig. 4.1, operating both with and without PC. All system parameters were summarized in Table 4.3.

The BER performance of the pervasive DAS aided FFR architecture assisted by PC is characterized in Fig. 4.15, where the parameters of the PDA detector and of the convolutional channel code are summarized in Table 4.3. When using PC, the MSs roaming in the cell-edge area are capable of achieving $BER \leq 10^{-3}$ even in the "worst-case area", while we have $BER \leq 10^{-2}$ when the MSs roam in the cell-center area, since the ICI is significantly stronger in the cell-center than in the cell-edge area as evidenced by Fig. 4.11.

4.4.6 Chapter Summary

We proposed a pervasive DAS/FFR scheme, where the DAS was invoked for increasing the coverage of the entire cell area, while MRs were advocated for increasing the diversity in order to reduce the BER of the MSs roaming far away from the RAs. The CPAD MUD was designed for our pervasive DAS/FFR scheme operating in the uplink of a multiuser, multicell scenario, which was capable of reducing the BER by combining the soft information calculated from the signals received from the MS and MR. Although the CPDA is capable of reducing the BER even at a low transmit power, it relies on having an efficient MR selection strategy. We considered the extreme case of the MR being close to the MS and the scenario of the MR being close to the RA. Our simulation results showed that MRs

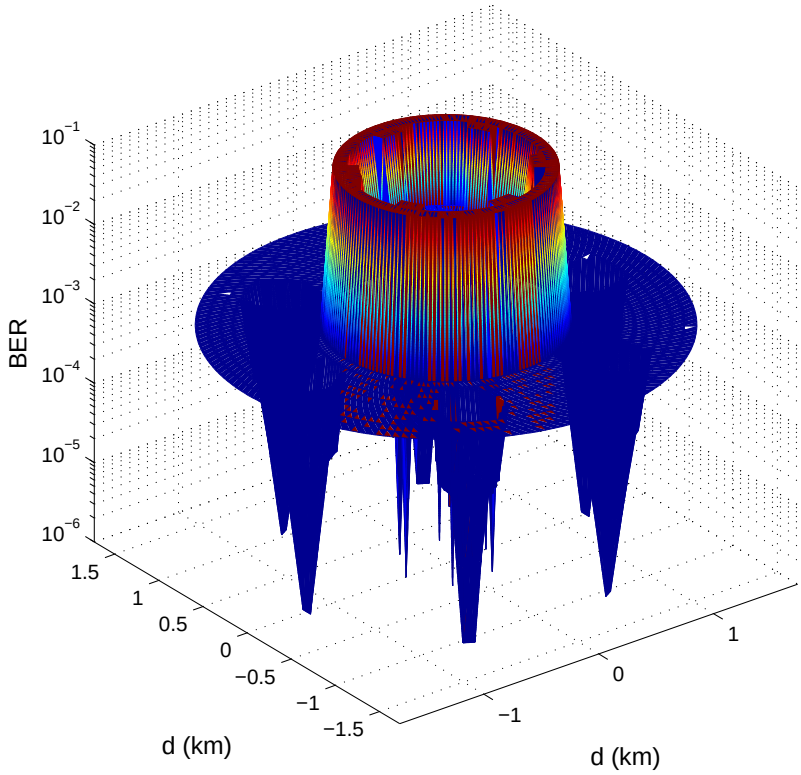

Figure 4.15: The 3D BER profile of our pervasive DAS aided FFR system assisted by PC. All system parameters were summarized in Table 4.3.

are capable of ensuring that 70% $\sim$ 80% of the area exhibits a BER lower than 10^{-4} as seen in Fig. 4.13 for the in pervasive DAS/FFR schemes.

4.5 Chapter Conclusions

In this chapter, our pervasive DAS as seen of Fig. 4.1 in Section 4.2 was combined with FFR for the sake of reducing the pathloss and for mitigating the CCI experienced by the MSs regardless of their position. MRs were also combined with our pervasive DAS/FFR scheme for the sake of increasing the attainable diversity gain. Our pervasive DAS/FFR scheme was then benchmarked against conventional BS cooperation, as seen in Fig. 4.2 of Section 4.2 in the uplink of a multiuser multicell scenario.

In Section 4.3, the received signal model of our pervasive DAS/FFR scheme operating either with or without MRs as well as that of the conventional BS cooperation scheme, where the latter was modeled as a $(N_r \times N_m)$-element virtual MIMO in Section 4.3.4. In Section 4.3.4, four typical multiuser detection techniques, namely the "full search" ML in

Section 4.3.4.1, the PDA in Section 4.3.4.2, ”knowledge sharing” based combined PDA in Section 4.3.5 and the “interference cancellation“ based MMSE-OSIC in Section 4.3.6 were applied. More explicitly, based on the aggregated soft decision information, the soft information directly received from the source MS and that from the corresponding MR was then combined by our novel PDA algorithm at a low computational complexity, which carries out efficient soft-information combining.

Our simulation results demonstrated in Section 4.4 that the conventional BS cooperation characterized in Fig. 4.7 with the aid of the system parameters of Table 4.4 exhibited a limited gain when the MSs roaming close to their own anchor-BS but quite far from the adjacent BSs. The attainable cooperative gain may be increased, when the MSs are roaming in the cell-edge area, provided that a high SINR is guaranteed. The BER performance of our pervasive DAS aided FFR scheme employing the system parameters of Table 4.3 was shown in Fig. 4.8 in the θ_{best} direction, while for the $\theta_{worst,mid}$ directions in Fig. 4.9 where we assumed that the MRs were roaming close to the MSs. When the MS-RA and the corresponding MR-RA channel are uncorrelated, MRs will provided the diversity gain, otherwise, the diversity gain is eroded when the corresponding relaying channel is correlated, as shown in Fig. 4.8 and Fig. 4.9. Furthermore, Fig. 4.10 characterized the BER performance of our pervasive DAS aided FFR scheme, when the MRs were roaming close to the RAs. The BER performance of our pervasive DAS aided FFR scheme recored across the entire cellular area is shown in Fig. 4.12 and Fig. 4.13. Our PDA aided multiuser detector invoked by the pervasive DAS/FFR scheme and assisted by the MRs is capable of reducing the BER across the entire cell area, even at a low transmit power of $P_t = 0dBm$. By contrast, according to Fig. 4.7 the conventional BS cooperation aided scheme has to have as high a transmit power as $P_t = 30dBm$. Generally, an efficient MR selection strategy is required by the Pervasive DAS/FFR scheme, which is capable of significantly reducing the BER right across the entire cell area, where $70\% \sim 80\%$ of the area exhibits a BER lower than 10^{-4} as seen in Fig. 4.13, when a transmit power of $P_t = 20dBm$ is allocated. On the other hand, when applying the PC technique and without assisted by the MRs, the BER across the entire cellular area are reduced, where $\leq 10^{-3}$ in the cell-edge area and $\leq 10^{-2}$ in the cell-center area as shown in Fig. 4.15. The performances of our BS cooperation scheme and of the pervasive DAS aided FFR assisted by MRs scheme was summarized in Table. 4.5

Table 4.5: Performance comparisons of BS cooperation and pervasive DAS/FFR when operating CPDA MUD and $P_t = 20dBm$

BS cooperation		
virtual MIMO	3 independent	6×6-elements
diversity	adjacent 2 BSs	
code modulation	QPSK	punctured convolutional code
decoder	Viterbi algorithm	
BER	cell-center area	cell-edge area
$\leq 10^{-4}$	40% area	none
$10^{-4} \sim 10^{-2}$	10% area	none
$\geq 10^{-2}$	none	50% area
pervasive DAS aided FFR		
virtual MIMO	2 independent	6×6-elements
diversity	MRs close to the RAs	additional time-slot
code modulation	QPSK	punctured convolutional code
decoder	Viterbi algorithm	
BER	cell-center area	cell-edge area
$\leq 10^{-4}$	40% area	40% area
$10^{-4} \sim 10^{-2}$	10% area	10% area
$\geq 10^{-2}$	none	none

Chapter 5

Effects of Imperfect Channel Knowledge on the DL and Non-coherent Systems for the UL

5.1 Introduction and Outline

The performance of Cooperative Multiple Point (COMP) techniques designed for both the DL and UL of DAS combined with FFR was investigated in Chapter 3 and Chapter 4. In order to achieve an improved SINR performance and an increased throughput across the entire cellular coverage area, the novel pervasive DAS/FFR scheme was conceived in Chapter 4. However, all our previous investigations relied on the idealized simplifying assumption of having perfect CSI knowledge. By contrast, in this chapter we consider the realistic practical scenario of having imperfect CSI knowledge. As a radical design alternative, we also conceived and investigated a non-coherent detection aided system, which is capable of dispensing with channel estimation.

In comparsion to the radical low-SINR UFR pattern and the higher-SINR FFR pattern, the DAS/FFR scheme is capable of increasing the cell-edge SINR, despite improving the spatial reuse factor [132]. Naturally, a DAS provides a shorter and hence reduced-pathloss link between the RA and the MSs by placing the RA near the cell edge. However, experiments demonstrate that this DAS positioning will impose strong CCI, which emanates from the neighbouring RAs in the case of the DL and from the MSs transmitting at the same time within the same band in the case of the UL, especially when the MSs are roaming near the angle halfway between the adjacent RAs [24]. A promising technique of mitigating the CCI in both the DL and UL is constituted by the MIMO COMP transmission philosophy

of [158], [135], which was detailed in Chapter 4. Initial studies demonstrate that the cell-edge MSs typically achieve higher SINRs in comparison to both UFR and FFR systems as well as to plain DAS without operating the aid of COMP transmissions [159] [160].

However, the original COMP transmission [161] requires full CSI of all links amongst all BSs and MSs at the transmitter side for the sake of approaching the theoretical upper-bound performance of a near-noise-limited system. Naturally, the presence of imperfect CSI at the transmitters will erode the efficiency of this CCI mitigation technique. As a result, the cell-edge MSs will benefit from an improved spatial diversity gain, as a benefit of gleaning information from all the RAs links, where the specific improvements attained will depend both on the accuracy of the CSI available at the transmitter as well as on that of the synchronisation between the RAs and the MSs.

On the other hand, the proposed COMP technique characterized in Chapter 3 and Chapter 4 is based on modelling the DAS scheme as a virtual MIMO, where mitigating the CCI remains a challenge in the UL even with the extra benefit of perfect CSI. In contrast to designing a multiuser detector for the UL, a simple solution to achieve lower BER performance is modelling the DAS scheme as a Single-Input Multiple-Output (SIMO) arrangement, where the mobile stations will be served by the nearest pair of RAs with the aid of a TDMA structure. The diversity gain of the resultant SIMO system provides an effective mechanism of combating the effects of channel-induced fading [162]. The resultant SIMO aided techniques are capable of increasing the achievable performance gain, provided that the CSI is accurately estimated at the receivers [163–166]. Most previous work on SIMO systems was based on the assumption of perfectly knowing the CSI and hence the corresponding data recovery typically relied on coherent detection. However, in practice it is hard to acquire accurate CSI, especially in rapidly fading mobile environments. Hence, it is of prime significance to design new non-coherent detection techniques, which dispense with channel estimation. More specifically, the soft-decision based low-complexity Star-QAM (StQAM) technique has been proposed in [88], which is capable of outperforming its hard-decision based StQAM counterpart [128], provided that it is supported by powerful soft-decision-aided channel coding schemes [167].

The outline and novel contributions of this chapter may be summarised as follows:

1. We investigate the impact of practical impairments on COMP aided DAS in the context of a FFR arrangement in the case of the DL, including the effects of CSI estimation errors, CSI quantisation errors as well as Orthogonal Frequency Division Multiplexing (OFDM) signal timing and frequency synchronisation errors. To make our investigations as complete as possible, in this chapter, we compare the COMP

aided DAS solution to the traditional UFR and FFR transmission regimes as well as to conventional plain DAS dispensing with COMP.

2. We investigated the uplink performance of FFR based multicell multiuser schemes, as a complement of the corresponding DL investigations detailed in [24]. We further extended the Single-Input Single-Output (SISO) based non-coherent 16StQAM scheme of [88] to a SIMO system. We investigated both the Turbo-Coded [167] 16StQAM and 16QAM [128] schemes in the multicell, multiuser UL system considered, when imperfect DOF links are considered.

The outline of the chapter is as follows. The effects of practical impairments on the DL of DAS/FFR networks are characterized in Section 5.2. In Section 5.2.1, our system model of the DL and our assumptions are provided. These discussions are followed by highlighting the benchmarker scenarios of UFR and FFR aided networks as well as of plain DAS dispensing with COMP. In Section 5.2.2, we impose a range of practical impairments on COMP-aided DASs. The system's SINR profiles are investigated in Section 5.2.3.

A turbo-coded StQAM technique dispensing with channel estimation is applied for the DAS/FFR aided UL, which is introduced in Section 5.3. Our system model of the UL is described in Section 5.3.1, while our results and discussions are detailed in Section 5.3.4. Finally, our conclusions are presented in Section 5.4.

5.2 Effects of Practical Impairments on the DAS/FFR Scheme in DL

5.2.1 System Description

5.2.1.1 Configurations and Assumptions

In this chapter we use the topology of Fig. 3.1 defined for the two-tier DAS aided FFR as that in Chapter 3 and we focus our attention on the wireless channel. Hence a perfect optical fiber backhaul is assumed between the BS and RAs. For convenience, we repeated Fig. 3.1 in this section as Fig 5.1. As seen in Fig 5.1, we let $\mathbb{B}_o$ denote the set containing 6 adjacent tier-one cells and 12 tier-two cells, with each having N_t^B transmit antennas. Within the centered area of a cell shown by the grey circle, MSs are served by the BSs using the frequency set F_c, while MSs roaming in the cell-edge area are served by RAs using one of the frequencies in the set $\{F_1, F_2, F_3\}$. Hence, the received SINRs of MSs

located near the cell-edge of the conventional cell may be improved as a benefit of their shorter and hence better link between the MSs and the RAs. However, severe CCI still exists when the MSs are located in the vicinity of the direction between two adjacent RAs, which constitutes the worst-case direction.

Against this background, COMP aided DAS may be employed for mitigating the CCI. Consider a general scenario constituted by N_b RAs hosted by the set $\mathbb{B}_c$, where each RA is equipped with N_t transmit antennas. Let us assume that a total of $N_u = N_b$ MSs hosted in the set $\mathbb{B}_u$ - each equipped with a single receive antenna - are involved in the cooperative transmissions, where each of the N_u MSs roams within the coverage area of its anchor RA, as portrayed in Fig. 5.1. Hence, the scenario may be described by the parameter combination of $\{\mathbb{B}_o, N_t^B, N_b, N_t, N_u, N_r\}$. Furthermore, we let $N_T = (N_b \times N_t)$ and $N_R = (N_u \times N_r)$ denote the total number of transmit and receive antennas in the cooperative transmission, respectively. Since we focus on COMP-aided DAS transmissions, the assumption of a single BS antenna is stipulated for simplicity, while the total power consumption P_t is assumed to be the same for the sake of a fair comparison.

Within the arrangement discussed, the assumption of perfect reception of the BSs' data at the RA becomes realistic, when an optical fibre link is used for connecting the RAs and the BS. As a benefit of having a high-bandwidth fibre link between the BS and the RAs, and of the so-called Precise Timing Protocol (PTP) invoked for the synchronisation between the BS and the RAs, the assumption of perfect synchronisation between BS and the RAs becomes reasonable.

5.2.1.2 DAS Aided FFR Scenario

In comparsion with the DAS aided FFR scheme considered in Chapter 3 and that in this chapter, both of them use the same topology of two tiers of nineteen cells as shown in Fig. 5.1, but the received signal in the cell-edge area as shown in Eq (3.8) in Section 3.3.1.2 only considered the interference from the local cell, since the interference from the second tier is capable of being ignored which has been proved in the simulation result as shown in Fig. 3.4 in Section 3.4. Although, the interference from the second tier is capable of being ignored which will simplify the modelling and simulation, we further study the wireless channel of the DAS aided FFR scheme in this chapter. Hence, the interference from the second tier is considered.

In the DAS aided FFR scenario of this chapter we assume that the total transmit power P_t is equally shared amongst the RAs for simplicity and the power available at each RA is denoted as P_a. In this scenario, N_b RAs can use the same channel for simultaneously

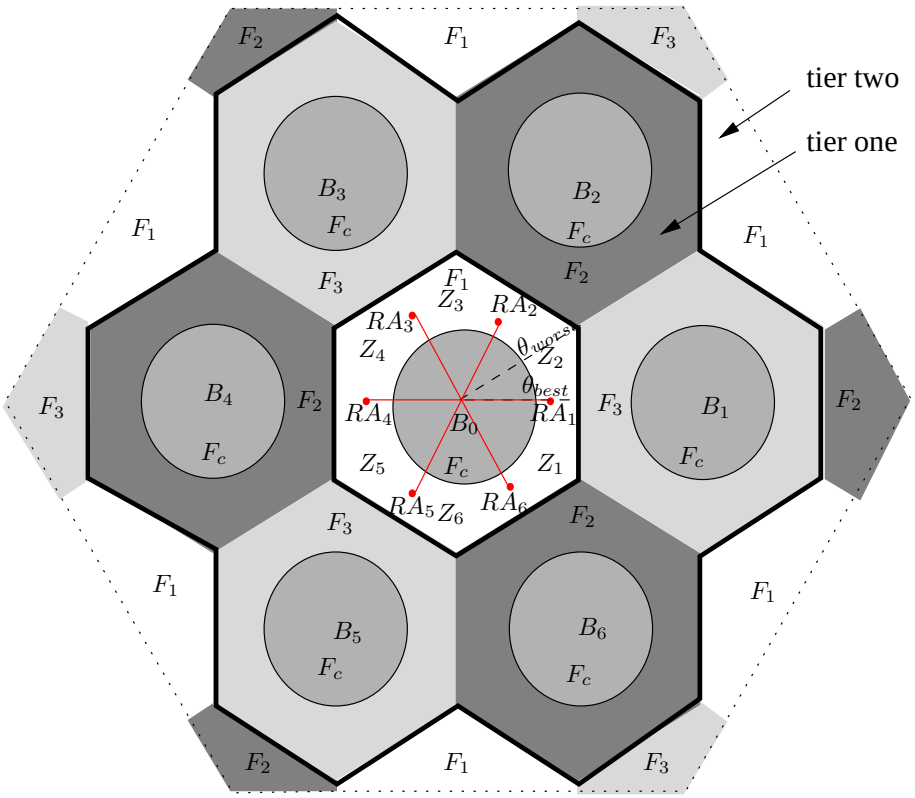

Figure 5.1: The cellular topology of two tiers of nineteen cells relying on a FFR and DAS arrangement, where $N_r = 6$ RAs are employed. The structure of the cells in tier two is the same as the ones in tier one which was repeated from Fig. 3.1 in Section 3 for convenience.

supporting more MSs, thus the discrete-time model of the signal received by MS j roaming in the cell-edge area may be expressed as

$$y_j = \mathbf{h}_{j,j}\mathbf{t}_{j,j}s_j + \sum_{i\in\mathbb{B}_{c,-j}} \mathbf{h}_{i,j}\mathbf{t}_{i,i}s_i + \sum_{i\in\mathbb{B}_f} \mathbf{h}^B_{i,j}\mathbf{t}^B_{i,i}s_i + n_j, \tag{5.1}$$

where the first term represents the desired signal, while the second and the third term denote the CCI of transmission from other RAs and of transmission within the tier-two cells using the same frequency set, respectively. Moreover, $\mathbf{h}_{i,j} \in \mathbb{C}^{1\times N_t}$ describes the DL channel between the ith RA and the jth MS, obeying i.i.d. complex Gaussian entries, while $\mathbf{t}_{i,i} = \sqrt{P_a/N_t}\left[1,1,\cdots,1\right]^T \in \mathbb{C}^{N_t\times 1}$ denotes the preprocessing employed at the ith RA. Similarly, the SINR of MS j roaming in the cell-edge area may be written as

$$\gamma_j^{das} = \frac{|\mathbf{h}_{j,j}\mathbf{t}_{j,j}s_j|^2}{\sum\limits_{i\in\mathbb{B}_{c,-j}} |\mathbf{h}_{i,j}\mathbf{t}_{i,i}s_i|^2 + \sum\limits_{i\in\mathbb{B}_f} |\mathbf{h}^B_{i,j}\mathbf{t}^B_{i,i}s_i|^2 + |n_j|^2}. \tag{5.2}$$

In contrast to the received SINR in Eq. (2.7) of Section 2.3.2 which only a single interfer was taken into account, here multiple interferes are taken into account in Eq. (5.2). While Eq. (5.2) and Eq. (3.8 are in the same form, the difference is that the former calculates the

interference from both the local cell and the second-tier operating the same frequency and the later only calculates the interference from the local cell.

5.2.2 Practical Impairments in COMP-Aided DAS

5.2.2.1 COMP-Aided DAS with FFR

In Section 3.3.2.2, the cooperative MMSE and cooperative egBF linear Transmit PreProcessing (TPP) techniques were invoked for mitigating the CCI, which entirely relied on the channel matrix used for preprocessing the transmit signal. In this more powerful chapter, we employ the linear Joint Signal-to-Leakage-Noise-Ratio (JSLNR) precoding technique [168] for mitigating the CCI. In a COMP scenario, each MS is jointly served by all RAs. Hence, the corresponding discrete-time DL model may be written as:

$$y_j = \mathbf{h}_j \mathbf{t}_j s_j + \sum_{i \in \mathbb{B}_{u,-j}} \mathbf{h}_j \mathbf{t}_i s_i + \sum_{i \in \mathbb{B}_f} \mathbf{h}^B_{i,j} \mathbf{t}^B_{i,i} s_i + n_j, \tag{5.3}$$

where the first two terms represent the desired signal and the Multi-User Interference (MUI) imposed by the simultaneous DL transmissions to other MSs in the cooperative site. The latter contributions are hosted in the set $\mathbb{B}_{u,-j}$. The difference in comparison to the system model of the Non-COMP transmission of Eq. (5.1) is that $\mathbf{h}_j \in \mathbb{C}^{1 \times N_T}$ denotes the joint DL channel between all the N_b cooperative RAs and the jth MS, where $\mathbf{h}_j = [\mathbf{h}_{1,j}, \mathbf{h}_{2,j}, \ldots, \mathbf{h}_{N_b,j}]$ denotes the joint channel vector. Still referring to Eq. (5.3), $\mathbf{t}_j \in \mathbb{C}^{N_T \times 1}$ denotes the joint precoding vector configured for the jth MS of the cooperative site. The third term of Eq. (5.3) represents the CCI arriving from the tier-two cells, which use the same channel set.

Precoding Scheme The JSLNR precoding technique [168] aims for maximising the received signal power at the intended MSs, whilst simultaneously minimising the signal power leaked to other MSs. More specifically, the SLNR η at MS j is given by

$$\eta_j = \frac{trace[\mathbf{t}_j^H \mathbf{h}_j^H \mathbf{h}_j \mathbf{t}_j]}{trace[\mathbf{t}_j^H (\#/P_j + \mathbf{h}_{-j}^H \mathbf{h}_{-j}) \mathbf{t}_j]}, \tag{5.4}$$

with $\# = \{N_r |n_j|^2 + \sum_{i \in \mathbb{B}_f} trace(\mathbf{t}^{B\,H}_{i,i} \mathbf{h}^{B\,H}_{i,j} \mathbf{h}^B_{i,j} \mathbf{t}^B_{i,i})\} \mathbf{I}_{N_T}$ and $\mathbf{h}_{-j} = [\mathbf{h}_1^T, \cdots, \mathbf{h}_{j-1}^T, \mathbf{h}_{j+1}^T, \cdots, \mathbf{h}_{N_u}^T]^T$. Hence, the optimisation problem may be stated as

$$\mathbf{t}_j = \arg \max_{\mathbf{t}_j} \eta_j. \tag{5.5}$$

It can be seen that the optimisation problem of Eq (5.5) requires the knowledge of power

allocation $P_j = \sum_{i=1}^{N_b} P_{i,j}$, which has to satisfy the per-RA power constraint

$$\mathbf{E}\{\sum_{j=1}^{N_u} trace[(\mathbf{t}_j x_j)(\mathbf{t}_j x_j)^H]\} = \sum_{j=1}^{N_u} trace(\mathbf{t}_j \mathbf{t}_j^H) \leq P_a. \tag{5.6}$$

In this chapter, a simple proportional power allocation strategy is advocated:

$$P_{i,j} = \frac{trace(\mathbf{h}_{i,j}\mathbf{h}_{i,j}^H)}{\sum_{j=1}^{N_u} trace(\mathbf{h}_{i,j}\mathbf{h}_{i,j}^H)} P_a. \tag{5.7}$$

Furthermore, the optimisation problem of Eq (5.5) may be decoupled into the individual optimisation processes by forcing $\mathbf{t}_j$ to be an orthonormal matrix as discussed in [168], where we have $\mathbf{t}_j = eigv(\mathbf{B}^{-1}A)$ representing the eigenvectors corresponding the largest eigenvalue of $\mathbf{B}^{-1}\mathbf{A}$, with $\mathbf{B} = \#/P_j + \mathbf{h}_{-j}^H \mathbf{h}_{-j}$ and $\mathbf{A} = \mathbf{h}_j^H \mathbf{h}_j$. Finally, the resultant linear precoding matrix $\mathbf{t}_{i,j}$ is multiplied by the allocated power $P_{i,j}$. Hence, the achievable SINR of COMP-aided DAS transmissions may be expressed as:

$$\gamma_j^{comp} = \frac{|\mathbf{h}_j \mathbf{t}_j s_j|^2}{\sum\limits_{i \in \mathbb{B}_{u,-j}} |\mathbf{h}_j \mathbf{t}_i s_i|^2 + \sum\limits_{i \in \mathbb{B}_f} |\mathbf{h}_{i,j}^B \mathbf{t}_{i,i}^B s_i|^2 + |n_j|^2}. \tag{5.8}$$

In contrast to the SINR of the cooperative DAS assisted FFR in Eq. (3.13) of Section 3.3.2 which only takes in to account the interference from the local cell, here Eq. (5.8) takes into account the interference from both the local cell and the second-tier operating the same frequency.

5.2.2.2 Practical Impairments

In Chapter 3, we calculated the imperfections imposed by the practical optical fibre link, but we assume having a perfect CSI knowledge for the wireless channel. Hence, in this chapter, we will consider a more practical finite-accuracy channel estimator and characterize the effects of the CSI estimation errors, CSI quantisation errors and synchronisation errors. Furthermore, the interference imposed by the second-tier of the DAS aided FFR scheme is also considered, while that was ignored in Chapter 3. The system performance of COMP is heavily dependent on the accuracy of the precoding matrix, which is a function of the instantaneous CSI. However, in practice, we are unlikely to have the luxury of perfect CSI both at the receiver and at the transmitter due to the combined effects of *CSI estimation errors* and the *CSI feedback quantisation errors*.

CSI Estimation Errors We assume that MS j is capable of estimating the joint CSI vector $\mathbf{h}_j = [\mathbf{h}_{1,j}, \mathbf{h}_{2,j}, \cdots, \mathbf{h}_{N_b,j}] \in \mathbb{C}^{1 \times N_T}$, subject to the assumption of a Gaussian CSI estimation error having a variance of σ_e^2. Then the channel vector of MS j may be

expressed as $\mathbf{h}_j = \hat{\mathbf{h}}_j + \mathbf{e}_j$, where $\mathbf{e}_j$ denotes a zero-mean complex Gaussian vector having a variance of σ_e^2.

CSI Quantisation Errors After obtaining the estimated CSI, we assume the employment of the Random Vector Quantisation (RVQ) scheme of [169] for quantising the Channel Direction Information (CDI) $\acute{\mathbf{h}}_j = \hat{\mathbf{h}}_j / \|\hat{\mathbf{h}}_j\|$, where $\|\cdot\|$ denotes the Euclidean norm and $\|\hat{\mathbf{h}}_j\|$ represents the Channel Quality Information (CQI), which is assumed to be perfectly fed back to the cooperative transmitters. This implies that a CDI quantisation codebook $\mathbf{C} = \{\mathbf{c}_1, \mathbf{c}_2, \ldots, \mathbf{c}_{N_q}\}$ consisting of $N_q = 2^b$ zero-mean unit-norm complex Gaussian vectors $\mathbf{c}_i \in \mathbb{C}^{1\times N_T}$ is constructed and made available to both the MS and to the cooperative transmitter, where b denotes the number of quantisation bits, i.e. codebook index bits. In the quantised feedback regime, the b bits representing the particular codebook index of $\kappa = \max_{i\in\{1,2,\ldots,N_q\}} \cos\theta, \theta = \angle(\acute{\mathbf{h}}_j, \mathbf{c}_i)$ are transmitted, where the codebook may be designed to satisfy diverse design criteria. If we let θ be the angle between the CDI $\acute{\mathbf{h}}_j$ and the quantisation vector $\mathbf{c}_\kappa$, then we have $\acute{\mathbf{h}}_j = \mathbf{c}_\kappa \cos\theta + \mathbf{g}_\kappa \sin\theta$, where $\mathbf{g}_\kappa$ is a unit vector that lies in the null-space of $\mathbf{c}_\kappa$. At the transmitter side, these received codebook-index bits are used for regenerating the quantised CSI by combining them with the CQI value.

COMP-aided DAS with imperfect CSI In the presence of imperfect CSI at the transmitter, the precoding vector $\tilde{\mathbf{t}}_j = \arg\max_{\tilde{\mathbf{t}}_j} \eta_j$ configured for MS j in the COMP-aided DAS will be designed based on the feedback quantised CSI $\{\tilde{\mathbf{h}}_1^T, \tilde{\mathbf{h}}_2^T, \cdots, \tilde{\mathbf{h}}_{N_u}^T\}$, where $\tilde{\mathbf{h}}_j$ are regenerated by combining the perfectly feedback CQI $\|\hat{\mathbf{h}}_j\|$ and the quantisation index κ. More specifically, the quantised CSI of MS j is given by $\tilde{\mathbf{h}}_j = \|\hat{\mathbf{h}}_j\|\mathbf{c}_\kappa \in \mathbb{C}^{1\times N_T}$. Thus, the SINR of MS j associated with imperfect CSI in Eq. (5.8) has to be modified to

$$\gamma_j^{comp,c} = \frac{|\mathbf{h}_j \tilde{\mathbf{t}}_j s_j|^2}{\sum\limits_{i\in\mathbb{B}_{u,-j}} |\mathbf{h}_j \tilde{\mathbf{t}}_i s_i|^2 + \sum\limits_{i\in\mathbb{B}_f} |\mathbf{h}_{i,j}^B \mathbf{t}_{i,i}^B s_i|^2 + |n_j|^2}. \tag{5.9}$$

5.2.2.3 Synchronisation Errors

One of the assumption in above-mentioned transmission scenarios is that the receivers and the transmitters are perfect synchronised, hence the transmitted signal from all transmitters is arrived at the receiver simultaneously. However in reality, when such as an OFDM-based physical layer technique is employed, there may be synchronisation errors due to both the phase-rotation, which is commensurate with the distance traveled between the transmitters and receivers as well as owing to the mismatch of local oscillator frequencies at the transmitter and receiver, which will erode the orthogonality of subcarriers. In contrast to the signal model of Eq. (3.10) in Section 3.3.2 and of Eq. (4.7) in Section 4.3.2, in this chapter,

both the time offset and frequency offset are taken into consideration. More explicitly, the demodulated data symbols $y_j[l,k]$ at MS j transmitted from RA j of the lth OFDM symbol and subcarrier k under perfect synchronisation can be shown to be

$$y_j[l,k] = \mathbf{h}_{j,j}[l,k]\mathbf{x}_{j,j}[l,k] + n_j[l,k], \tag{5.10}$$

where $\mathbf{x}_{j,j}[l,k] = \mathbf{t}_{j,j}[l,k]s_j \in \mathbb{C}^{N_t \times 1}$ denotes the transmitted symbol with $\mathbf{t}_{j,j}[l,k] \in \mathbb{C}^{N_t \times 1}$ being the preprocessing at the transmitter, while $\mathbf{h}_{j,j}[l,k]$ and $n_j[l,k]$ are channel transfer function (CTF) of frequency-selective fading channel and the noise at the receiver of the lth symbol and kth subcarrier, respectively. We henceforth omit the subscript for simplicity.

Time Offset When considering the average time offset of $\varepsilon = n_\varepsilon T$ between the transmitter and the receiver, where T denotes the sampling duration, Eq. (5.10) may be expressed as [170]

$$y_j = e^{j2\pi(k/N)n_\varepsilon}\alpha(n_\varepsilon)\mathbf{h}_{j,j}\mathbf{x}_{j,j} + n_j + n_{n_\varepsilon}, \tag{5.11}$$

where N is the Fast Fourier Transform (FFT) size of the OFDM modulation scheme, with the attenuation factor of $\alpha(n_\varepsilon) = \sum_m |\mathbf{h}_{j,j}(\tau_m)|^2 \frac{N - \Delta\varepsilon_m}{N}$ being negligible when the FFT size N is sufficiently high, where $\mathbf{h}_{j,j}(\tau_m)$ denotes the mth tap channel impulse response (CIR) at a delay of τ_m. Moreover, the Inter-Symbol-Interference (ISI) imposed by the time offset may be modeled as additional noise n_ε having a power of

$$\sigma_\varepsilon^2 = \sum_m |\mathbf{h}_{j,j}(\tau_m)|^2 \Big[2\frac{\Delta\varepsilon_m}{N} - (\frac{\Delta\varepsilon_m}{N})^2\Big], \tag{5.12}$$

where $\Delta\varepsilon_m$ may be expressed as

$$\Delta\varepsilon_m = \begin{cases} n_\varepsilon - \dfrac{\tau_m}{T}, & n_\varepsilon > \dfrac{\tau_m}{T} \\ \dfrac{\tau_m - T_g}{T} - n_\varepsilon, & 0 < n_\varepsilon < \dfrac{\tau_m}{T} - N_g \\ 0, & else, \end{cases} \tag{5.13}$$

where $N_g = T_g/T$ denotes the length of Cyclic Prefix (CP), with T_g being the time of the CP in one OFDM symbol.

Frequency Offset As far as the frequency offset of $\phi = \dfrac{\Delta f}{1/T_u}$ is considered with T_u representing the data period of one OFDM symbol, the demodulated data symbol in Eq. (5.10) may be written as [170]

$$y_j = \left\{e^{j\pi\phi}e^{j2\pi[(lN_s+N_g)/N]\phi}\right\}\beta(\phi)\mathbf{h}_{j,j}\mathbf{x}_{j,j} + n_j + n_\Omega, \tag{5.14}$$

Table 5.1: Simulation parameters.

Parameters	Value
Inter-cell distance	1000m
Carrier Frequency f_C	2.5GHz
System Bandwidth $B = 1/T$	15.36MHz
FFT Size N	1024
CP Length N_g	72
Subcarrier Bandwidth $1/T_u = B/N$	15kHz
No. of RA	6
Est. error σ_e	0.1
Pathloss $[\alpha^{pl}; \beta^{pl}]$	$[-3; 1.35 \times 10^7]$

where the attenuation factor of $\beta(\phi)$ may be neglected in the stable state, in which the local offset ϕ is usually small. Furthermore, the power of the additional frequency offset noise n_Ω may be approximated as

$$\sigma_\Omega^2 \approx \frac{\pi^2}{3}\phi^2. \tag{5.15}$$

When the above-mentioned two types of synchronisation errors coexist, the data symbol may be expressed as

$$y \approx e^{j2\pi(k/N)n_\varepsilon} e^{j2\pi\phi[(lT_u+T_g)/T_u]}\mathbf{h}_{j,j}\mathbf{x}_{j,j} + n_j + n_{n_\varepsilon} + n_\Omega. \tag{5.16}$$

COMP-aided DAS with synchronisation errors Thus, the SINR of MS j, which takes into account both time synchronisation errors and frequency synchronisation errors in our COMP-based DAS scenario may be expressed as

$$\gamma_j^{comp,s} \approx \frac{|\mathbf{h}_j\mathbf{t}_j x_j|^2}{\sum\limits_{i\in\mathbb{B}_{u,-j}} |\mathbf{h}_j\mathbf{t}_i x_i|^2 + \sum\limits_{i\in\mathbb{B}_f} |\mathbf{h}_{i,j}^B\mathbf{t}_{i,i}^B x_i|^2 + |n_t|^2}, \tag{5.17}$$

where $\mathbf{h}_j = [\mathbf{h}_{1,j}, \mathbf{h}_{2,j}, \cdots, \mathbf{h}_{N_b,j}]$ denotes the joint channel of MS j, while in contrast to the SINR of MS j without synchronisation errors of Eq. 5.2 and Eq. 5.9, here $|n_t|^2 = |n_j|^2 + |n_{n_\varepsilon}|^2 + |n_\Omega|^2$ represents the overall noise constituted by the white noise and by the synchronisation errors at receiver.

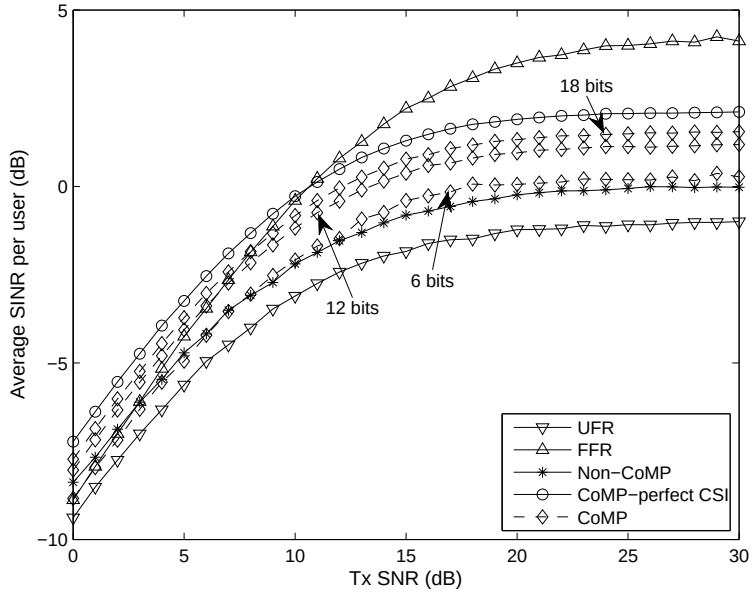

Figure 5.2: Achievable SINR per user versus SNR, when the MSs are located in the worst-case direction of Fig. 5.1 in the presence of both imperfect CSI and synchronisation errors, when using the system parameters of Table. 5.1.

5.2.3 Performance Evaluation

In this section, we consider a practical DAS system, consisting of 19 cells, 6 RAs and the correspondent 6 MSs, which may be described by the parameter combination of

$$\{\mathbb{B}_o, N_t^B, N_b, N_t, N_u, N_r\} = \{19, 1, 6, 1, 6, 1\}.$$

The most important simulation parameters are summarised in Table 5.1.

Here, we considered the Urban Micro setup [137], where the inter-cell distance (ISD) and the BS radius were defined as $D = 1000m$ and $R = D/\sqrt{3}$, respectively. The MISO channels of each BS-MS pair are constituted by two components, i.e. by $\mathbf{h}_{i,j} = (A_{i,j}^{pl})^{1/2}\mathbf{h}_{i,j}^{f}$, where $\mathbf{h}_{i,j}^{f} \in \mathbb{C}^{N_r \times N_t^B}$ represents the fast fading component, which is assumed to be frequency-flat with zero-mean and unity-variance complex Gaussian entries, while $A_{i,j}^{pl} = \beta^{pl} d_{i,j}^{\alpha^{pl}}$ describes the pathloss component, where $d_{i,j}$ denotes the distance in meter between the ith BS and jth MS, while we have $[\alpha^{pl}; \beta^{pl}] = [-3; 1.35 \times 10^7]$ [171]. The channel between the RA-MS pair is defined similarly. In this chapter, we investigate the system performance of MSs, which are located in the worst-case direction using 20 000 Monte-Carlo simulations runs, when considering the effect of both imperfect CSI and synchronisation errors.

5.2.3.1 Achievable SINR of Users in the Worst-case Direction

We consider the scenario in which the MSs are located in the angle halfway between the adjacent RAs and experience both imperfect CSI and synchronisation errors. Fig. 5.2 illustrates the average SINR per user in the worst-case direction of the different transmission arrangements corresponding to three different quantisation bits and time synchronisation offset of $n_\varepsilon = 0.2N_g$ as well as frequency offset of $\Delta f = 0.05$ as a function of Tx SNR[1]. It may be observed in Fig. 5.2 that as expected, the achievable average SINR of all transmission scenarios improves across the entire SNR range spanning from zero to 30dB. Specifically, the SINR of the FFR scenario is the best at high SNRs as a benefit of having no MUI and a low CCI arriving from tier-two cells. The achievable SINR of COMP-aided DAS relying on perfect CSI is better than that of the FFR scenario at low SNRs and it also outperforms the other two benchmarker scenarios across the entire SNR range. However, in reality we do not have the luxury of perfect CSI either at the receiver or at the transmitter. Hence, the realistically achievable SINRs are degraded, as indicated by the curves marked by the diamond for the imperfect CSI scenario associated with different number of quantisation bits. Naturally, increasing the number of quantisation bits is capable of improving the achievable SINRs. Importantly, even in the presence of imperfect CSI, the achievable SINRs remain superior in comparison to both the plain DAS transmission indicated by the label Non-COMP and to the UFR transmission. When compared to the FFR scenario, the COMP-aided DAS provides beneficial SINR improvements at SNRs below $10dB$, but performs worse in the high-SNR region, although again, a factor of six spectral efficiency improvement was achieved, which is twice as high as that of the UFR scenario.

5.2.3.2 Effects of Time-Offset and Frequency-Offset

Fig. 5.3 and Fig. 5.4 quantify the average SINR loss corresponding to users, which are located in the worst-case direction at an SNR of 20dB as a function of both the time-offset and of the frequency-offset, respectively. As for the effects of time synchronisation errors, the SINR loss of all transmission scenarios is increased as the time offset n_ε increased from zero to 115. Specifically, the SINR loss of the traditional FFR scenario is the highest amongst all other scenarios, since the dominant SINR loss is due to the time-synchronisation errors. The same argument applies to the COMP-aided DAS, where the SINR loss imposed by time-synchronisation errors is also prominent. On the other hand, since the system performance in both the Non-COMP aided DAS and in the UFR trans-

[1]Tx SNR here is defined as the transmit power at the transmitter divided by the power of noise at the receiver.

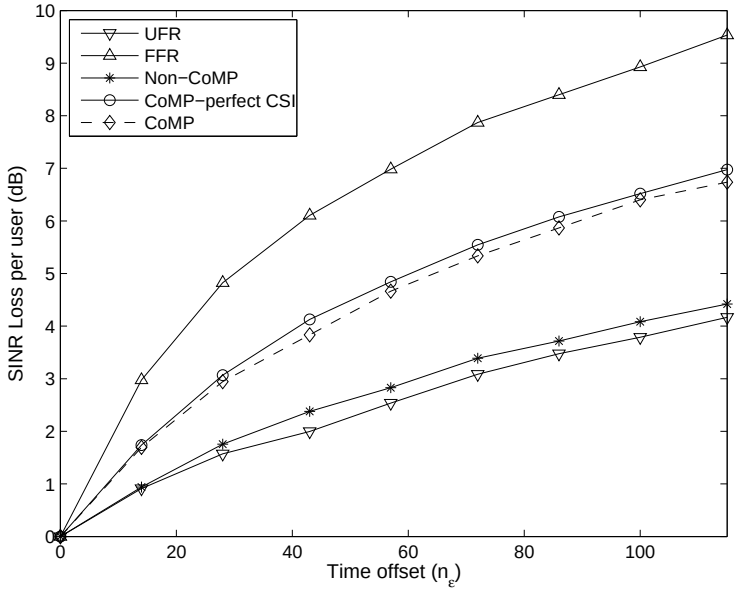

Figure 5.3: Average SINR loss versus time offset between the transmitter and the receiver without frequency synchronisation errors, when using the system parameters of Table. 5.1.

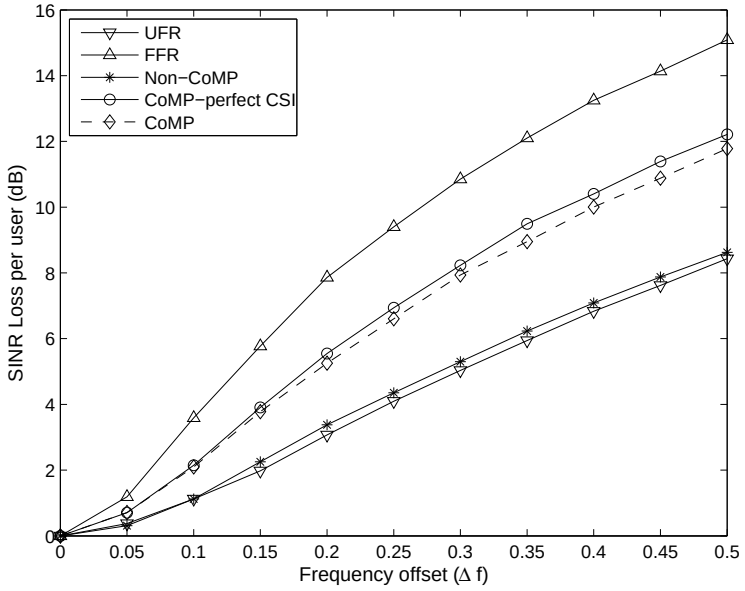

Figure 5.4: Average SINR loss versus frequency offset between the transmitter and the receiver without time synchronisation errors when using the system parameters of Table. 5.1.

mission scenarios is mainly affected by the MUI and CCI, respectively, the SINR loss due to time-synchronisation errors is not obvious. Quantitatively, for both scenarios we have a degradation of no more than 4dB owning to time-synchronisation errors. As for the impact of frequency errors, the SINR loss curves exhibit similar trends as in the case of time-synchronisation errors, when the frequency offset increases from zero to $0.5\Delta f$.

5.2.4 Summary of Section 5.2

We investigated the JSLNR precoding based COMP-aided DAS in conjunction with FFR under imperfect CSI and synchronisation errors, where a superior received SINR was achieved in comparison to both the plain Non-COMP DAS transmission, to traditional UFR transmission as well as to FFR transmission at low SNR, when the number of quantisation bits was higher than 12, with the additional benefit of a six-fold improved spectral efficiency in the cell-edge area, when compared to the FFR scenario and a doubled spectral efficiency, when compared to the UFR scenario. Additionally, the sensitivity of the system's performance subjected to synchronisation errors between the transmitter and the receiver was also investigated. Our future work will be related to the optimisation of our proposed COMP-aided DAS system.

5.3 Turbo-Coded Star-QAM for Distributed Antennas Relying on FFR in the UL

5.3.1 System Model and Analysis

In Chapter 4, the pervasive DAS aided FFR of Fig. 4.1 was modelled as a virtual MIMO for both the cell-center as well as cell-edge areas and mobile relays were invoked for increasing the attainable diversity gain. In this chapter, we focus our attention on the cell-edge area of Fig. 5.5a, where the mobile stations will be served by either the nearest single RA or by the nearest pair of RAs with the aid of a TDMA structure. Hence, the system can be modelled as a SISO or SIMO scenario.

In this chapter, the topology of the FFR based multicell, multiuser scheme is shown in Fig. 5.5a is the same as that of Fig. 3.1 and Fig. 4.1, where there are two-tiers of 19 hexagonal cells surrounding the central Base-Station (BS) B_0 at the origin. The frequency-partitioning strategy of the total available bandwidth F is characterized by $F_c \bigcap F_e = \oslash$, where F_c and F_e represent the cell center's frequency band and the cell edge's frequency

band, respectively. Furthermore, F_e is divided into three orthogonal frequency bands F_i, for $i \in \{1,2,3\}$. In Fig. 5.5a, D denotes the distance between two adjacent BSs, while $R_{cell} = D/\sqrt{3}$ is the radius of each hexagonal cell. We employ $D = 3$ km for the Urban-Macro propagation scenario of [24],

We will specifically investigate the performance of the uplink transmission when the mobile unit is located at locations A and B, as shown in Fig. 5.5b, because these are the worst case scenario at the cell-edge. The mobile unit will be served by the nearest RA or the nearest two RAs, in the SISO or SIMO scenario, respectively.

Table 5.2: Topology parameters.

DAS aided FFR	Location	Polar coordinates
RA	cell-edge R_i	$[\theta_{R_i}, L_{R_i}] = [2\pi(i-1)/N_r, d]$ $i \in [1, N_r]$
BS	B_0	origin
	tier-one	$[\theta_{Bj}, L_{Bj}] = [2\pi(j-1)/6, \sqrt{3}R]$ $j \in [1,6]$
MS	Z_i	$[\theta_{Z_i}, L_{Z_i}]$ $i \in [1, N_m]$, roaming randomly

5.3.2 Imperfect Optical Fibre Model

In contrast to the optical fibre model in of Section 3.2.2 which considered the effects of fiber-induced dispersion and nonlinearity, where the phase-rotations imposed by the imperfect optical fiber were assumed to be perfectly compensated. In this chapter, we additionally take into account the effects of the phase-rotations imposed by the imperfect optical fiber. We assume that the links spanning from the RAs to the BS B_0, as shown in Fig. 5.5b and Fig. 5.6, are constituted by realistic- rather than perfect-optical fiber links. The Nonlinear Schrödinger (NLS) equation can be simplified as [111] [24] [172]:

$$\frac{\partial A(z,t)}{\partial z} = \left(\underbrace{-i\frac{\beta_2}{2}\frac{\partial^2}{\partial t^2}}_{\widehat{D}} + \underbrace{i\xi|A|^2}_{\widehat{N}} \right) A(z,t), \tag{5.18}$$

which was repeated from Eq. (3.3) for convenience, where the terms $\widehat{D}$ and $\widehat{N}$ are the simplified forms of the linear dispersion and the nonlinear dispersion, respectively. Additionally, $A(z,t)$ is a slowly varying envelope function associated with the optical pulse in

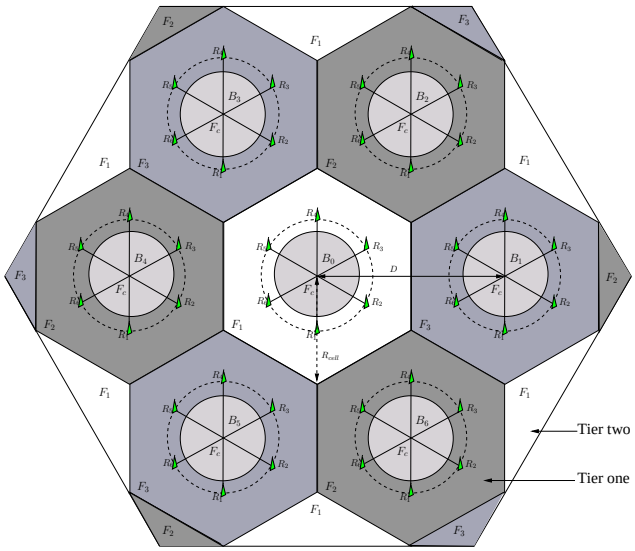

(a)

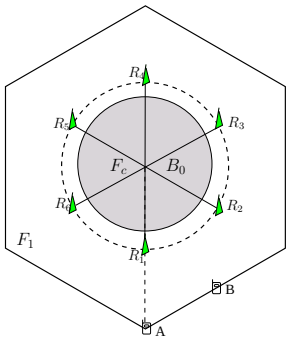

(b)

Figure 5.5: Topology of the 19-cell two-tier FFR based arrangement, where $N = 6$ RAs are employed in each cell. The structure of the central cell and the MS locations A and B. In comparsion with the topology of Fig. 3.1 in Chapter 3 and that of Fig. 4.1 in Chapter 4, we only focus our attention on the typical location A and B which are the worst position.All the topology parameters are summarized in Table 5.2.

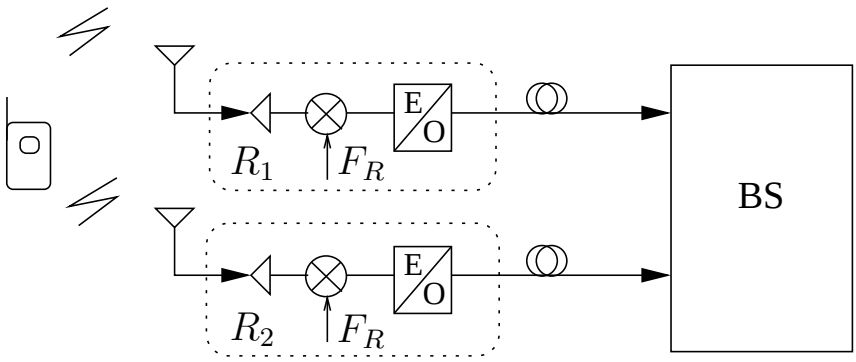

Figure 5.6: The simplified system block diagram of our proposed uplink wireless-optical SIMO system, where F_R is the radio frequency carrier and R_i denote the ith RA.

the optical-fiber, where z is the propagation distance and $t = t' - z/v_g$[2] is the time, while β_2 is the second order propagation constant and the coefficient ξ characterizes the nonlinear effects. However, the NLS equation in Eq(5.18) cannot be solved analytically, when both linear dispersion and optical transmission-induced the nonlinear effects are present, except for specific transmission. The *split-step Fourier* (SSF) method [111] [172] is one of the popular numerical algorithms used for solving NLS equations, owing to its accuracy and relatively modest computational cost. In contrast to the split-step scheme invoked in Eq. (3.4) of Section 3.2.2, in this chapter the so-called symmetric split-step scheme where the main difference is that the effect of nonlinearity is included in the middle of the segment rather than at the segment boundary, the solution of Eq(5.18) may be approximated as:

$$A(z+l,T) \approx \exp\left(\frac{l}{2}\widehat{D}\right) \cdot \exp\left[\frac{l}{2}(\widehat{N}(z) + \widehat{N}(z+l))\right] \cdot \exp\left(\frac{h}{2}\widehat{D}\right) A(z,T). \tag{5.19}$$

Since the linear dispersion and the nonlinear operators do not commute in general, the solution given in Eq(5.19) constitutes an approximation of the exact solution. The entire fiber length $L = ml$ may be decomposed into m consecutive l-length elements. The total optical fiber attenuation, computed based on Eq(5.19), is denoted by A_L for simplicity.

Additionally, we have also investigated the phase-rotation imposed by an imperfect optical fiber. Specifically, the phase of the kth optical pulse may be modeled by:

$$\theta_k = \theta_{k-1} + \tilde{\delta}\,, \tag{5.20}$$

where $\tilde{\delta} \in [-\delta, \delta]$ is the phase difference between the k and the $(k-1)$st optical pulse and δ is the maximum phase difference considered.

5.3.3 Detection Model

Again, in this section, the received signal model of the wireless channel which is additionally contaminated by the optical fibre imperfections, is different from that in Eq (2.5) of Section 2.3.2, Eq (3.5) of Section 3.3 and Eq (4.6) of Section 4.3.1 because both the fibre's amplitude attenuation and the phase-rotation are taken into account. During the first step of the transmission seen in Fig. 5.6, the MS transmits its information to both the RAs R_1 and R_2. The kth symbol received at the ith RA R_i may be expressed as:

$$y_{sr_i,k} = \sqrt{\mathcal{L}_{sr_i}} h_{sr_i,k} x_{s,k} + n_{sr_i,k}, \tag{5.21}$$

[2] t' is the physical time, while v_g is the group velocity at the center wavelength.

where $k \in \{1, ..., K\}$ and K is the number of symbols transmitted from the mobile unit, while $h_{sr_i,k}$ denotes the Rayleigh fading coefficient between the mobile unit and R_i. Furthermore, $n_{sr_i,k}$ represents the Additive While Gaussian Noise (AWGN) having a variance of $N_0/2$ per dimension. Note that $\mathcal{L}_{sr_i} = 10^{-L_{sr_i}/10}$ denotes the path-loss factor between the source (mobile unit) and the ith RA R_i, where $L_{sr_i} = 10\aleph \log_{10}[\frac{d_{sr_i}}{d_0}]$ [173] is the pathloss attenuation in decibel, while $\aleph$ is the pathloss exponent, d_{sr_i} is the distance between the mobile unit and R_i and d_0 is the reference distance for the antenna far-field. We have considered $\aleph = 2$ and $d_0 = 1$ km in this study.

Then, the received signals from R_i are communicated to the BS on a symbol-by-symbol basis, without demodulation or decoding. More specifically, the received signal at BS from R_i could be expressed as:

$$y_{i,k} = A_L e^{j\theta_k} y_{sr_i,k} + n_f, \tag{5.22}$$

$$= A_L e^{j\theta_k} \sqrt{\mathcal{L}_{sr_i}} x_{s,k} h_{sr_i,k} + A_L e^{j\theta_k} n_{sr_i,k} + n_f, \tag{5.23}$$

where again A_L is the optical fiber's amplitude attenuation, θ_k is the phase-rotation introduced by the imperfect optical fiber, $n_{sr_i,k}$ is the noise at R_i and n_f is Gaussian-distributed noise with a zero mean for the optical link between R_i and the BS. We considered $N_r = 2$ RAs in our SIMO scheme. By denoting the $(1 \times N_r)$-element received signal vector by $\mathbf{Y}_k$, the $(1 \times N_r)$-element Rayleigh fading channel vector by $\mathbf{H}_k$ and the total $(1 \times N_r)$-element AWGN vector by $\mathbf{N}_k$, the received signal at the BS may be expressed as:

$$\mathbf{Y}_k = A_L e^{j\theta_k} x_{s,k} \mathbf{H}_k + \mathbf{N}_k, \tag{5.24}$$

where $N_r = 2$. In contrast the Eq. (3.10) of Section 3.3.2 and Eq. (4.7) of Section 4.3.2, in this chapter both the fibre's amplitude attenuation and the phase-rotation are taken into account in Eq. (5.24).

At the BS, the soft-decision aided 16StQAM [88] is used, which dispenses with channel estimation for the sake of low-complexity detection. The corresponding probability density function (pdf) of receiving $y_{i,k}$ when an 8PSK symbol w_k and the amplitude-selection bit b_a were transmitted may be written as:

$$P(y_{i,k}|w_k, b_a = 0) = \frac{1}{\pi N_0^{(0)}} e^{\frac{-\left|y_{i,k} - y_{i,k-1}\alpha^{(0)} w_k\right|^2}{N_0^{(0)}}}, \tag{5.25}$$

$$P(y_{i,k}|w_k, b_a = 1) = \frac{1}{\pi N_0^{(1)}} e^{\frac{-\left|y_{i,k} - y_{i,k-1}\alpha^{(1)} w_k\right|^2}{N_0^{(1)}}} + \frac{1}{\pi N_0^{(2)}} e^{\frac{-\left|y_{i,k} - y_{i,k-1}\alpha^{(2)} w_k\right|^2}{N_0^{(2)}}}, \tag{5.26}$$

where b_a is the bit used for the selection of the two possible amplitudes, $a^{(1)}$, $a^{(2)}$ and the amplitude ratio $\alpha^{(i)}$ may be expressed as:

$$\alpha^{(i)} = \begin{cases} \frac{a^{(1)}}{a^{(1)}} \text{ or } \frac{a^{(2)}}{a^{(2)}} = 1 \; ; & i = 0 \\ \frac{a^{(1)}}{a^{(2)}} \; ; & i = 1 \\ \frac{a^{(2)}}{a^{(1)}} \; ; & i = 2. \end{cases} \tag{5.27}$$

The effective noise variance related to the noise at R_i and BS, $n_{i,k}$, depends on the amplitude ratio α_i used at the kth time instant, which may be estimated as:

$$N_0^{(i)} = N_f + |\alpha^{(i)}|^2 |A_L|^2 |w_k|^2 N_0 \,, \tag{5.28}$$

$$= N_f + |\alpha^{(i)}|^2 |A_L|^2 N_0 \,, \tag{5.29}$$

where the amplitude of an 8PSK symbol is unity, $|w_k| = 1$, while the noise at the BS n_f represents the AWGN having a variance of $N_f/2$ per dimension. Finally, the pdf of receiving $y_{1,k}$ and $y_{2,k}$ conditioned on the transmission of $\{b_0, b_1, b_2\}$(the three bits mapped to an 8PSK symbol) and b_a can be computed as:

$$P(y_{1,k}, y_{2,k}|b_0, b_1, b_2, b_a) = P(y_{1,k}|w_k, b_a) \times P(y_{2,k}|w_k, b_a) \,, \tag{5.30}$$

which is then fed to the Turbo decoder [167] for yielding the original information bit sequence transmitted by the mobile user.

5.3.4 Simulation Results

In this section, we characterize the proposed system of Fig. 5.5b where the simulation parameters are summarized in Table 5.3. The Turbo-Coded 16QAM (TC-16QAM) scheme is used in this section as the benchmark.

Fig. 5.7 denotes the Bit Error Ratio (BER) versus SNR performance of both TC-16QAM and TC-16StQAM schemes when transmitting over correlated Rayleigh fading and imperfect optical channels. As seen in Fig. 5.7, the performance at locations A and

Table 5.3: Simulation parameters.

Modulation	16StQAM, 16QAM
Mapping	Set Partitioning (SP) [128]
Coding	TC
Constituent Code	Half-rate Recursive Systematic Convolutional (RSC) code Code Polynomial G=[15 17]
Code Memory	3
Outer iterations	1
Inner TC iterations	4
Decoder	Approximate Log-MAP
Symbols per block	1 200
Number of frames	5 000
Channel	Correlated Rayleigh fading channel having a normalised Doppler frequency of 0.01, Optical channel

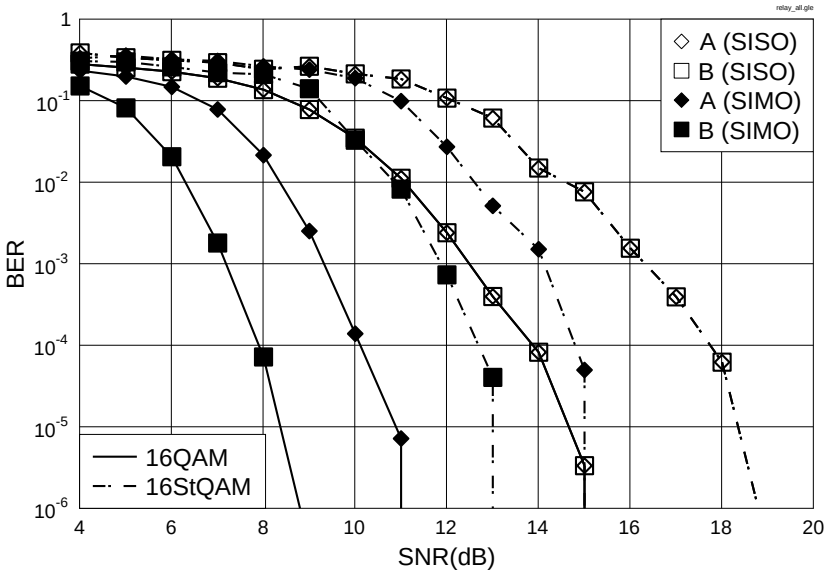

Figure 5.7: BER versus SNR performance of the TC-16QAM and TC-16StQAM schemes when transmitting over correlated Rayleigh fading and imperfect optical fibre channels. The simulation parameters are summarised in Table 5.3 and the corresponding cellular structure is shown in Fig. 5.5b, while the transceiver schematic is seen in Fig. 5.6.

B are identical for the SISO scenario because they have an identical transmission distance of $d_{sr_i} = \sqrt{3}/2$ km from the nearest RA, according to Fig. 5.5b. The TC-16QAM-SISO scheme outperforms the TC-16StQAM-SISO scheme by approximately 4 dB at a BER of 10^{-6}, when a perfect CSI is available at the BS. When the SIMO scheme is considered, the performance at location B improves more significantly than that at location A. This is because location B has the same distance from R_1 and R_2 according to Fig. 5.5b, while location A is further away from R_2. More specifically, the TC-16QAM-SIMO scheme performs approximately 6 dB better than the TC-16QAM-SISO scheme at a BER of 10^{-6}.

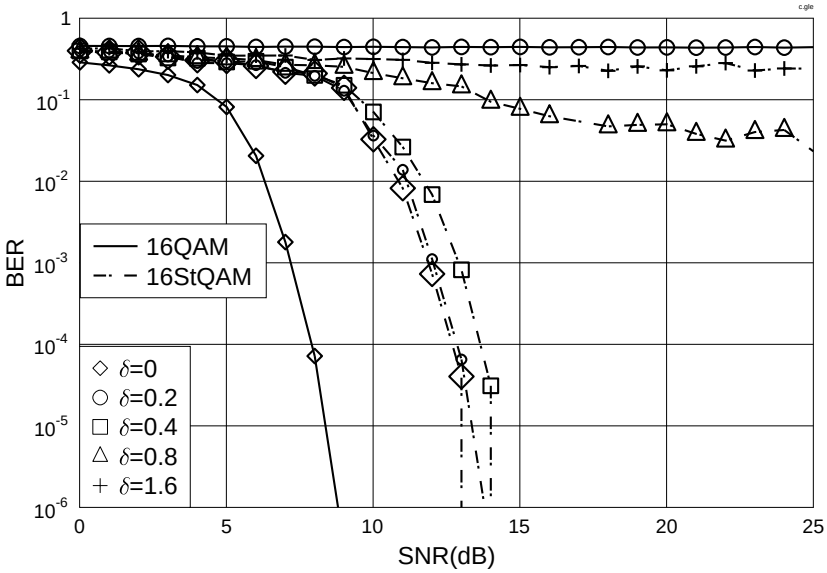

Figure 5.8: BER versus SNR performance of the TC-16QAM-SIMO and 16StQAM-TC-SIMO schemes for transmission over correlated Rayleigh fading and imperfect optical channels. The simulation parameters are summarised in Table 5.3 and the corresponding cellular structure is shown in Fig. 5.5b, while the transceiver schematic is seen in Fig. 5.6. Phase rotations of upto $\delta = \{0, 0.2, 0.4, 0.8, 1.6\}$ radian are considered in the optical link.

However, the 16QAM-based scheme cannot work well when phase-rotation due to the imperfect optical-fiber is not available at the BS. More specifically, Fig. 5.8 shows the performance of both TC-16QAM-SIMO and TC-16StQAM-SIMO schemes when phase rotations of upto $\delta = \{0, 0.2, 0.4, 0.8, 1.6\}$ radian are considered in the optical link. We assume that the CSI of the wireless link is available at the BS for the TC-16QAM-SIMO but the phase-rotation in the optical-fiber link is not available. As seen from Fig. 5.8, the TC-16QAM-SIMO breaks down at $\delta = 0.2$ radian, while the proposed TC-16StQAM-SIMO can still perform very well when $\delta = 0.4$ radian.

Let us investigate the BER performance at the whole cell-edge of Fig. 5.5b in our FFR-

based cellular system. The 3D BER versus SNR performance of the TC-16StQAM-SISO scheme is shown in Fig. 5.9a when SNR = 5 dB. There are 12 BER peaks in Fig. 5.9a, which correspond to all locations of A and B (each 60^o sector has one location A and one location B) in the hexagonal cell.

When two RAs are used to detect the mobile user's signals, the 3D BER performance of the TC-16StQAM-SIMO scheme is depicted in Fig. 5.9b when the same SNR of 5 dB is used. The six BER peaks corresponding to the six locations of B have disappeared thanks to the SIMO scheme. The six BER peaks corresponding to the six locations of A have been reduced, although not completely removed. The BER surface in Fig. 5.9b exhibits a larger low-BER area compared to that in Fig. 5.9a. This signifies that a better uplink transmission quality can be achieved when the SIMO scheme is invoked.

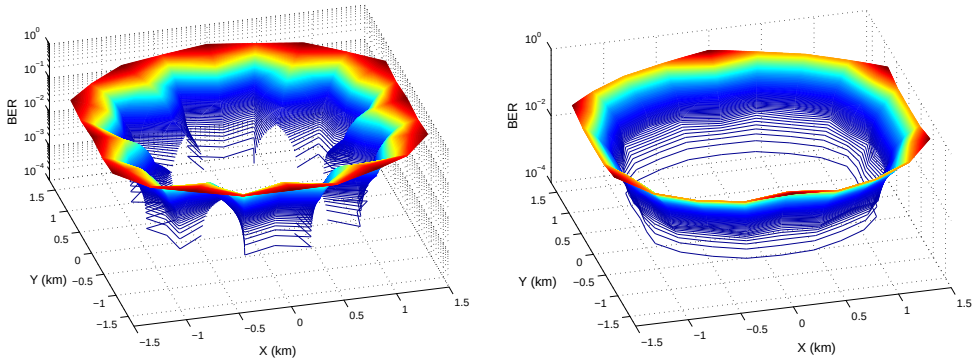

(a) SISO (b) SIMO

Figure 5.9: The 3D BER versus SNR performance of the TC-16StQAM-SISO and SIMO scheme of Fig. 5.5b for transmission over correlated Rayleigh fading and imperfect optical channels for the whole cell with SNR = 5 dB. A phase rotation upto $\delta = 0.1$ radian is considered in the optical link. The simulation parameters are summarised in Table 5.3 and the corresponding cellular structure is shown in Fig. 5.5b, while the transceiver schematic is seen in Fig. 5.6

5.3.5 Summary of Section 5.3

In this contribution, we have investigated the uplink performance of the FFR based multicell multiuser schemes, where cooperative wireless and optical-fiber communication is invoked. We have derived the SIMO-based soft-demodulation for StQAM and found that the proposed TC-StQAM scheme is robust to both wireless and optical-fiber induced channel impairments. More explicitly, the proposed TC-StQAM-SIMO scheme is capable of removing 6 out of 12 BER peaks at the cell-edge, despite not requiring the CSI of both

wireless and optical-fiber links. The proposed TC-StQAM-SIMO is an attractive low-complexity detection candidate for the FFR based multicell multiuser LTE and WiMAX systems.

5.4 Chapter Conclusions

This chapter provided a further study of the DL scheme of Fig. 5.1 and UL DAS/FFR scheme of Fig. 5.5a, as a complement to the DL DAS/FFR study of Chapter 3 and to the UL DAS/FFR investigations of Chapter 4. In Section 5.2, we investigated the effects of imperfect channel knowledge, CSI estimation errors, CSI quantisation errors as well as OFDM signal timing and frequency synchronisation errors on the DL of our DAS/FFR scheme. The received signal model of our DAS/FFR scheme and that of the UFR and FFR based benchmarkers were compared in Section 5.2.1.2, where the above-mentioned different networks result in different levels of received SINR at the MSs as shown in (5.2). In Section 5.2.2, the JSLNR precoding technique [168] was invoked for maximizing the received signal power at the intended MS, whilst simultaneously minimizing the signal power leaked to other MSs. Imperfect channel knowledge was assumed. Our simulation results were portrayed in Fig. 5.2, Fig. 5.3 and Fig. 5.4. Fig. 5.2 shows that the SINR of the FFR scenario is the best at high SNRs, as a benefit of having no MUI and a low CCI arriving from the tier-two cells. It is also seen in Fig. 5.2, that the achievable SINR of our COMP-aided DAS relying on perfect CSI is better than that of the FFR scenario at low SNRs and that increasing the number of quantisation bits is capable of improving the achievable SINRs. The effects of time-offset and frequency-offset are similar to each other, as evidenced by Fig. 5.3 and Fig. 5.4, where the SINR loss of the COMP-aided DAS/FFR scheme is lower than that of the conventional FFR scenario, but higher than that of the Non-COMP aided DAS/FFR scheme and that of the UFR scenario.

Naturally, the assumption of perfect channel knowledge is an idealized simplifying assumption, hence the COMP technique's performance will be degraded in conjunction with imperfect channel knowledge for both the DL and UL. Hence, in Section 5.3 we designed a turbo coded 16-level StQAM scheme for supporting optical-fiber-aided cooperative wireless transmission, where the receiver does not have to estimate the channel state information. In Section 5.3.1, a low-complexity cooperative DAS/FFR scheme was introduced. When a MS is located near the cell-edge, the two nearest RAs can be invoked for detecting and forwarding the user's signal to the base-station, whilst relying on the SIMO principle. In Section 5.3.3, a lower detection complexity was imposed compare to the co-

herently detected schemes, albeit naturally, at a 3 dB power-loss. We also investigated the effects of phase-rotations imposed by imperfect optical-fiber links. Our simulation results of Fig. 5.7 and Fig. 5.8 demonstrated that our non-coherent TC-StQAM scheme is robust to both wireless and optical-fiber imperfections. The BER performance of the entire cell-edge area may be observed in Fig. 5.9b, where the SIMO method exhibits a better uplink transmission quality than the SISO method, as shown in Fig. 5.9a.

Chapter 6

Conclusions of the Thesis

In this concluding chapter, a summary of the thesis and the main findings of our investigations will be presented. This will be followed by a range of ideas on future research.

6.1 Summary and Conclusions

In Chapter 1, we provided a generic overview of the evolution from the UFR based cellular structure of Fig. 1.1a and from the FFR concept of Fig. 1.1b to the DAS aided FFR of Fig. 1.3 and to our pervasive DAS aided FFR scheme of Fig. 1.4. Following a brief historic perspective, in section 1.2 we described the system's architecture in the context of our digital optical fibre aided DAS relying on an FFR scheme in both the DL and UL of Fig. 1.5. Based on this system architecture the central processing algorithms conceived both for the DL and UL of multicell, multiuser scenario will be further studied in the following chapters. Finally, we highlighted both the organization as well as the main findings of this thesis.

In Chapter 2, we briefly compared the two typical optical fibre backhaul techniques, namely the DOF and ROF arrangements shown in Fig. 2.2, since a DAS requires a reliable backhaul. We then focused our attention on the DOF link, which was modelled on the basis of optical pulse propagation theory. In the LTE-advanced standard [91], the backhaul is expected to support high-rate transmission, hence the optical fibre backhaul may no longer be treated as a perfect channel, because the typical imperfections, such as the fibre loss, group-velocity dispersion, nonlinear effects, amplified spontaneous emission and polarization mode dispersion may degrade the overall performance, as highlighted in Section 2.2.2. In Section 2.3.1, we introduced the Shamai-Wyner interference model of two cells relying on an FFR arrangement, as shown in Fig. 2.5, where a DOF link was

used for connecting the BS to a fixed relay. In Section 2.3.2.2 three different interference mitigation techniques (IMT) were considered for reducing the CCI , namely the eigen-beamforming technique, a reduced-power based technique and the hybrid technique of combing both the eigen-beamforming and reduced-power solutions. We demonstrated in Fig. 2.10 that the hybrid technique of combing both the eigen-beamforming and reduced-power arrangements may improve the throughput of the cell-edge MS without reducing that of the cell-center MS, where both the cell-edge and cell-center area are may benefit from a throughput of $2 bits/s/Hz$, if the inter-pulse interference (IPI) level is lower than $0.2W^{1/2}/km$. The performance of the composite channel of a DOF-aided wireless relay system was summarized in Table. 2.2. As a conclusion, the system performance observed in Chapter 2 is summarized in the Table. 6.1.

Table 6.1: Performance characterization of the composite channel of a DOF-aided wireless relay system relying on the topology of Fig. 2.5 and using the system parameters of Table 2.1

Effects of IPI	different levels of IPI
SINR of MS 'a' and 'c'	Fig. 2.8a
Throughput of MS 'a' and 'c'	Fig. 2.11
Effects of four types of IMT	no IPI
SINR of MS 'a' and 'c'	Fig. 2.8b
Throughput of MS 'a' and 'c'	Fig. 2.10

In Chapter 3, we studied the DAS aided FFR scheme in a multiuser, multicell network, where the DL was investigated. The DOF link was modelled by the split-step Fourier method introduced in Section 3.2.2, which is capable of analysing the effects of both dispersion and of the nonlinearity of the optical fibre link on the throughput of the wireless system. The received signal model of both a noncooperative and of a cooperative DAS aided FFR scheme was introduced in Section 3.3 and the Transmit PreProcessing (TPP) was invoked for mitigating the CCI in Section 3.3.2.2. Our simulation results of Fig. 3.9 revealed that the non-cooperative RA aided FFR system may not always lead to an improved throughput in the entire cell-edge area. This performance-limitation is attributable to the 'worst-case direction' problem caused by the intra-cell interference, which was portrayed in the coverage-contours of Fig. 3.9, furthermore, having an increased number of RAs may lead to an increased number of 'worst-case directions', as seen in Fig. 3.9. Hence transmit preprocessing techniques may be invoked for improving the attainable throughput across the entire cellular coverage area, which are capable of achieving a throughput

of $\eta = 5bits/s/Hz$, regardless of the specific geographic distribution of the users. As a further enhancement, in Section 3.4.4 power control (PC) was invoked for the multiuser DL, in order to improve the SIR of the MS, since in interference-limited situations we have $SINR \simeq SIR$. As a result, the throughout of the MSs roaming in the entire cell-edge area becomes $\eta \leq 3bits/s/Hz$, as shown in Fig. 3.13. The performance of the DOF assisted DAS aided FFR system was summarized in Table. 3.6. As a conclusion, the system performance characterized in Chapter 3 may be revisited with the aid of Table. 6.2.

Table 6.2: Performance of characterization of the DOF assisted DAS aided FFR system with relying on the topology of Fig. 3.1 and using the system parameters of Table 3.4

Noncooperative DOF assisted DAS aided FFR scheme	
Typical directions θ_{best}, θ_{worst}, θ_{mid}	Fig. 3.5, Fig. 3.6,Fig. 3.7
Nonlinear effects of the optical fibre	Fig. 3.5
Dispersion effects of the optical fibre	Fig. 3.6
Effects of the numbers of RAs $(6, 12)$	Fig. 3.8, Fig. 3.9
PC technique	Fig. 3.12, Fig. 3.13
Cooperative DOF assisted DAS aided FFR scheme	
Typical directions θ_{best}, θ_{worst}	Fig. 3.10
Nonlinear and linear dispersion effects of the optical fibre	Fig. 3.10
Throughput enhancement across the entire cellular area	Fig. 3.11

In Chapter 4, we investigated a pervasive DAS/FFR architecture operating in a multiuser, multicell network in the context of the UL introduced in Fig. 4.1. The system structure of the pervasive DAS/FFR scheme and of the conventional BS cooperation scheme was introduced in Section. 4.2. The optical fibre soliton technique may invoked for creating a perfect optical fibre backhaul, which is shown in Fig. 4.3. Then the received signal model of our pervasive DAS/FFR scheme was introduced in Section 4.3. In order to increase the achievable diversity gain, the cooperative relaying technique was combined with our pervasive DAS/FFR regime. Different COMP techniques, namely the maximum-likelihood detection scheme of Section 4.3.4.1, the probabilistic data association technique of Section 4.3.4.2 and the MMSE based optimal user ordering aided successive interference cancellation scheme of Section 4.3.6 were invoked for improving the BER performance for the users freely roaming across the entire cell area. The simulation results of Fig. 4.7 demonstrated that the conventional BS cooperation architecture is capable of improving the cell-edge coverage at the cost of having a transmit power of at least $P_t = 30dBm$. Ad-

ditionally, BS-Cooperation increases the complexity by invoking pervasive "knowledge sharing" amongst the BSs. By contrast, observe in Fig. 4.8b that in the proposed pervasive DAS/FFR system of Section 4.3.4.2, the MSs roaming across the entire cell area are capable of achieving a reduced BER, despite operating at a reduced transmit power of $P_t \leq 20dBm$. When the CPDA MUD of Section 4.3.5 was invoked by the MR aided pervasive DAS/FFR architecture, Fig. 4.13 demonstrated that it was capable of substantially reducing the BER for the MSs roaming freely at arbitrary positions, especially in the 'worst-case direction'. Observe in Fig. 4.13 that $70\% \sim 80\%$ of the cellular coverage area exhibits BERs lower than 10^{-4}, when the transmit power of $P_t = 20dBm$ was allocated. On the other hand, in Section 4.4.5 PC was invoked for our multiuser UL scenario to improve the SIR of the MS. Observe in Fig. 4.15 that the MSs operating without the assistance of MRs had a BER below 10^{-3}. By contrast, the MSs roaming in the "problem area" of in the "worst-case directions" had a BER of $\leq 10^{-2}$, as shown in Fig. 4.15. The performance of our pervasive DAS/FFR system was summarized in Table. 4.5. As a conclusion, the system performance observed in Chapter 4 is characterized in the Table. 6.3.

Table 6.3: BER performance characterization of the pervasive DAS aided FFR system relying on the topology of Fig. 4.1 and the system parameters of Table 4.3

Conventional BS Cooperation	MMSE-OSIC, Joint-ML, PDA and CPDA MUD techniques
Effects of transmitted power	Fig. 4.7
Pervasive DAS/FFR	the MMSE-OSIC, Joint-ML PDA, CPDA MUD
Effects of transmitted power in θ_{best}	Fig. 4.8
In typical directions θ_{best}, θ_{worst}, θ_{mid}	Fig. 4.8, Fig. 4.9
MR Selection	Fig. 4.10
Analyses across the entire cellular area	Fig. 4.12, Fig. 4.13
Effects of PC	Fig. 4.14, Fig. 4.15

In Chapter 5, we further studied the DL and UL of our DAS/FFR scheme in practical application scenarios. Specifically, in the case of the DAS/FFR DL, we investigated the effects of imperfect channel estimation errors, CSI quantisation errors as well as OFDM signal timing and frequency synchronisation errors in Section 5.2.2. These results were provided in Figures 5.2, 5.3 and 5.4. Similarly, in Section 5.3 we demonstrated for the COMP technique that its performance will be degraded by imperfect channel knowledge for both the DL and UL. As a design alternative, we conceived a turbo coded 16-level

StQAM scheme for supporting non-coherent detection assisted optical-fiber-aided cooperative wireless transmissions, where the receiver does not have to estimate the channel state information. This scheme was characterized in Fig. 5.6.

In conclusion, the benefit of the proposed DAS aided FFR assisted by the proposed optical fibre backhaul architecture is that of substantially increasing the SINR for both the DL and the UL as demonstrated in Chapter 3 and Chapter 4, respectively. In Section 3.4.4 and Section 4.4.5, we use a normalized SIR model. Since the multiuser, multicell scenario is interference-limited, where we have $SINR \simeq SIR$ as justified in Section 3.4.4, the $SIR(dB)$ model is useful for the comparsion of different network architectures, as observed in Figures 6.1, 6.2, 6.3 and 6.4. Based on these figures we may infer the following conclusions:

1. The conventional UFR architecture of Fig. 6.1a only has a high SIR, when the user is roaming close to the BS, which decays to $[-10 \sim 0dB]$ in the cell-edge area. By contrast, the SIR of the conventional FFR architecture shown in Fig. 6.1b was improved in the cell-edge area to about $[0 \sim 10dB]$.

2. Fig. 6.2 characterizes the SIR distribution of the DAS aided FFR architecture in the DL scenario, which is based on the topology shown in Fig. 3.1. When observing the cell-edge area, a high SIR is achieved for the users roaming in the vicinity of the RA, as shown in Fig. 6.2a. However, the SIR still remains as low as $-10dB$ in the angle halfway between two adjacent RAs, which is caused by the "worst-case direction" problem introduced in Section 2.3.3.

3. The difference between Fig. 6.2a and Fig. 6.2b is that in the former we only take into account the interfering RAs in the reference cell, while in the latter we additionally considered the interfering RAs of the second-tier cells, which operate at the same frequency. Nonetheless, the SIR performances observed in Fig. 6.2a and Fig. 6.2b are almost the same, because the interference imposed by the second-tier cells was significantly reduced by the combined effects of the DAS and FFR technique. Hence it is a reasonable approximation to focus our attention on the reference cell only, when we calculate the effects of the interference in the DAS aided FFR architecture.

4. Fig. 6.3 characterizes the SIR performance of the DAS aided FFR relying on 12 RAs, where the SIR of the cell-edge area is reduced to about $40dB$, when the users are roaming quite close to the RAs. This SIR is higher than that of the conventional UFR and FFR architecture, but lower than that of the DAS aided FFR employing 6 RAs. Hence, increasing the number of RAs leads to increasing the interference,

which results in a reduced SIR and to an increased number of "worst-case" directions, where the SIR may become as low as $-10dB$ in the angle halfway between two adjacent RAs. Similarly to the case of Fig. 6.2a and Fig. 6.2b, the difference between Fig. 6.3a and Fig. 6.3b is that we only consider the interfering RAs in the reference cell in Fig. 6.3a, but also count the interfering RAs of the second-tier cells in Fig. 6.3b which operate at the same frequency. Observe that the SIR performance seen in Fig. 6.3a and Fig. 6.3b is similar, suggesting that increasing the number of interferers does not lead to a reduced SIR in the context of Eq.(3.20). The reason for this observation is that the SIR_i reduction imposed by the second-tier cells may be neglected by combining the beneficial effects of the DAS and FFR techniques.

5. Fig. 6.4 compares the SIR performance of the conventional BS cooperation and of our pervasive DAS aided FFR, where a maximum SIR of $20dB$ is reached, when the users are roaming quite close to the BS, while the cell-edge SIR is in the range of $[-20 \sim -10dB]$, as shown in Fig. 6.4a. When using our pervasive DAS aided FFR architecture, the SIR may reach $40dB$ in the cell-center area, when the user is roaming quite close to the RAs, as shown in Fig. 6.4b. The "worst-case direction" problem of the DL scenario also persists in the UL scenario, when the user is roaming close to the angle halfway between two adjacent RAs, where the SIR is reduced to $-20dB$.

6.2 Suggestions for Future Work

We conclude by suggesting the following future research problems:

1. We adopted an optical fiber link as backhaul for the communications network considered, which is capable of providing a high capacity at a high cost. Hence, promising alternative may be to consider the other backhaul techniques, such as a free-space optical or a microwave radio backhaul [90]. More explicitly, the free-space optical backhaul constitutes a line-of-sight technology using invisible beams of light to provide optical connections. Hence it does not require fiber optic cable. A microwave radio backhaul may also be employed cost-effectively. Hence, free-space optical and microwave radio backhauls may be considered for our DAS aided FFR scheme.

2. It was demonstrated that the DAS technique has the benefit of increasing the coverage area, despite reducing the transmission power which is an advantage of central

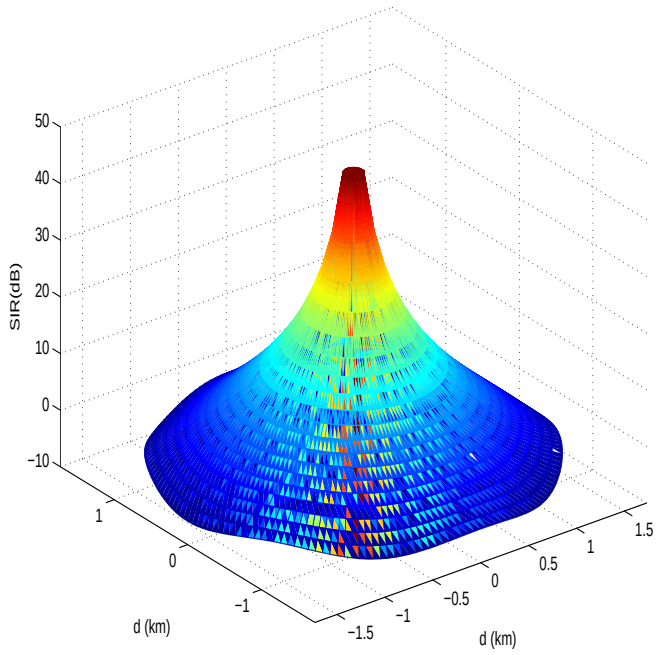

(a) Conventional UFR of Fig. 1.1a

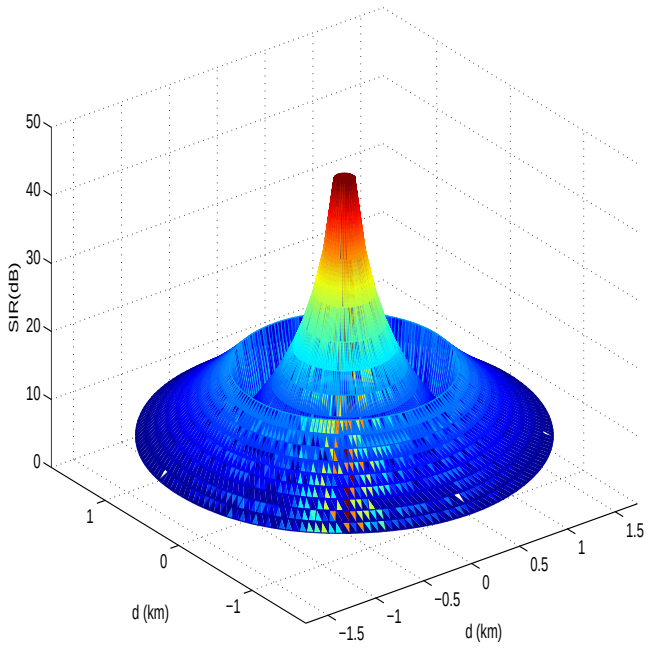

(b) FFR of Fig. 1.1b

Figure 6.1: Simulated average SIR (dB) profile of a hexagonal cell in the DL, when employing conventional UFR, and the FFR regime introduced in Fig. 1.1 a two-tier structure of nineteen cells.

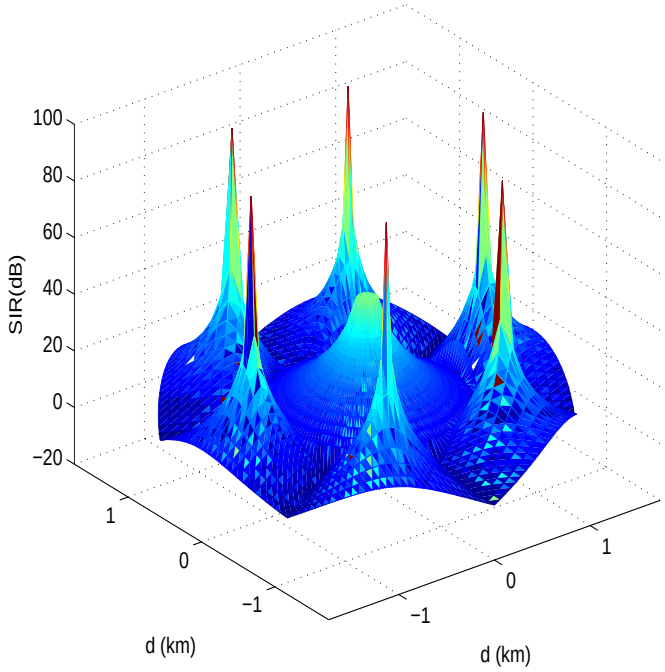

(a) DAS aided FFR with 6 RAs, interference arrives only from the reference cell, as seen in Fig. 3.1

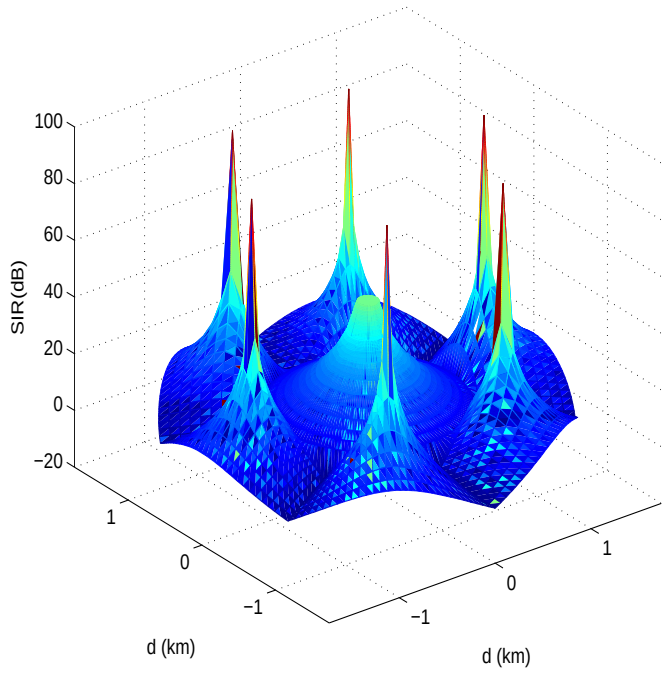

(b) DAS aided FFR with 6 RAs, interference arrives from both the reference cell and the second-tier, as seen in Fig. 3.1

Figure 6.2: Simulated average SIR (dB) profile of a hexagonal cell of the DL, employing DAS aided FFR architecture proposed in Chapter 3 which is in a two-tier structure of nineteen cells, as seen in Fig. 3.1 employing 6 RAs. In Fig. 6.2a, the interference arrives only from the reference cell, while in Fig. 6.2b, the interference arrives from both the reference cell and the second-tier.

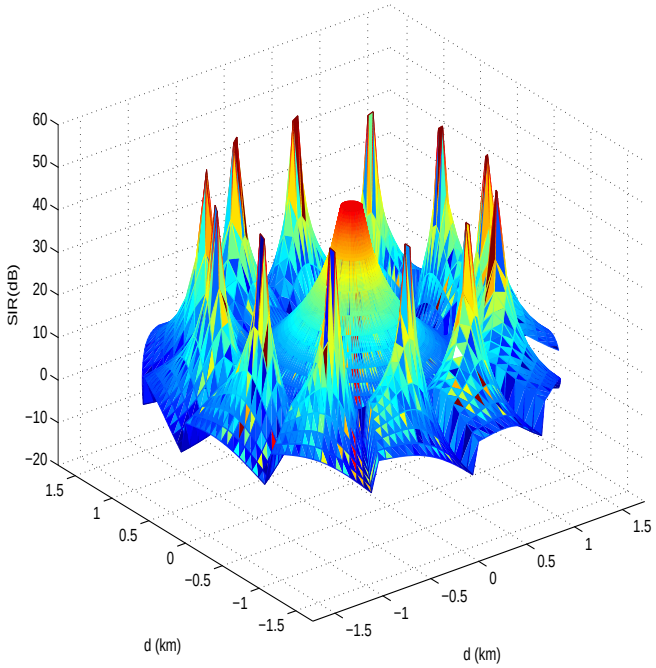

(a) DAS aided FFR with 12 RAs, interference arrives only from the reference cell, as seen in Fig. 3.1

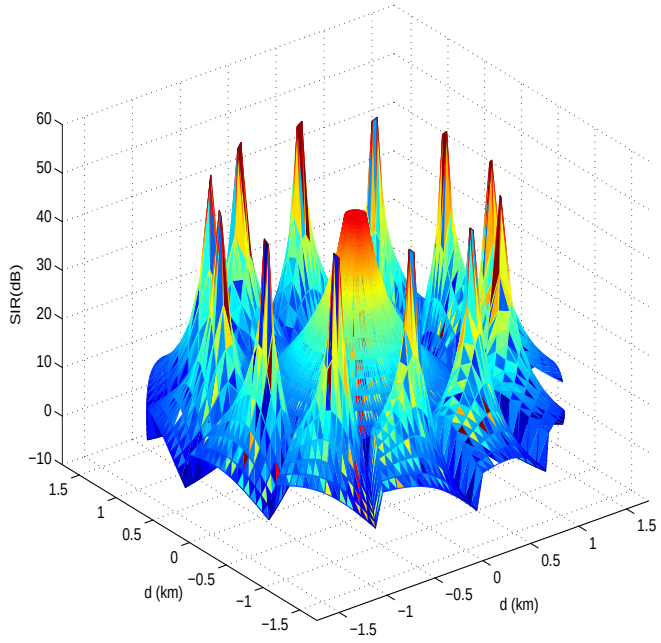

(b) DAS aided FFR with 12 RAs, interference arrives from both the reference cell and the second-tier, as seen in Fig. 3.1

Figure 6.3: Simulated average SIR (dB) profile of a hexagonal cell of the DL, employing DAS aided FFR architecture proposed in Chapter 3 which is in a two-tier structure of nineteen cells as seen in Fig. 3.1 where $RA = 12$. In Fig. 6.3a, the interference arrives only from the reference cell, while in Fig. 6.3b, the interference arrives from both the reference cell and the second-tier.

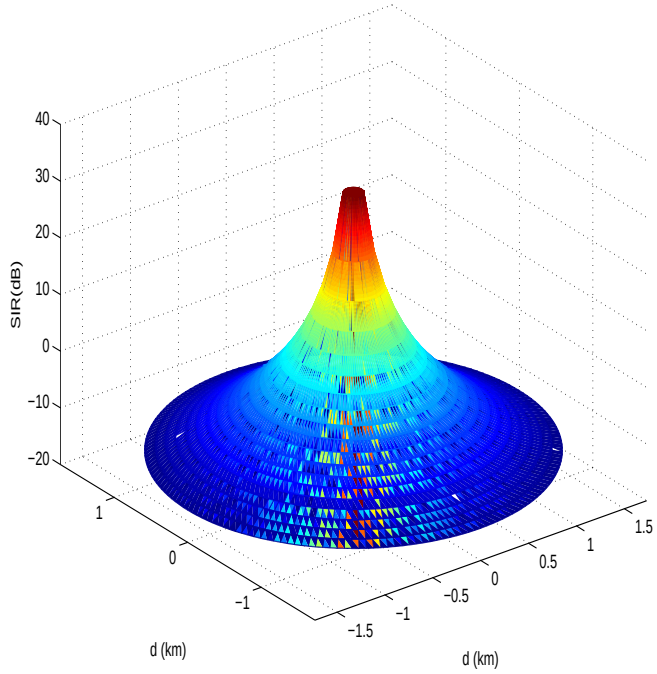

(a) Conventional BS cooperation of Fig. 4.2

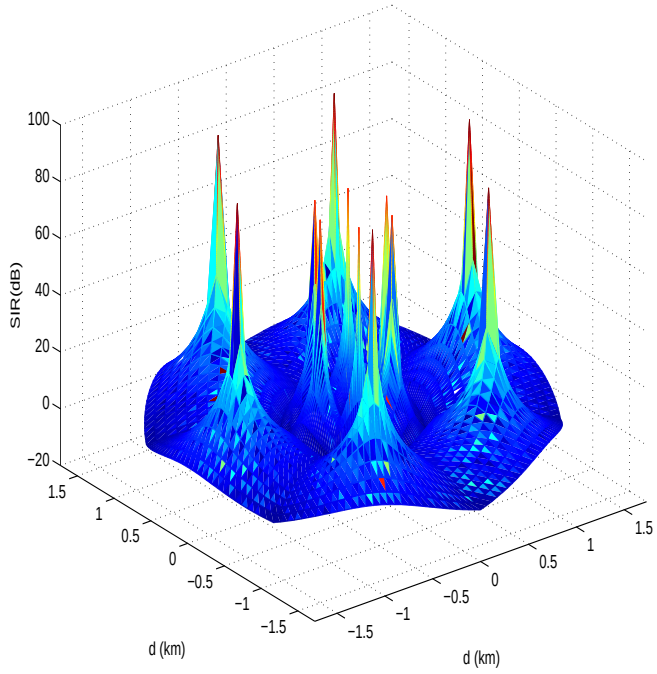

(b) Pervasive DAS aided FFR of Fig. 4.1

Figure 6.4: Simulated average SIR (dB) profile of a hexagonal cell of the UL, employing BS cooperation across 3 adjacent BSs, where 6 centralized antennas are employed at BS and 6 MSs randomly roaming across the entire cell area, as shown in Fig. 4.2. Furthermore, our pervasive DAS aided FFR architecture is also characterized, where 6 distributed antennas are employed and 6 MSs randomly roam in both the cell-center and cell-edge area of a two-tier structure of nineteen cells as seen in Fig. 4.1.

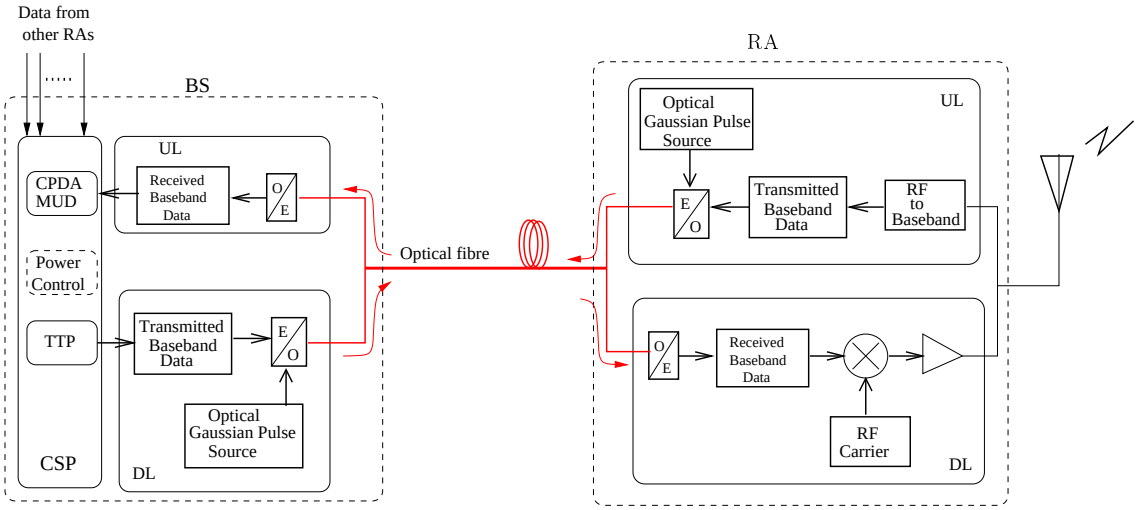

Figure 6.5: The system structure of the DOF link designed for the DAS aided FFR architecture, which invokes a power control scheme in the CSP at the BS.

processing. The distributed antenna concept may be further refined with the aid of the ultimate distributed source constituted by leaky feeders [174].

3. Mobile relaying is also capable of achieving a beneficial diversity gain, which substantially improves the performance of our pervasive DAS/FFR across the entire cellular area. In Chapter 4, we only invoked a simple Amplify-Forward (AF) relay and assumed perfect relaying. This work may be further developed to Decode-Forward (DF) relaying, by optimizing the relay selection strategy and by using more powerful forward error correction (FEC) codes.

4. In order to reduce the CCI of the DAS aided FFR architecture, we invoked the TPP technique for the DL scenario in Section 3.3.2.2 and the strategy of CPDA MUD for the UL scenario in Chapter 4 based on the system structure of Fig. 6.5, while assuming that the desired signal and the interferers have the same transmit power. Hence, the SIR was formulated in Eq. (3.20). However, the DAS aided FFR architecture operating in a multicell, multiuser scenario is an interference-limited system [142], hence the SIR calculated by Eq. (3.20) is related to both the distance and also to the transmit power of both the signal and of the interferer, when they are allocated different transmit powers by the power-control (PC). Hence, for example the BER-based power control algorithm of [142] may be invoked for achieving a balanced Quality of Service (QoS) across the entire cell. Naturally, using accurate and prompt PC for supporting a multiplicity of active users in the multiuser, multicell scenario considered imposes a potentially high complexity on the BS. The authors of [175] proposed a power control strategy for the UL of a multicell wire-

less system, but only supported a single active user per time instant. The prior work disseminated in [176] [177] [178] introduced the concepts of *game theory* for solving the PC problem for a multiplicity of active users. In these PC games, the users are modeled as players having individual goals and strategies. They are competing or cooperating with each other, until they agree on an acceptable resource allocation outcome. Existing research can be categorized into two types, non-cooperative games [177] [179] [180] and cooperative games [181] [182] [183]. Hence, an attractive research area is that of using *game theory* for designing a PC strategy for the DAS aided FFR architecture operating in a multiuser, multicell scenario, as shown in the system structure of Fig. 6.5.

5. Although we opted for invoking the DOF link of Fig. 2.2a for the backhaul of our pervasive DAS/FFR scheme, a study comparing the DOF and ROF is also of interest. On the other hand, the quality of the optical backhaul plays an important role in determining the quality of the entire DAS scheme. The Silicon Photonics Group in Southampton successfully demonstrated the feasibility of the integrated silicon-photonics based transceiver seen in Fig. 6.6, which is capable of operating at $10Gb/s$, whilst a $20Gb/s$ version is under construction. This demonstrates the successful integration of all the photonic and electronic components within a silicon die. The next challenge may be to additionally incorporate a wireless transceiver within the same silicon die. since the transmitted signal stream is typically digital [184] [185], using the DOF technique is appropriate for the backhaul of a DAS aided communication network, where the backhaul is extended to the RAs. Nonetheless, the ROF technique [186] [187] may be used for reducing the complexity and cost of RAs. Hence, both the DOF and ROF technique may remain attractive for years to come in diverse applications.

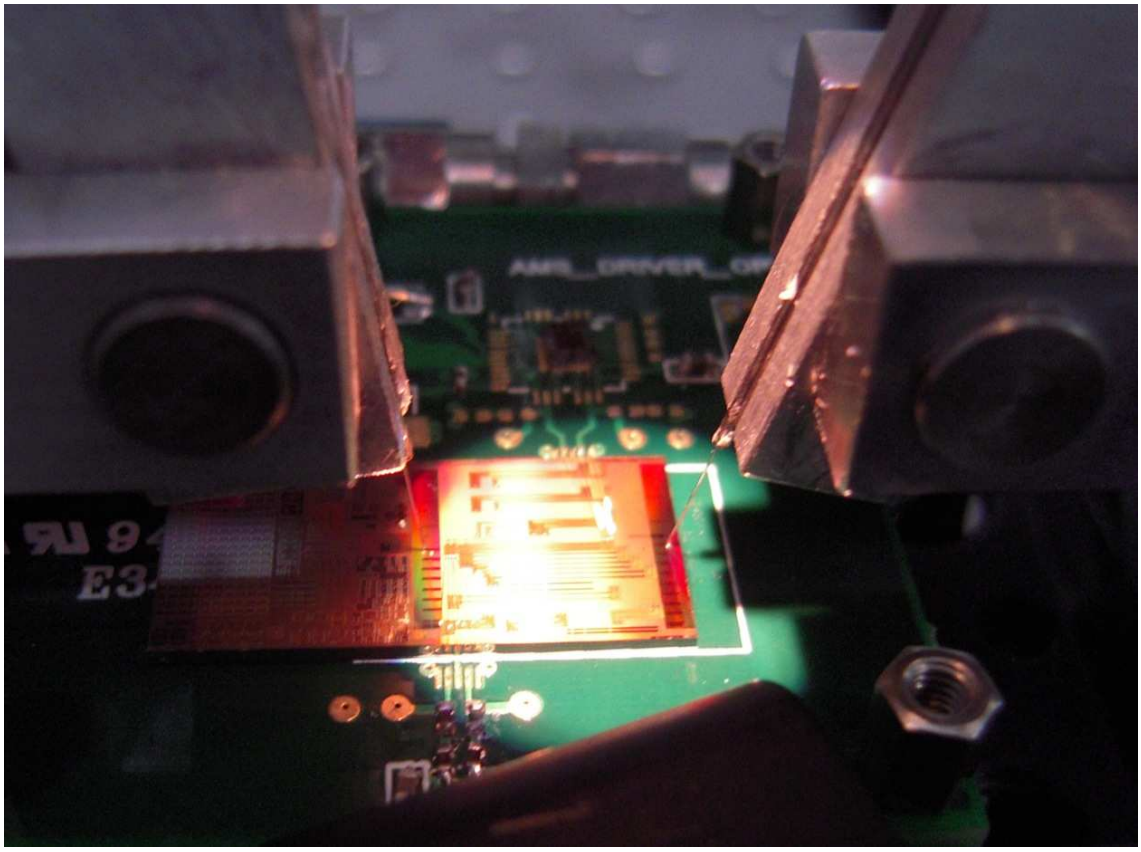

Figure 6.6: The Silicon Photonics Group in Southampton successfully created a silicon-photonics based transceiver operating at 10Gb/s within a single silicon die.

Appendix A

Split-Step Fourier Method

The matlab code of simulating pulse propagation along the imperfect optical fibre in order to analyze both the linear dispersion and nonlinearity effects in Section 3.2.2, where the SSF method is invoked to solve the NLS equation.

```
    ln =1;
i =sqrt(-1);
Po=0.00064;
alpha=0;
alph=alpha/(4.343);
gamma=0.003;
to=125e-12;
C=-2;
b2=-20e-27;
Ld=(to^2)/(abs(b2));
pi=3.1415926535;
Ao=sqrt(Po);
tau =- 4096e-12:1e-12: 4095e-12;
dt=1e-12;
rel_error = 1e - 5;
h=1000;
for
ii=0.1:0.1:1.5
z=ii*Ld;
u = Ao * exp(-((1 + i * (-C))/2) * (tau/to).^2);
```

```
l=max(size(u));
fwhm1 = find(abs(u) > abs(max(u)/2));
fwhm1=length(fwhm1);
dw=1/l/dt*2*pi;
w=(-1*l/2:1:l/2-1)*dw;
u=fftshift(u);
w=fftshift(w);
spectrum=fft(fftshift(u));
for jj=h:h:z
spectrum = spectrum.*exp(-alph*(h/2)+i*b2/2*w.^2*(h/2));
f=ifft(spectrum);
f = f.*exp(i*gamma*((abs(f)).^2)*(h));
spectrum=fft(f);
spectrum = spectrum.*exp(-alph*(h/2)+i*b2/2*w.^2*(h/2));
end
f=ifft(spectrum);
op_pulse(ln,:) = abs(f);
fwhm = find(abs(f) > abs(max(f)/2));
fwhm=length(fwhm);
ratio=fwhm/fwhm1;
pbratio(ln)=ratio;
dd=atand((abs(imag(f)))/(abs(real(f))));
phadisp(ln)=dd;
ln=ln+1;
end
```

Appendix B

Fibre Soliton

The matlab code of simulating fiber soliton propagation which may be invoked as a perfect optical fiber backhaul in Section 4.2.1.3.

```
    ln =1;
i =sqrt(-1);
Po=0.00064;
alpha=0;
alph=alpha/(4.343);
gamma=0.003;
to=125e-12;
C=-2;
b2=-20e-27;
Ld=(to^2)/(abs(b2));
pi=3.1415926535;
Ao=sqrt(Po);
tau =- 4096e-12:1e-12: 4095e-12;
dt=1e-12;
rel_error = 1e - 5;
h=1000;
for
ii=0.1:0.1:1.5
z=ii*Ld;
u = Ao * exp(-((1 + i * (-C))/2) * (tau/to).^2);
l=max(size(u));
```

$fwhm1 = find(abs(u) > abs(max(u)/2));$

fwhm1=length(fwhm1);

dw=1/l/dt*2*pi;

w=(-1*l/2:1:l/2-1)*dw;

u=fftshift(u);

w=fftshift(w);

spectrum=fft(fftshift(u));

for jj=h:h:z

$spectrum = spectrum.*exp(-alph*(h/2)+i*b2/2*w.^2*(h/2));$

f=ifft(spectrum);

$f = f.*exp(i*gamma*((abs(f)).^2)*(h));$

spectrum=fft(f);

$spectrum = spectrum.*exp(-alph*(h/2)+i*b2/2*w.^2*(h/2));$

end

f=ifft(spectrum);

$op_{pulse}(ln,:) = abs(f);$

$fwhm = find(abs(f) > abs(max(f)/2));$

fwhm=length(fwhm);

ratio=fwhm/fwhm1;

pbratio(ln)=ratio;

dd=atand((abs(imag(f)))/(abs(real(f))));

phadisp(ln)=dd;

ln=ln+1;

end

Bibliography

[1] 3GPP TSG-RAN, “Futher Advancements for E-UTRA; Physical Layer Aspects,” tech. rep., 3GPP Std. TR 36.814 v.0.4.1, 2009.

[2] IEEE 802.16m, “System Requirements Document (SDD),” tech. rep., IEEE 802.16m-09/0002r10, Jan. 2011.

[3] IEEE 802.16m, “Evaluation Methodology (EMD),” tech. rep., IEEE 802.16m-09-0004r5, 2009.

[4] IEEE P802.16m/D4, “Advanced Air Interface,” tech. rep., IEEE, Feb. 2010.

[5] N. Himayat, S. Talwar, A. Rao, and R. Soni, “Interference management for 4G cellular standards,” *IEEE Communications Magazine*, vol. 48, pp. 86–9, Aug. 2010.

[6] R. Ghaffar and R. Knopp, “Interference suppression strategy for cell-edge users in the downlink,” *IEEE Transactions on Wireless Communications*, vol. 11, pp. 154–165, Jan. 2012.

[7] T. Novlan, R. Ganti, A. Ghosh, and J. Andrews, “Analytical evaluation of fractional frequency reuse for heterogeneous cellular networks,” *IEEE Transactions on Communications*, vol. 60, pp. 2029–2039, Jul. 2012.

[8] R. Giuliano, C. Monti, and P. Loreti, “WiMAX fractional frequency reuse for rural environments,” *IEEE Transactions on Wireless Communications*, vol. 15, pp. 60–65, Jun. 2008.

[9] S. Parkvall, A. Furuskar, and E. Dahlman, “Evolution of LTE toward IMT-advanced,” *IEEE Communications Magazine*, vol. 49, pp. 84–91, Feb. 2011.

[10] M. Baker, “From LTE-advanced to the future,” *IEEE Communications Magazine*, vol. 50, pp. 116–120, Feb. 2012.

[11] K. Kerpez, "A radio access system with distributed antennas," *IEEE Transactions on Vehicular Technology*, vol. 45, pp. 265–275, May 1996.

[12] S. Sun, Q. Gao, Y. Peng, Y. Wang, and L. Song, "Interference management through CoMP in 3GPP LTE-advanced networks," *IEEE Wireless Communications*, vol. 20, pp. 59–66, Feb. 2012.

[13] O. Simeone, O. Somekh, Y. Bar-Ness, and U. Spagnolini, "Uplink throughput of TDMA cellular systems with multicell processing and amplify-and-forward cooperation between mobiles," *IEEE Transactions on Wireless Communications*, vol. 6, pp. 942–2951, 2007.

[14] M. Sawahashi, Y. Kishiyama, A. Morimoto, D. Nishikawa, and M. Tanno, "Coordinated multipoint transmission/reception techniques for LTE-advanced [coordinated and distributed MIMO]," *IEEE Wireless Communications*, vol. 17, pp. 26–34, Jun. 2010.

[15] N. Krishnan, R. Yates, N. Mandayam, and J. Panchal, "Bandwidth sharing for relaying in cellular systems," *IEEE Transactions on Wireless Communications*, vol. 11, pp. 117–129, Jan. 2012.

[16] I. Stiakogiannakis, G. Athanasiadou, G. Tsoulos, and D. Kaklamani, "Performance analysis of fractional frequency reuse for multi-cell WiMAX networks based on site-specific propagation modeling," *IEEE Antennas and Propagation Magazine*, vol. 54, pp. 214–226, Feb. 2012.

[17] T. Novlan, J. Andrews, I. Sohn, R. Ganti, and A. Ghosh, "Comparison of fractional frequency reuse approaches in the OFDMA cellular downlink," in *IEEE Global Telecommunications Conference (GLOBECOM)*, pp. 1–5, Dec. 2010.

[18] M. Frullone, G. Riva, P. Grazioso, and G. Falciasecca, "Advanced planning criteria for cellular systems," *IEEE Personal Communications*, vol. 3, pp. 10–15, Dec. 1996.

[19] P. Cardieri and T. Rappaport, "Application of narrow-beam antennas and fractional loading factor in cellular communication systems," *IEEE Transactions on Vehicular Technology*, vol. 50, pp. 430–440, Mar. 2001.

[20] K. Begain, G. Rozsa, A. Pfening, and M. Telek, "Performance analysis of GSM networks with intelligent underlay-overlay," in *Seventh International Symposium on Proceedings of Computers and Communications (ISCC).*, pp. 135–141, 2002.

[21] M. Sternad, T. Ottosson, A. Ahlen, and A. Svensson, "Attaining both coverage and high spectral efficiency with adaptive OFDM downlinks," in *Vehicular Technology Conference (VTC) Fall. 2003 IEEE 58th*, vol. 4, pp. 2486–2490, 2003.

[22] J. Chang, J. Heo, and W. Sung, "Cooperative interference mitigation using fractional frequency reuse and intercell spatial demultiplexing," *Journal of Communications and Networks*, vol. 10, pp. 127–136, Jun. 2008.

[23] V. Chandrasekhar and J. Andrews, "Spectrum allocation in tiered cellular networks," *IEEE Transactions on Communications*, vol. 57, pp. 3059–3068, Oct. 2009.

[24] X. Xu, R. Zhang, and L. Hanzo, "Imperfect digital fibre optic link based cooperative distributed antennas with fractional frequency reuse in multicell multiuser networks," *IEEE Transactions on Vehicular Technology*, vol. 60, pp. 4439–4449, Nov. 2011.

[25] Z. Xu, G. Li, C. Yang, and X. Zhu, "Throughput and optimal threshold for FFR schemes in OFDMA cellular networks," *Wireless Communications, IEEE Transactions on*, vol. 11, pp. 2776–2785, Aug. 2012.

[26] T. Novlan and J. Andrews, "Analytical evaluation of uplink fractional frequency reuse," *IEEE Transactions on Communications*, no. 99, pp. 1–11, 2013.

[27] K. Kerpez, "A radio access system with distributed antennas," *IEEE Transactions on Vehicular Technology*, vol. 45, pp. 265–275, May 1996.

[28] J. Zhang and J. Andrews, "Distributed antenna systems with randomness," *IEEE Transactions on Wireless Communications*, vol. 7, pp. 3636–3646, Sep. 2008.

[29] D. Castanheira and A. Gameiro, "Distributed antenna system capacity scaling [coordinated and distributed MIMO]," *IEEE Transactions on Wireless Communications*, vol. 17, no. 3, pp. 68–75, 2010.

[30] J. Park, E. Song, and W. Sung, "Capacity analysis for distributed antenna systems using cooperative transmission schemes in fading channels," *IEEE Transactions on Wireless Communications*, vol. 8, pp. 586–592, Feb. 2009.

[31] A. A. Saleh, A. Rustako, and R. Roman, "Distributed antennas for indoor radio communications," *IEEE Transactions on Communications*, vol. 35, pp. 1245–1251, Dec. 1987.

[32] H. Zhuang, L. Dai, L. Xiao, and Y. Yao, "Spectral efficiency of distributed antenna system with random antenna layout," *Electronics Letters*, vol. 39, pp. 495–496, Mar. 2003.

[33] L. Dai, S. Zhou, and Y. Yao, "Capacity analysis in CDMA distributed antenna systems," *IEEE Transactions on Wireless Communications*, vol. 4, no. 6, pp. 2613–2620, 2005.

[34] S. Han, S. Zhou, J. Wang, and W. Park, "Transmit antenna selection with power and rate allocation for spatial multiplexing in distributed antenna systems," *Tsinghua Science and Technology*, vol. 11, pp. 259–263, Jun. 2006.

[35] W. Choi and J. Andrews, "Downlink performance and capacity of distributed antenna systems in a multicell environment," *IEEE Transactions on Wireless Communications*, vol. 6, pp. 69–73, Jan. 2007.

[36] D. Wake, A. Nkansah, and N. J. Gomes, "Radio over fiber link design for next generation wireless systems," *Journal of Lightwave Technology*, vol. 28, pp. 2456–2464, 2010.

[37] E. Park, S.-R. Lee, and I. Lee, "Antenna placement optimization for distributed antenna systems," *IEEE Transactions on Wireless Communications*, vol. 11, pp. 2468–2477, Jul. 2012.

[38] A. Ozgur, O. Leveque, and D. Tse, "Spatial degrees of freedom of large distributed mimo systems and wireless ad hoc networks," *IEEE Journal on Selected Areas in Communications*, vol. 31, pp. 202–214, Feb. 2013.

[39] X. Xu, R. Zhang, and L. Hanzo, "Imperfect radio-over-fibre aided cooperative distributed antennas with fractional frequency reuse," in *Proc. of IEEE Vehicular Technology Conference (VTC)*, (Ottawa, Canada), pp. 1–5, September 2010.

[40] J. Lee, Y. Kim, H. Lee, B. L. Ng, D. Mazzarese, J. Liu, W. Xiao, and Y. Zhou, "Coordinated multipoint transmission and reception in lte-advanced systems," *IEEE Communications Magazine*, vol. 50, pp. 44–50, Nov. 2012.

[41] C. Yang, S. Han, X. Hou, and A. Molisch, "How do we design CoMP to achieve its promised potential ?," *IEEE Wireless Communications*, vol. 20, pp. 67–74, Feb. 2013.

[42] C.-B. Chae, D. Mazzarese, T. Inoue, and R. Heath, "Coordinated beamforming for the multiuser MIMO broadcast channel with limited feedforward," *IEEE Transactions on Signal Processing*, vol. 56, pp. 6044–6056, Dec. 2008.

[43] L. Venturino, N. Prasad, and X. Wang, "Coordinated linear beamforming in downlink multi-cell wireless networks," *IEEE Transactions on Wireless Communications*, vol. 9, pp. 1451–1461, Apr. 2010.

[44] I. Koutsopoulos and L. Tassiulas, "Joint optimal access point selection and channel assignment in wireless networks," *IEEE/ACM Transactions on Networking*, vol. 15, pp. 521–532, Jun. 2007.

[45] M. Feng, X. She, L. Chen, and Y. Kishiyama, "Enhanced dynamic cell selection with muting scheme for dl comp in lte-a," in *Vehicular Technology Conference (VTC 2010-Spring), 2010 IEEE 71st*, pp. 1–5, May 2010.

[46] D. Ben Cheikh, J.-M. Kelif, M. Coupechoux, and P. Godlewski, "Analytical joint processing multi-point cooperation performance in rayleigh fading," *IEEE Wireless Communications Letters*, vol. 1, pp. 272–275, Aug. 2012.

[47] X. Tao, X. Xu, and Q. Cui, "An overview of cooperative communications," *IEEE Communications Magazine*, vol. 50, pp. 65–71, Jun. 2012.

[48] F. Yuan and C. Yang, "Bit allocation between per-cell codebook and phase ambiguity quantization for limited feedback coordinated multi-point transmission systems," *IEEE Transactions on Communications*, vol. 60, pp. 2546–2559, Sep. 2012.

[49] L. Choi and R. Murch, "A transmit preprocessing technique for multiuser MIMO systems using a decomposition approach," *IEEE Transactions on Wireless Communications*, vol. 3, pp. 20–24, Jan. 2004.

[50] W. Zhang, S. Vedantam, and U. Mitra, "Joint transmission and state estimation: A constrained channel coding approach," *IEEE Transactions on Information Theory*, vol. 57, pp. 7084–7095, Oct. 2011.

[51] S. Moshavi, "Multi-user detection for DS-CDMA communications," *IEEE Communications Magazine*, vol. 34, no. 10, pp. 124–136, 1996.

[52] L. Wei and H. Qi, "Near-optimal limited-search detection on ISI/CDMA channels and decoding of long convolutional codes," *IEEE Transactions on Information Theory*, vol. 46, pp. 1459–1482, Jul. 2000.

[53] J. Luo, K. Pattipati, P. Willett, and F. Hasegawa, "Near-optimal multiuser detection in synchronous cdma using probabilistic data association," *Communications Letters, IEEE*, vol. 5, pp. 361–363, Sep. 2001.

[54] D. Pham, K. Pattipati, P. Willett, and J. Luo, "A generalized probabilistic data association detector for multiple antenna systems," *IEEE Communications Letters*, vol. 8, pp. 205–207, Apr. 2004.

[55] H. Poor and S. Verdu, "Probability of error in MMSE multiuser detection," *IEEE Transactions on Information Theory*, vol. 43, pp. 858–871, May 1997.

[56] D. Tse and S. Hanly, "Linear multiuser receivers: effective interference, effective bandwidth and user capacity," *IEEE Transactions on Information Theory*, vol. 45, no. 2, pp. 641–657, 1999.

[57] P. Marsch and G. Fettweis, "Uplink CoMP under a constrained backhaul and imperfect channel knowledge," *IEEE Transactions on Wireless Communications*, vol. 10, pp. 1730–1742, Jun. 2011.

[58] S. Yang, T. Lv, G. R. Maunder, and L. Hanzo, "Distributed probabilistic data association based soft reception employing base station cooperation in MIMO-aided multi-user multi-cell systems," *IEEE Transactions on Vehicular Technology*, vol. 60, Sept. 2011.

[59] M. Meurer, H. Troger, T. Weber, and P. Baier, "Synthesis of joint detection and joint transmission in CDMA downlinks," *Electronics Letters*, vol. 37, pp. 919–920, Jul. 2001.

[60] M. Sawahashi, Y. Kishiyama, A. Morimoto, D. Nishikawa, and M. Tanno, "Coordinated multipoint transmission/reception techniques for LTE-advanced [coordinated and distributed MIMO]," *IEEE Wireless Communications*, vol. 17, pp. 26–34, Jun. 2010.

[61] A. Papadogiannis, H. Bang, D. Gesbert, and E. Hardouin, "Efficient selective feedback design for multicell cooperative networks," *IEEE Transactions on Vehicular Technology*, vol. 60, pp. 196–205, Jan. 2011.

[62] V. Annapureddy, A. El Gamal, and V. Veeravalli, "Degrees of freedom of interference channels with comp transmission and reception," *IEEE Transactions on Information Theory*, vol. 58, pp. 5740–5760, Sep. 2012.

[63] O. Tipmongkolsilp, S. Zaghloul, and A. Jukan, "The evolution of cellular backhaul technologies: Current issues and future trends," *IEEE Communications Surveys Tutorials*, vol. 13, pp. 97–113, Sep. 2011.

[64] S. Chia, M. Gasparroni, and P. Brick, "The next challenge for cellular networks: backhaul," *IEEE Microwave Magazine*, vol. 10, pp. 54–66, Aug. 2009.

[65] J. Salehi, "Code division multiple-access techniques in optical fiber networks. I. fundamental principles," *IEEE Transactions on Communications*, vol. 37, pp. 824–833, Aug. 1989.

[66] J. Salehi and C. Brackett, "Code division multiple-access techniques in optical fiber networks. II. systems performance analysis," *IEEE Transactions on Communications*, vol. 37, pp. 834–842, Aug. 1989.

[67] C. Brackett, "Dense wavelength division multiplexing networks: principles and applications," *IEEE Journal on Selected Areas in Communications*, vol. 8, pp. 948–964, Aug. 1990.

[68] R. Barry, V. W. S. Chan, K. Hall, E. Kintzer, J. Moores, K. Rauschenbach, E. Swanson, L. Adams, C. Doerr, S. Finn, H. Haus, E. Ippen, W. Wong, and M. Haner, "All-optical network consortium-ultrafast TDM networks," *IEEE Journal on Selected Areas in Communications*, vol. 14, pp. 999–1013, Jun. 1996.

[69] X. Liu, S. Chandrasekhar, B. Zhu, P. Winzer, A. Gnauck, and D. Peckham, "448-Gb/s reduced-guard-interval CO-OFDM transmission over 2000 km of ultra-large-area fiber and five 80-ghz-grid ROADMs," *Journal of Lightwave Technology*, vol. 29, pp. 483–490, Feb. 2011.

[70] P. Winzer, "Optical networking beyond WDM," *IEEE Journal of Photonics*, vol. 4, pp. 647–651, Apr. 2012.

[71] J. Kahn and J. Barry, "Wireless infrared communications," *Proceedings of the IEEE*, vol. 85, pp. 265–298, Feb. 1997.

[72] A. Gnauck and P. Winzer, "Optical phase-shift-keyed transmission," *Journal of Lightwave Technology*, vol. 23, pp. 115–130, Jan. 2005.

[73] T. Pfau, S. Hoffmann, and R. Noe, "Hardware-efficient coherent digital receiver concept with feedforward carrier recovery for m -qam constellations," *Journal of Lightwave Technology*, vol. 27, pp. 989–999, Apr. 2009.

[74] N. Kikuchi, K. Mandai, K. Sekine, and S. Sasaki, "Incoherent 32-level optical multilevel signaling technologies," *Journal of Lightwave Technology*, vol. 26, pp. 150–157, Jan. 2008.

[75] M. Sauer, A. Kobyakov, and J. George, "Radio over fiber for picocellular network architectures," *Journal of Lightwave Technology*, vol. 25, pp. 3301–3320, Aug. 2007.

[76] O. Sinkin, R. Holzlohner, J. Zweck, and C. Menyuk, "Optimization of the split-step fourier method in modeling optical-fiber communications systems," *Lightwave Technology, Journal of*, vol. 21, pp. 61–68, Jan. 2003.

[77] A. Nirmalathas, P. Gamage, C. Lim, D. Novak, R. Waterhouse, and Y. Yang, "Digitized rf transmission over fiber," *Microwave Magazine, IEEE*, vol. 10, pp. 75–81, Jun. 2009.

[78] R. J. Essiambre, G. Kramer, P. Winzer, G. Foschini, and B. Goebel, "Capacity limits of optical fiber networks," *Journal of Lightwave Technology*, vol. 28, pp. 662–701, Feb. 2010.

[79] R. Dar, M. Feder, and M. Shtaif, "The jacobi mimo channel," *IEEE Transactions on Information Theory*, vol. 59, pp. 2426–2441, Apr. 2013.

[80] A. Wyner, "Shannon-theoretic approach to a gaussian cellular multiple-access channel," *IEEE Transactions on Information Theory*, vol. 40, pp. 1713–1727, Nov. 1994.

[81] D. Tse and P. Viswanath, *Fundamentals of Wireless Communication*. Cambridge University Press, 2005.

[82] Y. Miyahara, "Next-generation wireless technologies trends for ultra low energy," in *International Symposium on Low Power Electronics and Design ISLPED*, pp. 345–345, Aug. 2011.

[83] G. P. Agrawal, *Fiber Optical Communications Systems*. John Wiley & Sons, Inc., 2002.

[84] J.G.Proakis, *Digital Communications*. McGrawHill, 2001.

[85] C. Rasmussen and G. Hager, "Probabilistic data association methods for tracking complex visual objects," *Pattern Analysis and Machine Intelligence, IEEE Transactions on*, vol. 23, pp. 560–576, Jun 2001.

[86] X. Xu, R. Zhang, and L. Hanzo, "Digital RoF aided cooperative distributed antennas with FFR in multicell multiuser networks," in *Proc. of IEEE Vehicular Technology Conference (VTC)*, (San Francisco, United States), pp. 1–5, Fall 2011.

[87] J. Zhang, R. Zhang, X. Xu, G. Li, and L. Hanzo, "Effects of practical impairments on cooperative distributed antennas combined with fractional frequency reuse," in *IEEE Wireless Communications and Networking Conference (WCNC)*, pp. 1088–1092, Apr. 2012.

[88] D. Liang, S. X. Ng, and L. Hanzo, "Soft-decision Star-QAM aided BICM-ID," *IEEE Signal Processing Letters*, vol. 18, pp. 169–172, Mar. 2011.

[89] O. Tipmongkolsilp, S. Zaghloul, and A. Jukan, "The evolution of cellular backhaul technologies: Current issues and future trends," *IEEE Communications Surveys tutorials*, pp. 97–113, First Quarter 2011.

[90] S. Chia, M. Gasparroni, and P. Brick, "The next challenge for cellular networks: backhaul," *IEEE Mirowave magazine*, pp. 54–66, Aug. 2009.

[91] A. Ghosh, R. Ratasuk, B. Mondal, N. Mangalvedhe, and T. Thomas, "Lte-advanced: next-generation wireless broadband technology [invited paper]," *Wireless Communications, IEEE*, vol. 17, pp. 10–22, Jun. 2010.

[92] H. Burchardt and H. Haas, "Multicell cooperation: evolution of coordination and cooperation in large-scale networks," *IEEE Wireless Communications*, vol. 20, pp. 19–26, Feb. 2013.

[93] L. Hanzo and T. Keller, *OFDM and MC-CDMA: A Primer*. Wiley-IEEE Press, 2006.

[94] L. Hanzo, C. Wong, and M. Yee, *Adaptive Wireless Transceivers: Turbo-Coded, Space-Time Coded TDMA, CDMA and OFDM Systems*. Wiley-IEEE Press, 2002.

[95] H. Ekstrom, A. Furuskar, J. Karlsson, M. Meyer, S. Parkvall, J. Torsner, and M. Wahlqvist, "Technical solutions for the 3G long-term evolution," *IEEE Communications Magazine*, vol. 44, pp. 38–45, Mar. 2006.

[96] A. Ghosh, D. Wolter, J. Andrews, and R. Chen, "Broadband wireless access with WiMax/802.16: current performance benchmarks and future potential," *IEEE Communications Magazine*, vol. 43, pp. 129–136, Feb. 2005.

[97] R. Pabst, B. Walke, D. Schultz, P. Herhold, H. Yanikomeroglu, S. Mukherjee, H. Viswanathan, M. Lott, W. Zirwas, M. Dohler, H. Aghvami, D. Falconer, and G. Fettweis, "Relay-based deployment concepts for wireless and mobile broadband radio," *IEEE Communications Magazine*, vol. 42, pp. 80–89, Sep 2004.

[98] T. Cover and J. Thomas, *Elements of Information Theory*. Wiley, 1991.

[99] D. Wake, M. Webster, G. Wimpenny, K. Beacham, and L. Crawford, "Radio over fiber for mobile communications," in *IEEE International Topical Meeting on Microwave Photonics*, pp. 157–160, Oct. 2004.

[100] X. Zhou, L. Nelson, and P. Magill, "Rate-adaptable optics for next generation long-haul transport networks," *IEEE Communications Magazine*, vol. 20, pp. 41–49, Mar. 2013.

[101] J. E. Mitchell, "Performance of OFDM at 5.8 GHz using radio over fibre link," *Electronics Letters*, vol. 40, pp. 1353–1354, Oct. 2004.

[102] B. Zaidel, S. Shamai, and S. Verdu, "Multicell uplink spectral efficiency of coded DS-CDMA with random signatures," *IEEE Journal on Selected Areas in Communications,*, vol. 19, pp. 1556–1569, Aug. 2001.

[103] P. Marsch and G. P. Fettweis, *Coordinated Multi-Point in Mobile Communications: From Theory to Practice*. Cambridge University Press, 2011.

[104] M. Crisp, S. Li, A. Watts, R. Penty, and I. White, "Uplink and downlink coverage improvements of 802.11g signals using a distributed antenna network," *Journal of Lightwave Technology*, vol. 25, pp. 3388–3395, 2007.

[105] D. Wake, "Trends and prospects for radio over fibre picocells," in *Proc.of Microwave Photonics (MWP)*, pp. 21–24, Nov. 2002.

[106] G. Kardaras, T. P. Tien, J. Soler, and L. Dittmann, "Analysis of control and management plane for hybrid fiber radio architectures," in *IEEE International Conference on Communication Technology (ICCT)*, (Nanjing, China), pp. 281–284, November 2010.

[107] P. A. Gamage, A. Nirmalathas, C. Lim, D. Novak, and R. Waterhouse, "Design and analysis of digitized RF-over-fiber links," *Journal of Lightwave Technology*, vol. 27, pp. 2052–2061, 2009.

[108] C. I. Cox, E. Ackerman, G. Betts, and J. Prince, "Limits on the performance of RF-over-fiber links and their impact on device design," *IEEE Transactions on Microwave Theory and Techniques*, vol. 54, pp. 906–920, 2006.

[109] X. Qi, J. Liu, X. Zhang, and L. Xie, "Fiber dispersion and nonlinearity influences on transmissions of AM and FM data modulation signals in radio-over-fiber system," *IEEE Journal of Quantum Electronics*, vol. 46, pp. 1170–1177, 2010.

[110] X. Gu, Y. He, H. Kosek, and X. Fernando, "Transmission efficiency improvement in microwave fiber-optic link using sub-pico meter optic bandpass filter," in *Proc. of the SPIE Photonic North Conference*, (Toronto, Canada), Sep. 2005.

[111] G. P. Agrawal, *Nonlinear fiber optics*. Academic Press, 2006.

[112] N. Kikuchi, K. Mandai, K. Sekine, and S. Sasaki, "Incoherent 32-level optical multilevel signaling technologies," *Journal of Lightwave Technology*, vol. 26, pp. 150–157, 2008.

[113] N. Kikuchi and S. Sasaki, "Highly sensitive optical multilevel transmission of arbitrary quadrature-amplitude modulation (QAM) signals with direct detection," *Journal of Lightwave Technology*, vol. 28, pp. 123–130, 2010.

[114] B. Widrow, K. Duvall, R. Gooch, and W. Newman, "Signal cancellation phenomena in adaptive antennas: Causes and cures," *IEEE Transactions on Antennas and Propagation*, vol. 30, pp. 469–478, May 1982.

[115] C. Saradhi and S. Subramaniam, "Physical layer impairment aware routing (PLIAR) in WDM optical networks: issues and challenges," *IEEE Communications Surveys Tutorials,*, vol. 11, pp. 109–130, Apr. 2009.

[116] R. Smart, J. Zyskind, and D. DiGiovanni, "Two-stage erbium-doped fibre amplifiers suitable for use in long-haul soliton systems," *Electronics Letters*, vol. 30, pp. 50–52, Jan. 1994.

[117] B. Dong, L. Wei, and D.-P. Zhou, "Coupling between the small-core-diameter dispersion compensation fiber and single-mode fiber and its applications in fiber lasers," *Journal of Lightwave Technology*, vol. 28, pp. 1363–1367, May. 2010.

[118] A. Galtarossa, L. Palmieri, M. Schiano, and T. Tambosso, "Single-end polarization mode dispersion measurement using backreflected spectra through a linear polarizer," *Journal of Lightwave Technology*, vol. 17, pp. 1835–1842, Oct. 1999.

[119] A. Yeniay, J.-M. Delavaux, and J. Toulouse, "Spontaneous and stimulated brillouin scattering gain spectra in optical fibers," *Journal of Lightwave Technology*, vol. 20, pp. 1425–1432, Aug 2002.

[120] H. Kim, K. Han, and Y. Chung, "Performance limitation of hybrid WDM systems due to stimulated raman scattering," *IEEE Photonics Technology Letters*, vol. 13, pp. 1118–1120, Oct. 2001.

[121] L. Wooten, "A review of lithium niobate modulators for fiber-optic communications systems," *IEEE Journal of Selected Topics in Quantum Electronics*, vol. 6, pp. 69–82, Feb. 2000.

[122] L. W. and, "Efficient continuous-wave 1053-nm Nd:GYSGG laser with passively q-switched dual-wavelength operation for terahertz generation," *IEEE Journal of Quantum Electronics*, vol. 49, pp. 375–379, Mar. 2013.

[123] X. Liu and Y.-H. Kao, "Chirped RZ-DPSK based on single mach-zehnder modulator and its nonlinear transmission performance," *IEEE Photonics Technology Letters*, vol. 17, pp. 1531–1533, jul. 2005.

[124] S. Betti and M. Giaconi, "Analysis of the cross-phase modulation effect in WDM optical systems," *IEEE Photonics Technology Letters*, vol. 13, pp. 43–45, Jan. 2001.

[125] S. Shamai and A. Wyner, "Information-theoretic considerations for symmetric, cellular, multiple-access fading channels," *IEEE Transactions on Information Theory*, vol. 6, pp. 1877–1894, Nov 1997.

[126] J.K.Shaw, *Mathematical Principles of Optical Fiber Communications*. Society for Industrial and Applied Mathematics, 2004.

[127] G. Caire, G. Taricco, and E. Biglieri, "Bit-interleaved coded modulation," *IEEE Transactions on Information Theory*, vol. 44, pp. 927–946, May 1998.

[128] L. Hanzo, S. X. Ng, T. Keller, and W. Webb, *Quadrature Amplitude Modulation:From Basics to Adaptive Trellis-Coded, Turbo-Equalised and Space-Time Coded OFDM, CDMA and MC-CDMA Systems*. Wiley-IEEE Press, 2004.

[129] J. Hagenauer, "Rate-compatible punctured convolutional codes (RCPC codes) and their applications," *IEEE Transactions on Communications*, vol. 36, pp. 389–400, Apr. 1988.

[130] B. Hassibi and M. Sharif, "Fundamental limits in MIMO broadcast channels," *IEEE Journal on Selected Areas in Communications*, vol. 25, pp. 1333–1344, Sep. 2007.

[131] Y. Xiang, J. Luo, and C. Hartmann, "Inter-cell interference mitigation through flexible resource reuse in OFDMA based communication networks," *Proc. of European Wireless*, vol. 43, pp. 1–7, Apr. 2007.

[132] R. Zhang and L. Hanzo, "Wireless cellular networks," *IEEE Vehicular Technology Magazine*, vol. 5, pp. 31–39, 2010.

[133] S. Hunziker and W. Baechtold, "Cellular remote antenna feeding: optical fibre or coaxial cable?," *Electronics Letters*, vol. 34, pp. 1038–1040, May. 1998.

[134] C. Wan and J. Andrews, "Downlink performance and capacity of distributed antenna systems in a multicell environment," *IEEE Transactions on Wireless Communications*, vol. 6, pp. 69–73, Jan 2007.

[135] H. Zhang and H. Dai, "Cochannel interference mitigation and cooperative processing in downlink multicell multiuser MIMO networks," *EURASIP Journal on Wireless Communications and Networking*, vol. 2004, pp. 1687–1472, 2004.

[136] Y. Takasaki, M. Tanaka, N. Maeda, K. Yamashita, and K. Nagano, "Optical pulse formats for fiber optic digital communications," *Communications, IEEE Transactions on*, vol. 24, pp. 404–413, Apr. 1976.

[137] R. Steele and L. Hanzo, *Mobile Radio Communications*. IEEE Press - John Wiley, 1999.

[138] O. Sinkin, R. Z. J. Holzlohner, and C. Menyuk, "Optimization of the split-step fourier method in modeling optical-fiber communications systems," *Journal of Lightwave Technology*, vol. 21, pp. 61–68, 2003.

[139] "Spatial channel model for MIMO simulations." Technical specification group radio access network, 2008. ftp://ftp.3gpp.org/.

[140] L. Hanzo, J. Blogh, and S. Ni, *3G, HSDPA, HSUPA and Intelligent FDD versus TDD Networking: Smart Antennas and Adaptive Modulation*. IEEE Press - John Wiley, 2008.

[141] A. Hekkala, M. Lasanen, and I. Harjula, "Analysis of and compensation for non-ideal RoF links in DAS," *IEEE Transactions on Wireless Communications*, vol. 17, pp. 52–59, 2010.

[142] L. Hanzo, P. Cherriman, and J. Streit, *Wireless Video Communications: Second to Third Generation and Beyond*. Wiley-IEEE Press, 2001.

[143] R. Zhang and L. Hanzo, "Cooperative downlink multicell preprocessing relying on reduced-rate back-haul data exchange," *IEEE Transactions on Vehicular Technology*, vol. 60, pp. 539–545, 2011.

[144] W. Jang and W. Wu, "Distributed and centralized multiuser detection with antenna arrays," *IEEE Transactions on Wireless Communications*, vol. 4, pp. 855–860, May 2005.

[145] X. Li, T. Jiang, S. Cui, J. An, and Q. Zhang, "Cooperative communications based on rateless network coding in distributed MIMO systems," *IEEE Wireless Communications*, vol. 17, pp. 60–67, 2010.

[146] A. Sadek, Z. Han, and K. Liu, "Distributed relay-assignment protocols for coverage expansion in cooperative wireless networks," *IEEE Transactions on Mobile Computing*, vol. 9, pp. 505–515, Apr. 2010.

[147] P. Omiyi, H. Haas, and G. Auer, "Analysis of TDD cellular interference mitigation using busy-bursts," *IEEE Transactions on Wireless Communications*, vol. 6, pp. 2721–2731, Jul. 2007.

[148] D. S. Michalopoulos, A. s. Lioumpas, G. K. Karagiannidis, and R. Schober, "Selective cooperative relaying over time-varying channels," *IEEE Transactions on Communications*, vol. 58, pp. 2402–2412, Aug. 2010.

[149] D. Radji and H. Leib, "Interference cancellation based detection for V-BLAST with diversity maximizing channel partition," *IEEE Journal of Selected Topics in Signal Processing*, vol. 3, pp. 1000–1015, Dec. 2009.

[150] J. Lee, J.-W. Choi, H.-L. Lou, and J. Park, "Soft MIMO ML demodulation based on bitwise constellation partitioning," *IEEE Communications Letters*, vol. 13, pp. 736–738, Oct. 2009.

[151] Y. Jia, C. Vithanage, C. Andrieu, and R. Piechocki, "Probabilistic data association for symbol detection in mimo systems," *Electronics Letters*, vol. 42, pp. 38–40, Jan. 2006.

[152] E. Katranaras, M. Imran, and C. Tzaras, "Uplink capacity of a variable density cellular system with multicell processing," *IEEE Transactions on Communications*, vol. 57, pp. 2098–2108, Jul. 2009.

[153] P. Marsch and G. P. Fettweis, *Coordinated Multi-Point in Mobile Communications*. Cambridge University Press, 2011.

[154] K. Lau, "RF transport over optical fiber in urban wireless infrastructures," *IEEE/OSA Journal of Optical Communications and Networking*, vol. 4, pp. 326–335, Apr. 2012.

[155] T. Rappaport and L. Milstein, "Effects of radio propagation path loss on DS-CDMA cellular frequency reuse efficiency for the reverse channel," *IEEE Transactions on Vehicular Technology*, vol. 41, pp. 231–242, Aug 1992.

[156] Y. Jia, C. M. Vithanage, C. Andrieu, and R. Piechocki, "Probabilistic data association for symbol detection in MIMO systems," *Electronics Letters*, vol. 42, 2006.

[157] J. Luo, K. Pattipati, P. Willett, and F. Hasegawa, "Near-optimal multiuser detection in synchronous CDMA using probabilistic data association," *IEEE Communications Letters*, vol. 2, pp. 361–363, 2001.

[158] S. Shamai and B. M. Zaidel, "Enhancing the cellular downlink capacity via co-processing at the transmitting end," in *Proc. of 53rd IEEE Vehicular Technology Conference, (VTC' 2001-Spring)*, vol. 3, (Rhodes, Greece), pp. 1745–1749, May 2001.

[159] B. K. Lau, M. Jensen, J. Medbo, and J. Furuskog, "Single and multi-user cooperative MIMO in a measured urban macrocellular environment," *IEEE Transactions on Antennas and Propagation*, vol. 60, pp. 624–632, Feb. 2012.

[160] Z. Ding, T. Ratnarajah, and C. Cowan, "On the diversity-multiplexing tradeoff for wireless cooperative multiple access systems," *IEEE Transactions on Signal Processing,*, vol. 55, pp. 4627–4638, Sep. 2007.

[161] C.-X. Wang, X. Hong, X. Ge, X. Cheng, G. Zhang, and J. Thompson, "Cooperative MIMO channel models: A survey," *IEEE Communications Magazine*, vol. 48, pp. 80–87, Feb. 2010.

[162] O. A. M. E.-H. L. Hanzo and N. Wu, *Near-Capacity Multi Functional MIMO Systems*. Wiley-IEEE Press, 2009.

[163] K. J. R. Liu, A. K. Sadek, and A. K. W. Su, *Cooperative Communications and Networking*. Cambridge University Press, 2008.

[164] T. Cover and A. Gamal, "Capacity theorems for the relay channel," *IEEE Transactions on Information Theory*, vol. 25, pp. 572–584, Sep. 1979.

[165] A. Sendonaris, E. Erkip, and B. Aazhang, "User cooperation diversity. Part I. System description," *IEEE Transactions on Communications*, vol. 51, pp. 1927–1938, Nov. 2003.

[166] A. Sendonaris, E. Erkip, and B. Aazhang, "User cooperation diversity. Part II. Implementation aspects and performance analysis," *IEEE Transactions on Communications*, vol. 51, pp. 1939–1948, Nov. 2003.

[167] L. Hanzo, T. H. Liew, B. L. Yeap, R. Y. S. Tee, and S. X. Ng, *Turbo Coding, Turbo Equalisation and Space-Time Coding: EXIT-Chart-Aided Near-Capacity Designs for Wireless Channels*. Wiley-IEEE Press, 2011.

[168] M. Sadek, A. Tarighat, and A. Sayed, "A leakage-based precoding scheme for downlink multi-user MIMO channels," *IEEE Transactions on Wireless Communications*, vol. 6, pp. 1711–1721, May 2007.

[169] W. Santipach and M. L. Honig, "Capacity of a multiple-antenna fading channel with a quantized precoding matrix," *IEEE Transactions on Information Theory*, vol. 55, pp. 1218–1234, Mar. 2009.

[170] M. Speth, S. A. Fechtel, G. Fock, and H. Meyr, "Optimum receiver design for wireless broad-band systems using OFDM - Part I," *IEEE Transactions on Communications*, vol. 47, pp. 1668–1677, Nov. 1999.

[171] T. S. Rappaport, *Wireless Communications: Principles and Practice*. Prentice-Hall, 1996.

[172] J. Shaw, *Mathematical principles of optical fiber communications*. Philadelphia: Society for Industrial and Applied Mathematics, 2004.

[173] A. Goldsmith, *Wireless Communications*. Cambridge University Press, 2005.

[174] J. Torrance, T. Keller, and L. Hanzo, "Multi-level modulation in the indoors leaky feeder environment," in *IEEE 46th Vehicular Technology Conference, 'Mobile Technology for the Human Race'*, vol. 3, pp. 1554–1558, Spring 1996.

[175] R. Chen, J. Andrews, R. Heath, and A. Ghosh, "Uplink power control in multi-cell spatial multiplexing wireless systems," *IEEE Transactions on Wireless Communications*, vol. 6, pp. 2700–2711, Jul. 2007.

[176] D. Goodman and N. Mandayam, "Power control for wireless data," *IEEE Personal Communications*, vol. 7, pp. 48–54, Apr. 2000.

[177] C. Saraydar, N. Mandayam, and D. Goodman, "Pricing and power control in a multicell wireless data network," *IEEE Journal on Selected Areas in Communications*, vol. 19, pp. 1883–1892, Oct. 2001.

[178] R. Yates, "A framework for uplink power control in cellular radio systems," *IEEE Journal on Selected Areas in Communications*, vol. 13, pp. 1341–1347, Sep. 1995.

[179] Y. Su and M. Schaar, "A new perspective on multi-user power control games in interference channels," *Wireless Communications, IEEE Transactions on*, vol. 8, pp. 2910–2919, Jun. 2009.

[180] Z. Wang, D. Yang, and L. Milstein, "Multi-user resource allocation for a distributed multi-carrier DS-CDMA network," *IEEE Transactions on Communications*, vol. 60, pp. 143–152, Jan. 2012.

[181] J. Huang, R. Berry, and M. Honig, "Distributed interference compensation for wireless networks," *IEEE Journal on Selected Areas in Communications*, vol. 24, pp. 1074–1084, May 2006.

[182] R. Cendrillon, W. Yu, M. Moonen, J. Verlinden, and T. Bostoen, "Optimal multiuser spectrum balancing for digital subscriber lines," *IEEE Transactions on Communications*, vol. 54, pp. 922–933, May 2006.

[183] R. Cendrillon, J. Huang, M. Chiang, and M. Moonen, "Autonomous spectrum balancing for digital subscriber lines," *IEEE Transactions on Signal Processing*, vol. 55, pp. 4241–4257, Aug. 2007.

[184] N. Madamopoulos, S. Peiris, N. Antoniades, D. Richards, B. Pathak, G. Ellinas, R. Dorsinville, and M. Ali, "A fully distributed 10G-epon-based converged fixed-mobile networking transport infrastructure for next generation broadband access," *IEEE/OSA Journal of Optical Communications and Networking*, vol. 4, pp. 366–377, May. 2012.

[185] R. Yadav, "Passive optical network (PON) based converged access network [invited]," *IEEE/OSA Journal of Optical Communications and Networking*, vol. 4, pp. B124–B130, Nov. 2012.

[186] C. Lethien, D. Wake, B. Verbeke, J. Vilcot, C. Loyez, M. Zegaoui, N. Gomes, N. Rolland, and P. Rolland, "Energy-autonomous picocell remote antenna unit for

radio-over-fiber system using the multiservices concept," *IEEE Photonics Technology Letters*, vol. 24, pp. 649–651, Apr. 2012.

[187] J. Guillory, E. Tanguy, A. Pizzinat, B. Charbonnier, S. Meyer, C. Algani, and H. Li, "A 60 GHz wireless home area network with radio over fiber repeaters," *Journal of Lightwave Technology*, vol. 29, pp. 2482–2488, Aug. 2011.

Subject Index

A

Amplifier Spontaneous Emission Noise21
ASEN 22

B

Benchmarker 50
Best Direction 59, 63, 97

C

Cell-Center Area 57
Cell-center Area 97
Cell-Centre Area 48
Cell-Edge Area 49, 63
Cell-edge Area 94
Central Signal Processing 86
Centralized Antennas 74
COMP-aided DAS with FFR 111
Composite Channel of a DOF-Aided Wireless Relaying System 23
Conventional BS Cooperation 78, 91
Coordinated Multipoint Transmission . . 7
Correlation Relaying Channel 85
CPDA 89
Cross-phase Modulation 23
CSI 29
CSI Estimation Errors 112
CSI Quantisation Errors 113

D

DAS aide FFR 2
DAS aided FFR 43, 109
Digital Fibre Soliton Aided Backhaul . 80
Digital Over Fibre and Radio Over Fibre Techniques 17
Direct-Relaying Scheme 34
Dispersion Effect 59
Distributed Antenna Systems 3
DL 40, 108
DOF 17
DOF Aided Cooperative DAS Assisted FFR 50
DOF aided Non-Cooperative DAS Assisted FFR system 48
DOF Link 54

E

egBF 29, 34, 52
Entire Cell Area 61, 65
Entire cell Area 98

F

FFR 2
Fibre Loss 19
Four-wave Mixing 23
Fractional Frequency Reuse 2
fundamental soliton 82
FXM 23

G

GVD 20

H

Hybrid Technique 30, 35

I

Imperfect Channel Knowledge 106
Imperfect Optical Fibre Model . . 44, 120
IMT 27
Interference Mitigation Techniques . . . 25
Intermediate Direction 60
IPI 26, 35
IRI 56

L

Linear Effects 19
Linear Transmit PreProcessing 52

M

ML Multiuser Detector 86
MMSE 52
MMSE-OSIC Detector 90
MR Selection 97
Multicell, Multiuser System Topology 43, 76

N

NLS 46, 81
Non-cooperative DAS Relying on FFR 57
Nonlinear Effects 22, 59

O

Optical Fibre Backhaul 8, 17
Optical Fibre Based Fixed Relay Aided System 24
Optical Fibre Channel 19
Optical Fibre channel 25

P

PDA Aided Multiuser Detector 87
Pervasive DAS/FFR 76, 82, 94
PMD 21
Polarization Effects 21
Power Control 65, 100
Practical Impairments 112
pulse-broadening 26

R

Received Signal Strength 25
Reduced-Power Technique 34
Reduced-power Technique 29
ROF 17

S

SBS 23
Self-phase Modulation 22
Shamai-Wyner Interference Model . . . 24
SIMO 119
SINR 50
SIR 66, 100, 134
soft-decision aided 16StQAM 122
SSF method 46, 121
Synchronisation Errors 113

T

Throughput 30, 32, 55
TPP 52, 111

U

UFR 1
UFR and FFR 1
UL 73, 119

V

Virtual MIMO 84

W

Wireless channel 26
Worst Direction 60, 64, 94, 117
worst Direction 41

X

XPM 23

Author Index

A

Aazhang, B. [165] 107
Aazhang, B. [166] 107
Ackerman, E.I. [108] 17, 41
Adams, L.E. [68] 9, 10
Aghvami, H. [97] 16
Agrawal, G.P. [83] . 11, 19–23, 38, 45, 46
Agrawal, G.P. [111] 17, 22, 23, 38, 42, 46, 55, 73, 80–82, 84, 85, 120, 121
Ahlen, A. [21] 5
Alamri, O. [162] 107
Algani, C. [187] 141
Ali, M.A. [184] 141
An, J. [145] 74
Andrews, J.G. [96] 16, 40
Andrews, J.G. [35] 6
Andrews, J.G. [175] 140
Andrews, J.G. [28] 3, 6
Andrews, J.G. [23] 5
Andrews, J.G. [17] 2, 5
Andrews, J.G. [7] 1
Andrews, J. [26] 5
Andrieu, C. [151] 75
Andrieu, C. [156] 89
Annapureddy, V.S. [62] 8
Antoniades, N. [184] 141
Athanasiadou, G.E. [16] 2
Auer, G. [147] 75

B

Baechtold, W. [133] 40
Baier, P.W. [59] 8
Baker, M. [10] 1
Bang, H.J. [61] 8
Bar-Ness, Y. [13] 1, 74
Barry, J.R. [71] 9
Barry, R.A. [68] 9, 10
Beacham, K. [99] 16, 17, 41, 74
Begain, K. [20] 5
Ben Cheikh, D. [46] 7
Benyuan Zhu, [69] 9, 10
Berry, R.A. [181] 140
Betti, S. [124] 23
Betts, G.E. [108] 17, 41
Biglieri, E. [127] 31
Blogh, J. [140] 52
Bo Dong, [117] 21
Boon Loong Ng, [40] 7
Bostoen, T. [182] 140
Brackett, C.A. [66] 9, 10
Brackett, C.A. [67] 9, 10
Brick, P. [64] 8
Brick, P. [90] 15
Buon Kiong Lau, [159] 107
Burchardt, H. [92] 15

C

Caire, G. [127] 31
Cardieri, P. [19] 5
Castanheira, D. [29] 3, 6
Cendrillon, R. [182] 140
Cendrillon, R. [183] 140
Chan-Byoung Chae, [42] 7, 8
Chandrasekhar, S. [69] 9, 10
Chandrasekhar, V. [23] 5
Charbonnier, B. [187] 141
Chen, R. [96] 16, 40
Chen, R. [175] 140
Cheng-Xiang Wang, [161] 107
Chenyang Yang, [48] 7
Cherriman, P. [142] 67, 140
Chia, S. [64] 8
Chia, S. [90] 15
Choi, L. [49] 7
Chung, Y.C. [120] 22
Cover, T. [164] 107
Cover, T. [98] 16
Cowan, C.C.F. [160] 107
Crawford, L. [99] 16, 17, 41, 74
Crisp, M.J. [104] 17, 41
Cui, Q. [47] 7
Cui, S. [145] 74

D

Da-Peng Zhou, [117] 21
Dacheng Yang, [180] 140
Dahlman, E. [9] 1
Dar, R. [79] 10
David Tse, [81] 10, 29, 52, 90
Delavaux, J.-M. [119] 22
DiGiovanni, D.J. [116] 20
Ding, Z. [160] 107
Dittmann, L. [106] 17, 41
Doerr, C.R. [68] 9, 10
Dohler, M. [97] 16
Dorsinville, R. [184] 141
Duvall, K. [114] 19

E

Ekstrom, H. [95] 16, 40, 73
El Gamal, A. [62] 8
El-Hajjar, M. [162] 107
Ellinas, G. [184] 141
Erkip, E. [165] 107
Erkip, E. [166] 107
Euiseok Song, [30] 3, 6
Eunsung Park, [37] 6

F

Falciasecca, G. [18] 5
Falconer, D.D. [97] 16
Fang Yuan, [48] 7
Fechtel, S.A. [170] 114
Feder, M. [79] 10
Fernando, X. [110] 17, 41
Fettweis, G.P. [153] 78
Fettweis, G.P. [97] 16
Fettweis, G. [57] 7
Fettweis, Gerhard P. [103] 17
Finn, S.G. [68] 9, 10
Fock, G. [170] 114
Foschini, G.J. [78] 10
Frullone, M. [18] 5
Furuskar, A. [95] 16, 40, 73
Furuskar, A. [9] 1
Furuskog, J. [159] 107

G

Galtarossa, A. [118] 21
Gamage, P.A. [77] 10
Gamage, P.A. [107] 17, 41

Gamal, A.E. [164] 107
Gameiro, A. [29] 3, 6
Ganti, R.K. [17] 2, 5
Ganti, R.K. [7] 1
Gao, Q. [12] 1, 7
Gasparroni, M. [64] 8
Gasparroni, M. [90] 15
George, J. [75] 9, 10
Gesbert, D. [61] 8
Ghaffar, R. [6] 1
Ghosh, A. [96] 16, 40
Ghosh, A. [175] 140
Ghosh, A. [91] . . . 15, 17, 42, 73, 80, 130
Ghosh, A. [17] 2, 5
Ghosh, A. [7] 1
Giaconi, M. [124] 23
Giuliano, R. [8] 1
Gnauck, A.H. [72] 9, 10
Gnauck, A.H. [69] 9, 10
Goebel, B. [78] 10
Goldsmith, A. [173] 123
Gomes, N.J. [36] 6, 42, 80
Gomes, N. [186] 141
Gong Zhang, [161] 107
Gooch, R. [114] 19
Goodman, D.J. [177] 140
Goodman, D. [176] 140
Grazioso, P. [18] 5
Gu, X. [110] 17, 41
Guillory, J. [187] 141

H

H Dai, [135] 41, 50, 52, 107
H Zhang, [135] 41, 50, 52, 107
Haas, H. [147] 75
Haas, H. [92] 15
Hagenauer, J. [129] 31, 53
Hager, G.D. [85] 11
Hairuo Zhuang, [32] 6
Hall, K.L. [68] 9, 10
Han, K.H. [120] 22
Han, S. [41] 7, 8
Haner, M. [68] 9, 10
Hanly, S.V. [56] 7
Hanzo, L. [88] 13, 107, 108, 123
Hanzo, L. [87] 13
Hanzo, L. [162] 107
Hanzo, L. [174] 135
Hanzo, L. [140] 52
Hanzo, L. [94] 15
Hanzo, L. [137] 43, 116
Hanzo, L. [93] 15, 49
Hanzo, L. [128] 31, 107, 108, 125
Hanzo, L. [167] 107, 108, 124
Hanzo, L. [142] 67, 140
Hanzo, L. [132] 40, 41, 106
Hanzo, L. [58] 7, 74, 75, 89, 90
Hardouin, E. [61] 8
Harjula, Ilkka. [141] 53
Hartmann, C. [131] 40, 73
Hasegawa, F. [53] 7
Hasegawa, F. [157] 89
Hassibi, B. [130] 37
Haus, H. [68] 9, 10
He, Y. [110] 17, 41
Heath, R.W. [175] 140
Heath, R.W. [42] 7, 8
Hekkala, A. [141] 53
Herhold, P. [97] 16
Himayat, N. [5] 1
Hoffmann, S. [73] 9
Holzlohner, R.Zweck J. [138] 46
Holzlohner, R. [76] 10

Honghui Qi, [52] 7, 8
Hongwu Li, [187] 141
Honig, M.L. [181] 140
Honig, M.L. [169] 113
Hou, X. [41] 7, 8
Hui-Ling Lou, [150] 75
Hunziker, S. [133] 40
Hyojin Lee, [40] 7

I

III Cox, C.H. [108] 17, 41
Illsoo Sohn, [17] 2, 5
Imran, M. [152] 78
Inkyu Lee, [37] 6
Inoue, T. [42] 7, 8
Ippen, E.P. [68] 9, 10

J

J Essiambre, R. [78] 10
J.G Andrews, [134] 40, 73
J.G.Proakis, [84] 11
J.K.Shaw, [126] 26
Jaewon Chang, [22] 5
Jang, W.M. [144] 74
Jensen, M.A. [159] 107
Ji-Woong Choi, [150] 75
Jia, Y. [151] 75
Jia, Y. [156] 89
Jiang, T. [145] 74
Jianghua Liu, [40] 7
Jianwei Huang, [181] 140
Jianwei Huang, [183] 140
Jing Wang, [34] 6
Jonghyun Park, [30] 3, 6
Jongsun Park, [150] 75
Juho Lee, [40] 7
Jukan, A. [63] 8
Jukan, A. [89] 15
Jun Heo, [22] 5
Jun Zhang, [28] 3, 6
Jungwon Lee, [150] 75

K

Kahn, J.M. [71] 9
Kaklamani, D.I. [16] 2
Kao, Y.-H. [123] 23
Karagiannidis, G.K. [148] 75
Kardaras, G. [106] 17, 41
Karlsson, J. [95] 16, 40, 73
Katranaras, E. [152] 78
Keller, T. [174] 135
Keller, T. [128] 31, 107, 108, 125
Kenro Sekine, [74] 9
Kerpez, K.J. [27] 3, 17
Kerpez, K.J. [11] 1
Kikuchi, N. [74] 9
Kikuchi, N. [112] 17, 41
Kikuchi, N. [113] 17, 41
Kim, H. [120] 22
Kintzer, E.S. [68] 9, 10
Kishiyama, Y. [60] 8
Kishiyama, Y. [45] 7
Kishiyama, Y. [14] 1
Knopp, R. [6] 1
Kobyakov, A. [75] 9, 10
Kosek, H. [110] 17, 41
Koutsopoulos, I. [44] 7, 8
Kramer, G. [78] 10
Krishnan, N. [15] 2
Kwasinski, A. [163] 107

L

L Hanzo, [24] . 5, 6, 12, 13, 74–76, 106, 108, 120

L Hanzo, [143] 70
L Hanzo, [39] 7, 41, 60
L Hanzo, [86] 12
Lan Chen, [45] 7
Lasanen, M. [141] 53
Lau, K.Y. [154] 80
Lei Wei, [52] 7, 8
Leib, H. [149] 75
Lethien, C. [186] 141
Leveque, O. [38] 6
Li, G.Y. [25] 5
Li, G. [87] 13
Li, S. [104] 17, 41
Li, X. [145] 74
Li Wei, [117] 21
Liang, D. [88] 13, 107, 108, 123
Liang Xiao, [32] 6
Liew, T.H. [167] 107, 108, 124
Lim, C. [77] 10
Lim, C. [107] 17, 41
Lin Dai, [32] 6
Lin Dai, [33] 6
Lioumpas, A.s. [148] 75
Liu, J. [109] 17, 19, 41, 44
Liu, K.J.R. [146] 75
Loreti, P. [8] 1
Lott, M. [97] 16
Loyez, C. [186] 141
Luo, J. [54] 7
Luo, J. [53] 7
Luo, J. [157] 89
Luo, J. [131] 40, 73
Lv, T. [58] 7, 74, 75, 89, 90

M

Madamopoulos, N. [184] 141
Maeda, N. [136] 41
Magill, P. [100] 17
Mandai, K. [74] 9
Mandai, K. [112] 17, 41
Mandayam, N.B. [15] 2
Mandayam, N.B. [177] 140
Mandayam, N. [176] 140
Mangalvedhe, N. [91] . 15, 17, 42, 73, 80, 130
Marsch, P. [57] 7
Marsch, P. [153] 78
Maunder, G.R. [58] 7, 74, 75, 89, 90
Mazzarese, D. [42] 7, 8
Mazzarese, D. [40] 7
Medbo, J. [159] 107
Menyuk, C.R. [76] 10
Menyuk, C.R. [138] 46
Meurer, M. [59] 8
Meyer, M. [95] 16, 40, 73
Meyer, S. [187] 141
Meyr, H. [170] 114
Michalopoulos, D.S. [148] 75
Milstein, L.B. [155] 85
Milstein, L.B. [180] 140
Minghai Feng, [45] 7
Mitchell, John E. [101] 17
Mitra, U. [50] 7
Miyahara, Y. [82] 10
Molisch, A.F. [41] 7, 8
Mondal, B. [91] . . 15, 17, 42, 73, 80, 130
Monti, C. [8] 1
Moonen, M. [182] 140
Moonen, M. [183] 140
Moores, J.D. [68] 9, 10
Morimoto, A. [60] 8
Morimoto, A. [14] 1
Moshavi, S. [51] 7, 8

Mukherjee, S. [97] 16
Mung Chiang, [183] 140
Murch, R.D. [49] 7

N

Nagano, K. [136] 41
Nelson, L.E. [100] 17
Newman, W. [114] 19
Ng, S.X. [88] 13, 107, 108, 123
Ng, S.X. [128] 31, 107, 108, 125
Ng, S.X. [167] 107, 108, 124
Ni, S. [140] 52
Nirmalathas, A. [77] 10
Nirmalathas, A. [107] 17, 41
Nishikawa, D. [60] 8
Nishikawa, D. [14] 1
Nkansah, A. [36] 6, 42, 80
Noe, R. [73] 9
Novak, D. [77] 10
Novak, D. [107] 17, 41
Novlan, T.D. [7] 1
Novlan, T. [17] 2, 5
Novlan, T. [26] 5

O

Omiyi, P. [147] 75
Ottosson, T. [21] 5
Ozgur, A. [38] 6

P

Pabst, R. [97] 16
Palmieri, L. [118] 21
Panchal, J.S. [15] 2
Papadogiannis, A. [61] 8
Parkvall, S. [9] 1
Parkvall, S. [95] 16, 40, 73
Pathak, B. [184] 141
Patrick Marsch, [103] 17
Pattipati, K.R. [54] 7
Pattipati, K.R. [53] 7
Pattipati, K.R. [157] 89
Peckham, D.W. [69] 9, 10
Peiris, S. [184] 141
Peng, Y. [12] 1, 7
Penty, R.V. [104] 17, 41
Pfau, T. [73] 9
Pfening, A. [20] 5
Pham, D. [54] 7
Piechocki, R.J. [151] 75
Piechocki, R.J. [156] 89
Pizzinat, A. [187] 141
Poor, H.V. [55] 7, 8
Pramod Viswanath, [81] . . 10, 29, 52, 90
Prasad, N. [43] 7
Prince, J.L. [108] 17, 41

Q

Q Zhang, [145] 74
Qi, X. [109] 17, 19, 41, 44

R

Radji, D. [149] 75
Rao, A. [5] 1
Rappaport, T.S. [155] 85
Rappaport, T.S. [19] 5
Rappaport, T.S. [171] 116
Rasmussen, C. [85] 11
Ratasuk, R. [91] . . 15, 17, 42, 73, 80, 130
Ratnarajah, T. [160] 107
Rauschenbach, K.A. [68] 9, 10
Ray Liu, K.J. [163] 107
Richards, D. [184] 141
Riva, G. [18] 5
Rolland, N. [186] 141
Rolland, P.A. [186] 141

Roman, R. [31] 6
Rozsa, G.I. [20] 5
Rustako, A.J. [31] 6

S

Sadek, A.K. [146] 75
Sadek, A.K. [163] 107
Sadek, M. [168] 111, 112, 128
Saleh, A.A. [31] 6
Salehi, J.A. [65] 9, 10
Salehi, J.A. [66] 9, 10
Sang-Rim Lee, [37] 6
Santipach, W. [169] 113
Saradhi, C.V. [115] 19, 22, 23
Saraydar, C.U. [177] 140
Sasaki, S. [74] 9
Sasaki, S. [112] 17, 41
Sasaki, S. [113] 17, 41
Sauer, M. [75] 9, 10
Sawahashi, M. [60] 8
Sawahashi, M. [14] 1
Sayed, A.H. [168] 111, 112, 128
Schaar, M. [179] 140
Schiano, M. [118] 21
Schober, R. [148] 75
Schultz, D.C. [97] 16
Sekine, K. [112] 17, 41
Sendonaris, A. [165] 107
Sendonaris, A. [166] 107
Shamai, S. [102] 17
Shamai, S. [125] 24
Shamai, S. [158] 107
Sharif, M. [130] 37
Shaw, J.K. [172] 120, 121
Shidong Zhou, [33] 6
Shidong Zhou, [34] 6
Shtaif, M. [79] 10
Shuangfeng Han, [34] 6
Simeone, O. [13] 1, 74
Sinkin, O.V. [76] 10
Sinkin, O.V. [138] 46
Smart, R.G. [116] 20
Soler, J. [106] 17, 41
Somekh, O. [13] 1, 74
Song, L. [12] 1, 7
Soni, R. [5] 1
Spagnolini, U. [13] 1, 74
Speth, M. [170] 114
Steele, R. [137] 43, 116
Sternad, M. [21] 5
Stiakogiannakis, I.N. [16] 2
Streit, J. [142] 67, 140
Su, W. [163] 107
Subramaniam, S. [115] 19, 22, 23
Sun, S. [12] 1, 7
Svensson, A. [21] 5
Swanson, E.A. [68] 9, 10

T

T Keller, [93] 15, 49
Takasaki, Y. [136] 41
Talwar, S. [5] 1
Tambosso, T. [118] 21
Tanaka, M. [136] 41
Tanguy, E. [187] 141
Tanno, M. [60] 8
Tanno, M. [14] 1
Tao, X. [47] 7
Taricco, G. [127] 31
Tarighat, A. [168] 111, 112, 128
Tassiulas, L. [44] 7, 8
Tee, R.Y.S. [167] 107, 108, 124
Telek, M. [20] 5
Thomas, J. [98] 16

Thomas, T. [91] . . 15, 17, 42, 73, 80, 130
Thompson, J. [161] 107
Tien, T.P. [106] 17, 41
Tipmongkolsilp, O. [63] 8
Tipmongkolsilp, O. [89] 15
Torrance, J.M. [174] 135
Torsner, J. [95] 16, 40, 73
Toulouse, J. [119] 22
Troger, H. [59] 8
Tse, D.N.C. [56] 7
Tse, D. [38] 6
Tsoulos, G.V. [16] 2
Tzaras, C. [152] 78

V

Vedantam, S. [50] 7
Venturino, L. [43] 7
Verbeke, B. [186] 141
Verdu, S. [55] 7, 8
Verdu, S. [102] 17
Verlinden, J. [182] 140
Vilcot, J.P. [186] 141
Viswanathan, H. [97] 16
Vithanage, C.M. [151] 75
Vithanage, C.M. [156] 89

W

W S Chan, V. [68] 9, 10
Wahlqvist, M. [95] 16, 40, 73
Wake, D. [99] 16, 17, 41, 74
Wake, D. [186] 141
Wake, D. [105] 17, 41
Wake, D. [36] 6, 42, 80
Walke, B.H. [97] 16
Wan, C. [134] 40, 73
Wan Choi, [35] 6
Wang, Y. [12] 1, 7
Waterhouse, R. [77] 10
Waterhouse, R. [107] 17, 41
Watts, A.. [104] 17, 41
Webb, W. [128] 31, 107, 108, 125
Weber, T. [59] 8
Webster, M. [99] 16, 17, 41, 74
Wei Yu, [182] 140
Weimin Xiao, [40] 7
Wenyi Zhang, [50] 7
White, I.H. [104] 17, 41
Widrow, B. [114] 19
Willett, P.K. [54] 7
Willett, P.K. [53] 7
Willett, P.K. [157] 89
Wimpenny, G. [99] 16, 17, 41, 74
Winzer, P.J. [72] 9, 10
Winzer, P.J. [78] 10
Winzer, P.J. [69] 9, 10
Winzer, P.J. [70] 9, 10
Wolter, D.R. [96] 16, 40
Wong, C.H. [94] 15
Wong, W.S. [68] 9, 10
Wonjin Sung, [30] 3, 6
Wonjin Sung, [22] 5
Woogoo Park, [34] 6
Wooten, L. [122] 22
Wooten, L. [121] 22
Wu, N. [162] 107
Wu, W. [144] 74
Wyner, A.D. [125] 24
Wyner, A.D. [80] 10

X

Xiang, Y. [131] 40, 73
Xiang Cheng, [161] 107
Xiang Liu, [123] 23
Xiang Liu, [69] 9, 10

Xiaodong Wang, [43] 7
Xiaohu Ge, [161] 107
Xiaoming She, [45] 7
Xie, L. [109] 17, 19, 41, 44
Xu, X. [24] 5, 6, 12, 13, 74–76, 106, 108, 120
Xu, X. [47] 7
Xu, X. [87] 13
Xu, X. [39] 7, 41, 60
Xu, X. [86] 12
Xu, Z. [25] 5
Xuemin Hong, [161] 107

Y

Yamashita, K. [136] 41
Yan Yao, [32] 6
Yan Yao, [33] 6
Yang, C. [25] 5
Yang, C. [41] 7, 8
Yang, S. [58] 7, 74, 75, 89, 90
Yanikomeroglu, H. [97] 16
Yates, R.D. [178] 140
Yates, R.D. [15] 2
Yeap, B.L. [167] 107, 108, 124
Yee, M.S. [94] 15
Yeniay, A. [119] 22
Yi Su, [179] 140
Yizhuo Yang, [77] 10
Yongxing Zhou, [40] 7
Younsun Kim, [40] 7

Z

Zaghloul, S. [63] 8
Zaghloul, S. [89] 15
Zaidel, B.M. [102] 17
Zaidel, B.M. [158] 107
Zegaoui, M. [186] 141
Zhang, J. [87] 13
Zhang, R. [24] . 5, 6, 12, 13, 74–76, 106, 108, 120
Zhang, R. [87] 13
Zhang, R. [143] 70
Zhang, R. [39] 7, 41, 60
Zhang, R. [86] 12
Zhang, R. [132] 40, 41, 106
Zhang, X. [109] 17, 19, 41, 44
Zhou, X. [100] 17
Zhu, X. [25] 5
Zhu Han, [146] 75
Zhuwei Wang, [180] 140
Zirwas, W. [97] 16
Zweck, J. [76] 10
Zyskind, J.L. [116] 20